Stony Brook University

Towards application of one- and two-dimensional nanomaterials for reinforcement of polymeric nanocomposite bone grafts

A Dissertation Presented

by

Behzad Farshid

to

The Graduate School

in Partial Fulfillment of the

Requirements

for the Degree of

Doctor of Philosophy

in

Materials Science and Engineering

Stony Brook University

August 2015

Stony Brook University

The Graduate School

Behzad Farshid

We, the dissertation committee for the above candidate for the
Doctor of Philosophy degree, hereby recommend
acceptance of this dissertation.

Balaji Sitharaman - Dissertation Advisor

Associate Professor of Biomedical Engineering, Stony Brook University

Yizhi Meng - Chairperson of Defense

Assistant Professor of Materialse Science and Engineering, Stony Brook University

T. A. Venkatesh

Assistant Professor of Materialse Science and Engineering, Stony Brook University

John Simonsen

Professor of Wood Science and Engineering, Oregone State University

Charles Taber

Dean of the Graduate School

Abstract of the dissertation

Towards application of one- and two-dimensional nanomaterials for reinforcement of polymeric nanocomposite bone grafts

By:

Behzad Farshid

Candidate for Doctor of Philosophy Degree

Materials Science and Engineering

Stony Brook University

2015

One- and two-dimensional (1-D and 2-D) nanomaterials possess extraordinary physiochemical properties such as large surface area, excellent mechanical properties, high surface energy and good dispersivity in organic and biological solvents, therefore, they have been extensively used as reinforcing agents to improve the mechanical properties of polymeric scaffolds for bone tissue engineering applications. Carbon nanomaterials such as carbon nanotubes and graphene have been used as reinforcing agents for biodegradable polymeric scaffolds and composites, however, their short- and long-term *in vitro* cytotoxicity and *in vivo* biocompatibility is an area of extensive debate. In this study, we have systematically investigated the effects of addition of low concentrations (0.01-0.2 wt. %) of 1-D and 2-D carbon nanomaterials (graphene oxide nanoplatelets, graphene oxide nanoribbons and carbon nanotubes) and inorganic nanomaterials (boron nitride nanotubes, boron nitride nanoplatelers, tungsten disulfide nanotubes and molybdenum disulfide nanoplatelets) on the mechanical properties,

cytocompatibility, and bioactivity of poly(propylene fumarate) (PPF) nanocomposites towards their potential applications as porous and nonporous implants for bone tissue engineering. Addition of nanomaterials in the PPF matrix improved the compressive and flexural mechanical properties of non-porous crosslinked PPF nanocomposites and porous PPF scaffolds. Our results suggest that in addition to high surface roughness and surface area of the nanomaterials, the presence of functional groups on the surface of nanomaterials leads to an increased nanomaterial-polymer interaction and a uniform dispersion of nanomaterials in polymer matrix which may be the key factors responsible for an improved mechanical reinforcement. The *in vitro* studies showed an excellent cytocompatibility for both carbon and inorganic nanomaterial reinforced PPF nanocomposites and scaffolds. Protein adsorption studies and *in vitro* osteogenic differentiation studies also showed that addition of these 1-D and 2-D carbon and inorganic nanomaterials leads to an improved protein adsorption that promotes osteogenic differentiation and calcium mineralization *in vitro*. and good cytocompatibility of PPF nanocomposites. The long term implication of this research focuses on the development of mechanically strong, biocompatible, biodegradable and bioactive nanocomposites that can potentially replace commercial bone grafts that often lack the required mechanical properties for load bearing bone tissue engineering applications.

Dedication

I would like to dedicate this dissertation to my parents, Houshang and Azar and my siblings, Reza and Parisa. Without their continuing love,support, and encouragement, I could not finish this difficult journey.

Table of Contents

List of tables xi
List of figures xii
List of abbreviations xiv
Acknowledgements xv
Chapter 1: Introduction 1
1.1. Bone defects and clinical need for bone grafts 1
1.2. Implantable bone grafts 2
1.2.1. Properties of a desirable bone graft 2
1.2.2. Types of bone implants 3
1.3. Development of mechanically-strong composite polymeric bone grafts 5
1.4. Emerge of polymeric nanocomposites for bone tissue engineering applications 7
1.5. Motivation of this study 8
1.6. Selection of nanomaterials for this study 10
1.6.1. Single-walled carbon nanotubes (SWCNTs) 10
1.6.2. Multi-walled carbon nanotubes (MWCNTs) 11
1.6.3. Boron nitride nanotubes (BNNTs) 12
1.6.4. Tungsten disulfide nanotubes (WSNTs) 12
1.6.5. Single-walled graphene oxide nanoribbons (SWGONRs) 13
1.6.6. Multi-walled graphene oxide nanoribbons 13
1.6.7. Graphene oxide nanoplatelets (GONPs) 14
1.6.8. Boron nitride nanoplatelets (BNNPs) 14
1.6.9. Molybdenum disulfide nanoplatelets (MSNPs) 15
1.7. Selection of polymer for this study 15
1.7.1. Previous studies on PPF nanocomposites 16
1.8. Outline of this research 16
1.8.1. Tables 18
1.8.2. Figures 18
Chapter 2: Materials and methods 21
2.1. Purchased Materials 21
2.2. Synthesis of PPF polymer 21
2.3. Synthesis of nanomaterials 22
2.4. Characterization of materials and structures 22
2.4.1. Characterization of the synthesized polymer 22

2.4.2. Raman spectroscopy of nanomaterials 23
2.4.3. Transmission electron microscopy (TEM) of nanomaterials 23
2.4.4. Surface area analysis of nanomaterials 23
2.5. Fabrication of porous and nonporous nanocomposite samples 24
2.5.1. Preparation of nonporous nanocomposites 24
2.5.2. Preparation of porous nanocomposite scaffolds 24
2.6. Structural characterization of nanocomposites 25
2.6.1. Transmission electron microscopy (TEM) of nanocomposites 25
2.6.2. Scanning electron microscopy (SEM) of scaffolds 25
2.6.3. Sol-fraction analysis 26
2.6.4. Apparent density measurement of scaffolds 26
2.7. Mechanical testing 27
2.7.1. The mechanical properties of nonporous nanocomposites 27
2.7.2. Mechanical testing of porous nanocomposites 28
2.8. Protein adsorption studies 28
2.9. Cell culture 30
2.9.1. Cell culture for cytotoxicity study of nonporous nanocomposites 30
2.9.2. Cell culture for cellularity study of porous nanocomposite scaffolds 30
2.9.3. Cell culture for differentiation study of MC3T3 cells on nanocomposite scaffolds 31
2.10. *In vitro* studies on nonporous nanocomposites 32
2.10.1. *In vitro* assays 32
2.10.2. Cytocompatibility studies on nanocomposites 34
2.11. Cell attachment and spreading on the surface on nonporous nanocomposites 36
2.11.1. Quantifying attached cells on the surface of nonporous nanocomposites 36
2.11.2. Cell spreading evaluation by confocal fluorescence microscopy 37
2.11.3. Study of cell spreading by Scanning electron microscope (SEM) 38
2.12. *In vitro* cell studies on porous scaffolds 38
2.12.1. Cellularity study using double stranded-DNA (ds-DNA) assay 38
2.12.2. Study of cell spreading on the scaffolds using confocal florescence microscopy 39
2.12.3. Study of cell spreading using scanning electron microscopy (SEM) 39
2.13. Immunohistochemistry (IHC) study of protein expression 40
2.13.1. Immunohistochemistry (IHC) of collagen-I expression 40
2.13.2. Immunohistochemistry (IHC) of integrin β-1 expression 40
2.14. Study of bioactivity on nanocomposite scaffolds 41
2.14.1. Measurement of alkaline phosphatase (ALP) activity 41

2.14.2. Measurement of calcium mineralization 42
2.15. Osmolarity measurements 42
2.16. Statistical analysis 43
2.17. Tables 44
2.18. Figures 45
Chapter 3: Characterization of PPF polymer and nanomaterials 46
3.1. Introduction 47
3.2. Characterization of PPF polymer 47
3.3. Characterization of nanomaterials 47
3.3.1. Raman spectroscopy of nanomaterials 47
3.3.2. Transmission electron microscopy (TEM) study of nanomaterials 48
3.3.3. Atomic force microscopy (AFM) study of nanomaterials 48
3.3.4. Brunauer–Emmett–Teller (BET) analysis to measure specific surface area of nanomaterials 50
3.4. Discussions 50
3.5. Summary 52
3.6. Tables 53
3.7. Figures 54
Chapter 4: Mechanical properties of nonporous 1-D and 2-D nanocomposites 58
4.1. Introduction 58
4.2. Results 61
4.2.1. Compressional and flexural mechanical properties of nanocomposites 61
4.2.2. Sol-fraction analysis of nanocomposites 63
4.2.3. Transmission electron microscopy (TEM) of nanocomposites 64
4.3. Discussions 64
4.4. Conclusions 71
4.5. Tables 73
4.6. Figures 76
Chapter 5: *In vitro* cytocompatibility of nonporous 1-D and 2-D nanomaterial reinforced PPF nanocomposites 81
5.1. Introduction 81
5.2. Results 83
5.2.1. *In vitro* studies to examine the effects of unreacted macromers 83
5.2.2. *In vitro* studies to examine the effects of crosslinked nanocomposites 84
5.2.3. *In vitro* studies to examine the effects of degradation products 85

5.2.4. *In vitro* studies to characterize the cell attachment and spreading on crosslinked nanocomposites 86
5.3. Discussions 88
5.4. Conclusions 92
5.5. Figures 93
Chapter 6: Boron Nitride Reinforced Polymeric Nanocomposites for Bone Tissue Engineering 104
6.1. Introduction 104
6.2. Results 106
6.2.1. Transmission electron microscopy (TEM) of nanocomposites 106
6.2.2. Compressive mechanical properties of nanocomposites 106
6.2.3. Sol-fraction analysis 107
6.2.4. Protein adsorption on crosslinked nanocomposites 107
6.2.5. *In vitro* cytocompatibility study of nanocomposites 108
6.3. Discussions 112
6.4. Conclusions 119
6.5. Tables 120
6.6. Figures 121
Chapter 7: Mechanical properties and cytocompatibility of porous biodegradable PPF nanocomposites 131
7.1. Introduction 131
7.2. Results 133
7.2.1. Characterization of porous scaffolds with SEM 133
7.2.2. Compressive mechanical testing of scaffolds 133
7.2.3. Sol-fraction analysis of scaffolds 135
7.2.4. Protein adsorption 136
7.2.5. Cellularity on nanocomposite scaffolds 137
7.2.6. *In vitro* studies to characterize cellular spreading and infiltration into the scaffolds 138
7.2.7. Collagen-I expression on nanocomposite scaffolds 139
7.3. Discussions 139
7.4. Conclusions 147
7.5. Tables 149
7.6. Figures 151
Chapter 8: Ostogenic Differentiation and Calcium Mineralization in 1-D and 2-D Nanomaterial-Reinforced Polymeric Scaffolds 163
8.1. Introduction 163

8.2. Results 165
8.2.1. Structural characterization of nanocomposite scaffolds 165
8.2.2. Cellularity of MC3T3 cells on scaffolds 165
8.2.3. Alkaline phosphatase activity (ALP) of MC3T3 cells 167
8.2.4. Calcium deposition on scaffolds 167
8.3. Discussions 168
8.4. Conclusions 173
8.5. Tables 175
8.6. Figures 177
Chapter 9: Summary, conclusions and suggestion for future research 182
9.1. Summary 182
9.2. Conclusions 189
9.3. Suggestions for future work 191
References 193

List of tables

Table 1.1. Mechanical properties of human bone. 18
Table 1.2. Mechanical properties of clinically used orthopedic biomaterials 18
Table 2.1. Materials used in this study. 44
Table 3.1. Aspect ratio of nanomaterials used in this study. 53
Table 3.2. Specific surface area of nanomaterials 53
Table 4.1. Compressive modulus of various PPF nanocomposites. 73
Table 6.1. Mechanical properties of PPF nanocomposites. 120
Table 7.1. Porosity of: A) inorganic and B) carbon nanocomposite scaffolds. 149
Table 7.2. Comparison of compressive mechanical properties for nanocomposite scaffolds: (A) compressive modulus, (B) offset yield strength and (C) ultimate strength. 149
Table 8.1. Porosity of the experimental groups used for this study. 175
Table 8.2. Comparison of alkaline phosphatase (ALP) activity after 28 days. 176
Table 8.3. Comparison of calcium mineralization on different experimental groups after 28 days. 176

List of figures

Figure 1.1. Structural representation of 1-D and 2-D nanomaterials used in this study. 19
Figure 1.2. Chemical structure of (a) polypropylene fumarate and (b) N-vinylpyrrolidone..... 20
Figure 2.1. Flow chart of preparing porous and nonporous nanocomposites and testing. 45
Figure 3.1. Nuclear magnetic resonance (NMR) spectra of PPF polymer. 54
Figure 3.2. Raman spectra of nanomaterials. 54
Figure 3.3. TEM images of nanomaterials. 55
Figure 3.4. AFM images of nanomaterials. 56
Figure 4.1. Flowchart depicting the investigation of mechanical properties of PPF nanocomposites..... 76
Figure 4.2.A) Compressive modulus and B) compressive yield strength of PPF nanocomposites as a function of nanostructure loading concentration..... 77
Figure 4.3. Sol fraction analysis of crosslinked PPF nanocomposites 79
Figure 4.4. Representative transmission electron microscopy images of crosslinked PPF nanocomposites at 0.1 wt. % loading concentration of nanomaterials 80
Figure 5.1. Flowchart depicting the experimental outline for cytocompatibility analysis. 93
Figure 5.2. Viability and LDH release of: A) NIH3T3 and B) MC3T3 cells, after 24-h exposure to extracts of unreacted micromeres. 94
Figure 5.3. Viability and LDH release of: A) NIH3T3 and B) MC3T3 cells, after 24-h exposure to extracts of crosslinked nanocomposites. 96
Figure 5.4. Viability and LDH release of: A) NIH3T3 and B) MC3T3 cells, after 24-h exposure to extracts of degradation products 98
Figure 5.5. Osmolality of the extracts of degradation products used for culture of: A) NIH3T3 and B) MC3T3 cells..... 100
Figure 5.6. Fraction of attached cells to the tissue culture poly styrene (TCPS), baseline PPF control and nanocomposites after 24-h incubation.. 101
Figure 5.7. Representative fluorescent microscopy images of attached cells on crosslinked nanocomposites after 5 days of cell culture for NIH3T3 and MC3T3 cells 102
Figure 5.8. Representative SEM images of GONP nanocomposite after cell culture for: A) 1 day and B) 5 days 103
Figure 6.1. TEM images of: A) BNNT and B) BNNP nanocomposites 121
Figure 6.2.A) Compressive modulus, B) compressive yield strength and C) crosslinking density of PPF nanocomposites. 121
Figure 6.3. Adsorption of: A) collagen I, B) fibrin and C) fibronectin after 1, 5 and 9 days incubation at 37°C on the crosslinked PPF nanocomposites 123
Figure 6.4.A) Viability and B) LDH release for MC3T3 cells after 24-h exposure to: the aqueous dispersions of nanomaterials. 125
Figure 6.5. Osmolarity of degradation extracts..... 129
Figure 6.6.A) Fraction of attached MC3T3 cells on the surface of nanocomposites and TCPS control after 24-h incubation 129
Figure 7.1. Flowchart of studying the A) mechanical properties, B) cytocompatibility and C) ECM formation of nanocomposite scaffolds 151
Figure 7.2.A) SEM image of: A) PPF baseline control B) BNNP nanocomposite scaffolds (due to similarity in SEM images between experimental groups only PPF data is shown). 152
Figure 7.3. The mechanical properties of inorganic nanocomposites scaffolds: A) Compressive modulus, B) compressive yield strength C) offset yield strength and D) sol-fraction analysis 153

Figure 7.4. The mechanical properties of nanocomposites scaffolds: (A) Compressive modulus, (B) offset yield strength. 155
Figure 7.5. Collagen-I protein adsorption after 1, 5, and 9 days incubation at 37°C on the PPF nanocomposites. 157
Figure 7.6. Number of viable of MC3T3 cells on porous inorganic scaffolds after 1, 5 and 9 days incubation using: (A) Quantiflour® and (B) Presto Blue® assays 158
Figure 7.7.A) Representative fluorescent microscopy images of attached MC3T3 cells on nanocomposite scaffolds after 5 days incubation 160
Figure 7.8. Representative SEM images of: A) PPF baseline control and B) BNNP nanocomposite scaffolds after 5 days of cell culture 161
Figure 7.9. Immunohistochemistry images of collagen-I expression on nanocomposite scaffolds 162
Figure 8.1. Flowchart of the experimental procedure used in this chapter. 177
Figure 8.2. SEM image of BNNP nanocomposite scaffold 177
Figure 8.3. Number of viable cells on nanocomposite scaffolds and PPF baseline control detected using Quantifluor® assay. 178
Figure 8.4. Fluorescence confocal scanning laser microscopy of MC3T3 cells on experimental samples after 14 days of incubation. 178
Figure 8.5. SEM image of BNNP nanocomposite scaffold after MC3T3 cell culture for 14 days. 179
Figure 8.6. Immunohistochemistry of integrin-β1 expression on experimental groups after 14 days. 179
Figure 8.7. Alkaline phosphatase activity of MC3T3 cells after 14, 21 and 28 days of cell culture on experimental groups 180
Figure 8.8. Calcium mineralization by MC3T3 cells after 14, 21 and 28 days of cell culture on experimental groups 180

List of abbreviations

Abbreviation	Name
AFM	Atomic force microscopy
BCA	bicinchoninic acid assay
BET	Brunauer–Emmett–Teller
BNNT	Boron nitride nanotubes
BNNP	Boron nitride nanoplatelets
DMSO	Dimethyl sulfoxide
DMEM	Dulbecco's Modified Eagle Medium
GONP	Graphene oxide nanoplatelets
GPC	Gel permeation chromatograph
MSNP	Molybdenum disulfide nanoplatelets
MEM-Alfa	Minimum Essential Medium Eagle Alfa
MWGONR	Multi-walled graphene oxide nanoribbons
MWCNT	Multi-walled carbon nanotube
NMR	Nuclear magnetic renounce
PPF	Poly(propylene fumarate)
SEM	Scanning electron microscope
SWCNT	Single-walled carbon nanotubes
SWGONR	Single-walled graphene oxide nanoribbons
TEM	Transmission electron microscope
WSNT	Tungsten disulfide nanotubes

Acknowledgements

I would like to sincerely thank the people who continuously helped me during my research. Firstly, I would like to thank my father who introduced me to the world of materials engineering. I also want to extend my gratitude to Dr. Balaji Sitharaman, my advisor, for his endless help during my doctoral research. I would like to thank Dr. John Simonsen and Dr. Yi-Xian Qin for providing me access to their laboratory facilities. I am grateful to my Ph.D. committee members: Dr. Yizhi Meng and Dr. T. A. Venktash for their guidance and feedback during my research. I would like to thank Dr. Gaurav Lalwani and Meisam ShirMohammadi for their continuous help during my experiments. I would like to thank all the present members and alumni of nano-biosystems laboratory: Dr. Sayan Mullick Chowdhury, Dr. Shruti Kanakia, Sunny Patel, Yahfi Talukdar, Jason Rashkow, Shawn Xie, Stephen Lee and Cassandra Surhland, who always helped me when needed. I acknowledge the support of Dr. Guo Wei Tian, Dr. Stefan Judex, Dr. Liangjun Lin, Jeyantt Srinivas and Susan Van Horn for their help during various stages of this project.

This research was carried out in part at the Center for Functional Nanomaterials (Brookhaven national laboratory, Upton, NY, USA) supported by the office of basic energy sciences (Department of Energy) under contract No. DE-AC02-98CH10886U.S. This work was sponsored by National Institute of Health (NIH) under grant No. 1-DP2OD007394-01.

Chapter 1: Introduction

1.1. Bone defects and clinical need for bone grafts

Bone defects occur due to accidents (fractures), aging (osteoporosis), diseases (such as obesity and osteosarcoma) and surgical procedures. When the bone defect is larger than a critical size (~15mm [1]), external intervention for bone healing is required. The external intervention for small and simple non-critical bone defects is keeping the damaged bone fixed using external fixtures. However, severe and complex bone injuries require surgical procedures that implant artificial bone grafts or implants in the defect site. In the United States, more than 2.2 million surgeries to assist bone regeneration were performed in 2007 with >4 billion dollars being spent annually on bone grafts [2, 3] and an annual growth rate of 6-9% is expected through year 2019 for biomedical implants market [4]. Furthermore, due to obesity and aging population, the rapid rise in the incidences of bone fractures, injuries and trauma have highlighted the pressing need and importance of developing novel technologies and strategies for the development of the next-generation of multifunctional biomaterials for bone tissue engineering.

Depending on the type of bone fracture, the intervention may be passive or active. Passive intervention is performed by using inert orthopedic components that are usually made of non-biodegradable metals such as titanium, stainless steel, gold, and other alloys. Active intervention involves the use of bone grafts (usually fabricated using synthetic materials or natural bone) that are gradually excluded from the body and replaced by newly synthesized bone. Based on the source of natural bone grafts, they are categorized as: (1) autografts, (2) allografts and (3) xenografts. Autografts are harvested from patient's own body, allografts are harvested from a donor and xenografts are extracted from a different species than the recipient. Passive

intervention usually utilizes non-porous devices with desirable properties such as high mechanical strength, biocompatibility and ease of application and its focus is on providing mechanical support to bone during wound healing, On the contrary, the focus of active intervention is not only to provide passive mechanical support but additionally promote ossification (formation of new bone) by assisting the bone regeneration processs by providing osteoinductive and bioactive cues for accelerated bone healing. Furthermore, passive intervention require a secondary surgery for implant extraction whereas active intervention do not since the implants are biodegradable.

In order to address the clinical need for multifunctional, mechanically stable, biocompatible, biodegradable, and bioactive bone grafts, interdisciplinary research focusing on integrating material properties with bone physiology and tissue engineering methods has to be performed [5]. Furthermore, novel approaches such as external graft stimulation, drug delivery, and bioimaging could be combined with conventional bone defect treatments to allow a better control and simultaneous non-invasive monitoring of bone healing processes. In this study, the focus is towards developing new biomaterials for active bone healing that possess multifunctional attributes that have the potential to be harnessed for the abover mentioned next-generation tissue engineering approaches.

1.2. Implantable bone grafts

1.2.1. Properties of a desirable bone graft

Bone grafts should exhibit similar mechanical properties comparable to that of natural bone (Table. 1.1). These properties include (but are not limited to) yield strength, elastic modulus (tensional, compressive and flexural) and toughness. An implant with superior mechanical

properties than native bone leads to abnormal bone growth and bone atrophy due to stress shielding whereas an implant with lower mechanical properties than native bone may fail under external load experienced by the body. Lower toughness will cause graft failure under instantaneous loading which will require expensive follow-up treatments such as replacement and corrective surgeries. In order to promote new bone formation, the graft should be osteoconductive (support extracellular matrix deposition, osteogenic differentiation of mesenchymal stem cells, and bone mineralization) and osteoinductive (ability to induce new bone formation) [6, 7]. Scaffolds are porous structures fabricated using biocompatible, biodegradable polymers that support bone formation, however, their mechanical properties are low making them unsuitable for load bearing bone tissue engineering applications [8]. Furthermore, the synthetic bone grafts need to be safe for clinical use, their safety and efficacy needs to be evaulated first *in-vitro* using cell lines (cytocompatibility) followed by small and large animal studies (biocompatibility) before moving towards clinical trials and eventual human use.

1.2.2. Types of bone implants

Based on the source, the bone grafts are categorized as natural or synthetic. The natural grafts are usually taken from living sources and are categorized as: autografts (from patient own body), allografts (from other donor patients), and xenografts (from other animals/different species). The use of natural bone grafts is often associated with several risks such as disease transfer, lack of consistent supply and donor site morbidity [9]. The synthetic bone grafts can easily be synthesized in bulk-scale with controlled physical and chemical properties. Furthermore, synthetic graft allow ease of sterilization and lack of immunogenity compared to

their natural counterparts. Synthetic bone grafts have been around for two centuries, and recently an extensive amount of effort has been devoted towards their development [10]. Synthetic biomaterials such as metals, ceramics, polymers and their composites have been used as bone grafts. Table 1.2 summarizes the mechanical properties of some of these synthetic biomaterials.

1.2.2.1. Metals

Several inert metals such as stainless steel, titanium, magnesium, and nickel have been used as implants to support bone healing [11]. As Table 1.2 shows, the mechanical properties of metallic implants are significantly higher than native bone, which is beneficial for load bearing applications but may lead to stress shielding and abnormal tissue growth at bone-implant interface [12]. Although biodegradable magnesium implants [13] have been developed recently, the majority of metallic implants release toxic metallic ions when they undergo corrosion, and they need to be extracted by a follow-up surgery.

1.2.2.2. Ceramics

Ceramics such as alumina, zirconia, titania, and calcium phosphate compounds have been used towards the fabrication of bone implants [14]. As seen in Table 1.2, these ceramics usually have higher mechanical properties compared to the native bone that might lead to concerns such as stress shielding. Furthermore, majority of the ceramics are brittle and have low toughness, therefore, they might fail when subjected to tensional or flexural forces or sudden impacts [15].

1.2.2.3. Polymers

Different polymers such as: poly(l-lactide) (LPLA), poly(glycolide) (PGA), poly(dl-lactide) (DLPLA), poly(dioxanone) (PDO), poly(dl-lactide-co-l-lactide) (LDLPLA), poly(dl-lactide-co-glycolide) (DLPLG), poly(glycolide-co-trimethylene carbonate) (PGA), poly(l-lactide-co-glycolide) (LPLG), poly(ε-caprolactone) (PCL), poly(ethylene glycol) (PEG), poly(propylene fumarate) (PPF), polyurethane (PU), poly(lactic acid) (PLA), poly(glycolic acid) (PLGA), poly(butylene succinate) (PBSC) have been used to fabricate polymeric bone implants [16-22]. Interestingly, some of these polymers such as PPF can undergo *in situ* crosslinking after injection and undergo biodegradation. Injectable implants can be applied through minimally invasive methods and can their crosslinking can be triggered by heat, photo-thermal waves, and electro-magnetic waves at physiological temperatures. However, a general limitation of polymeric scaffolds is their low mechanical properties (especially for porous scaffolds) that may lead to failure under physiological loads making them unsuitable for load bearing applications.

1.2.2.4. Composites

To combine the advantages of metals, ceramics and polymers several multi-phasic implants have been developed with polymer/metal, ceramic/polymer and ceramic/metal compositions both at the macro-scale (such as metal/polymer hybrid components) as well as the micron-scale (ceramic incorporated polymers).

1.3. Development of mechanically-strong composite polymeric bone grafts

Over the last decade, several strategies have been used to improve the mechanical properties of polymeric composites and scaffolds for bone tissue engineering applications such as 1) Synthesis of polymers with higher mechanical strength by tailoring molecular weight, type of crosslinker and crosslinking conditions, 2) Optimization of the implant fabrication process to

eliminate defects and inhomogeneity in the structure and 3) Introduction of secondary phase materials with higher mechanical properties (such as nanomaterials, powders and fibers). Among these methods, fabrication of polymeric nanocomposites (reinforcement using nanomaterials) has shown to be an effective method of improving their mechanical properties. With recent advances in nanotechnology, several multi-propose nanostructured polymeric nanocomposites have been developed [23]. There is a high demand for such bone grafts; the global bone implant market is ~29 billion dollars (2007) [3] with a 15% market share for bioresorbable bone grafts [24].

Based on physical properties of polymers such as viscosity, melting point, and attributes such as thermosetting or thermoplastic, various methods such as solution casting, extrusion, injection molding have been used to prepare nanomaterial-reinforced polymeric nanocomposites [25]. Methods such as casting after rotavaporation combined with sheer mixing or micro-wave assisted dispersion of nanomaterials result in a better control over microstructure homogeneity in the polymer. Moreover, techniques such as salt leaching [26], melt-spinning, electro-spinning, drawing, sol-gel, and solid free-form fabrication (or 3-D printing) [27] have led to the fabrication of nanocomposite structures with complicated shapes, uniform porosity, and matrix homogeneity (uniform dispersion of nanomaterials in the polymer matrix) which is challenging both at the macro scale (pore size, distribution and morphology) and the micron scale (nanomaterials dispersion). For amorphous injectable polymers such as bone cements, the control over the microstructure is more limited compared to their dense counterparts and the options for controlling the microstructure are very limited. To address this challenge, multi-phase polymeric nanocomposites with different degradation rates have been used to produce uniform porous structures [28-32].

1.4. Emerge of polymeric nanocomposites for bone tissue engineering applications

The use of nanomaterials with high surface energy, increased surface roughness, high specific surface area, structural defects and excellent mechanical properties as polymeric reinforcing agents results in an efficient load transfer from polymeric network to the nanomaterials [23]. Functionalization of nanomaterials with groups such as oxy, epoxy, oxysulfide, nitrate and carboxy etc results in a uniform dispersion of nanomaterials in the polymer matrix and increase in the crosslinking density of the polymer that improves the mechanical properties of the nanocomposites [33-35]. Due to these potential benefits, several inorganic nanomaterials (such as alumoxane [36], hydroxyapatite [37], titania [38], zirconia [39], alumina [40], silica [41] and aluminosilicate [42]), as well as organic nanomaterials (such as carbon nanotubes [43] and graphite [44]) have been used as reinforcing agents. However, the study of nanomaterials for bone tissue engineering applications has been limited to materials such as aluminosilicate [42] or calcium-phosphate reinforced polymeric nanocomposites [45]. A systematic study on the possible effects of nanomaterials with varied morphology and extraordinary physiochemical properties (inorganic and organic one- and two-dimensional (1-D and 2-D) nanomaterials such as carbon nanotubes [46] and graphene [47, 48]) on the mechanical properties of biodegradable polymeric nanocomposites needs to be investigated.

A variety of characterization methods such as scanning electron microscopy (SEM), transmission electron microscopy (TEM), atomic force microscopy (AFM), optical microscopy (OM), Brunauer-Emmett-Teller (BET) specific surface area measurement, x-ray microcomputed tomography (microCT) porosimetry, and viscometry have been widely used to evaluate structural characteristics of nanomaterials and nanomaterial-reinforced polymeric nanocomposites [26, 49, 50]. Mechanical properties (tensile, compressive, flexural, hardness,

fatigue and toughness) of the polymeric bone grafts has been reported prior to implantation, in contact with cells, and post-implantation using *in vitro* and *in vivo* studies. Although intrinsic mechanical properties of the polymer nanocomposites can be derived from mechanical testing before implantation, the true mechanical properties of bone grafts after implantation can only be assessed using *in vivo* models that include data on body/biomaterials interactions [3, 51, 52]. This research will use many of the aforementioned methods for development of new multifunctional nanocomposite bone grafts.

1.5. Motivation of this study

There is a need for development of multifunctional and mechanically robust polymeric bone implants for load bearing applications as majority of the FDA-approved polymeric composite grafts such as Allofuse®, Boneplast®, Healos®, Opteform® and Mastergraft® utilize demineralized bone matrix (DBM, derived from euthanized animals) or calcium phosphate compounds [53] which cannot be stimulated using external sources, and they cannot be monitored *in vivo* for tissue regeneration. Although such secondary phase materials have shown various degrees of improvement in the mechanical properties of polymeric bone grafts, their mechanical properties are low to permit the tissue engineering of load bearing bones [2]. Furthermore, it is desirable to have the capability to control and monitor bone healing post scaffold implantation. Towards this aim, we decided to use one- and two-dimensional (1-D and 2-D) carbon and inorganic nanomaterials as polymeric reinforcing agents to improve the mechanical properties of PPF polymer due to the following factors:

a) These nanomaterial have high intrinsic mechanical properties, defects in their structure, high surface energy and specific surface area. Therefore, potentially, these nanomaterials

can provide effective mechanical reinforcement against tensile, compressional and flexural loading at low nanomaterial loading concentrations [54].

b) Unlike DBM that is associated with risks of disease transfer, these synthetic nanomaterials are easy to sterilize and synthesize.

c) Responsiveness of these nanomaterial to light [55] and electro-magnetic waves [56] which may enable forming, curing, shaping and monitoring of the nanocomposite post surgical or injectable implantation [57-60].

d) High thermal conductivity, large specific surface area and the presence of functional groups on the surface of these nanomaterials can improve the crosslinking density of polymeric nanocomposites even at lower crosslinking temperatures thereby improving the mechanical properties.

e) These nanomaterial for are highly functionalizable, therefore, their physical properties can be further modified for multifunctional stimulus responsive applications such as drug delivery and treatment monitoring [61, 62].

f) An increase in the surface energy of nanocomposites due to the presence of nanomaterials can lead to improved biomaterial/cell interactions, critical for tissue engineering and regenerative medicine applications [63].

Based on these potential benefits, we propose that by incorporation of 1-D and 2-D nanomaterials with extraordinary physiochemical properties mentioned above, we can increase the load transfer ability from the polymer matrix to underlying nanomaterials and improve the crosslinking density of polymeric networks. These effects can significantly increase the mechanical properties of nanocomposites even at low nanomaterial loading concentrations. Additionally, the electrical and magnetic properties of these nanomaterials can be exploited to

fabricate stimulus responsive scaffolds capable of *in situ* forming (via controlled crosslinking), for real-time non-invasive monitoring (to investigate the accuracy of injection, the integrity of implant during healing process and ossification) and drug delivery (by delivering bone morphogenic growth factors) applications. Moreover, it is expected that the increased surface energy and roughness of nanomaterials will improve cell proliferation, extracellular matrix (ECM) deposition, and eventual differentiation of stem cells to osteoblasts [64-66]. To show the potential application of these nanocomposites for bone tissue engineering applications, we also investigated their *in vitro* cytocompatibility and bioactivity.

1.6. Selection of nanomaterials for this study

As we reviewed earlier, various inorganic and organic 1-D and 2-D nanomaterials such as single- and multi-walled carbon nanotubes (SWCNTs and MWCNTs), boron nitride nanotubes (BNNTs), tungsten disulfide nanoplatelets (WSNTs), single- and multi-walled graphene oxide nanoribbons (SWGONRs and MWGONRs), graphene oxide nanoplatelets (GONPs), boron nitride nanoplatelets (BNNPs) and molybdenum disulfide nanoplatelets (MSNPs) were used in this study. This section provides a introduction of their physiochemical properties.

1.6.1. Single-walled carbon nanotubes (SWCNTs)

SWCNTs (Figure 1.1) are 1-D carbon nanostructures that have been widely used for electronics (transistors [67]), energy (supercapacitors [68], batteries [69] and hydrogen storage [70]) and biomedical (drug delivery [71], photo-thermal therapy [72] and bioimaging [73]) applications. SWCNTs exhibit excellent compressive modulus (~1600-6000 GPa [74]) and have been used as reinforcing agents for PLGA [75], PU [74], PCLA [76], PLLA [77] and PPF [78]

polymers. Functionalization of SWCNTs and their effect on mechanical properties of polymeric nanocomposites has been reported previously [79]. Shi et al. have reported the *in vitro* cytocompatibility [80] and Sitharaman et al. have reported the *in vivo* biocompatibility of SWCNTs reinforced PPF nanocomposites and scaffolds in a rabbit model [81]. Li et al. have reported the osteoinductivity of SWCNTs [82] for bone tissue engineering applications.

1.6.2. Multi-walled carbon nanotubes (MWCNTs)

MWCNTs (Table 1.1) are 1-D carbon nanostructures that have been used in energy storage (supercapacitors [83] and batteries [84]), electronic devices [85], gas sensors [86] and biomedical (bioimaging [87] and drug delivery [88]) applications. MWCNTs exhibit a high compressive modulus (~1800 GPa [89]) and, therefore, have been used as reinforcing agents to improve the mechanical properties of PLGA [90], PCLA [91], PLA [92] and PU [93] polymers for bone tissue engineering applications. Addition of MWCNTs has resulted in the improvement of fracture toughness [94] and tensile strength of polymeric nanocomposites [95] at low nanomaterial loading concentrations (>0.3 wt.%). Zhang et al. have reported cytocompatibility of MWCNT-PLLA nanocomposites for tissue engineering, Abarrategi et al. reported the cytompatibility of MWCNT-chitosan nanocomposites using myoblastic mouse cells [96] and Sahiti et al. [97] have reported the osteoinductivity of MWCNT reinforced PLA polymer for bone tissue engineering applications. Carbon nanotubes also have been used to trigger cell stimulation [98] and to fabricate shape memory components [91].

1.6.3. Boron nitride nanotubes (BNNTs)

BNNTs are 1-D inorganic nanostructures (Figure 1.1) and have been used for energy storage (hydrogen storage [99]), electronic devices [100], force sensors [101], pH sensors [102] and biomedical (biosensors [103], bioimaging [104] and drug delivery [105]) applications. Because BNNTs exhibit an excellent compressive modulus (~600 GPa [106]), they have been used as reinforcing agents to improve the mechanical properties of PLGA [107] polymer for bone tissue engineering applications. Additionally they have shown improvement in fracture toughness of ceramics [108]. Ricotti et al. [107] and Ciofani et al. [109] have reported the *in vitro* and *in vivo* cyto- and bio-compatibility of BNNTs. Moreover, Li et al. showed an increased osteoinductivity in presence of BNNTs [110]. Addition of BNNTs results in an improved thermal conductivity in polymeric nanocomposites [111]. BNNTs have also been investigated as stimulus responsive materials for inducing osteogenic differentiation [112].

1.6.4. Tungsten disulfide nanotubes (WSNTs)

WSNTs are 1-D inorganic nanostructures (Figure 1.1) that have been used in energy storage devices (batteries [113]), electronic devices [114], lubricants [115] and biosensors [116]. WSNTs show an extra-low friction constant [117] and a high compressive modulus (~200 GPa [118]) and therefore they have been used as reinforcing agents to improve the mechanical properties of PLGA polymer [119] for bone tissue engineering applications. Moreover, WSNTs have extremely low coefficient of friction and, therefore, they may potentially be beneficial to improve the injectability of polymeric nanocomposites by reducing viscosity [120]. Goldman et al. showed cytocompatibility of WSNTs for biomedical engineering applications [121].

1.6.5. Single-walled graphene oxide nanoribbons (SWGONRs)

SWGONRs are 2-D carbon nanostructures (Figure 1.1) synthesized by unzipping of SWCNTs through ion bombardment [122] or by using strong oxidizers ($KMnO_4$) [123]. They have been used in energy applications (thermally conductive components [124]), electronic devices [125], and biomedical engineering applications (drug delivery [126]). They possess a high compressive modulus (~250 GPa [127]) and have been used as reinforcing agents to improve the mechanical properties of epoxy resins [128] for industrial applications. Moreover, SWGONRs have structural defects due to unzipping reaction [129] that increases nanomaterial/polymer interface. Tian et al. and Akhavan et al. have reported the cyto- and bio-compatibility of SWGONRs for biomedical applications [130, 131].

1.6.6. Multi-walled graphene oxide nanoribbons

MWGONRs are 2-D carbon nanostructures (Figure 1.1) synthesized by the longitudinal unzipping of MWCNTs [123] and have been used in energy storage (supercapacitors [132]), electronic (devices [133]), and biomedical (biosensors [134] and drug delivery [135]) applications. Although the mechanical properties of MWGONRs have not been investigated independently, we expect them to exhibit similar defects and mechanical properties to SWGONRs [128]. Based on these potential benefits, they have been used as reinforcing agents to improve the mechanical properties of PVA [136], PLGA [137] and PU [138] polymerc for biomedical applications. Furthermore, electrical properties of reduced graphene oxide have been harnessed towards the development of shape memory polymeric nanocomposites [139]. Chowdhuri et al. [135] and Zhang et al. [140] have reported the cyto- and bio-compatibility of MWGONRs for biomedical engineering applications.

1.6.7. Graphene oxide nanoplatelets (GONPs)

GONPs are 2-D carbon nanostructures (Figure 1.1) synthesized by exfoliating graphite powder [141] using a modified Hummer's method for preparation of graphitic oxide [142]. GONPs have been used in energy devices (photo catalysts [143], supercapacitors [144] and batteries [145]), electronic devices [146], and biomedical applications (bioimaging [147], biosensors [148] and drug delivery [149]). GONPs are semiconductor [150] and have excellent mechanical properties similar to other carbon nanostructures (compressive modulus of ~1000 GPa [151]) and therefore have been used as reinforcing agents to improve the mechanical properties of chitosan [152] and PLA [153] polymers for biomedical applications. Wu et al. [154] and Zhan et al. [155] have reported the cyto- and bio-compatibility of GONPs for tissue engineering applications, respectively, and Bressen et al. have reported the osteoinductivity of GONPs [156].

1.6.8. Boron nitride nanoplatelets (BNNPs)

BNNPs are 2-D inorganic nanostructures (Figure 1.1) synthesized by chemical exfoliation of boron nitride powder [157] and have been used in energy applications (thermally conductive components [158]), electronic devices [159], lubricants [160] and biomedical applications (bioimaging [161] and biosensors [162]). BNNPs show excellent mechanical properties (compressive modulus ~200 GPa [163]) and an increased fracture toughness [158]. Therefore, they have been used as reinforcing agents to improve the mechanical properties of epoxy [164] and PBS [16] for industrial applications, respectively. Weng et al. demonstrated cytocompatibility of BNNPs for biomedical applications [165].

1.6.9. Molybdenum disulfide nanoplatelets (MSNPs)

MSNPs are 2-D inorganic nanostructures (Figure 1.1) synthesized by chemical vapor deposition (CVD) [166]. They have been used in energy storage (batteries [167], photo catalysts [166]), sensors [168], electronic devices [169] and biomedical (bioimaging [170] and drug delivery [171]) applications. MSNPs have a extremely low coefficient of friction [172] and excellent mechanical properties (~150 GPa compressive modulus [118]). MSNPs have been used as reinforcing agents to improve the mechanical properties of chitosan polymer for biomedical applications[173]. Additionally they exhibit a very low coefficient of friction and therefore may potentially be beneficial to improve the injectability of polymeric nanocomposites by reducing viscosity. Wu et al. have reported their cytocompatibility for biomedical applications [174].

1.7. Selection of polymer for this study

Poly(propylene fumarate) (PPF) polymer was used in this study as the polymer matrix and N-vinyl pyrrolidone (NVP) was used as the crosslinker (Figure 1.2). PPF is a biocompatible, biodegradable and injectable polymer [19, 175-177] widely used in bone tissue engineering [178, 179], bioimaging [180] and drug delivery [181] applications. PPF is synthesized via a two-step reaction of propylene glycol and di-ethyl fumarate [175] and has similar mechanical properties compared to cancellous bone with a compressive modulus of ~1 GPa [19]. NVP crosslinker is a cytocompatible [182] and biodegradable [183] polymer. Studies have elucidated the crosslinking mechanism of PPF polymer. Briefly, an exothermic crosslinking reaction starts as the free radical initiator breaks down the C=C double bonds in NVP and C=O bonds in PPF. Post bond cleavage, the radical centers coalasce leading to the crosslinking of PPF and NVP [19].

1.7.1. Previous studies on PPF nanocomposites

Carbon nanomaterials such as single-walled carbon nanotubes (SWCNTs) [184], carbon fullerenes (C_{60}) [185] and inorganic nanomaterials such as hydroxyapatite (HAP) [186-188], silica [189], titania [190], zirconia [191] and alumoxane [192-194] have been used as reinforcing agents to improve the mechanical properties of PPF nanocomposites [26]. Among these nanomaterials, only carbon nanotubes exhibit a large aspect ratio and are stimulus responsive. Shi et al. [80] and Sitharaman et al. [49, 195] have reported cytocompatibility, mechanical properties and biocompatibility of SWCNT reinforced PPF nanocomposites. Horch et al. [196] and Mistry et al. [194, 197] have reported the mechanical properties, cytocompatibility and biocompatibility of alumoxane reinforced PPF nanocomposites.

1.8. Outline of this research

As a first step towards the application of nanomaterial reinforced PPF nanocomposite as potential bone grafts, their mechanical properties and *in vitro* cytocompatibility need to be thoroughly investigated. Toward this goal, we first investigated the efficacy of 1-D and 2-D carbon and inorganic nanomaterials as reinforcing agents to improve the mechanical properties of non-porous and porous PPF nanocomposites at low (0.01-0.2 wt. %) loading concentrations. Next, we investigated the *in vitro* cytotoxicity and protein adsorption capabilities of porous and non-porous PPF nanocomposites using MC3T3 pre-osteoblast cell line and various (collagen-I, fibrin, and fibronectin) proteins. Finally, we investigated the effects of nanostructure loading on the expression of extracellular matrix (ECM) proteins such as integrin and fibronectin and calcium mineralization by MC3T3 cells cultured on porous and non-porous PPF nanocomposites. Our results provide new insights towards the use of novel 1-D and 2-D carbon

and inorganic nanomaterials towards the fabrication of mechanically strong, biodegradable, biocompatible and bioactive multifunctional polymeric nanocomposites for bone tissue engineering applications.

1.8.1. Tables

Table 1.1. Mechanical properties of human bone [198].

Type of bone	Compressive strength (MPa)	Bending strength (MPa)	Compressive modulus (GPa)	Fracture Toughness (MPa $m^{1/2}$)
Cancellous	2–12	—	0.05–0.5	—
Cortical	100–230	50–150	7–30	2–12

Table 1.2. Mechanical properties of clinically used orthopedic biomaterials [199, 200].

Material	**Density (g/ml)**	**Elastic modulus (GPa)**	**Modulus/density**
Alumina	3.9	345	88.5
Hydroxyapatite	3.2	279	87.2
Aluminum	2.7	70	25.9
Stainless steel	8.0	193	24.1
Titanium	5.0	114	22.8
Zirconium	6.5	83	12.8
Graphite	1.8	276	153.3
Cortical bone	2.1	20	9.5
Cancellous bone	1	0.1	1
Poly(methyl methacrylate) PMMA)	1.2	3	2.5
Poly (propylene fumarate) (PPF)	1.4	1	0.7

1.8.2. Figures

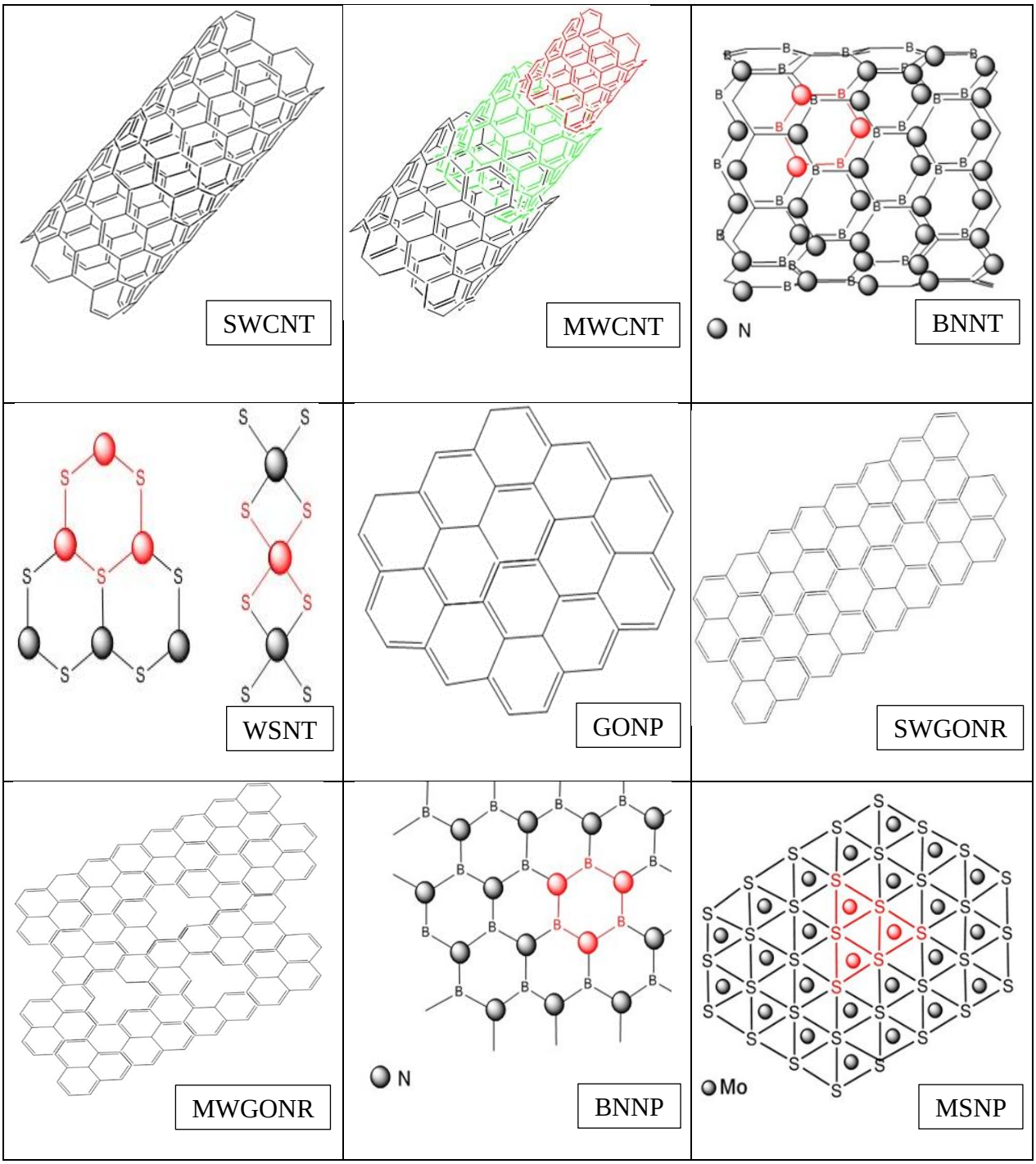

Figure 1.1. Structural representation of 1-D and 2-D nanomaterials used in this study (created using ChemDraw® software). SWCNTs (single walled carbon nanotubes), MWCNTs (multi walled carbon nanotubes), BNNTs (boron nitride nanotubes), WSNTs (tungsten disulfide nanotubes), GONPs (graphene oxide nanoplatelets), SWGONRs (single walled graphene oxide nanoribbons), MWGONRs (multi walled graphene oxide nanoribbons), BNNPs (boron nitride nanoplatelets) and MSNPs (molybdenum disulfide nanoplatelets).

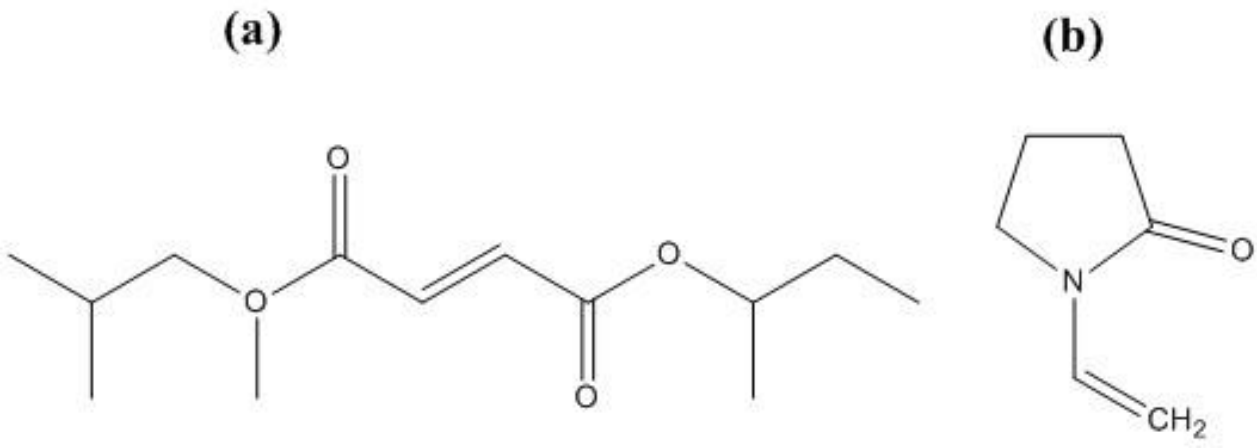

Figure 1.2. Chemical structure of (a) polypropylene fumarate and (b) N-vinylpyrrolidone (created using ChemDraw® software).

Chapter 2: Materials and methods

This chapter describes the materials, methods, and experimental techniques used in this study. The flowchart in Figure 1 describes the experimental procedure followed in this study.

2.1. Purchased Materials

Diethyl fumarate, hydroquinone, N-vinyl pyrrolidone (NVP), potassium permanganate, zinc chloride, benzoyl peroxide (BP), graphite, molybdenum trioxide, sulfur and multi-walled carbon nanotubes were obtained from Sigma Aldrich (St. Louis, MO, USA). Other analytical grade materials such as hydrogen peroxide, ethyl ether, sodium sulfate, methylene chloride, isopropanol, ethanol, chloroform, hydrochloric acid, phosphoric acid, sulfuric acid and calcium hydroxide were purchased from Fisher Scientific (Pittsburgh, PA, USA). Propylene glycol was purchased from Acros Organics (Pittsburgh, PA, USA). SWCNTs were purchased from CheapTubes Incorporated (Battleboro, VT, USA) and WSNTs were donated by Nanomaterials Ltd. (Yavne, Israel). BNNTs and BNNPs were purchased from Daekin University (Daekin, Victoria, Australia) and PHmatter (Columbus, OH, USA), respectively. Nanomaterials were not subjected to any chemical treatment (i. e. functionalization) for this study.

2.2. Synthesis of PPF polymer

PPF was synthesized according to a well established method following a two-step reaction of propylene glycol and diethyl fumarate [175]. The molecular weight of the synthesized

PPF polymer was monitored throughout the synthesis process using gel permeation chromatograph (GPC, Thermo Fisher Inc., Vernon Hills, IL, USA).

2.3. Synthesis of nanomaterials

SWGONRs, MWGONRs, GONPs, and MSNPs were synthesized for this study. Single- and multi-walled graphene oxide nanoribbons were synthesized according to an oxidative unzipping method developed by Kosynkin et al. [123] from single- and multi-walled carbon nanotubes, respectively. GONPs were synthesized according to a modified Hummer's method [201]. MSNPs were synthesized reaction of molybdenum trioxide and sulfur at high temperatures inside a tube furnace using a blanket of inert gas [202].

2.4. Characterization of materials and structures

2.4.1. Characterization of the synthesized polymer

The structure of polymer was characterized using a 500Hz Oxford proton nuclear magnetic resonance spectroscope (NMR, Oxford, UK). Samples were dissolved in 0.5 ml of deuterated- chloroform (d-chloroform Sigma Aldrich, St. Louis, MO) prior to analysis and transferred to NMR tubes (Norell, Landsville, NJ, USA). The molecular weight of the polymer was characterized by gel permeation chromatograph (GPC, Thermo Fisher Inc., Vernon Hills, IL, USA).

2.4.2. Raman spectroscopy of nanomaterials

A ProRaman-L spectroscope (TSI, Shoreview, MN, USA) was used to acquire Raman spectra of nanomaterials in 100-3000 cm^{-1} wavenumber range. The nanomaterials were dispersed in a 50:50 mixture of ethanol:distilled water, bath sonicated for 15 minutes (FS30H, Fisher Scientific, Madison, CT, USA), and probe sonicated for 2 minutes (2 sec 'on', 1 sec 'off' cycle, LX750, Cole-Parmer, Vernon Hills, IL, USA) in microcentrifuge tubes (Eppendorf AG, Schönenbuch, Switzerland). Next, the tubes were subjected to centrifugation at 10,000 rpm for 5 minutes and 20 μL of supernatant was drop casted onto fresh cleaved silicon wafers (Ted Pella, Redding, CA, USA), air-dried, and used for Raman spectroscopy.

2.4.3. Transmission electron microscopy (TEM) of nanomaterials

TEM was used for morphological characterization of nanomaterials and nanocomposites. The nanomaterial dispersions used for Raman spectroscopy were drop casted, on TEM grids (mesh size: 300, holey lacey carbon grid, Ted Pella, Redding, CA, USA). Then, the grids were air-dried overnight and used for microscopy. Imaging was carried out using a TECNAI BioTwin G^2 TEM (FEI Technologies, Hillsboro, OR, USA) at an accelerating voltage of 80 kV.

2.4.4. Surface area analysis of nanomaterials

The surface area analysis of nanomaterials was performed using a Brunaur-Emmett-Teller (BET) method by gas adsorption at 77 K using nitrogen (for WSNTs, SWCNTs and MWCNTs) and krypton (for SWGONRs, MWGONRs, GONPs and MSNPs).

2.5. Fabrication of porous and nonporous nanocomposite samples

2.5.1. Preparation of nonporous nanocomposites

PPF Polymer nanocomposites were fabricated as reported in literature [50, 62]. The 0.01-0.2 wt. % loading concentration of each nanomaterial (listed in Table 2.1) was selected because this concentration of nanomaterials does not lead to a viscoelastic behavior in the nanomaterial/polymeric blend and elliminates difficulties while injection (like trapped air bubbles) [50, 62]. Briefly, PPF and NVP were mixed in chloroform followed by addition of of BNNTs, SWCNTs, MWCNTs, WSNTs, SWGONRs, MWGONRs, GONPs, BNNPs and MSNPs. The blend of PPF, NVP, and nanomaterials were subjected to bath sonication for 30 minutes (FS30H sonicator, Fisher Scientific, Madison, CT, USA) followed by probe sonication for 2 minutes (2 sec 'on' and 1 sec 'off' cycle; LPX-750 sonicator, Cole Parmer, Vernon Hills, IL, USA). Chloroform was removed from the mixture using a rotavaporator (R-215, Büchi, New Castle, DE, USA), and thermal cross-linking of nanocomposite was initiated by addition of 1 wt. % benzoyl peroxide (BP) as radical initiator. The crosslinking of nanocomposites was completed overnight at 60 °C inside custom made Teflon molds (Mcmaster-carr, Princeton, NJ, USA). Cylindrical specimens with diameter of 6.5 mm and height of 14 mm were cut into disks with 1 mm thickness by a low-speed diamond saw (Model 650, South Bay Technology, Redondo Beach, CA, USA).

2.5.2. Preparation of porous nanocomposite scaffolds

For fabrication of porous scaffolds, nanocomposite mixtures were prepared similarly to the previous section. After the nanocomposite blends were subjected to rotavaporation (R-215 Rotavap, Büchi, New Castle, DE, USA) for chloroform removal, thermal crosslinking of nanocomposite was started by adding 1 wt. % benzoyl peroxide (Sigma Aldrich, St. Louis, MO,

USA). The nanocomposite mixture was then mixed with sodium chloride (Fisher Scientific, Agawam, MA, USA) to induce porosity (weight of NaCl was calculated as described by Shi et al. [26] for 85% porosity). Crosslinking of the nanocomposite/salt blend was completed overnight in Teflon molds at 80°C (Mcmaster-carr, Princeton, NJ, USA) and cylindrical nanocomposite samples with 6.5 mm diameter and 16 mm height were fabricated. Then, the cylinders were placed inside sealed glass containers and immersed in DI water (refreshed every day) for 14 days on a shaker table at 100 rpm. Porous samples were used for mechanical testing, structural characterization, *in vitro* cytocompatibility, protein adsorption studies, and bioactivity assesment.

2.6. Structural characterization of nanocomposites

2.6.1. Transmission electron microscopy (TEM) of nanocomposites

Structure of nanocomposite was analyzed using TEM. The nonporous nanocomposite specimens were cut into 500 nm thick slices using an ultra-microtome and mounted on TEM grids (mesh size:400, Copper grid, Ted Pella, Redding, CA, USA). Imaging was performed using a TECNAI BioTwin G^2 TEM (FEI Technologies, Hillsboro, OR, USA) at an accelerating voltage of 80 kV.

2.6.2. Scanning electron microscopy (SEM) of scaffolds

SEM was used to study the microstructure of nanocomposite scaffolds. The scaffolds were fixed on SEM sample holders using a double-sided tape (Ted Pella, Redding, CA, USA), and sputter coated with gold (Au). Secondary electron imaging was carried our an accelerating voltage of 5 kV using a JOEL 7600F high resolution SEM (Peabody, MA, USA) at the Center of

Functional Nanomaterials (CFN) located at Brookhaven National Laboratory (BNL, Upton, NY, USA).

2.6.3. Sol-fraction analysis

Sol-fraction analysis was performed to assess the crosslinking density of PPF nanocomposites as reported previously [50, 62]. The rationale of sol-fraction analysis is based on the fact that non-crosslinked polymer is soluble in methylene chloride whereas the crosslinked polymer is not [184]. Nanocomposite samples after crosslinking were crushed, and approximately 2.5 gram of their crushed powder was placed inside a sealed vial containing 20 mL of methylene chloride. The vials were kept on a shaker plate at 100 rpm for 14 days at room temperature. After 14 days, the contents were passed through a filter paper (Whatman® N.40 filter, Madison, CT, USA). The respective weights for solid residual material were recorded (accuracy 0.0001 gram), and the sol-fraction was calculated using the following equation:

$$\text{Sol-Fraction } (\%) = \frac{Wi-(Wf+p-Wp)}{Wi} * 100$$

Where W_i is the initial weight of nanocomposite, W_{f+p} is the weight of filter paper and recovered nanocomposite specimen after 14 days, and W_p is the weight of filter paper. PPF polymer served as a baseline control, and a sample size of n=5 was used for each experimental group.

2.6.4. Apparent density measurement of scaffolds

The weight change and dimensions of scaffolds before and after salt leaching were recorded, and the apparent porosity of scaffolds was calculated using following equation:

$$\varepsilon\ (\%) = 100 * V_{NaCl} / (V_{NaCl} + V_{nc})$$

Where ε stands for apparent porosity, V_{NaCl} is the volume of NaCl progen and V_{nc} is the volume of nanocomposite. V_{NaCl} and V_{nc} were calculated based on theoretical density of NaCl (2.16 g/cm^3) and crosslinked PPF nanocomposites (1.50 g/cm^3).

2.7. Mechanical testing

2.7.1. The mechanical properties of nonporous nanocomposites

2.7.1.1. Compressive mechanical testing

The compressive mechanical testing of the nonporous specimens was carried out using an uniaxial mechanical testing system (Instron 4010, Norwood, MA, USA) according to American society of testing materials (ASTM) standard D695-08 [203]. The cylindrical specimens were compressed along their longitudinal axis at 0.1 mm/min strain rate with a 10 KN load cell. The force-displacement data was recorded and converted to stress-strain curve. The compressive modulus was determined as the slope of the initial linear portion of stress-strain curve whereas the compressive yield strength was determined as the maximum recorded stress for each specimen before plastic deformation (offset yield strength at 0.2% strain). A sample size of n=5 was used for compressive mechanical testing and PPF scaffolds was used as a baseline control.

2.7.1.2. Flexural mechanical testing

The flexural mechanical testing was performed on nonporous nanocomposites according to ASTM standard D790-07 [204] using a three-point bending setup. The samples (strips with 10 mm width and 70 mm) were placed on spans 55 mm apart and load was inserted midway until failure. Force and displacement were recorded, and the following equations were used for calculation of flexural modulus and flexural strength, respectively:

$E_F = L^3 s/4wd^3$

$F_M = 3\mathrm{PL}/2\mathrm{wt}^2$

2.7.2. Mechanical testing of porous nanocomposites

2.7.2.2. Compressive mechanical testing

Compressive mechanical testing of nanocomposite scaffolds was performed using an uniaxial Instron 4301 mechanical testing system (Norwood, MA, USA) according to American society of testing materials (ASTM) standard (D695-02a) [205]. Compression testing was carried out along longitudinal axis of scaffolds at a 0.2 min^{-1} strain rate using a 220 N load cell. The force versus displacement was recorded during compressive testing and then converted to a stress-strain curve with respect to gauge length. The slope of linear portion in stress-strain curve showed the compressive modulus, intersection of stress-strain curve and a line parallel to linear portion at 0.2% strain represented the offset yield strength and the maximum stress in sample represented ultimate strength for the scaffolds. The crosslinked PPF scaffolds served as baseline control and three specimens (n=3) were studied for compression mechanical testing.

2.8. Protein adsorption studies

A well-established solution depletion method was used to study protein adsorption (from a solution with knows protein concentration) on the surface of the crosslinked nanocomposites and porous scaffolds using bicinchoninic acid (BCA) assay [206]. The bicinchoninic acid chelates with Cu^{+} ions (formed as a result of Cu^{+2} reduction present in cupric sulfate reagent). The reduction of Cu^{2+} ions is directly proportional to protein concentration in the solution that can be quantified using a plate reader [207]. Solutions of fetal bovine serum (FBS), bovine

collagen-I, human fibronectin and mouse fibrin (Sigma Aldrich, St. Louis, MO, USA) were used for this study (concentration of 400 μg/dL). Briefly, collagen-I was dissolved in 1 mL acetic acid (Fisher Scientific, Madison, CT, USA) and fibrin was dissolved in a 0.01 N sodium hydroxide solution (Fisher Scientific, Madison, CT, USA). Fibronectin and FBS were dissolved in DPBS. Solutions containing FBS, collagen-I, fibrin and fibronectin were then added to DPBS to prepare experimental protein solutions. The nanocomposite disks or scaffolds were placed inside 24-well plates and incubated at 37°C with protein solutions for 1, 5 and 9 days. After each time point, 15 μL of supernatant was transferred to a fresh 96-well plate in order to quantify its protein concentration using BCA assay (Thermo Scientific, Madison, CT, USA). For the assay, 200 μL of working solution was added to each well, then, the plates were incubated for 30 minutes, and the absorbance was recorded at 562 nm using a spectramax-M2 plate reader (Molecular Devices, Sunnyvale, CA, USA). A standard curve was prepared according to the manufacturer's protocol using bovine serum albumin (BSA) solution at different concentrations as standards. The fraction of adsorbed proteins on the specimens was calculated using the following equation:

$$\text{Fraction of adsorbed protein } (\%) = \left(\frac{Ci - Cs}{Ci}\right) * 100$$

Where C_i is the initial concentration of proteins in the solution and C_s is the concentration of proteins in the solution after incubation. For protein adsorption studies, polystyrene (PS) 24-well plates (non-plasma treated to minimize erroneous protein adsorption by substrate) were used. Wells containing protein solutions served as positive controls, wells containing DPBS served as negative controls, and PPF polymer served as a baseline control. Six samples (n=6) were tested for each experimental group.

2.9. Cell culture

2.9.1. Cell culture for cytotoxicity study of nonporous nanocomposites

MC3T3 pre-osteoblasts and NIH3T3 fibroblasts were used for *in vitro* cytotoxicity studies. MC3T3 cells (passages 10-14) were suspended in minimum essential medium-alpha (MEM-α, Gibco, Grand Island, NY, USA) and NIH3T3 cells were suspended in Dulbecco's minimum essential medium (DMEM, Gibco, Grand Island, NY, USA). Both MEM-α and DMEM were supplemented with 10 vol. % fetal bovine serum (FBS, Gibco, Grand Island, NY, USA) and 1 vol. % antibiotics (Penicillin-streptomycin, Gibco, Grand Island, NY, USA) and seeded inside tissue culture polystyrene (TCPS) petri-dish with 10 cm diameter (Sarsdedt®, Newton, NC, USA). The cells were incubated in a humidified atmosphere at 37°C with 5% carbon dioxide (95% air). For cytotoxicity studies, MC3T3 cells were washed using Dulbecco's phosphate buffer saline (DPBS, Gibco, Grand Island, NY, USA), trypsinized using 0.05% Trypsin-EDTA (Gibco, Grand Island, NY). Then, the cells were seeded in 96-well plates (BD Falcon, Franklin Lakes, NJ, USA) at a density of 5000 cells/well. The cells were incubated for 24 hours before commencement of the assays. For cell attachment study, MC3T3 cells were seeded at a density of 50,000 cells/well in 6-well plates (Corning Inc., NY, USA) for 24 hours.

2.9.2. Cell culture for cellularity study of porous nanocomposite scaffolds

MC3T3 pre-osteoblasts were used for *in vitro* analysis of cellularity and collagen-I expression. Briefly, the frozen MC3T3 cells (passages 10-14) were suspended in minimum essential medium-alpha (MEM-α, Gibco, Grand Island, NY, USA) supplemented with 10 vol. % fetal bovine serum (FBS, Gibco, Grand Island, NY, USA) and 1 vol. % penicillin-streptomycin antibiotics (pen-strep®, Gibco, Grand Island, NY, USA). The suspension was centrifuged, and cells were seeded in tissue culture polystyrene petri-dish (TCPS, Sarsdedt®, Newton, NC, USA)

containing MEM-α media. Next, the petri-dishes were stored in a humidified incubator at 37°C with of 5% carbon dioxide (95% air). After 85% confluency (observed under light microscope) the cells were detached using 0.05% Trypsin-EDTA (Gibco, Grand Island, NY) and seeded on sterilized (under UV for three hours) scaffolds inside 6-well plates (Corning Inc., Corning, NY, USA) at a density of 100,000 cells/specimen. Cell suspensions were gradually added to the scaffolds (in 20 µL portions) to ensure attachment to the scaffolds. After 24 hours of incubation at 37°C, the scaffolds were transferred to a fresh 6-well plate containing MEM-α media. The cellularity and collagen-I expression on scaffolds were studied later.

2.9.3. Cell culture for differentiation study of MC3T3 cells on nanocomposite scaffolds

MC3T3 pre-osteoblasts were used for *in vitro* analysis of osteogenic differentiation and calcium mineralization studies. Briefly, frozen MC3T3 cells (passages 10-14) were thawed in minimum essential medium-alpha (MEM-α, Gibco, Grand Island, NY, USA) supplemented with 10 vol. % fetal bovine serum (FBS, Gibco, Grand Island, NY, USA) and 1 vol. % penicillin-streptomycin antibiotics (pen-strep®, Gibco, Grand Island, NY, USA). After centrifugation, the cells were seeded in polystyrene tissue culture dishes (TCPS). After reaching 85% confluency, the cells were trypsinized (Gibco, Grand Island, NY, USA) and subsequently seeded on sterilized scaffolds (under ultraviolet light for 3 hours) inside 24-well plate (BD Falcon, Franklin Lakes, NJ, USA) at a density of 50,000 cells/scaffold. After 24 hours of incubation at 37°C, the scaffolds were transferred to a fresh 24-well plate (in order to eliminate the cells adhered to the wells) and 1 ml osteogenic media was added to each well. To prepare osteogenic media, 50 mg/ml ascorbic acid (Sigma-Aldrich, St. Louis, MO, USA) and 10mM β-glycerophosphate

(Sigma-Aldrich, St. Louis, MO, USA) were dissolved in MEM-α. The media was changed at 2 day intervals throughout the entire study.

2.10. *In vitro* studies on nonporous nanocomposites

2.10.1. *In vitro* assays

2.10.1.1. Presto Blue assay

Cell viability was assessed using a resazurin-based Presto Blue® assay (Invitrogen, Grand Island, NY, USA) according to the manufacturer's protocol. To determine the viability of cells using Presto Blue, the enzymatic reduction of cell permeable resazurin dye into highly fluorescent pink resorufin dye was measured. The reduction happens only in the presence of viable cells that can be quantified by measuring the color change [208]. After 24 hours of exposure to the experimental media, 10 μL of Presto Blue working solution was added to each well. After 2 hours of incubation in the dark, fluorescence spectra of plates were recorded using a spectramax-M2 plate reader (Molecular Devices, Sunnyvale, CA, USA) at excitation and emission wavelengths of 560 and 590 nm, respectively. Cell numbers were determined using a standard curve. Wells containing known numbers of viable cells served as live (positive) controls whereas blank wells containing only media (without cells) served as dead (negative) controls. Six wells (n=6) were tested for each experimental group. The fraction of live cells for each experimental group was calculated using the following equation:

$$\text{Viability } (\%) = \frac{Fs - Fb}{Fc - Fb} * 100$$

Where F_s is fluorescence of tested specimen, F_b is the background fluorescence for the blank media and F_c is the fluorescence of live (positive) control.

2.10.1.2. Lactate dehydrogenase (LDH) assay

The membrane integrity of cells was investigated as an indicator of cytotoxicity using an enzyme based lactate dehydrogenase assay (LDH-TOX7; Sigma Aldrich, St. Louis, MO, USA) according the manufacturer's protocol. Thia assay measures the cytotoxicity by quantifying the amount of intracellular LDH enzyme released in the media by apoptotic or necrotic cells [209]. After 24 hours of exposure to experimental solutions, 96-well plates were subjected to centrifugation at 4000 rpm to remove cellular debris. 50 µL of supernatant was transferred to a fresh 96-well plate and mixed with 100 µL of LDH working solution. After 45 minutes of incubation in dark, absorbance of each well was recorded using a spectramax-M2 plate reader (Molecular Devices, Sunnyvale, CA, USA) at an absorbance wavelength of 492 nm. To compare cytotoxicity among experimental groups, LDH release was determined by normalizing the measured absorbance of experimental wells to reference wells (with 5000 lysed NIH3T3 or MC3T3 cells) and using a standard curve. Wells containing lysed cells (exposed to 20 µL of lysis buffer for 15 minutes) served as a positive (dead) control whereas wells containing only cell culture media (without cells) served as a negative (live) control. Six wells (n=6) were tested for each experimental group. The LDH release was calculated using the following equation:

$$\text{LDH release (\%)} = \frac{As-Ab}{Ac-Ab} * 100$$

Where A_s is the absorbance of experimental sample, A_b is the back ground absorbance of blank media, and A_c is the absorbance of positive control (lysed cells) [135].

2.10.1.3. Calcein-AM (LIVE) staining

Calcein-acetoxymethyl ester (calcein-AM) staining has been widely used to selectively stain metabolically active cells [80]. Briefly, 5 µL of calcein-AM stock solution (40mM, Sigma

Aldrich, St. Louis, MO, USA) was mixed with 10 mL DBPS to prepare a working concentration of 4 μM. The working solution was added to each well containing nanocomposite specimens (after cells culture) and was incubated at 37°C for 25 minutes. Specimens were rinsed with DPBS and placed in 35-mm glass bottom petri dishes (Mattek Corp., Ashland, MA, USA) for confocal fluorescence microscopy at 485 excitation wavelength and 530 nm emission wavelength. TCPS wells with same surface area (compared to nanocomposite samples), after seeding at 5000 cells/well and 24-h incubation, served as positive (live) control whereas PPF disks after seeding at 5000 cells/well and 24-h incubation after 15 minutes treated with lysis solution served as negative controls. Two samples (n=2) were stained for each experimental group.

2.10.2. Cytocompatibility studies on nanocomposites

2.10.2.1. Cytocompatibility study of nanomaterials

To evaluate the cytotoxicity of nanomaterials, a direct extraction method according to ISO 10993-5 [210] standard was used. Cytotoxicity of all carbon nanomaterials at concentrations used in this study has been studied before, therefore, cytotoxicity analysis was performed only for BNNTs and BNNPs. Briefly, the nanomaterials were dispersed in MEM-α media and subjected to bath sonication for 30 minutes (FS30H, Fisher Scientific, Madison, CT, USA). Stock solution of nanomaterial dispersions at 100 μg/mL concentration were prepared and further diluted using blank media to prepare 10 μg/mL and 1 μg/mL dilutions. Then, media containing 100, 10 and 1 μg/mL nanomaterials were added to 96-well plates containing MC3T3 cells at a density of 5000 cells/well. Finally, after incubation for 24 hours at 37°C, cell viability

was evaluated using Presto Blue and LDH assay. Six samples (n=6) were studied for each experimental group.

2.10.2.2. Cytocompatibility study of components prior to crosslinking

To evaluate the cytotoxicity of nanocomposite components before crosslinking, blends of PPF/NVP and PPF/NVP/Nanomaterials were prepared by dispersing nanomaterials at 0.2 wt. % concentration in non-crosslinked PPF/NVP (50:50) blend. After UV-sterilization, cytotoxicity evaluation was performed according to the extract dilution testing method [210]. The blends were incubated with MEM-α or DMEM media for 24 hours (0.33 mL media per cm^2 contact area). After incubation, the supernatant was extracted and diluted 10 and 100 folds to prepare 1X, 10X, and 100X experimental media. MC3T3 or NIH3T3 cells were exposed to 1X, 10X, and 100X experimental media for 24 hours. Cell viability was evaluated using Presto Blue assay whereas cytotoxicity of non-crosslinked nanocomposites against NIH3T3 and MC3T3 cells was quantified using LDH assay. Six samples (n=6) were studied for each experimental group.

2.10.2.3. Cytocompatibility study of the crosslinked nanocomposites

Cytotoxicity of crosslinked nanocomposites was assessed using an extract-dilution method as previously described [210]. Crosslinked nanocomposite disc specimens (6 mm diameter, 0.5 mm thickness) were UV-sterilized for 3 hours, washed with DPBS, and incubated with MEM-α or DMEM media for 24 hours (0.33 mL per cm^2 contact area). MC3T3 cells were treated with extracted media (1X) and their 10X and 100X dilutions for 24 hours. Cell viability was evaluated using Presto Blue. The cytotoxicity of crosslinked nanocomposites for MC3T3

and NIH3T3 cells was quantified using LDH assay. Six samples (n=6) were studied for each experimental group, and PPF composite served as a baseline control.

2.10.2.4. Cytocompatibility study of nanocomposite degradation products

Crushed nanocomposite powders were subjected to accelerated degradation using calcium hydroxide ($Ca(OH)_2$, Fisher Scientific, Madison, CT, USA) and phosphoric acid (H_3PO_4, Fisher Scientific, Madison, CT, USA) [80]. 2.5 grams of the crushed nanocomposite powder were added into a 20 mL glass vial containing 1N $Ca(OH)_2$ and placed on a shaker table at 100 rpm for 14 days. The degradation products were then neutralized (pH ~7.4) using H_3PO_4 and filtered. Due to the absence of ingredients and supplements for cell survival in the degradation products, after neutralization and filtering, the degradation mixture was added to cell culture media at a 1:1 ratio to prepare 2X experimental media. 10X and 100X experimental media were prepared by 10 and 100 fold dilutions of the degradation products. MC3T3 or NIH3T3 cells were incubated with 2X, 10X, and 100X experimental solutions for 24 hours. Cell viability was evaluated using Presto Blue assay and cytotoxicity of degradation products was quantified using LDH assay. Degradation products of crosslinked PPF polymer were used as a baseline control. Six samples (n=6) were used for each experimental group.

2.11. Cell attachment and spreading on the surface on nonporous nanocomposites

2.11.1. Quantifying attached cells on the surface of nonporous nanocomposites

UV-sterilized crosslinked nanocomposite disc specimens were placed inside 6-well plates. Autoclaved stainless steel rings were placed on top of each disk and NIH3T3 and MC3T3 cells were seeded at a density of 20,000 cell/specimen inside the steel rings gradually over a span

of 30 minutes. After another 30 minutes of incubation, 100 μL MEM-α or DEM media was added inside each ring and incubated for 90 minutes. Next, the rings were removed, and 1.8 mL MEM-α or DEM media was added to each well. After 24-h incubation, cells were trypsinized and counted using a hemacytometer (Fisher Scientific, Madison, CT, USA). Cell attachment (fraction of attached cells) was calculated for n=3 samples using the following equation:

$$\text{Cell attachment } (\%) = (\frac{Ns}{Ni})*100$$

Where N_s is the number of cells counted using hemocytometer and N_i is the initial number of cells. Fraction of cells attached to TCPS with the same surface area was recorded for comparison.

2.11.2. Cell spreading evaluation by confocal fluorescence microscopy

NIH3T3 and MC3T3 cells were seeded onto nanocomposite disk specimens at a cell density of 5×10^4 cells/specimen and incubated for 5 days. Then, the disks were washed with phosphate buffered solution (DPBS), incubated with calcein-AM (4μM) for 25 minutes (for selective staining of viable cells [211]), and placed in a glass-bottom petri-dish (Mattek Corporation, Ashland, MA, USA) for fluorescence imaging using a confocal laser scanning microscope (LSM 510 META, Carl Zeiss, Thornwood, NY, USA) equipped with a 10X objective lens. Imaging was carried out at excitation and emission wavelengths of 488 and 515 nm, respectively. Tissue-culture polystyrene (TCPS) samples with same surface area after seeding and incubation for 24 hours were used as positive controls whereas cell cultured PPF after 15 minutes treatment with lysis solution served as negative controls. PPF composites were used as a baseline control. Two samples (n=2) were imaged for each experimental group.

2.11.3. Study of cell spreading by Scanning electron microscope (SEM)

The cellular attachment and spreading of MC3T3 cells on nanocomposite surfaces were investigated by SEM. The nanocomposite disks used for confocal microscopy were fixed using 2.5 % glutaraldehyde (Electron Microscopy Sciences Inc., Hatfield, PA, USA) solution, washed twice using DBPS, dehydrated in gradient series of ethanol solutions (70%, 80%, 90% and 100% ethanol), and vacuum dried overnight. The disks were sputter coated using gold (coating thickness: 3 nm) and imaged at 5 kV using a high resolution 7600F HRSEM (JEOL, Peabody, MA, USA) at the Center for Functional Nanomaterials (CFN) in Brookhaven National Laboratory (Upton, NY, USA).

2.12. *In vitro* cell studies on porous scaffolds

2.12.1. Cellularity study using double stranded-DNA (ds-DNA) assay

Number of viable MC3T3 cells (cellularity) on each scaffold was quantified for n=5 samples using quantifluor®-ds DNA assay (Promega, Madison, WI, USA). Briefly, after 1, 5 and 9 days of incubation, scaffolds were washed twice using ice cold DPBS (Gibco Life, Grand Island, NY, USA) and placed inside microcentrifuge tubes (Eppendorff AG, Hamburg, Germany) and subjected to double freeze-thawing cycles followed by 30 minutes of bath sonication (FS30H, Fisher Scientific, Madison, CT, USA) to lyse the attached cells. The cell lysates were then centrifuged for 5 minutes at 10000 rpm to expel cellular debris. Finally, 100 µL of supernatant was collected and placed in a fresh 96-well plate and mixed with 100 µL of Quantifluor® working solution to determine ds-DNA content according to manufacturer's protocol. After mixing the lysate with working solution and 10 minutes of incubation in dark, the florescence spectra was recorded using a spctramax-M2 palate reader (Molecular devices, Sunnyvale, CA, USA) at an excitation wavelength of 480 nm and an emission wavelength of 570

nm. PPF scaffold without cells served as a negative control and PPF scaffolds (with cells) served as a baseline control.

2.12.2. Study of cell spreading on the scaffolds using confocal florescence microscopy

Spreading of the cells on nanocomposite scaffolds was studied using a LSM 510-META laser scanning microscope (Carl Ziess, Thornwood, NY, USA) for n=2 samples. After 5 days of incubation, the scaffolds were washed twice using ice-cold DBPS and stained using 0.05 vol. % calcein-AM solution in DPBS (40 mM, Life Technologies, Grand Island, NY, USA). After incubation in the dark for 45 minutes, the scaffolds were placed inside glass-bottom petri-dishes (Mattek Corporation, Ashland, MA, USA) and laser confocal images were acquired at excitation and emission wavelengths of 488 nm and 515 nm, respectively. PPF scaffolds (without cells) served as a negative control whereas PPF scaffolds (with cells) were used as baseline controls.

2.12.3. Study of cell spreading using scanning electron microscopy (SEM)

SEM imaging was performed to visualize cell spreading and attachment on the nanocomposite scaffolds. Briefly, after 5 days of incubation, the scaffolds were washed twice with ice-cold DPBS and fixed using a 2.5 % glutaraldehyde solution in DPBS (Electron Microscopy Sciences Inc., Hatfield, PA, USA) for 45 minutes. Then, the samples were washed with gradient series of ethanol (70%, 80%, 90% and 100%), dried in air and vacuum-dried overnight. Next, SEM samples were sputter coated with gold (Au) and imaging was carried out at 5 kV using a high resolution 7600F HRSEM (JEOL, Peabody, MA, USA) at the Center for Functional Nanomaterials (CFN) in Brookhaven National Laboratory (Upton, NY, USA).

2.13. Immunohistochemistry (IHC) study of protein expression

2.13.1. Immunohistochemistry (IHC) of collagen-I expression

Collagen-I expression by MC3T3 cells on nanocomposite scaffolds was studied as reported previously to assess the formation of extracellular network (ECM). Two (n=2) samples were used for analysis [212, 213]. After 5 days of cell culture, the scaffolds were fixed using 2.5 % glutaraldehyde in DBPS. Next, the samples were blocked using a buffer containing 0.3 M glycine and 1 % bovine serum albumin (BSA, Sigma-Aldrich, St. Louis, MO, USA) for 30 minutes. Next, the scaffolds were washed using immunofluorescence buffer (IFB, 0.1% BSA in DPBS) and placed inside 6-well plates for antibody staining. For primary antibody staining, the scaffolds were incubated with a working solution (2 µl/ml in IFB) of mouse collagen-I monoclonal antibody produced in mouse (cat. No. C 2455, Sigma-Aldrich, St. Louis, MO, USA) for 60 minutes. The scaffolds were washed twice using IFB and incubated for 60 minutes in secondary antibody working solution. For secondary antibody staining, the scaffolds were incubated in a 6-well plate with a 2 µl/ml working solution of rhodamine (TRITC)–conjugated anti-mouse secondary antibody (cat. No. T 2402, Sigma-Aldrich, St. Louis, MO, USA) in IFB. Finally, the scaffolds were washed twice using IFB and used for confocal microscopy. The confocal microscopy was carried out using a LSM 510-META laser scanning microscope (Carl Ziess, Thornwood, NY, USA) at an excitation wave length of 600 nm and an emission wavelength of 688 nm.

2.13.2. Immunohistochemistry (IHC) of integrin β-1 expression

To analyse the expression of integrin β-1, the nanocomposite scaffolds after 7 days of cell culture at 37°C were fixed using 2.5 % glutaraldehyde in DPBS. Cells were permeabilized for 10 min using aqueous 0.1 % Triton 100X solution (Fisher Scientific, Pittsburg, PA, USA) in DPBS.

Then, the scaffolds were immersed in a blocking buffer of 0.3 M glycine and 1 % bovine serum albumin (BSA, Sigma-Aldrich, St. Louis, MO, USA) in DPBS for 30 minutes. The Scaffolds were then washed with immunofluorescence buffer (IFB, 0.1% BSA in DPBS) and placed inside 6-well plates for antibody staining. First, the scaffolds were incubated with primary mouse anti-integrin (β-1) antibody (2 µl/ml in IFB, Abcam, Cambridge, MA, USA) for 60 minutes, then the scaffolds were washed twice using IFB. Next, the scaffolds were incubated for 60 minutes at 37°C in dark using mouse secondary antibody working solution (2 µl/ml in IFB) of rhodamine (TRITC)–conjugated anti-mouse secondary antibody (cat. No. T 2402, Sigma-Aldrich, St. Louis, MO, USA). Then, the scaffolds were washed using IFB (2x). Fluorescence imaging was carried out using a LSM 510-META confocal microscope (Carl Ziess, Thornwood, NJ, USA) at an excitation wave length of 600 nm and an emission wavelength of 688 nm for n=2 samples. PPF scaffold without cells served as negative control while PPF scaffold after 7 days of cell culture served as a baseline control.

2.14.Study of bioactivity on nanocomposite scaffolds

2.14.1. Measurement of alkaline phosphatase (ALP) activity

To quantify ALP activity, 100 µL of the cell lysate was mixed with 100 µL of 1 mg/mL p-nitrophenyl phosphate (Sigma-Aldrich, St. Louis, MO, USA) and incubated at 37°C for 30 minutes. The reaction was then stopped by adding 50 µL of 2N sodium hydroxide (NaOH, Fisher Scientific, Pittsburg, PA, USA) and absorbance spectra was recorded at 405 nm using a spectra max-M2 plate reader (Molecular devices, Sunnydale, CA, USA). The standard curve was prepared according to manufacturer's protocols. This value was then normalized to number of cells on the scaffolds. The activity of intracellular alkaline phosphatase (ALP) of MC3T3 cells

after 14, 21 and 28 days of incubation at 37°C in osteogenic media was quantified using five (n=5) samples from each experimental and control group.

2.14.2. Measurement of calcium mineralization

To assess calcium mineralization, 100 µL of cell lysate was mixed with 100 µL of 1M acetic acid (Fisher Scientific, Pittsburg, PA, USA) and incubated overnight. Then, 20 µL of solution was transferred to a fresh 96-well plate and 300 µL of Arsenazo-III assay (Fisher Diagnostics Inc., Middleton, VA, USA) solution was added. After 60 seconds of incubation in the dark, the absorbance spectra was recorded at 650 nm using a spectra max-M2 plate reader (Molecular devices, Sunnydale, CA, USA). A standard curve for calcium contentment was prepared according to the manufacturer's protocol and normalized with respect to the number of cells quantified using Quantifluor assay. The calcium content in cell lysate after 14, 21 and 28 days of incubation at 37°C in osteogenic media was studied using three (n=3) samples from each experimental and control group.

2.15. Osmolarity measurements

To assess the cytotoxicity of nanocomposite degradation products against NIH3T3 or MC3T3 cells, the osmolarity of 2X, 10X and 100X experimental solutions was measured using a 3D3 osmometer (Advanced Instruments Inc., Norwood, MA, USA) for n=3 samples. Degradation extracts of PPF composites and scaffolds were used as a baseline control. The osmolarity of DEM, MEM-α media, filtered 400 µg/ml $Ca_3(PO)_4$ suspension was also recorded for comparison purposes.

2.16. Statistical analysis

All statistical analysis was performed for a 95% ($p<0.05$) confidence interval and using GraphPad Prism® software. To determine the significant differences among results, a single factor analysis of variance (one way ANOVA) followed by Tukey's post-hoc test [214] was performed. Data is reported as mean ± standard deviation.

2.17. Tables

Table 2.1. Experminetal groups used in this study.

Abbreviation	Name
PPF	polypropylene fumarate
SWCNTs	single-walled carbon nanotubes
MWCNTs	multi-walled carbon nanotubes
SWGONRs	single-walled graphene oxide nanoribbons
MWGONRs	multi-walled graphene oxide nanoribbons
GONPs	graphene oxide nanoplatelets
WSNTs	tungsten disulfide nanotubes
BNNTs	boron nitride nanotubes
MSNPs	molybdenum disulfide nanoplatelets
BNNPs	boron nitride nanoplatelets

2.18. Figures

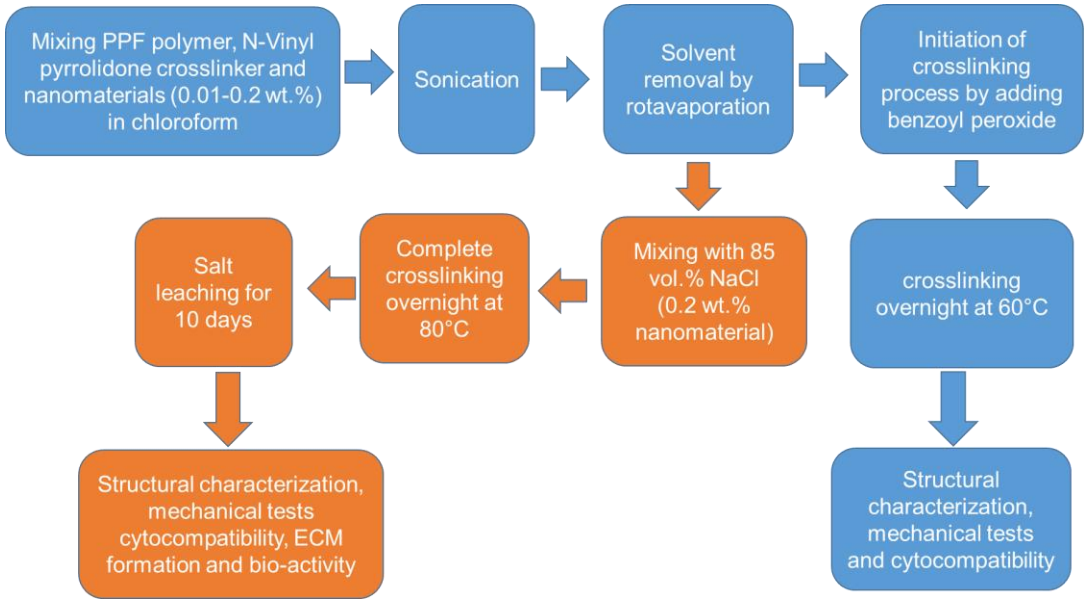

Figure 2.1. Flow chart of depicting the preparation of porous and nonporous nanocomposites for experiments.

Chapter 3: Characterization of PPF polymer and nanomaterials

Preface

The data in this chapter have been reproduced with permission from the following articles:

[1]. **Farshid, Behzad**, Gaurav Lalwani, and Balaji Sitharaman. "*In vitro* cytocompatibility of one-dimensional and two-dimensional nanostructure-reinforced biodegradable polymeric nanocomposites." Journal of Biomedical Materials Research Part A, 103(7), 2015, 2309-21.

[2]. Lalwani, Gaurav, Allan M. Henslee, **Behzad Farshid**, Priyanka Parmar, Liangjun Lin, Yi-Xian Qin, F. Kurtis Kasper, Antonios G. Mikos, and Balaji Sitharaman. "Tungsten disulfide nanotubes reinforced biodegradable polymers for bone tissue engineering." Acta biomaterialia 9, no. 9 (2013): 8365-8373.

[3]. Lalwani, Gaurav, Allan M. Henslee, **Behzad Farshid,** Liangjun Lin, F. Kurtis Kasper, Yi-Xian Qin, Antonios G. Mikos, and Balaji Sitharaman. "Two-dimensional nanostructure-reinforced biodegradable polymeric nanocomposites for bone tissue engineering." Biomacromolecules 14, no. 3 (2013): 900-90

The authors of these articles have contributed to the data presented in this chapter.

3.1. Introduction

This chapter discusses the various phyisochecmical properties of PPF polymer and nanomaterials. Structural and chemical characterization of nanomaterials was performed using transmission electron microscope (TEM) and Raman spectroscopy whereas PPF polymer was characterized using nuclear magnetic spectroscopy (NMR, structural characterization) and gel permeation chromatograph (GPC, molecular weight characterization).

3.2. Characterization of PPF polymer

The NMR spectra of PPF polymer (Figure 3.1) showed two major peaks at ~7 PPM and ~1.5 PPM along with two peaks of moderate intensity at ~4 PPM and ~5.7 PPM. Additionally, other minor peaks were observed in the NMR spectra. The molecular weight of PPF was ~3138 Da with a poly dispersity index (PDI) of ~1.38.

3.3. Characterization of nanomaterials

3.3.1. Raman spectroscopy of nanomaterials

Figure 3.2 displays Raman spectra of SWCNTs, MWCNTs, BNNTs, WSNTs, SWGONRs, MWGONRs, GONPs, BNNPs and MSNPs. Carbon nanomaterials (SWCNTs, MWCNTs, SWGONRs, MWGONRs, and GONPs) showed two peaks at ~1330 cm^{-1} and ~1580 cm^{-1} wavenumbers. Raman peaks at 1330 cm^{-1} and 1584 cm^{-1} were observed for SWCNTs (Figure 3.2.A). The peaks at 1340 cm^{-1} and 1573 cm^{-1} were observed for MWCNTs (Figure 3.2.B). SWGONRs (Figure 3.2.C) showed peaks at 1332 cm^{-1} and 1586 cm^{-1} while MWGONRs (Figure 3.2d) showed peaks at 1336 cm^{-1} and 1584 cm^{-1}. GONPs (Figure 3.2.E) showed peaks at 1338 cm^{-1} and 1574 cm^{-1}. WSNTs (3.2.F) showed peaks at 350 cm^{-1} and 420 cm^{-1} whereas BNNTs (Figure 3.2.G) showed three major peaks at 474 cm^{-1}, 1366 cm^{-1} (E_{2g} peak) and 2414

cm^{-1}. MSNPs (3.2.H) showed six peaks at 230 cm^{-1}, 274 cm^{-1}, 330 cm^{-1}, 400 cm^{-1}, 816 cm^{-1} and 1000 cm^{-1}. BNNPs (Figure 3.2.I) showed peaks at 1370 cm^{-1} (E_{2g} peak) and 2444 cm^{-1}.

3.3.2. Transmission electron microscopy (TEM) study of nanomaterials

Figure 3.3 displays TEM images of various nanomaterials used in this study. SWCNTs and MWCNTs were present as individual and bundled nanotubes. The diameter and length of SWCNTs were ~1-2 nm and ~20-30 μm, respectively. The diameter and length for MWCNTs were ~20-30 nm and ~200 μm, respectively. TEM images of SWGONRs and MWGONRs showed a smooth planar structure with few edge defects and indicated the complete unzipping of SWCNTs and MWCNTs into nanoribbons (width of nanoribbons ~π x diameter). The width and length of SWGONRs were ~4 nm and ~20-30 μm, respectively. The width and length for MWGONRs were ~20-30 nm and ~200 μm, respectively. GONPs were disk shaped with ~200-1600 nm diameter and ~5 nm thickness. MSNPs were hexagonal nanoplatelets with ~100 nm diameter and ~8 nm thickness. WSNTs were tube-shaped with ~15-100 nm diameter and ~4 μm length. BNNTs showed characteristic tubular morphology with ~100 nm diameter and 1-2 μm length. BNNPs were stacks of polygonal-shape platelets with smooth planar structure. BNNPs had diameter between 200-1800 nm.

3.3.3. Atomic force microscopy (AFM) study of nanomaterials

Figure 3.4 displays the structural characterization of nanostructures by AFM. AFM analysis of SWGONRs (Figure 3.4.A), and MWGONRs (3.4.B) showed their single and multi-layered ribbon-like shapes, respectively. Their nanoribbon structure was uniform and smooth, with few edge defects. AFM images of SWGONRs showed that they possess an average width of

3−6 nm and length 500−1000 nm; confirming complete unzipping of SWCNT (diameter 1−2 nm, length 1−1.5 μm, width of nanoribbon = π * diameter). Due to the displacement of the sp^3 hybridized carbon, and the presence of oxygen, SWGONRs are expected to be slightly thicker than pristine graphene sheet, which possesses a van der Waals thickness of 0.34 nm similar to the reports in the literature [215, 216]. AFM height profile indicates that SWGONRs are single-layered graphene oxide sheets (Z ≈ 1 nm). MWGONRs have an average width of 60−90 nm corresponding to the complete unzipping of MWCNTs possessing diameter ranging from 20 to 30 nm (π *diameter). MWGONRs show 500-1500 nm length and have a height (Z) of about 7 nm (AFM height profile) corresponding to ≈21 graphene layers (the value was calculated assuming single layer graphene thickness of ~0.34 nm). GONPs (Figure 3.4.C) were disk-shaped with ≈10−40 nm diameter and 3−5 nm height, corresponding to ≈9−14 graphene layers. MSNPs (Figure 3.4.D) had a hexagonal morphology, with diameters between 50 and 200 nm and height (Z) ≈8 nm. WSNTs (Figure 3.4.E) existed as individually dispersed sharp needle-like nanotubes possessing a mean outer diameter of ~100 nm and length between 1–15 μm.

For comparison purposes, AFM images of SWCNTs and MWCNTs are also included. SWCNTs (Figure 3.4.F) and MWCNTs (Figure 3.4.G) were present as individual and bundled nanotubes. The AFM height profile indicated the existing of SWCNTs as bundles of 2–5 nanotubes (considering the height (Z) of SWCNTs ~1 nm). Additionally, thick bundles of SWCNTs (~20–25 nanotubes) were also imaged. SWCNTs possess an average diameter of 1–2 nm and length of ~2–5 μm. MWCNTs were also imaged as individual and bundles of nanotubes possessing diameters of ~40–70 nm and lengths of ~0.5–2 μm. The nanotube structure of SWCNTs, MWCNTs and WSNTs appears smooth without any edge defects. Based on AFM and TEM analysis, the aspect ratio of nanomaterials were calculated and presented in Table 3.1.

3.3.4. Brunauer–Emmett–Teller (BET) analysis to measure specific surface area of nanomaterials

The specific surface area of nanomaterials used for this study is presented in Table 3.2. Results showed higher surface area for carbon nanomaterials compared to inorganic nanomaterials. Among nanomaterials, SWCNTs with specific surface area of 353 $m^2.g^{-1}$ exhibited the largest specific surface area while MSNPs showed the minimum specific surface area (17 $m^2.g^{-1}$). The specific surface area of SWCNTs, MWCNTs and MWGONRs were between ~200-300 $m^2.g^{-1}$, SWGONRs and GONPs exhibited specific surface area of ~95 $m^2.g^{-1}$ and 45 $m^2.g^{-1}$, respectively.

3.4. Discussions

Raman spectroscopy analysis of nanomaterials (Figure 3.2) shows that SWCNTs, MWCNTs, SWGONRs, MWGONRs, and GONPs exhibit the characteristic D (1330-1340 cm^{-1}), G (1573-1586 cm^{-1}) and G' (2650 cm^{-1}) bands of graphene. Structural defects and functional groups are the cause of the first order D band (one phonon double resonance resulting from the disruption of C=C bonds [217]), the G band is a result of in-plane vibrations involving sp^2 hybridized carbon atoms. G' band (also called 2-D) is a second order mode of the D band. Raman spectroscopy analysis of SWCNT and MWCNTs showed a low D/G ratio (I_D/I_G) suggesting a pristine structure of nanotubes. SWGONRs, MWGONRs, and GONPs showed an increase in the intensity ratio (I_D/I_G) which suggests the presence of structural defects due to functional groups that disrupt the sp^2 π-bonds of carbon atoms [217-219].

Raman spectra of BNNTs and BNNPs show intense peaks around ~1370 cm^{-1} for both nanomaterials due to the E_{2g} vibration mode in the hexagonal structure of boron nitride (in

opposite directions, parallel to x axis in x-y plane) [220, 221]. The other minor peak at ~474 cm^{-1} can be attributed to presence of boric acid residues from synthesis [220], whereas peaks at 2414 cm^{-1} and 2444 cm^{-1} (for BNNTs and BNNPs, respectively) are due to the presence of impurities, functional groups and/ or structural defects. For MSNPs, the peaks at 274 cm^{-1} and 400 cm^{-1} can be attributed to E_{1g} vibration modes in the crystalline MoS_2 and its nano-hexagonal structure, respectively [62]. For molybdenum disulfide, the J_2 peak at 230 cm^{-1} shows presence of $2a_{\circ}$ superlattice while J_3 peak at 330 cm^{-1} is due to structural distortion. The peaks at 816 cm^{-1}, and 1000 cm^{-1} are due to oxysulfide functional groups [50, 222]. For WSNTs, the peak at 350 cm^{-1} is due to E_{2g} atomic vibrations for tungsten and sulfur atoms in x-y plane (in opposite directions parallel to x axis), whereas the peak at 420 cm^{-1} corresponds to A_{1g} vibration mode of sulfur atoms in x-y plane (in opposite directions and parallel to y axis) [62, 223].

TEM images (Figure 3.3) confirm the tubular morphology of SWCNTs, MWCNTs, and WSNTs; ribbon morphology of SWGONRs and MWGONRs; disc-shaped morphology of GONPs and hexagonal morphology of MSNPs [50, 62, 135, 195, 224]. Also, TEM analysis confirmed the characteristic tubular morphology of BNNTs and hexagonal structure of BNNPs. AFM analysis was in agreement with TEM structural characterization of SWCNTs [225], MWCNTs [226], SWGONRs [227], MWGONRs [228], GONPs [216], MSNPs [229] and WSNTs [230].

BET analysis (Table 3.2) showed that all of the nanomaterials exhibit a large surface area. The formation of SWGONRs aggregates (during unzipping of SWCNTs) (as seen in Figure 3.3) led to less specific surface area for SWGONRs compared to MWGONRs. Our results were in agreement to the values reported in the literature. Specific surface area of ~80-1500 $m^2.g^{-1}$, ~20-1300 $m^2.g^{-1}$, ~430-510 $m^2.g^{-1}$, ~30-470 $m^2.g^{-1}$, ~8 $m^2.g^{-1}$, ~10-60 $m^2.g^{-1}$, ~220 $m^2.g^{-1}$ and

~230 $m^2.g^{-1}$ were observed for SWCNTs [231], MWCNTs [232], MWGORs [233], GONPs [234], WSNTs [235], MSNPs [236], BNNTs [237] and BNNPs [238], respectively.

3.5. Summary

In this chapter, we reported the structural characterization and chemical analysis of PPF polymer and the various organic and inorganic nanomaterials used for the preparation of PPF nanocomposites. The nanomaterials showed a large specific surface area and the presence of functional groups on their surface. The presence of functional groups and large surface area can affect the nanocomposite microstructure and in turn dictate cellular-material interactions which are reported in subsequent chapters.

3.6. Tables

Table 3.1. Aspect ratio of nanomaterials used in this study.

Nanomaterial	Aspect ratio
SWCNTs	~1000
MWCNTs	~10-400
SWGONRs	~80-350
MWGONRs	~5-25
GONPs	~1
WSNTs	~100-400
MSNPs	~1
BNNTs	~500-200
BNNPs	~1

Table 3.2. Specific surface area of nanomaterials.

Nanomaterial	Specific surface area (m^2/g)
SWCNTs	353
MWCNTs	211
SWGONRs	96
MWGONRs	384
GONPs	45
WSNTs	-
MSNPs	17
BNNTs	-
BNNPs	35

3.7.Figures

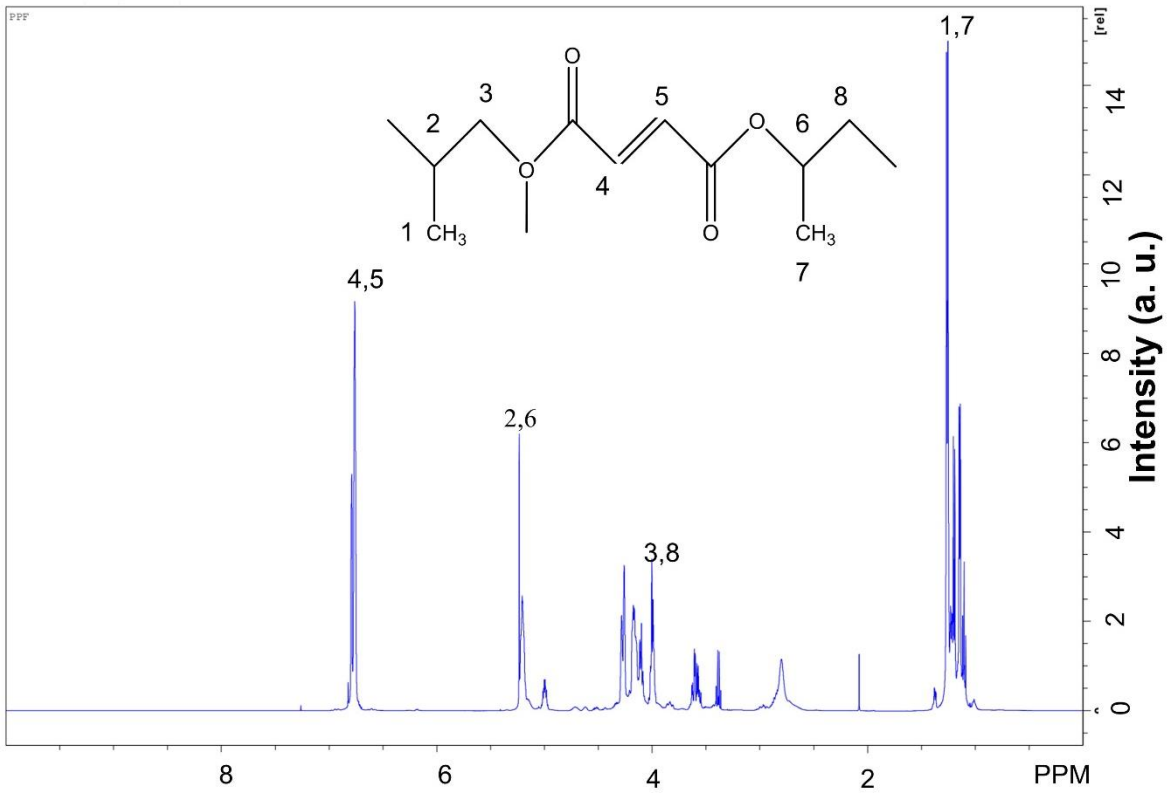

Figure 3.1. Nuclear magnetic resonance (NMR) spectra of PPF polymer.

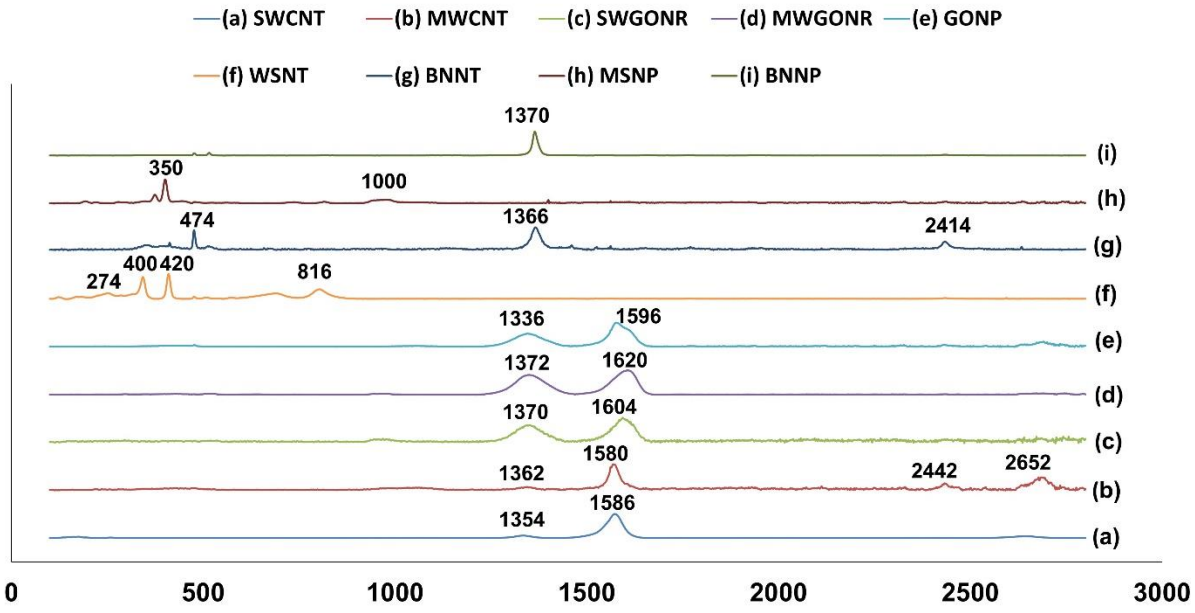

Figure 3.2. Raman spectra of nanomaterials.

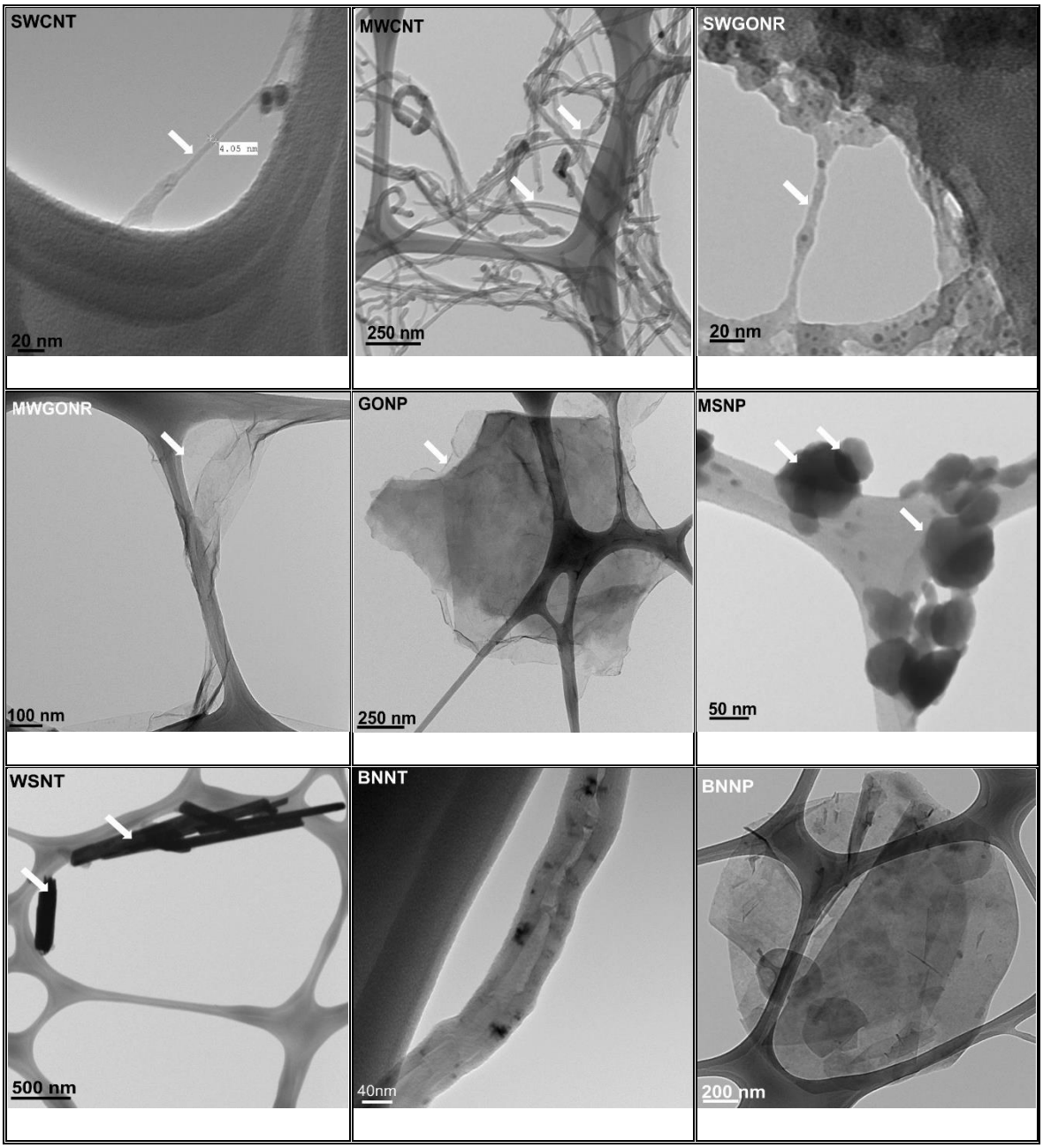

Figure 3.3. TEM images of nanomaterials.

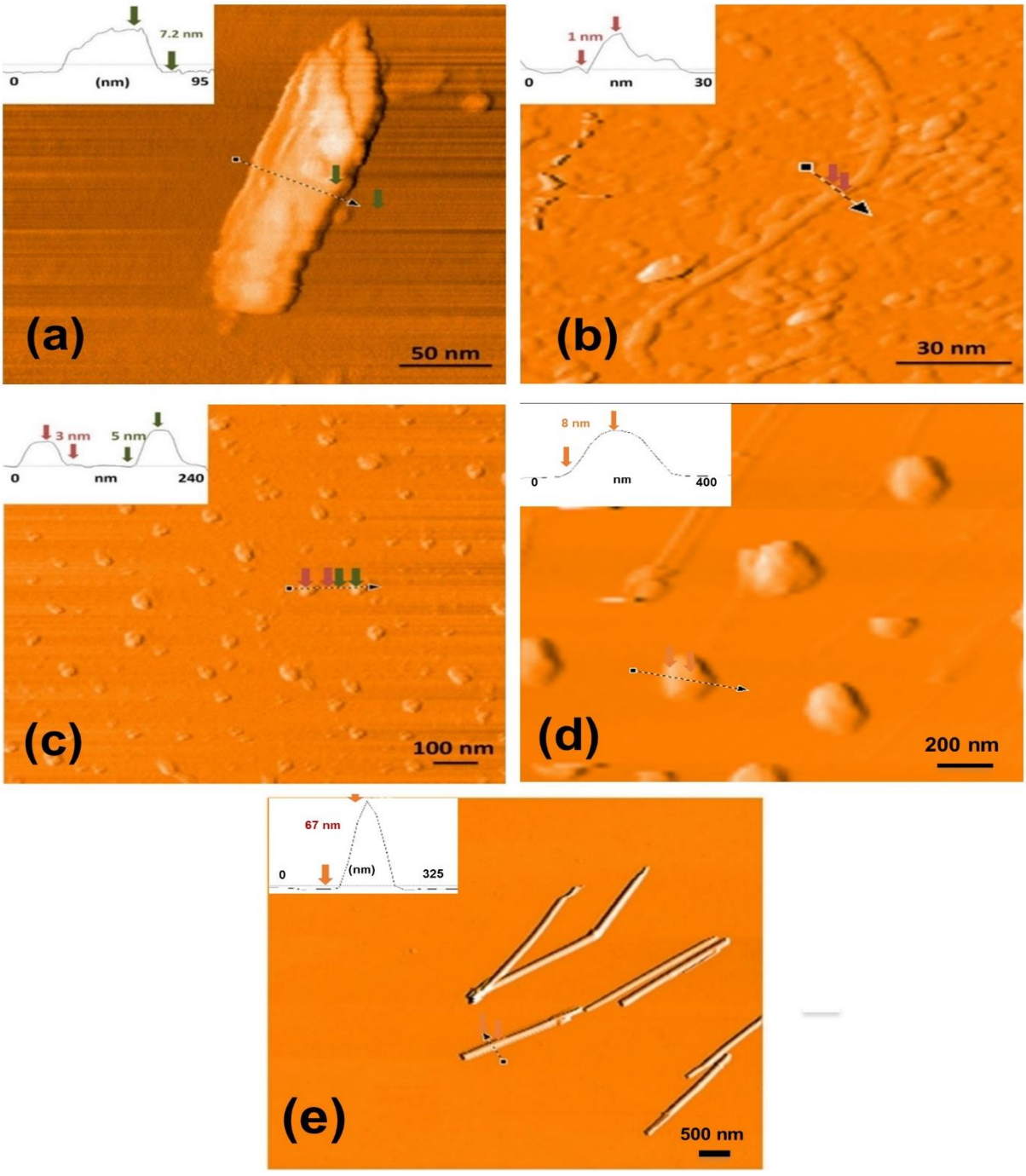

Figure 3.4. AFM images of a) SWGONRs, b) MWGONRs, c) GONPs, d) MSNPs and e) WSNTs (continued on the next page).

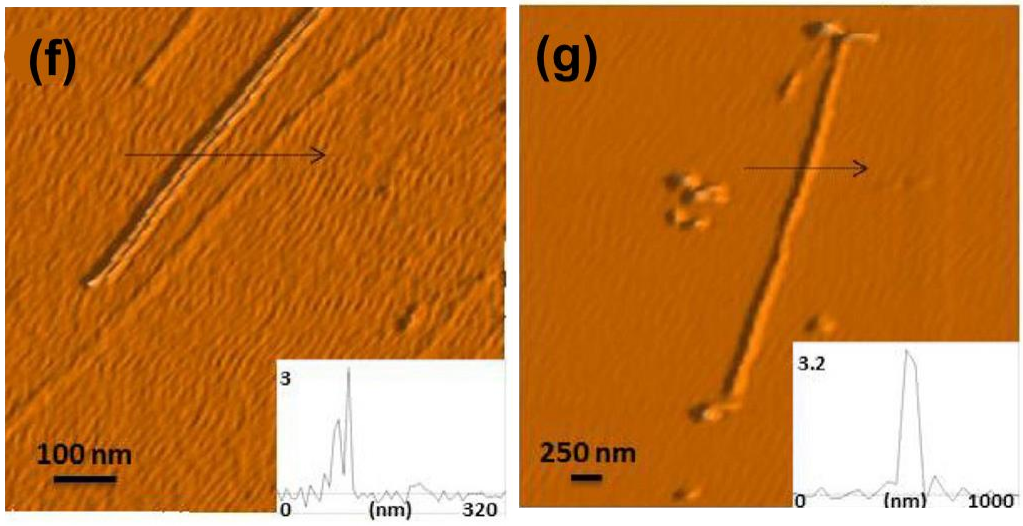

Figure 3.4. AFM images of f) SWCNTs and g) MWCNTs (Continued from the previous page).

Chapter 4: Mechanical properties of nonporous 1-D and 2-D nanocomposites

Preface

The data in this chapter have been reproduced with permission from the following articles:

[1]. Lalwani, Gaurav, Allan M. Henslee, **Behzad Farshid**, Priyanka Parmar, Liangjun Lin, Yi-Xian Qin, F. Kurtis Kasper, Antonios G. Mikos, and Balaji Sitharaman. "Tungsten disulfide nanotubes reinforced biodegradable polymers for bone tissue engineering." Acta biomaterialia 9, no. 9 (2013): 8365-8373 (with permission from Elsevier publishing group).

[2]. Lalwani, Gaurav, Allan M. Henslee, **Behzad Farshid,** Liangjun Lin, F. Kurtis Kasper, Yi-Xian Qin, Antonios G. Mikos, and Balaji Sitharaman. "Two-dimensional nanostructure-reinforced biodegradable polymeric nanocomposites for bone tissue engineering." Biomacromolecules 14, no. 3 (2013): 900-90 (with permission from American Chemical Society).

The authors of these articles have contributed to the data presented in this chapter.

4.1. Introduction

The limitations in clinical treatment of bone defects using autologous or allogenous bone grafts and permanent prosthetic implants has led to emergence of bone tissue engineering

strategies [239]. Especifically, there has been a growing interest to develop nanoparticle-reinforced biodegradable polymer nanocomposites for bone tissue engineering applications [49, 90, 194, 240-243]. A major motivation behind these studies is to enhance the mechanical properties of the biodegradable polymer for tissue engineering of load bearing bones. Carbon nanostructures such as fullerenes, single- and multi- walled carbon nanotubes, ultra-short carbon nanotubes, single- and multi-walled graphene oxide nanoribbons and graphene oxide nanoplatelets have been investigated as reinforcing agents [26, 49, 50, 78, 81, 184].

Reinforcing agents possessing high intrinsic mechanical property allow efficient load transfer, enhancing the load bearing capability of the nanocomposites. Theoretical studies show that although individual carbon nanotubes possess exceptionally high mechanical properties (Young's modulus in TPa range) [244], the effective Young's modulus of CNTs in polymeric composites is significantly lower (≈ 500 GPa) [245]. It has been shown that in order to achieve significant improvements in the mechanical properties of polymers, the presence of reinforcing agents as individual particles in the polymer matrix is highly recommended [246]. However, due to strong van der Walls interactions and π-π stacking (0.5 eV/nm) [247, 248], pristine carbon nanotubes exist as micron sized aggregates in the polymeric matrix resulting in stress concentration and failure [78].

In addition to carbon nanotubes, 2-D carbon nanostructures such as graphene oxide nanoribbons (single- and multi-walled) and graphene oxide nanoplatelets (GONPs) and show remarkable mechanical properties [249-251]. Additionally, inorganic 1-D and 2-D nanomaterials such as tungsten disulfide nanotubes (WSNTs), boron nitride nanotubes (BNNTs), boron nitride nanoplatelets (BNNPs) and molybdenum disulfide nanoplatelets (MSNPs) show high mechanical

strength and have been used to reinforce polymeric scaffolds and nanocomposites [50, 164, 252-254].

Graphene has been predicted to have remarkable mechanical stiffness comparable to graphite, and fracture strength similar to SWCNTs [255, 256]. Therefore, for a 2-D carbon nanostructure-reinforced polymer nanocomposite under mechanical stress, nanostructure possessing high stiffness should allow efficient transfer of load from the polymer matrix [48]. Moreover, 2-D carbon nanostructures show high surface area, structural defects, and possess functional groups (hydroxyl, carboxyl or sulfide groups) on the surface that should allow formation of good interfaces with the polymer matrix; key requirements for efficient load transfer [48]. Similarly, inorganic nanomaterials such as tungsten disulfide nanotubes (WSNTs), boron nitride nanotubes (BNNTs), boron nitride nanoplatelets (BNNPs) and molybdenum disulfide nanoplatelets (MSNPs) have been used as reinforcing agents to improve the mechanical properties of epoxy and poly(methyl methacrylate), and other polymers [50, 164, 252-254]. As discussed in chapter 1, these nanomaterials exhibit very high mechanical properties, structural defects, carry functional groups (such as sulfide and oxy-sulfide) on their surface, and can be readily dispersed in organic solvents and polymers [15]. The unique physical properties of these nanomaterial makes them good candidates for development of smart biomaterials responsive to external stimulus (pH, electrical and magnetic fields, thermal, acoustic and light waves) for an active control over shape and microstructure of the polymeric nanocomposites and may be utilized for multifunctional applications such as drug delivery and bioimaging. Based on these potential benefits, the efficacy of 2-D carbon nanostructures, as well as organic metallic sulfide nanomaterial fillers, needs to be systematically investigated.

In this study, poly(propylene fumarate) (PPF), an injectable, cross-linkable, biocompatible and biodegradable polyester, widely investigated for bone tissue engineering applications was used as the polymeric matrix [81, 178, 257]. WSNT, MSNP, SWGONR and MWGONR and GONP nanocomposites at 0.01-0.2 wt. % loading concentration were fabricated, and their mechanical properties were compared to carbon nanotube-reinforced nanocomposites (SWCNT, MWCNT) that were used as positive controls. Crosslinked PPF composites without nanomaterial loading were used as baseline control. Mechanical properties (compression and flexural), crosslinking density and dispersion state of nanomaterials in the polymer matrix were investigated (flowchart is shown in Figure 4.1).

4.2. Results

4.2.1. Compressional and flexural mechanical properties of nanocomposites

The mechanical properties (compressive modulus, compressive yield strength, flexural modulus and flexural yield strength) of the nanocomposites as a function of nanomaterial concentration (0.01-0.2 wt. %) are presented in Figures 4.2.A-D. Also, included are the mechanical properties of crosslinked PPF baseline control, and SWCNT and MWCNT nanocomposites (positive controls). Table 4.1.A-D tabulates the highest compressive modulus and yield strength, flexural modulus and bending yield strength, the corresponding loading concentration for each nanocomposite, and the percentage (%) increase compared to the baseline and positive controls.

A significant increase in the compressive modulus (Figure 4.2.A) and yield strength (Figure 4.2.B) was observed for all the nanocomposites at various loading concentrations compared to PPF baseline control. Importantly, most of the 2-D nanomaterials at various loading

concentrations exhibited a significant increase in the compressive modulus and yield strength compared to 1-D nanotube-reinforced SWCNT, MWCNT and WSNT nanocomposites. The highest compressive modulus values (Table 4.1.A) for 2-D nanocomposites were 35-108% greater compared to PPF composites, and up to 78% greater compared to the positive controls. The highest compressive yield strength values (Table 4.1.B) for the 2-D nanocomposites were 27-93% greater compared to PPF baseline controls, and up to 81% greater compared to the positive controls. On the other hand, inorganic 1-D nanocomposites showed lower compressive yield strength compared to 2-D nanocomposites. However, the compressive modulus (Figure 4.2.A) and compressive yield strength (Figure 4.2.B) of WSNT nanocomposites at all loading concentrations were significantly higher than PPF baseline controls. On the other hand, WSNT nanocomposites at various loading concentrations also showed a significant increase in the mechanical properties compared to positive controls. The highest compressive modulus for WSNT nanocomposites was ~60% greater compared to baseline control and ~12-48% greater than positive controls (Table 4.1.A). The highest compressive yield strength values for WSNT nanocomposites were ~55% greater than PPF baseline controls, and ~5-48% greater than positive controls (Table 4.1.B).

The flexural modulus (Figure 4.2.C) and flexural yield strength (Figure 4.2.D) for all the 2-D nanocomposites, at all nanomaterials loading concentrations, also show a significant increase compared to PPF baseline controls. The majority of 2-D nanostructure nanocomposites, at various loading concentrations, showed significant increase in the flexural modulus and flexural yield strength compared to 1-D nanocomposites and PPF baseline control. The highest flexural modulus (Table 4.1.C) for 2-D nanocomposites were 15-53% greater compared to PPF control, and up to 47% greater compared to the 1-D carbon nanocomposites. The highest flexural

yield strength values (Table 4.1.D) for the 2-D nanocomposites were 102-262% greater compared to PPF control, and up to 237% greater compared to the positive controls. On the other hand, inorganic WSNT nanocomposites had lower flexural strength and flexural modulus compared to 2-D nanocomposites, but they still showed a significant increase in the flexural modulus (Figure 4.2.C) at 0.02-0.2 wt. % nanomaterial loading concentration compared to PPF baseline controls. A significant increase in the flexural modulus, compared to positive controls was also observed at 0.05 wt. % WSNTs loading concentration. Additionally, WSNT nanocomposites showed a significant increase in the flexural yield strength at all concentrations compared to the baseline control, and at various concentrations (0.05-0.2 wt. %) compared to positive controls. The highest flexural modulus value for WSNT nanocomposites was ~28% greater than PPF control, and ~1-32% greater than positive controls (Table 4.1.C). The highest flexural yield strength value for 2D nanocomposites was ~191% greater than baseline control and ~28-127% greater than positive controls (Table 4.1.D).

4.2.2. Sol-fraction analysis of nanocomposites

The sol-fraction values for various nanocomposites is reported in Figure 4.3. The sol-fraction values for PPF, SWCNT, and MWCNT composites was ~14%, ~12.9-14.2% and ~12.1-14.2%, respectively. The sol-fraction for 2-D nanocomposites was ~10.2-12.2% for SWGONR, ~8.7-11.6% for MWGONR, ~9.5-12.3% for GONP and ~8.5-10% for MSNP nanocomposites. WSNT nanocomposites showed a lower sol-fraction (~7.7-9.8%) compared to PPF baseline control and positive controls. The highest crosslinking density was observed for all loading concentrations of MSNPs. Additionally, higher loading concentrations (0.1-0.2 wt. %) of GONPs

and MWGONRs also resulted in significant increase in the crosslinking density of nanocomposites compared to the positive and baseline controls.

4.2.3. Transmission electron microscopy (TEM) of nanocomposites

TEM was performed on the crosslinked nanocomposites to characterize the nanomaterial-polymer interface and assess the dispersion state of 1-D and 2-D nanostructures in the PPF matrix (Figure 4.4). TEM analysis was performed with special consideration to minimize local heating and prevent specimen damage. No solvent dissipation was observed. TEM images show that all nanostructures were coated with a thin layer of PPF polymer, and embedded in the PPF matrix. The analysis indicated that SWCNTs and MWCNTs were present in the nanocomposites as bundles of ~2-4 and ~2-3 nanotubes, respectively (Figures 4.4.A and 4.3.B). SWGONRs were dispersed as bundles of a few (~2-5) nanoribbons, and MWGONRs existed as individual nanoribbons (Figures 4.4.C and 4.4.D). GONPs and MSNPs also existed as individual nanoplatelets in the PPF matrix (Figures 4.4.D and 4.4.E). TEM images showed a defect-free nanomaterial/polymer interface in WSNT nanocomposite (Figure 4.4.F).

4.3. Discussions

For load-bearing applications, a bone graft with mechanical properties similar to the native bone is desired. Bone tissue engineering implants with lower or higher mechanical properties compared to the native bone could elicit structural failure or stress shielding in the surrounding bone tissue, respectively. One strategy to increase the mechanical properties of biodegradable polymers for bone tissue engineering application is the incorporation of secondary phase with higher intrinsic mechanical properties (compared to the native polymer). Towards this end, PPF nanocomposites were prepared by dispersing 1-D and 2-D organic (single- and

multi-walled carbon nanotubes, single- and multi-walled graphene oxide nanoribbons and graphene oxide nanoplatelets) and inorganic (molybdenum disulfide nanoplatelets and tungsten disulfide nanotubes) nanomaterials as reinforcing agents for the biodegradable polymer PPF at various loading concentrations (0.01-0.2 wt. %). PPF nanocomposites were fabricated using a radical-initiated thermal crosslinking method using benzoyl peroxide as the radical initiator. Compression and three-point bending tests were performed according to ASTM standards to characterize the mechanical properties of the nanocomposites. Sol-fraction analysis was performed to detect the changes in crosslinking density of the polymer in the presence of the nanomaterials. TEM analysis was performed on the crosslinked specimens to characterize the nanomaterial/polymer interface and assess the nanomaterial dispersion in the polymer matrix. The results were compared to carbon nanotubes (single-and multi-walled carbon nanotubes) - reinforced PPF nanocomposites which were used as the positive controls and PPF polymer without nanomaterial loading that served as a baseline control.

A few reports have investigated the mechanical properties of polymeric nanocomposites reinforced with 2-D and 1-D carbon or inorganic nanostructures [136, 258-261]; several studies have investigated the use of carbon nanotubes [49, 78, 81, 90, 184, 262]. Song et al. reported ~74% increase in the Young's modulus of polypropylene composites compared to pristine PPF polymer controls at 0.42 vol. % loading of exfoliated graphene platelets [259]. Koratkar et al. reported ~31% and ~30% increase in the Young's modulus of epoxy composites at ~0.1 wt.% loading of graphene platelets [260] and 0.3 wt.% loading of MWGONRs [233], respectively. Pinto et al. reported ~100% increase in the yield strength and Young's modulus of PLGA nanocomposite films (compared to pristine PLGA films) at 0.4 wt. % loading of exfoliated graphene oxide nanosheets and graphene nanoplatelets [259]. Chatterjee et al. reported ~80%

increase in toughness at 0.5 wt. % loading of surfactant dispersed graphene nanoplatelets in thermoplastic poly(amide) polymer [42]. Zhou et al. reported ~28% increase in the storage modulus and ~24% increase in the tensile strength upon the addition of 1-5 wt. % exfoliated molybdenum disulfide nanosheets in poly(vinyl alcohol) (PVA) [263]. The results of these various reports cannot be compared to each other directly, because of differences in fabrication methods and the chemical state (pristine or functionalized) of the nanomaterials. Nevertheless, these studies corroborate a salient result of this study that the 2-D and 1-D nanostructures can substantially enhance the mechanical properties of polymer nanocomposites even at very low loading concentrations.

The structural and chemical characterization of nanomaterials was discussed in chapter 3. SWGONRs, MWGONRs, GONPs, MSNPs, and PPF were synthesized according the well-established methods [123, 175, 202, 264]. As discussed in chapter 1, the presence of functional groups such as oxysulfide in GONPs, GONRs, WSNTs and MSNPs can act as handles for improved nanomaterial polymer interaction, thereby improving the mechanical properties of polymeric components [48]. The results of the mechanical properties (Figures 4.2.A-D and Tables 4.1.A-D) indicate a clear and consistent trend in the values for the nanocomposites: MSNP > GONP > MWGONR > SWGONR > WSNT > MWCNT > SWCNT> PPF controls. Results show that 2-D nanocomposites exhibit better mechanical properties compared to 1-D nanocomposites. The results taken together also indicate that, among the 2-D nanostructures, nanoplatelets are better reinforcing agents than nanoribbons and inorganic nanostructures and better reinforcing agents than carbon nanostructures. Among 1-D nanostructures, inorganic nanotubes WSNTs reinforce PPF polymer better than carbon nanotubes (SWCNTs and MWCNTs). The values of compressive (Young's) modulus, compressive strength, flexural

modulus and flexural strength for the PPF nanocomposites are lower than the mechanical properties of cortical bone, but greater or comparable to trabecular bone [265]. The higher mechanical properties of 2-D and 1-D nanocomposites compared to the baseline PPF control attribute to a complex interplay of several factors such as surface area, aspect ratio, surface energy and roughness, dispersion state of nanomaterials, and the crosslinking density of polymeric matrix. Several studies have reported that a high surface area of nanoparticles dispersed in polymer permits an efficient load transfer from the polymer matrix to the embedded nanoparticles [233].

Brunauer–Emmett–Teller (BET) was used to analyze surface area of the nanomaterials. The measured BET surface areas for all the nanostructures are listed in Table 3.2 (Chapter 3). The values follow the following trend: MWGONRs > SWCNTs > MWCNTs > SWGONRs > GONPs > MSNPs > WSNTs. Surface area values of SWCNTs, MWCNTs, MWGONRs, GONPs, and MSNPs, are within the range reported in the literature [123, 231-233, 236, 266, 267]. The values for SWGONRs have not been reported previously and are lower than SWCNTs. Interestingly, the surface area of graphene nanoparticles (SWGONRs, MWGONRs, and GONPs) are lower than the theoretical value of 2630 $m^2.g^{-1}$ for individual isolated graphene sheets. The surface area of WSNTs was 8.43 $m^2.g^{-1}$, significantly lower than previously reported values for SWCNTs and MWCNTs [50]. It is important to note that, for the solid nanostructure samples, a significant surface area is not available for nitrogen absorption due the presence of nanoparticles as aggregated bundles [268, 269]. However, during the preparation of polymeric nanocomposites, sonication could disrupt these aggregates, and further increase the surface area of the nanostructures. There is no method that allows a direct quantification of the surface area of nanostructures embedded in the polymer matrix. Nevertheless, the above results suggest that the

surface area of nanostructures may not be the major factor responsible for the observed trends in the mechanical properties.

The aspect ratio of fillers has been reported to affect the mechanical properties of polymeric composites [270]. The aspect ratio (length divided by diameter) values were calculated by measuring length and diameter of nanotubes from multiple TEM and AFM images, and were reported in Table 3.1 (Chapter 3). The values follow the trend: nanoplatelets < nanoribbons < nanotubes; an opposite trend compared to the results of mechanical properties. This trend suggests an inverse relationship between the aspect ratio (an important measure of size) of nanostructures and the mechanical properties of the nanocomposites. However, this relationship cannot be extrapolated for hydrophilic polymers reinforced with other nanomaterials. For instance, a recent study on pristine graphene-reinforced poly(vinyl alcohol) (PVA) nanocomposites showed an increased Young's modulus as the aspect ratio of graphene sheets increased [271].

Sol-fraction analysis was performed to assess changes in the crosslinking density of PPF in the presence of 2-D and 1-D nanostructures, since changes in the crosslinking density have been shown to alter the mechanical properties of nanoparticle-reinforced polymer nanocomposites [272]. The decrease in sol-fraction values of PPF nanocomposites compared to PPF baseline control signifies an increase in the crosslinking density of the polymer [184]. The sol-fraction results suggested the following trend: 2-D nanostructure nanocomposites > 1-D nanostructures nanocomposites > PPF baseline control. The presence of substantially higher number of hydroxyl, carboxyl, and sulfide functional groups on the 2-D nanostructures and WSNT nanotubes [123, 202, 223] compared to carbon nanotubes could lead to increased interactions between the nanostructures and the surrounding PPF matrix, and thus, a higher

crosslinking density. Therefore, the crosslinking density of nanocomposites is an important parameter responsible for the observed differences in the mechanical properties of various nanocomposite groups investigated in this study.

TEM imaging was performed to investigate nanomaterial/polymer interface and assess the dispersion state of nanomaterials in the polymeric matrix post thermal crosslinking. A uniform individual dispersion of nanoparticles in the polymer matrix is recommended for an efficient load transfer; presence of nanoparticles as aggregates in the polymer matrix can cause slippage between nanostructures leading to poor mechanical reinforcement [273]. These aggregates can also act as sources of stress concentration or crack initiation, especially under external loading. The existence of MWGONRs, GONPs and MSNPs as individual nanoparticles further corroborates the hypothesis that during the preparation of nanocomposites, sonication might effectively disrupt the aggregates of nanostructures, thereby increasing the surface area available for interaction with the polymer. TEM images indicate that SWCNTs and MWCNTs were present as micron sized aggregates, whereas WSNTs were present as individually-dispersed nanotubes. For WSNT nanocomposites, based on the consistently higher compressive and flexural mechanical properties compared to positive and baseline controls, it can be inferred that in addition to the changes in the crosslinking density, a uniform dispersion of nanoparticles in the polymer matrix might act as a key factor for the observed increased mechanical properties compared to baseline and positive controls. Additionally, these results also suggest that chemical composition of nanostructures is an important factor for the enhanced mechanical reinforcement, and inorganic nanotubes, in general, are better reinforcing agents compared to carbon nanotubes.

The results of this chapter taken together suggest that differences in surface energy, chemistry, surface area, aspect ratio and structural defects may be the key factors for the

observed increases in the mechanical properties of PPF nanocomposites compared to the baseline PPF control and carbon nanotube positive controls. Interestingly, the presence of structural defects and functional groups could bring about a better nanomaterial-polymer physiochemical interaction, leading to an increase in the crosslinking density in the nanocomposites [274]. Among the 2-D nanocomposites, based on the consistently higher values in the mechanical properties for nanoplatelets compared to nanoribbons, it can be inferred that other than differences in crosslinking density, the lower aspect ratio of nanoplatelets compared to nanoribbons may be responsible for their better mechanical reinforcement because of less stress concentration. Importantly, equivalent or better mechanical reinforcement using MSNPs suggest that chemical composition of the nanostructures may also play a role and inorganic 2-D nanostructures maybe more suitable to achieve enhancement for certain mechanical properties (e.g. compressive mechanical properties) compared to carbon and tungsten disulfide nanotubes. Among 1-D nanotubes, inorganic WSNTs were better reinforcing agents than carbon nanotubes. The range of the mechanical properties of these nanocomposites was comparable to the reported values of trabecular bone (Young's modulus ≈ 300-5000 MPa, compressive yield strength ~0.1-13 MPa, flexural modulus ~40-50 MPa, flexural yield strength ~1.8-10 MPa) [275-277]. However, the mechanical properties of nanocomposites are significantly lower than cortical bone (Young's modulus ~12,000-20,000 MPa, compressive yield strength ~170-190 MPa, flexural modulus ~5000-23,000 MPa, flexural yield strength ~130-295 MPa) [278-281].

This work significantly contributes to existing body of work on 2-D and 1-D nanostructure-reinforced polymer nanocomposites by providing direct comparisons of the efficacies of various nanostructures as reinforcing agents of polymer nanocomposites. Additionally, the promising mechanical property results of the 2-D and 1-D nanostructures

reinforced PPF nanocomposites for bone tissue engineering application opens avenues for *in vitro* and *in vivo* studies to assess their safety and efficacy.

4.4. Conclusions

In conclusion, biodegradable polymeric PPF nanocomposites reinforced with various 1-D and 2-D carbon and inorganic nanomaterials (single- and multi-walled carbon nanotubes, single- and multi-walled graphene oxide nanoribbons, graphene oxide nanoplatelets, molybdenum disulfide nanoplalets and tungsten disulfide nanotubes) at low nanomaterials loading concentrations were fabricated and their mechanical properties were investigated towards the development of mechanically robust polymeric bone implants. The mechanical properties (compressive modulus, compressive yield strength, flexural modulus and flexural yield strength) of all the 2-D nanocomposites were significantly higher in comparison to 1-D nanocomposites and PPF baseline control and follow the trend: 2-D inorganic nanocomposites > 2-D carbon nanocomposites > 1-D inorganic nanocomposites > 1-D carbon nanocomposites > PPF baseline control. The extent of mechanical reinforcement was closely dependent on the nanostructure morphology with nanoplatelets > nanoribbons > nanotubes. The inorganic 2-D nanostructure MSNPs consistently showed a better mechanical reinforcement compared to other nanocomposites and PPF baseline control. 2-D nanostructures caused an increase in the crosslinking density of nanocomposites compared to 1-D nanocomposites or PPF composites. The 2-D nanostructures (except SWGONRs) and WSNTs were present as individual particles in the crosslinked PPF matrix, while SWGONRs, SWCNTs, and MWCNTs were present in the PPF matrix as small aggregates (bundles of 2-5 nanoparticles). This study demonstrates that

harnessing the potentials of 2-D and 1-D nanostructures could lead to development of an entire new class of smart, ultra-strong and lightweight polymeric bone grafts.

4.5. Tables

Table 4.1.A) Compressive modulus of various PPF nanocomposites.

Nanostructure	Highest compressive modulus (MPa)	Concentration (wt. %)	% increase compared to PPF	% increase compared to SWCNTs	% increase compared to MWCNTs
SWGONR	1340.4 ± 83.6	0.1	35.3	0-12.4	0-15.7
MWGONR	1665.2 ± 99.0	0.1	68.1	23.3-41.9	8.3-43.7
GONP	1699.3 ± 69.4	0.1	71.6	25.8-44.7	10.6-46.7
MSNP	2061.8 ± 126.6	0.2	108.1	52.6-75.5	34.1-77.9
WSNT	1578.2 ± 71.39	0.02	60.6	26.5-43	12.4-48.5

Table 4.2.B) Compressive yield strength of various PPF nanocomposites.

Nanostructure	Highest compressive yield strength (MPa)	Concentration (wt. %)	% increase compared to PPF	% increase compared to SWCNTs	% increase compared to MWCNTs
SWGONR	53.2 ± 0.8	0.05	26.5	0-18.7	0-2.3
MWGONR	67.4 ± 1.1	0.02	60.1	22.1-50.3	10-29.5
GONP	68.6 ± 2.0	0.2	63.1	24.3-53.1	12-32
MSNP	81.3 ± 2.2	0.2	93.2	47.3-81.4	32.7-56.4
WSNT	64.7 ± 2.8	0.2	55.3	10.6-48.2	4.6-23.3

Table 4.2.C) Flexural modulus of various PPF nanocomposites.

Nanostructure	Highest flexural modulus (MPa)	Concentration (wt. %)	% increase compared to PPF	% increase compared to SWCNTs	% increase compared to MWCNTs
SWGONR	756.3 ± 40.2	0.2	15.0	0-10.3	0-17.9
MWGONR	817.6 ± 12.6	0.05	24.4	7.6-19.2	0-27.5
GONP	925.2 ± 5.4	0.05	40.7	21.7-34.9	10.2-44.2
MSNP	1005.8 ± 12.3	0.05	53.0	32.2-46.6	19.7-56.7
WSNT	845.5 ± 62.9	0.05	28.5	11.2-23.4	0.8-31.9

Table 4.2.D) Flexural yield strength of various PPF nanocomposites.

Nanostructure	Highest flexural yield strength (MPa)	Concentration (wt. %)	% increase compared to PPF	% increase compared to SWCNTs	% increase compared to MWCNTs
SWGONR	15.1 ± 0.8	0.05	101.7	9.3-87	0-51.5
MWGONR	24.7 ± 1.4	0.05	230.1	78.9-206.1	19.5-148.0
GONP	27.2 ± 0.1	0.05	263.1	96.8-236.7	31.5-172.8
MSNP	27.1 ± 0.9	0.1	262.2	96.3-235.8	31.1-172.1
WSNT	19.83 ± 2.19	0.1	190.7	40.3-127.4	27.9-73.18

Table 4.3. Mechanical properties of human cortical and trabecular bone with various PPF nanocomposites.

Mechanical Properties	Young's modulus (GPa)	Compressive yield strength (MPa)	Flexural modulus (GPa)	Flexural yield strength (MPa)
Trabecular bone	0.3-10	0.1-13	0.04-0.05	1.8-10
Cortical bone	12-20	170-193	5-23	133-295
SWGONR	1.2-1.3	46.3-53.2	0.7-0.75	8.8-15.1
MWGONR	1.3-1.6	52.6-67.4	0.68-0.81	15.1-24.7
GONP	1.3-1.7	59.2-68.6	0.82-0.92	17-27.2
MSNP	1.5-2	64-81.3	0.87-1.0	18.5-27.1

4.6. Figures

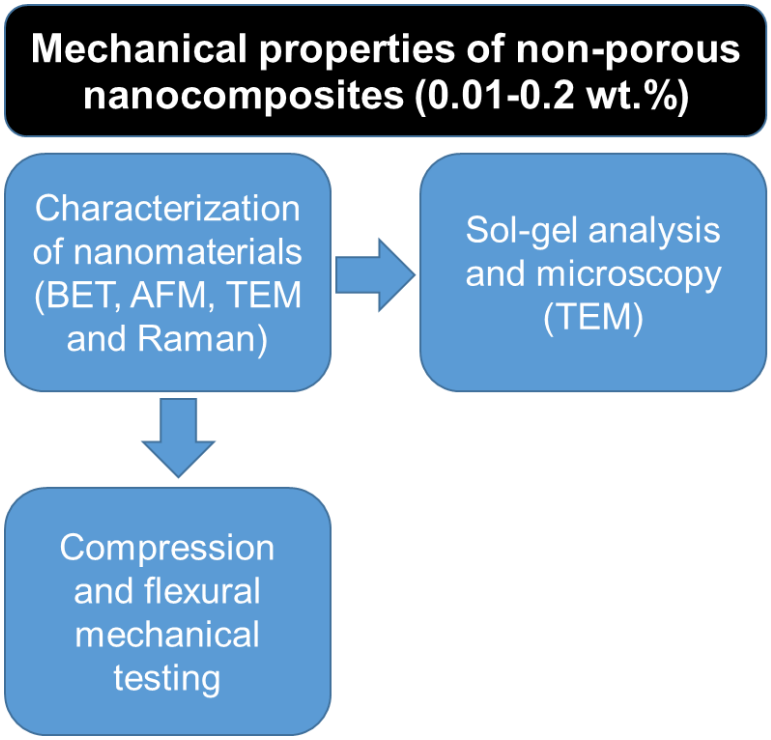

Figure 4.1. Flowchart depicting the investigation of mechanical properties of nonporous PPF nanocomposites.

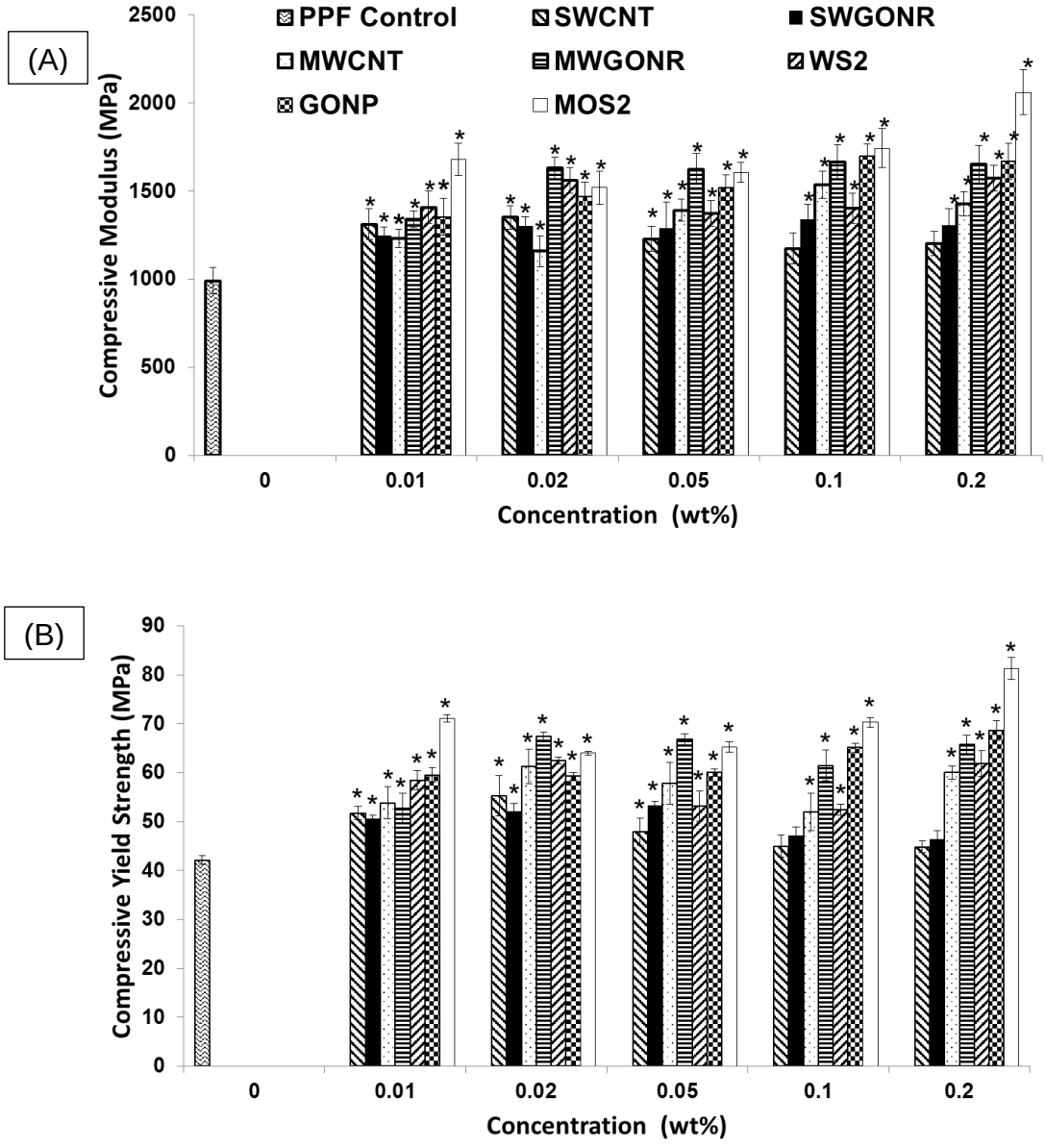

Figure 4.2.A) Compressive modulus and B) compressive yield strength of PPF nanocomposites as a function of nanostructure loading concentration. Error bars represent mean ± standard deviation for n=5. Groups with a significant difference compared to PPF composite are marked with the symbol "*" ($p < 0.05$) (Continued on the next page).

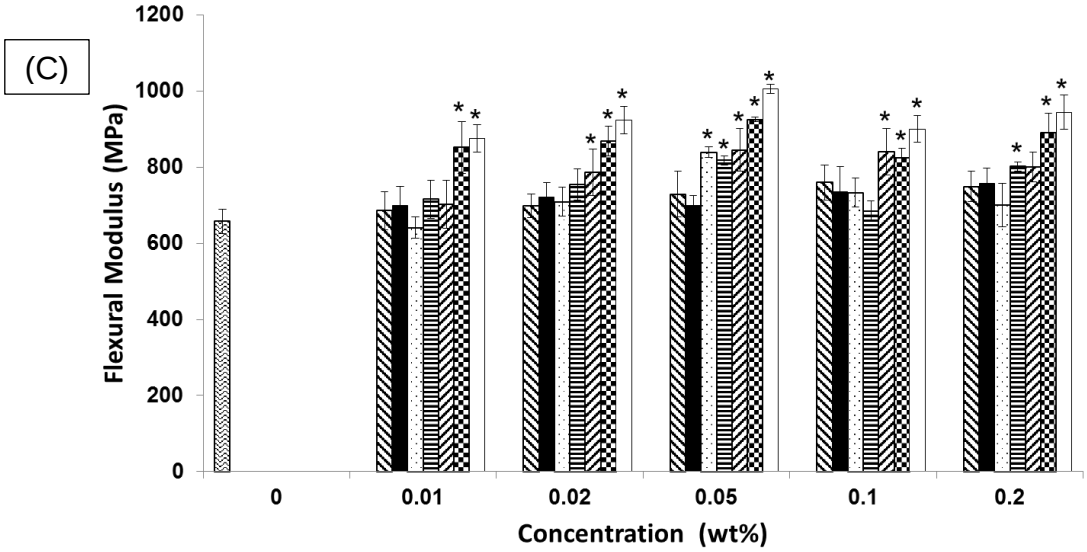

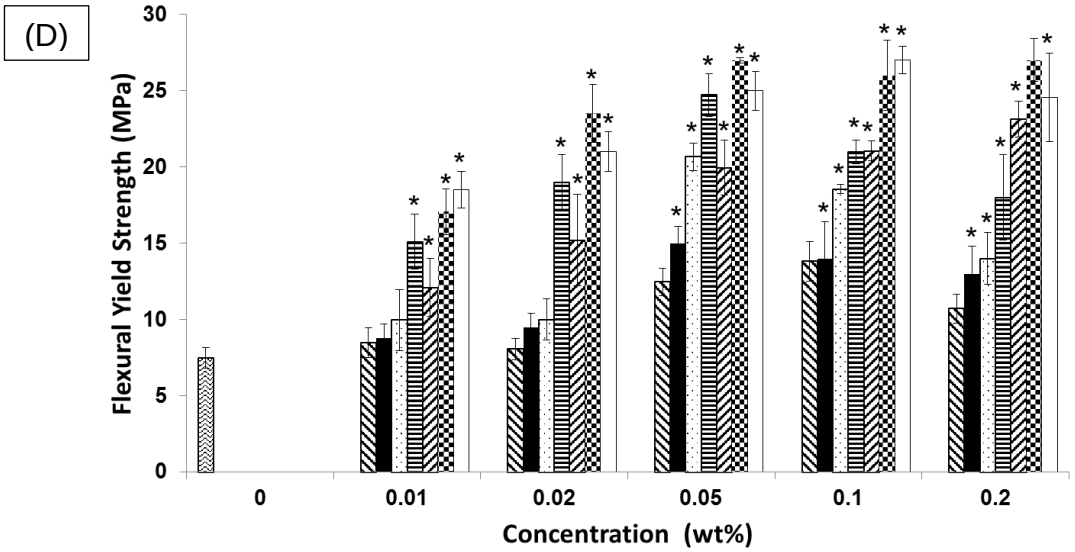

Figure 4.2.C) Flexural modulus and D) flexural yield strength of PPF nanocomposites as a function of nanostructure loading concentration. Error bars represent mean ± standard deviation for n=5. Groups with a significant difference compared to PPF composite are marked with the symbol "*" ($p < 0.05$) (Continued from the previous page).

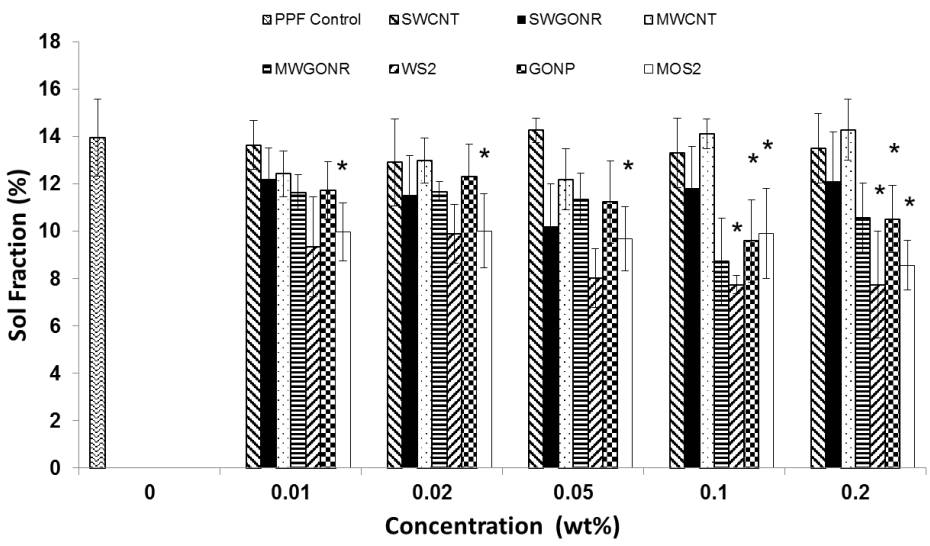

Figure 4.3. Sol fraction analysis of crosslinked PPF nanocomposites as a function of nanostructure loading (mean ± standard deviation for n=5 samples). Groups with a significant difference compared to PPF composite are marked with the symbol "*" ($p < 0.05$).

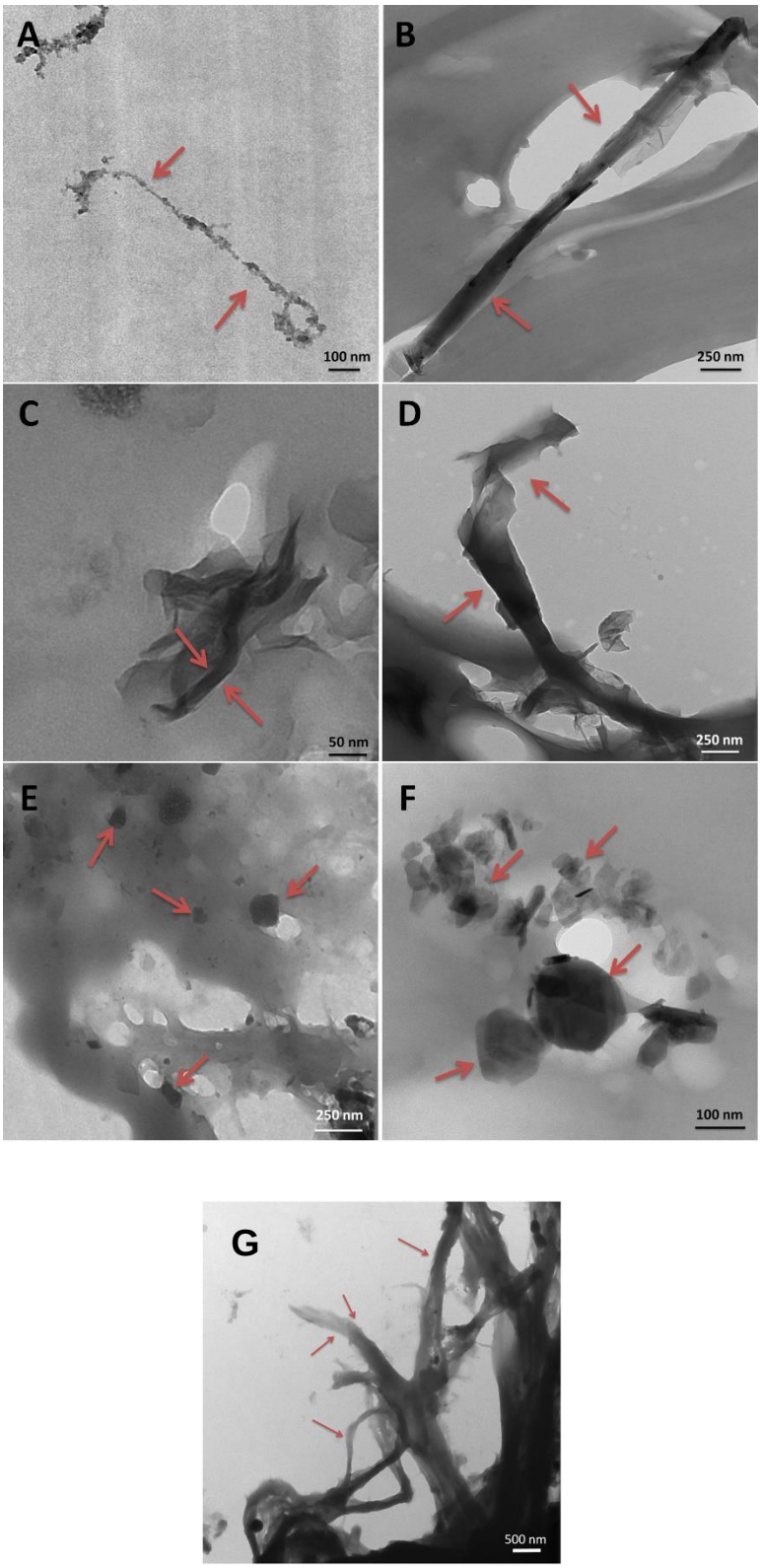

Figure 4.4. Representative transmission electron microscopy images of crosslinked PPF nanocomposites at 0.1 wt. % loading concentration of: A) SWCNT, B) MWCNT, C) SWGONR, D) MWGONR, E) GONP, F) MSNP and G) WSNT (nanostructures marked with red arrows).

Chapter 5: *In vitro* cytocompatibility of nonporous 1-D and 2-D nanomaterial reinforced PPF nanocomposites

Preface

The data in this chapter have been reproduced with permission from the following articles:

[1]. **Farshid, Behzad**, Gaurav Lalwani, and Balaji Sitharaman. "*In vitro* cytocompatibility of one-dimensional and two-dimensional nanostructure-reinforced biodegradable polymeric nanocomposites." Journal of Biomedical Materials Research Part A, 103(7), 2015, 2309-21.

The authors of these articles have contributed to the data presented in this chapter.

5.1. Introduction

Biodegradable polymers such as poly(lactic-co-glycolic acid) (PLGA) [282], poly(polypropylene fumarate) (PPF) [283], and non-biodegradable polymers such as polyurethane (PU) [284] have been employed to develop coatings for metallic implants [282] and non-porous prosthetic polymeric components such as compact rods [285] and interference screws [17]. The biodegradable polymers have also been used to fabricate porous scaffolds to treat bone loss due to fractures, traumatic musculoskeletal injuries, congenital abnormalities, or

other bone defects [19, 286-289]. For applications involving load bearing implants, these polymers lack adequate mechanical properties [290]. Studies show that incorporation of carbon and inorganic nanomaterials such as fullerenes [291], carbon nanotubes (CNTs) [292] and alumoxane nanomaterials [192] as reinforcing agents into these polymers significantly improves their mechanical properties [293].

In Chapter 4, we systematically investigated the efficacy of 1-D and 2-D organic and inorganic nanomaterials as reinforcing agents to improve the mechanical properties (compressive and flexural modulus, and yield strength) of the polymer PPF. Single- and multi-walled carbon nanotubes (SWCNTs, MWCNTs), single- and multi-walled graphene oxide nanoribbons (SWGONRs, MWGONRs), graphene oxide nanoplatelets (GONPs), molybdenum disulfide nanoplatelets (MSNPs), or tungsten disulfide nanotubes (WSNTs) were dispersed into PPF at various loading concentrations (0.01-0.2 wt%). These nanomaterial-reinforced PPF nanocomposites exhibited mechanical properties (e.g. compressive modulus was 1-1.6 GPa) that were similar to cancellous bone (0.3-10 GPa compressive modulus) [50, 62]. In this chapter, we will discuss the *in vitro* cytocompatibility of these nanocomposites.

Along with the efficacy studies, *in vitro* cytotoxicity and *in vivo* biocompatibility of nanomaterials-incorporated polymers also need to be thoroughly investigated. *In vitro* studies are typically the first step to screen various nanomaterials and nanocomposites formulations before more elaborate and costly *in vivo* animal experiments [291]. Various *in vitro* studies have investigated the cytotoxicity of SWCNTs [294], MWCNTs [295], GONPs [296], GONRs [135, 297], MSNPs [174] and WSNTs [298]. A few studies have investigated the *in vitro* cytotoxicity and *in vivo* biocompatibility of nonporous PPF nanocomposites [80, 299] and porous PPF scaffolds containing SWCNTs [26, 81] and alumoxane nanomaterials [192, 257, 300]. The *in*

vitro cytotoxicity of other carbon nanomaterials-reinforced PPF nanocomposites (MWCNTs, SWGONRs, MWGONRs, and GONPs) and inorganic nanomaterials-reinforced PPF nanocomposites (WSNTs and MSNPs) have not been reported. Cytocompatibility of some of these nanomaterials incorporated into other polymers such as PLGA (nonporous CNT/PLGA [301] and porous GONP/PLGA [137]), and PU (porous GONP/PU scaffolds [302]) has been investigated.

In this chapter, we will systematically examine the cytocompatibility of various 1-D and 2-D carbon (SWCNTs, MWCNTs. SWGONRs, MWGONRs and GONPs) and inorganic (WSNTs and MSNPs) nanomaterials-reinforced PPF nanocomposites using NIH3T3 fibroblasts and MC3T3 pre-osteoblasts. The comprehensive cytocompatibility assessment included assays to characterize the cytotoxicity of unreacted components, crosslinked nanocomposites, and their degradation products. Additionally, cell attachment and proliferation studies were performed on the crosslinked nanocomposites.

5.2. Results

5.2.1. *In vitro* studies to examine the effects of unreacted macromers

Flowchart of the experimental procedure is presented in Figure 5.1. The viability of the MC3T3 and NIH3T3 cells assessed using Presto Blue assay is shown in Figure 5.2. This assay exploits the reductive environment of viable cells and changes the blue-colored resazurin dye into pink-colored resorufin. This alteration indicates cell viability and proliferation [303, 304]. NIH3T3 cells (Figure 5.2.A) showed 8±3%, 63±9% and 100±4% viability, after 24 hours treatment, using 1X, 10X and 100X experimental media, respectively. MC3T3 cells (Figure 5.2.B), after 24 hours, showed 5±3%, 47±5% and 105±4% viability for 1X, 10X and 100X

experimental media, respectively. The experimental media of unreacted components followed a dose-dependent viability trend (1X<10X and 100X).

The cytotoxicity results obtained from the LDH assay is shown in Figures 5.2.C and 5.2D. LDH, a cytoplasmic marker for membrane integrity, provides an indirect means of assessing cytotoxicity. This assay specifically detects change in absorbance due to release of LDH enzyme that catalyzes interconversion of pyruvate (NADH) to lactate (NAD^+), and vice versa [209]. NIH3T3 cells (Figure 5.2.C) showed 90±5%, 31±8% and 2±5% LDH release (normalized to the dead control) for 1X, 10X and 100X experimental media, respectively. After 24 hours, MC3T3 cells (Figure 5.2.D) treated with 1X, 10X and 100X experimental media showed 89±10%, 55±4% and 4±4 % LDH release, respectively. The dose-dependent cytotoxicity followed the trend: 1X>10X>100X.

5.2.2. *In vitro* studies to examine the effects of crosslinked nanocomposites

Figures 5.3.A and 5.3.B show the results of the Presto Blue assay. NIH3T3 cells showed greater than 84% viability for all the 1X crosslinked nanocomposites. Cells treated with MWGONR nanocomposites exhibited 103±7% viability (maximum), GONP nanocomposites 84±3% viability (minimum), and PPF control 103±3% viability. Cells treated with 10X and 100X experimental solutions showed ~100% viability for all nanocomposites. MC3T3 cells (Figure 5.3.B) showed more than 78% viability for 1X extracts of crosslinked nanocomposites. Cells treated with MSNP nanocomposites exhibited 89±2% viability (maximum), MWCNT nanocomposites 84±3% viability (minimum), and PPF control 78±2% viability. Cells treated with 10X, and 100X experimental media showed ~100% viability for all nanocomposites. Presto

Blue results clearly indicated a dose-dependent (1X < 10 and 100 X) viability for crosslinked nanocomposites.

LDH cytotoxicity assay (Figure 5.3.C) for NIH3T3 cells showed 33±7% LDH release (maximum) for MWCNT nanocomposites, 20±5% LDH release (minimum) for WSNT nanocomposites and 25±8% LDH release for PPF control. 10X and 100X experimental media for all nanocomposites showed negligible (~0%) LDH release. MC3T3 cells (Figure 5.3.D) showed 21±8% (maximum) LDH release for MWGONR nanocomposites, 15±7% LDH release (minimum) for WSNT nanocomposites and 11±4% LDH release for PPF control. 10X and 100X experimental media of all nanocomposites showed ~0% LDH release. The LDH results of the crosslinked nanocomposites indicated a dose-dependent (1X < 10 and 100 X) cytotoxicity.

5.2.3. *In vitro* studies to examine the effects of degradation products

Figure 5.4 shows the results of the Presto Blue and LDH assay. NIH3T3 cells in Figure 5.4.A showed more than 23% viability upon treatment with 2X experimental media of degradation products. Cells treated with MSNP nanocomposites showed 48±3% viability (maximum), GONP nanocomposites 23±4% viability (minimum), and PPF control 38±2% viability. Cells treated with 10X, and 100X experimental media showed 76-97% and 89-104% viability, respectively. In general, MC3T3 cells (Figure 5.4.B) showed more than 25% viability after treatment with 2X experimental media. Cells treated with MSNP nanocomposites exhibited 37±6% viability (maximum), MWCNT nanocomposites 27±3% viability (minimum), and PPF control 37±5% viability. Cells treated with 10X, and 100X experimental media showed ~100% viability.

LDH assay results for NIH3T3 cells treated with 2X experimental media (Figure 5.4.C) showed 65±8% LDH release (maximum) for MWCNT nanocomposites, 40±4% LDH release (minimum) for MSNP nanocomposites, and 34±10% LDH release for PPF control. Cells treated with 10X, and 100X experimental media showed 4-23% and 3-8% LDH release, respectively. MC3T3 cells (Figure 5.4.D) treated with 2X experimental media showed 77±12% LDH release (maximum) for MWCNT nanocomposites, 62±7% LDH release (minimum) for MSNP nanocomposites, and 67±10% LDH release for PPF control. Cells treated with 10X and 100X experimental solutions showed 7-20% and 2-17% LDH release, respectively.

Osmolarity (Figure 5.5) of all 2X experimental media used for treating NIH3T3 cells were in range of 250-270 mOsm (significant differences marked with '*'); significantly lower compared to DMEM media (350 mOsm). Osmolarity of all 2X experimental media used for treating MC3T3 cells were in range of 235-250 mOsm; significantly lower compared to MEM-α media (309 mOsm). At 10X and 100X dilutions, osmolarity of nanocomposites approached the osmolarity of blank media (350 and 309 mOsm for DMEM and MEM-α, respectively) for both DMEM and MEM-α

5.2.4. *In vitro* studies to characterize the cell attachment and spreading on crosslinked nanocomposites

The cell attachment on crosslinked nanocomposites after 24 hours of incubation was characterized by counting the number of cells using a hemacytometer. Figure 5.6 shows the comparison of the fraction (in percentage) of initial seeded cells that were attached to the nanocomposites. Fraction of adherent NIH3T3 cells (Figure 5.6.A) was between 45-57% on the nanocomposites. The maximum attachment of 57±1% was observed for WSNT nanocomposites

and minimum 45±1% for SWCNT nanocomposites. PPF control showed 57±4% cell attachment whereas TCPS positive control showed 90±9% cell attachment. Fraction of the adherent MC3T3 cells (Figure 5.6.B) on the nanocomposites were 40-49% of the initial seeded cells. WSNT nanocomposites showed maximum attachment of 49±4% and SWCNT nanocomposites minimum attachment of 40±2%. MC3T3 cell attachment on PPF and TCPS controls was 46±4% and 93±3%, respectively. Number of attached cells on surface of nanocomposites were significantly lower than TCPS control (marked with "**" in Figure 5.6). Only SWCNT and MWCNT nanocomposites showed a significantly lower cell attachment compared to PPF control (marked with "*"). Overall, presence of nanomaterials evaluated in this study did not have a significant effect on cell attachment compared to PPF control although a greater number of cells attached to inorganic nanocomposites compared to the carbon nanocomposites.

Cell attachment and spreading on the various nanocomposites was further characterized using confocal fluorescence imaging (Figure 5.7) and SEM (Figure 5.8). For the fluorescence characterization, calcein-AM dye was used to stain the cells. This dye is a marker for intracellular esterase activity of viable cells indicated by enhanced green fluorescence [45]. After 5 days of incubation, stained NIH3T3 and MC3T3 cells showed viability, attachment and spreading on the nanocomposite surfaces similar to TCPS control (Figure 5.7).

SEM analysis in Figure 5.8 provided more details regarding the cell attachment and spreading on the surface of nanocomposites. As seen in Figure 5.8.A, after 24 hours incubation, although the cells were attached to the surface of nanocomposite, the surface of nanocomposite was partially covered by round cells (marked with white arrows in Figure 5.8.A). Filopodia extensions and extra cellular matrix (ECM) formation (black and white arrows, respectively) was

more clearly observed under SEM after incubations for five days. The white arrows point to cells although it is difficult to distinguish cells from surrounding ECM.

5.3. Discussions

The objective of this study was to systematically evaluate the *in vitro* cytotoxicity of PPF nanocomposites incorporated with various 1-D and 2-D carbon (SWCNTs, MWCNTs. SWGONRs, MWGONRs and GONPs) and inorganic (WSNTs and MSNPs) nanomaterials. The loading concentration of each nanomaterial was the concentration that showed maximum reinforcement of PPF polymer in chapter 4. The adherent NIH3T3 fibroblast-like cells [305, 306] and MC3T3 osteoblast precursor cells [307, 308] used in this study are widely accepted for *in vitro* cytotoxicity testing of materials for orthopedic or bone tissue engineering applications. *In vitro* cytotoxicity studies were performed before crosslinking, after crosslinking and after accelerated degradation of the nanocomposites. While cytotoxicity of crosslinked nanocomposites and their degradation products is necessary to obtain insights into the possible response of the nanocomposites post-implantation [309], assessment of cytotoxicity of nanocomposite components before crosslinking is necessary because these components would interact with tissues when injected into bone defect sites [49, 299].

As seen in Figure 5.2, the cytotoxic effects of unreacted components decreased in a dose-dependent manner after 24 hours of incubation. For applications that will employ *in situ* crosslinking of PPF nanocomposites, the crosslinking reaction time will be a few minutes. In such a scenario, the toxic, leachable components will be minimal. The three components in the uncrosslinked nanocomposites are PPF, nanomaterials, and NVP crosslinker. Previous reports show that PPF complete coats the nanomaterials [26, 50, 62, 294]. Thus, small PPF oligomers

and NVP crosslinker will be the only components that will directly interact with cells in the first 24 hours. Therefore, only PPF/ NVP blends were used for preparation of the experimental media. Our results are similar to a previous study that attributed the dose-dependent cytotoxicity mainly to the unreacted crosslinker [299].

The high cell viability and low LDH release (Figure 5.3) observed for 1X, 10X and 100X experimental media of all the crosslinked nanocomposites suggests that improved crosslinking prevented the leaching of potentially toxic components (such as unreacted NVP crosslinker [310] and BP radical initiator residue [311, 312]) during media extraction process. Indeed, all but SWGONR crosslinked nanocomposites, had previously exhibited increased crosslinking densities compared to PPF baseline control. SWCNT, MWCNT, SWGONR, MWGONR, GONP, MSNP and WSNT nanocomposites had shown 87±2%, 86±2%, 84±1%, 89±1%, 88±1%, 92±1% and 92%±2 crosslinking density compared to 84±2% crosslinking density for PPF polymer, respectively [50, 62].

The effects of the degradation components of the nanocomposites on cells during its gradual biodegradation is a necessary factor that needs to examined for the eventual use of these nanocomposites for *in vivo* applications. PPF [313] and carbon nanomaterials have been shown to undergo biodegradation [314]. However, PPF undergoes hydrolytic degradation while carbon nanomaterials can be degraded by oxidative reactions in the presence or absence of enzymes [314, 315]. The degradation of the inorganic nanomaterials still needs to be examined. Crosslinked PPF degrades very slowly. Thus an accelerated degradation method is typically employed that hydrolyses the PPF network in one week [294]. Previous reports employed NaOH and HCl to accelerate the hydrolysis of ester bonds in PPF/propylene fumarate-diacrylate (PF-DA) that caused substantial increase in the osmolarity [28]. It is well known that high osmolarity

could be cytotoxic [316, 317], and thus, it would be difficult to differentiate if any observed toxicity is due the degraded components or high osmolarity. Thus, weaker degrading agents such as calcium hydroxide ($Ca(OH)_2$) and phosphoric acid (H_3PO_4) that produce insoluble $Ca_3(PO_4)_2$ salt crystals after neutralization were used to resolve this issue. Unlike NaCl that undergoes complete ionization and increases osmolarity to values higher than 1000 mOsm [80, 316] (compared to plasma osmolarity of 282-295 mOsm), $Ca_3(PO_4)_2$ partially ionizes resulting in lower osmolality (235-270 mOsm) of the extracts of degradation products.

In this study, the nanomaterials were present at concentrations of ≤ 0.2 wt%. Thus, given what is known about degradation mechanism of the nanomaterials, and their presence in the polymer matrix at low concentration, the major degradation product that would have an adverse effect on cells would be fumaric acid generated from PPF. The degradation products of PPF, have been previously shown to elicit dose-dependent cytotoxicity [80, 299]. Since the dose-dependent cell viability and cell death results in Figure 5.4 is similar to those studies, we hypothesize the degradation products of PPF are mainly responsible for the observed dose-dependent cytotoxicity. This low osmolarity could also contribute partially to the cytotoxicity results since contact with solutions of lower osmolality brings about damages in cell membrane due to changes in cell volume.

The cell attachment and spreading on the nanocomposites were similar to PPF and lower compared to TCPS control (Figure 5.5). The increased cell attachment on TCPS control is due to the negatively charged surface of the TCPS plate that results in better cell spreading and attachment. Variations in the numbers of attached to nanocomposites compared to PPF control (Figure 5.6) maybe due to different opposing factors that affect cell attachment: nanomaterials (such as MWCNTs [318]) result in better adsorption of cell attachment proteins [319, 320], but

presence of attachment inhibitors such as insoluble poly (vinyl pyrrolidone) [299] and bundled nanomaterials [321] hinders cell attachment. In addition to the high density of cells on all nanocomposite surfaces (comparable to PPF control), significant cellular attachment and expansion observed after 5 days (Figures 5.7) is the reason for the increased deposition of ECM components on the surface of nanocomposites. As SEM micrograph in Figure 5.8 showed, formation of ECM (marked with black arrows) provided a matrix for further cells spreading and proliferation [322].

To the best of our knowledge, this is the first report that investigates and compares the *in vitro* cytocompatibility of various 1-D and 2-D carbon and inorganic nanomaterial incorporated polymeric nanocomposite for bone tissue engineering. As mentioned above, the loading concentration of each nanomaterial was one that showed maximum reinforcement of PPF polymer in chapter 4. Thus, even though loading concentrations of all the nanomaterials were low ($\leq$ 0.2 wt%), they were not similar. However, none of the nanocomposites showed significant differences in cellular response to the various forms (uncrosslinked, crosslinked and degraded) of the nanocomposites compared to PPF control. An initial minor cytotoxicity response and lower cell attachment was observed only for a few nanocomposite groups, none of the nanocomposites showed significant differences in cellular response to the various forms (uncrosslinked, crosslinked and degraded) of the nanocomposites compared to PPF control at later time points. The favorable *in vitro* results suggest that all these nanocomposites under these efficacious (enhanced mechanical properties compared to PPF) loading concentrations are suitable for *in vivo* bone replacement therapies.

5.4. Conclusions

The biodegradable PPF nanocomposites were fabricated using poly (propylene fumarate) polymer, N-vinyl pyrrolidone (NVP) crosslinker and 1-D and 2-D nanomaterials: single- and multi-walled carbon nanotubes, single- and multi-walled graphene oxide nanoribbons, graphene oxide nanoplatelets, molybdenum disulfide nanoplatelets and tungsten disulfide nanotubes at loading concentrations between 0.02-0.2 wt% do not show significant differences cellular response to their various forms (uncrosslinked, crosslinked and degraded nanocomposites) compared to PPF control. The extraction media of the uncrosslinked components elicit a significant dose-dependent cytotoxic effect. The extraction media of the uncrosslinked components elicit a significant dose-dependent cytotoxic effect. The extraction media of the crosslinked nanocomposite do not adversely affect viability of NIH3T3 and MC3T3 cells. Cells attached, proliferated and spread well on all the nanocomposite surfaces. The degradation products of nanocomposites induce a mild dose-dependent cytotoxic response The results of this chapter demonstrate that all the nanocomposites have favorable *in vitro* cytocompatibility and could be considered as implants for bone tissue engineering applications.

5.5.Figures

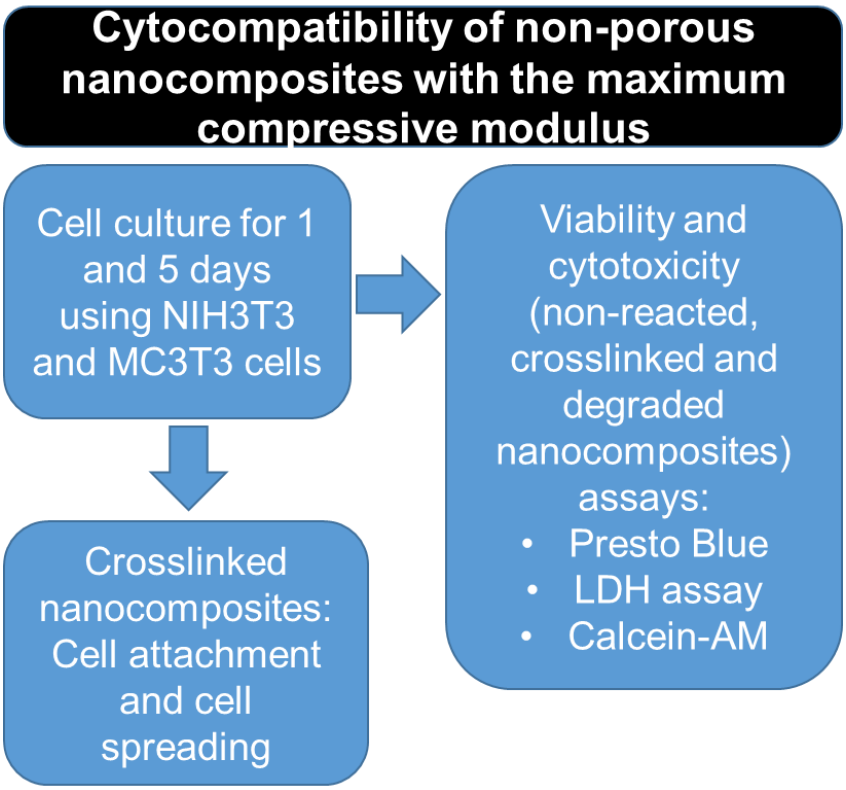

Figure 5.1. Flowchart depicting the experimental outline for cytocompatibility analysis.

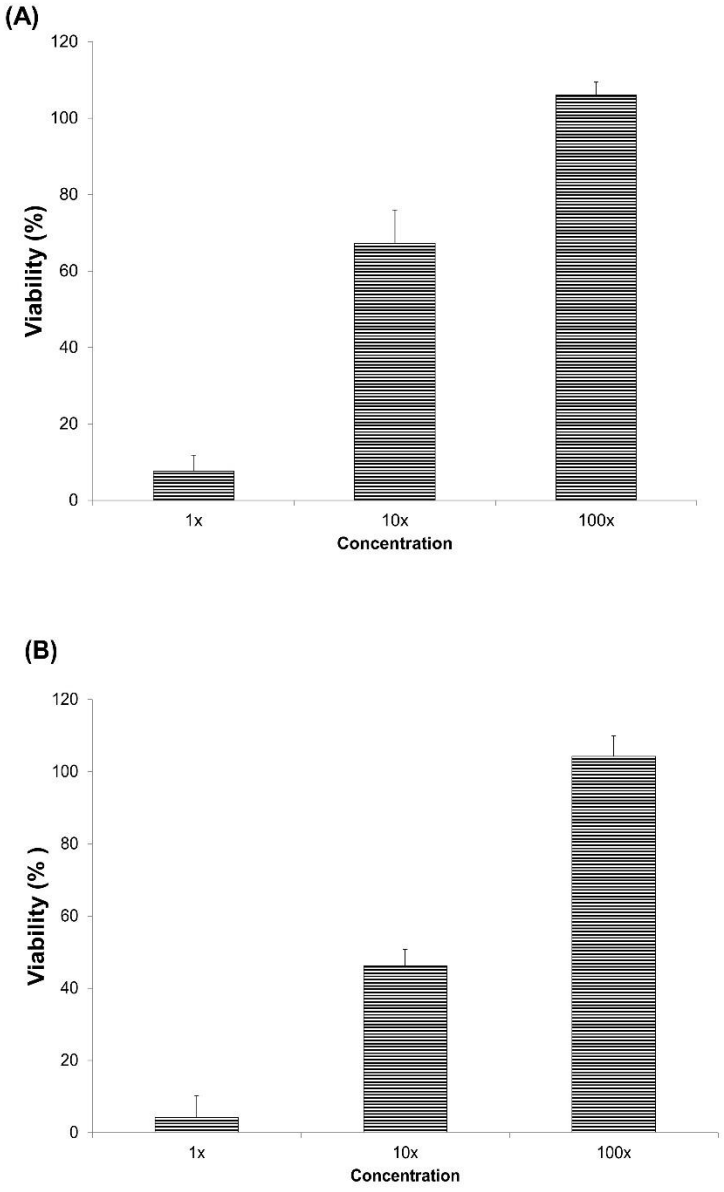

Figure 5.2. Viability of: A) NIH3T3 and B) MC3T3 cells, after 24-h exposure to extracts of unreacted micromeres. Data has been normalized with respect to the live control and error bars represent standard deviations for n=6 (Continued on the next page).

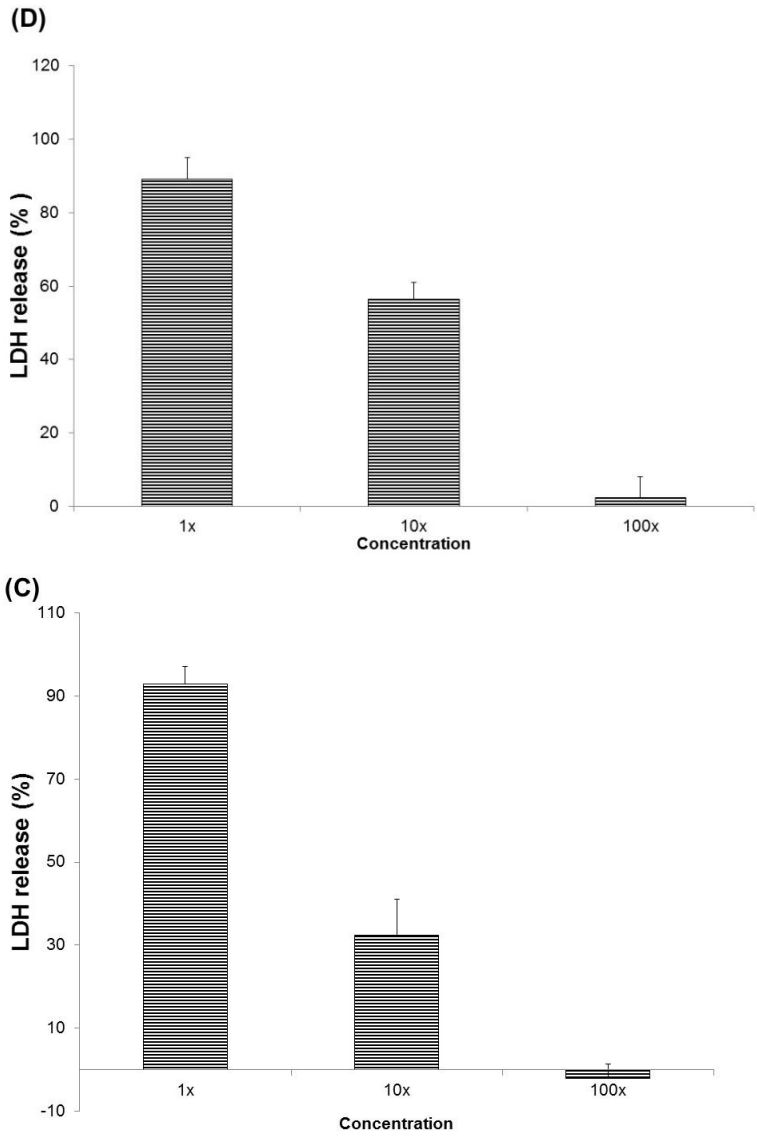

Figure 5.2. LDH release of C) NIH3T3 and D) MC3T3 cells, after 24-h exposure to extracts of unreacted micromeres. Data has been normalized with respect to the dead control and error bars represent standard deviations for n=6 samples.

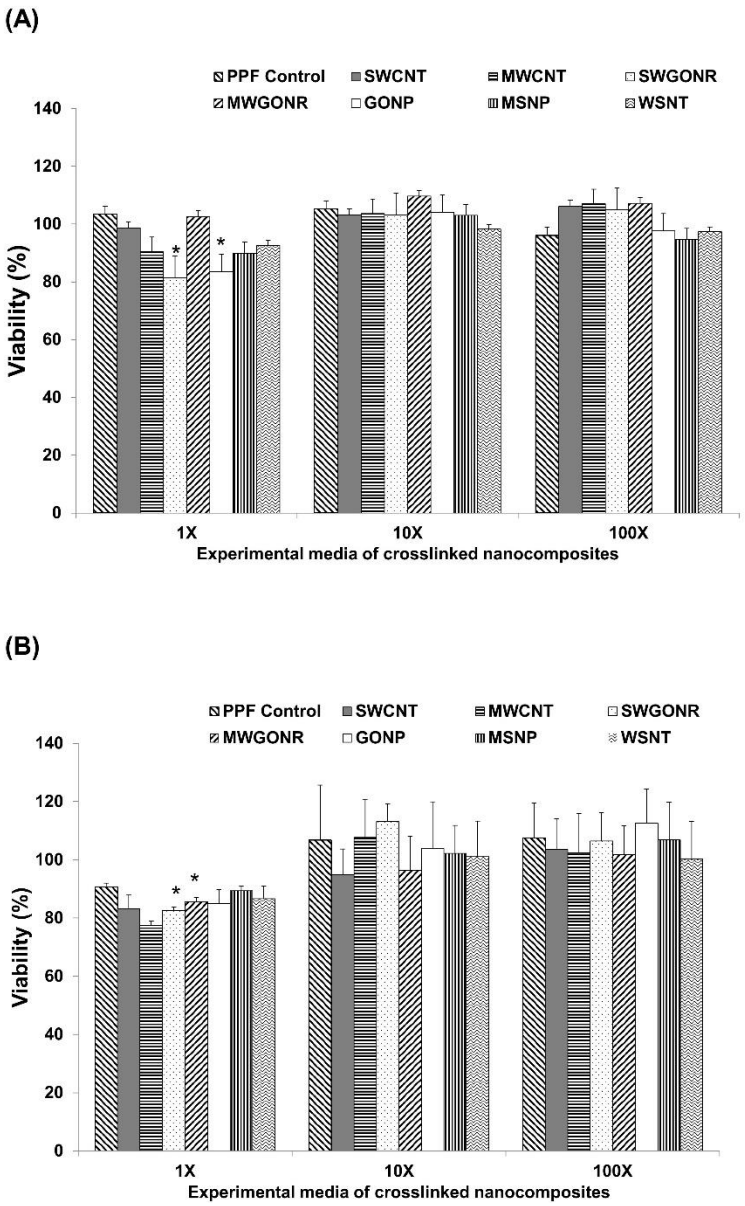

Figure 5.3. Viability of: A) NIH3T3 and B) MC3T3 cells, after 24-h exposure to extracts of crosslinked nanocomposites. Data has been normalized with respect to the live control and error bars represent standard deviations for n=6. The symbol "*" indicates statistically significant difference between PPF baseline and PPF nanocomposites ($p < 0.05$) (Continued on the next page).

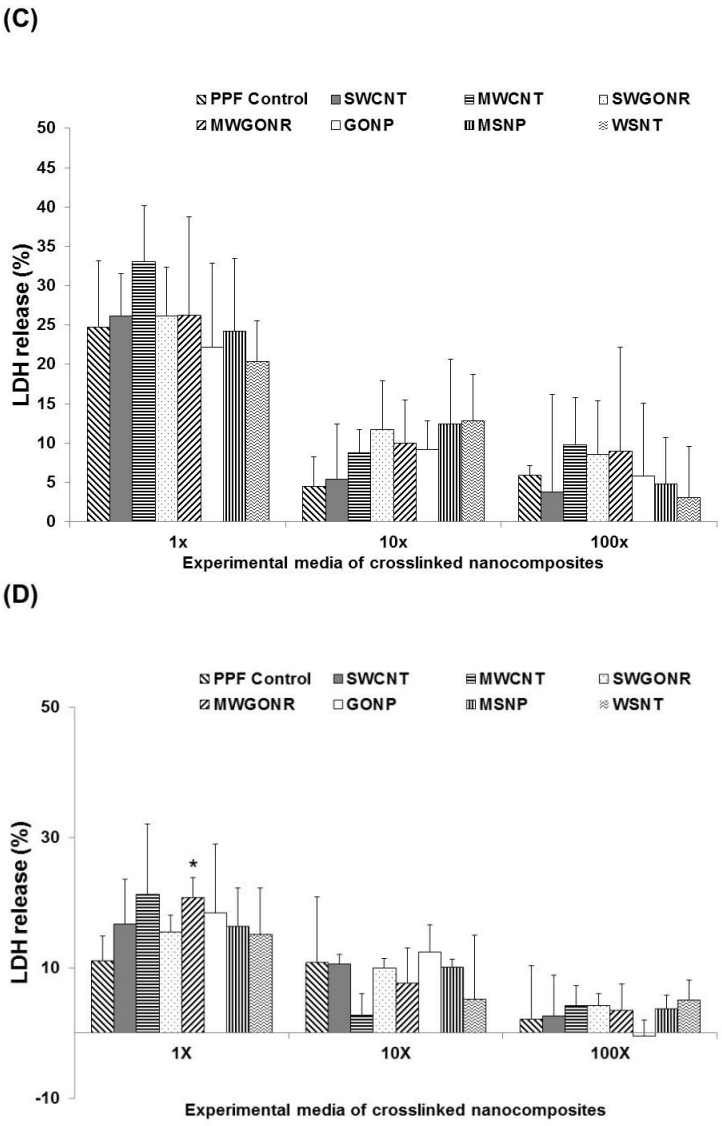

Figure 5.3. LDH release by: C) NIH3T3 and D) MC3T3 cells after 24-h exposure to extracts of crosslinked nanocomposites. Data has been normalized with respect to live and dead controls and error bars represent standard deviations for n=6. The symbol "*" indicates statistically significant difference between PPF baseline and PPF nanocomposites ($p < 0.05$) (Continued from the pevious page).

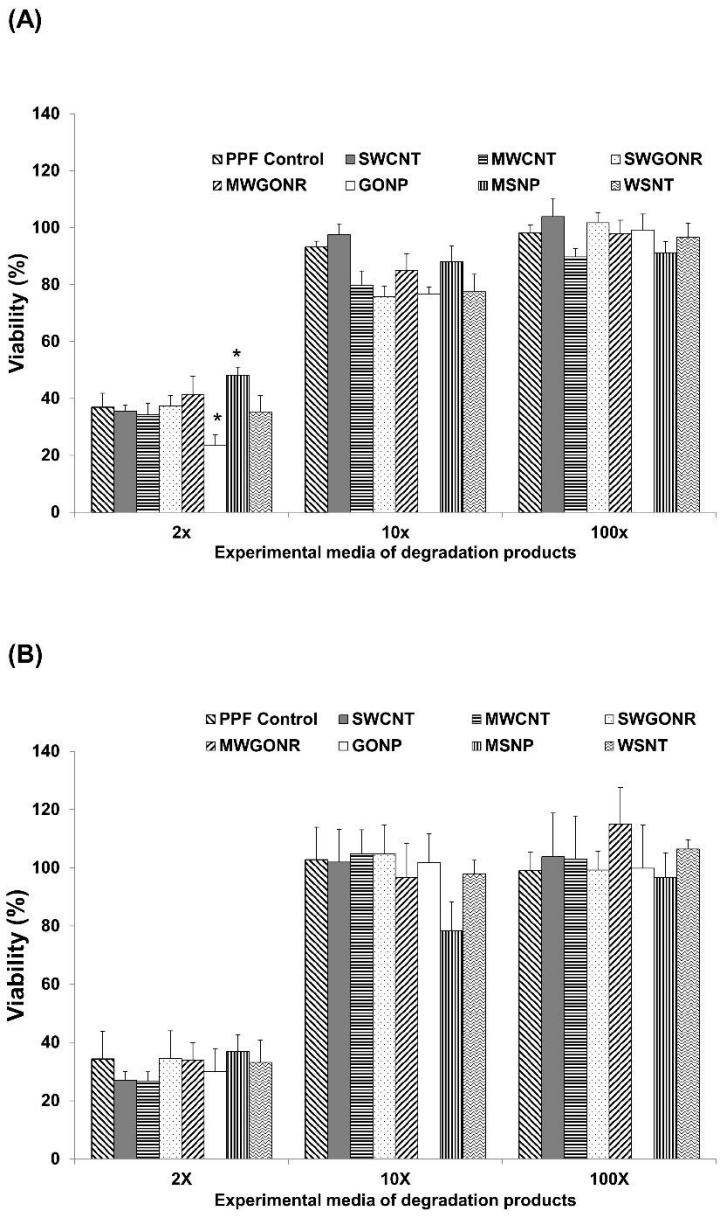

Figure 5.4. Viability of: A) NIH3T3 and B) MC3T3 cells, after 24-h exposure to extracts of degradation products. Data has been normalized with respect to live and dead controls, and error bars represent standard deviations for n=6. The symbol "*" indicates statistically significant difference between PPF baseline and PPF nanocomposites ($p < 0.05$) (Continued on the next page).

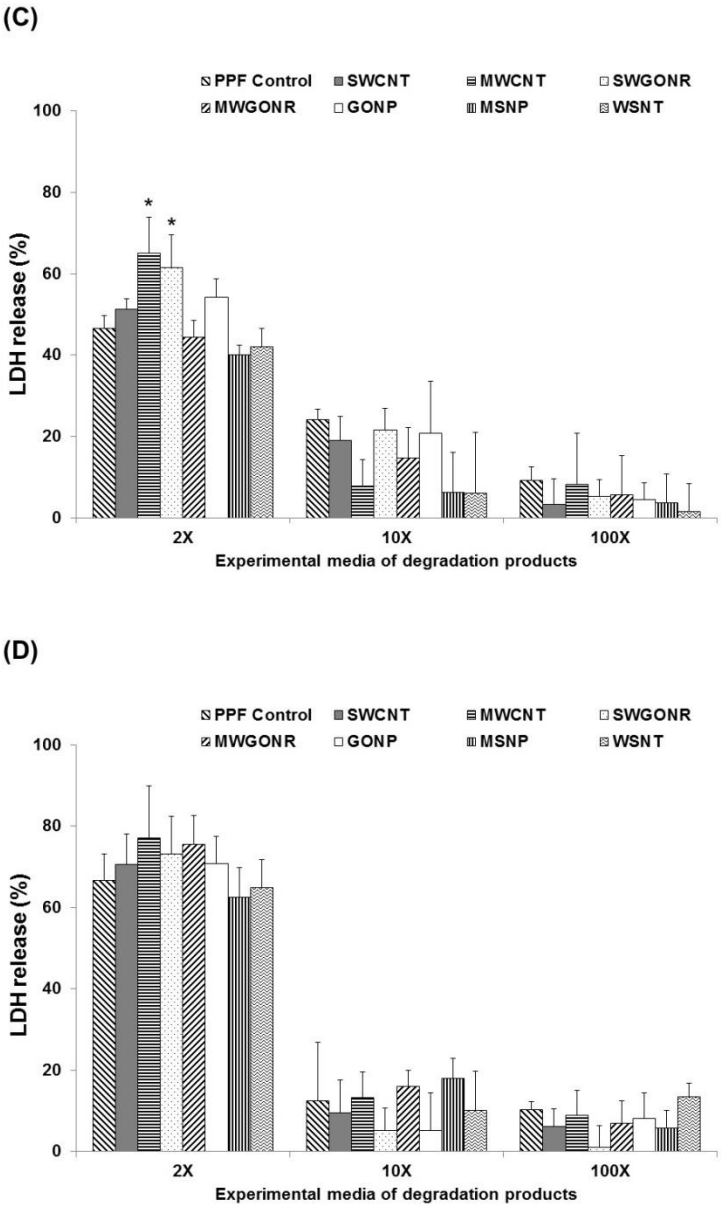

Figure 5.4. LDH release by: C) NIH3T3 and D) MC3T3 cells, after 24-h exposure to extracts of degradation products. Data has been normalized with respect to the dead control and error bars represent standard deviations for n=6. The symbol "*" indicates statistically significant difference between PPF baseline and PPF nanocomposites ($p < 0.05$) (Continued from the previous page).

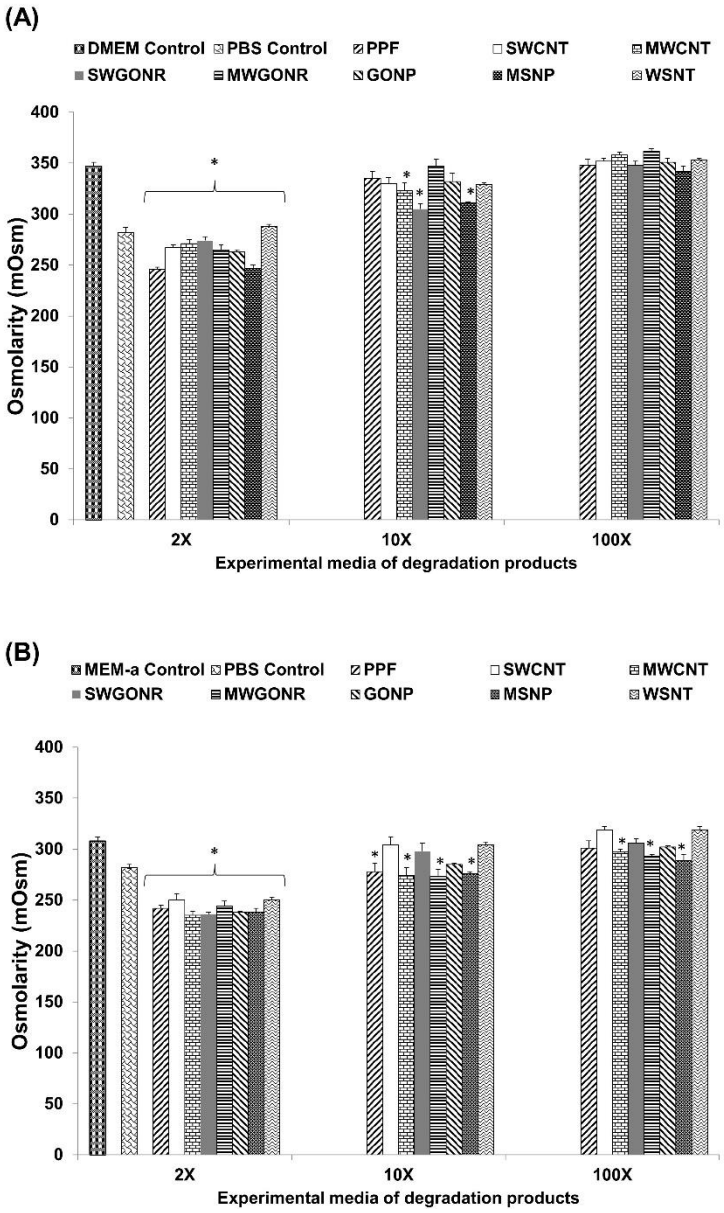

Figure 5.5. Osmolality of the extracts of degradation products used for culture of: A) NIH3T3 and B) MC3T3 cells. Error bars represent standard deviations for n=3. The symbol "*" indicates statistically significant difference between extracts of degradation products and unaltered cell culture media ($p < 0.05$).

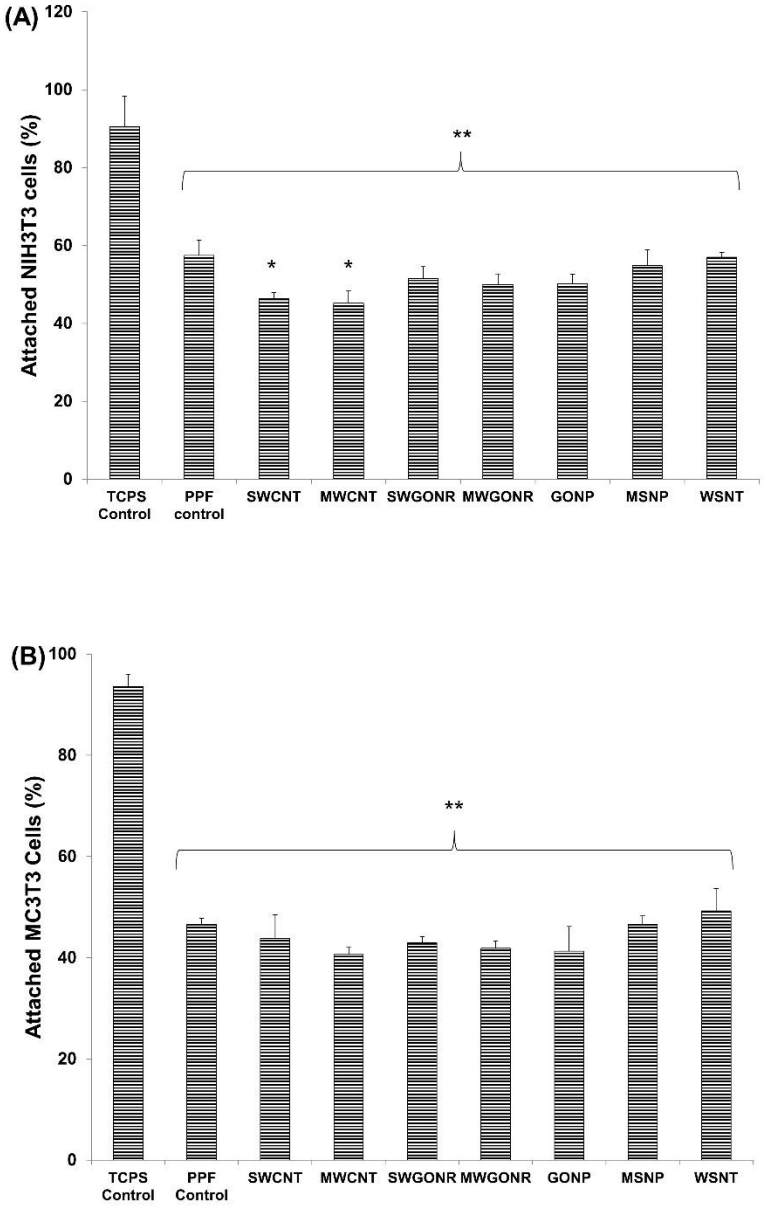

Figure 5.6. Fraction of attached cells to the tissue culture poly styrene (TCPS), baseline PPF control and nanocomposites after 24-h incubation. Initial seeding density was 400,000 cells/specimen. Error bars represent standard deviations for n=3. The symbol "*" indicates statistical significant difference between PPF baseline and PPF nanocomposites. The symbol "**" indicates significant difference between baseline control PPF, PPF nanocomposites and TCPS ($p < 0.05$).

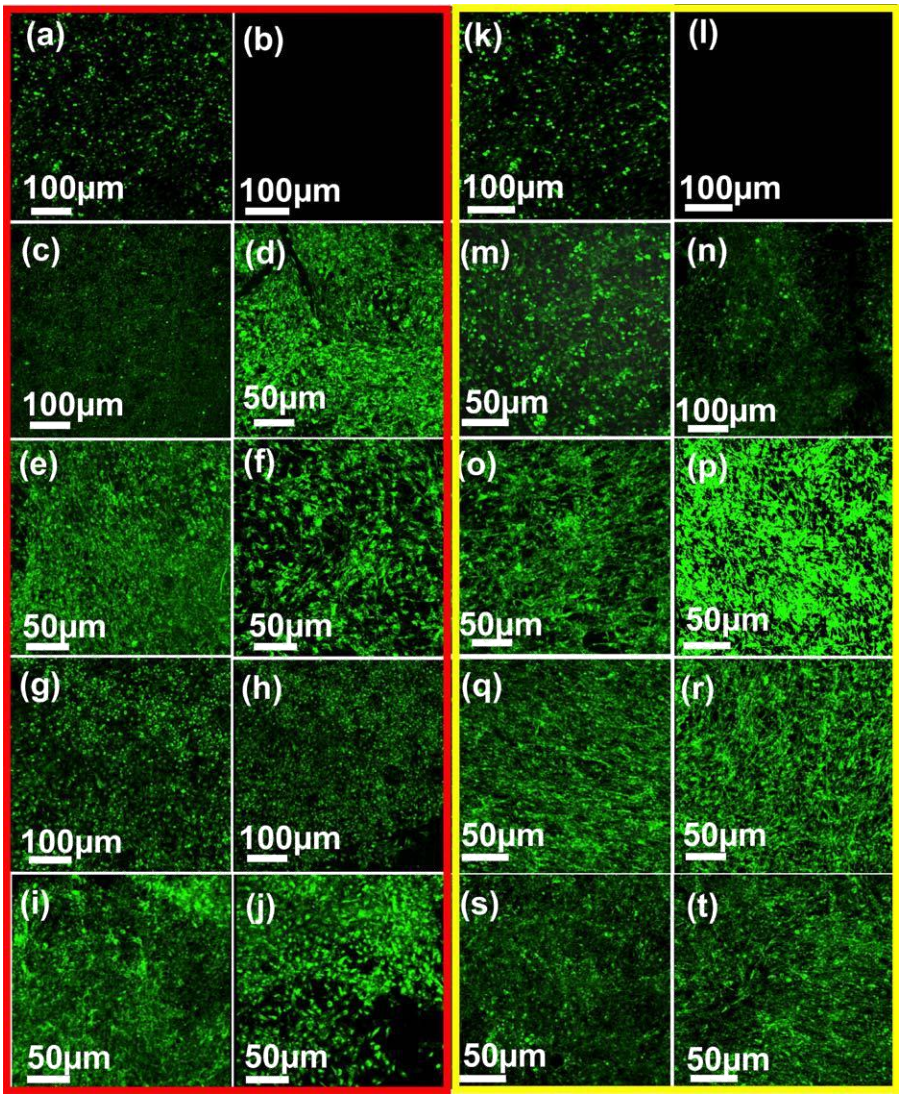

Figure 5.7. Representative fluorescent microscopy images of attached cells on crosslinked nanocomposites after 5 days of cell culture for NIH3T3 and MC3T3 cells, respectively: (a, k) TCPS (positive) control, (b, l) negative control, (c, m) PPF control, (d, n) GONP (e, o) MWCNT, (f, p) SWCNT, (g, q) MWGONR, (h, r) SWGONR, (i, s) MSNP and (j, t) WSNT nanocomposites.

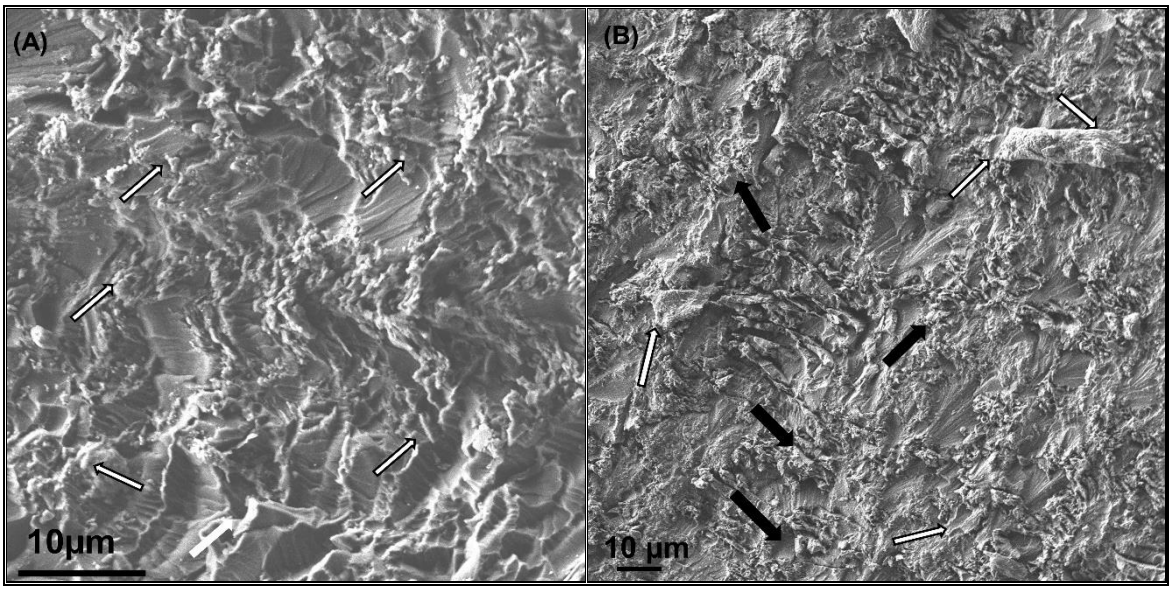

Figure 5.8. Representative SEM images of GONP nanocomposite after cell culture for: A) 1 day and B) 5 days (Cells and their filopodia extensions are marked with white arrows whereas ECM is marked with black arrows).

Chapter 6: Boron Nitride Reinforced Polymeric Nanocomposites for Bone Tissue Engineering

6.1. Introduction

In the previous chapters, we investigated the mechanical properties and cytocompatibility of biodegradable PPF nanocomposites reinforced using 1-D and 2-D inorganic and carbon nanostructures (SWCNTs, MWCNTs, SWGONRs, MWGONRs, GONPs, MSNPs, and WSNTs). This chapter will investigate the efficacy of boron nitride nanomaterials (nanotubes and nanoplatelets) as reinforcing agents for PPF polymer.

The unique physiochemical properties of one- and two-dimensional (1-D and 2-D) carbon and inorganic nanomaterials have been harnessed for therapeutic drug delivery, and bioimaging applications [227, 323-325]. Recently, in the field of tissue engineering, carbon nanomaterials fullerenes, carbon nanotubes (CNTs), and graphene have been employed as building blocks to fabricate three-dimensional (3-D) porous scaffolds [224, 326]. Over the last decade, pristine and functionalized formulations of these carbon nanomaterials as well as inorganic nanomaterials such as alumoxane nanoparticles [192], tungsten disulfide nanotubes [62] and molybdenum disulfide nanoplatelets [50] have been investigated as reinforcing agents to improve the mechanical properties of various biodegradable and biocompatible polymeric matrices for load bearing bone tissue engineering applications [50, 62, 80, 299].

In chapters 4 and 5 we discussed the efficacy of carbon (SWCNTs, MWCNTs, SWGONRs, MWGONRs and GONPs) and inorganic nanomaterials (WSNTs and MSNPs) as reinforcing agents to improve the mechanical properties of PPF nanocomposites and their *in*

vitro cytocompatibility. Our results show that while all the 1-D and 2-D nanocomposites were cytocompatible at low nanomaterials loading concentrations, inorganic nanomaterials are the better reinforcing agents than carbon nanomaterials. Missing from the above list of reinforcing agents for biodegradable polymers, are boron nitrides nanoparticles, which are structurally similar to carbon nanomaterials [327, 328].

The physiochemical properties of boron nitride nanomaterials are similar and in some cases superior to carbon nanomaterials [327, 329-331]. For example, boron nitride nanotubes (BNNTs) and boron nitride nanoplatelets (BNNPs, exfoliated bulk boron nitride - less than ten atomic layers) exhibit excellent mechanical properties [332]. Furthermore, BNNTs and BNNPs can be functionalized with various functional groups such as amines, nitriles, epoxides and oxides [332-334] that further improve their dispersion in polymer matrices and facilitate better polymer-nanomaterial interaction and allow efficient load transfer from the polymer to the nanomaterials [332].

Till date only BNNTs have been explored as reinforcing agent to improve tensile mechanical properties of polylactide-polycaprolactone [335] co-polymers. however their application as a part of a nanocomposite bone graft has not been thoroughly investigated. Herein we have investigated the efficacy of BNNTs and BNNPs as reinforcing agents to improve the compressive mechanical properties of biocompatible, and biodegradable polymer poly propylene fumarate (PPF); widely investigated for load bearing bone tissue engineering applications [19, 50, 62, 80, 184, 195, 336-338]. Additionally, along with efficacy studies, the *in vitro* cytotoxicity and *in vivo* biocompatibility of nanomaterials-incorporated polymers also need to be thoroughly investigated. To this aim, we thoroughly examined the *in vitro* cytocompatibility of BNNT and BNNP nanocomposites before crosslinking, after crosslinking and upon degradation using

murine MC3T3 pre-osteoblast cell line. Additionally, we have characterized cell attachment, cell spreading and protein adsorption on BNNT and BNNP nanocomposites.

6.2. Results

6.2.1. Transmission electron microscopy (TEM) of nanocomposites

TEM was used to characterize the dispersion of BNNTs and BNNPs in crosslinked PPF nanocomposites (Figure 6.1). BNNTs and BNNPs appear as well dispersed and embedded nanomaterials in the polymeric matrix and are present as individually dispersed nanoparticles, or aggregates of a few nanoparticles. The dimensions of BNNTs and BNNPs (diameter of ~100 μm and length of ~2μm for BNNTs and diameter of ~200-400 nm for BNNPs) dispersed in the polymeric matrices were approximately similar to the TEM images shown in chapter 3.

6.2.2. Compressive mechanical properties of nanocomposites

Figures 6.2.A and 6.2.B display the compressive modulus and compressive yield strength of BNNT and BNNP nanocomposites (at nanomaterial loading concentration = 0.2 wt. %). The addition of BNNTs and BNNPs to PPF polymer resulted in ~15% and ~38% increase in compressive modulus compared to PPF baseline control, respectively (Figure 6.2.A and Table 6.1). Furthermore, up to 6% and 31% increase in compressive yield strength were observed for BNNT and BNNP nanocomposites, respectively (Figure 6.2.B and Table 6.1). While both BNNP and BNNT nanocomposites showed an increase in compressive mechanical modulus and compressive mechanical strength compared to PPF baseline control, only BNNP nanocomposites showed a significant increase (marked with "*" in Figure 6.2.A).

6.2.3. Sol-fraction analysis

Figure 6.2.C displays the crosslinking density of nanocomposites versus PPF control. The crosslinking density was determined from sol-fraction analysis which is based on the rationale that uncrosslinked PPF and NVP are soluble in methylene chloride whereas crosslinked polymer is insoluble [184]. The crosslinking density of PPF, BNNT, and BNNP nanocomposites were ~85%, ~90% and ~86%, respectively. No statistically significant difference in the crosslinking density was observed between the three groups.

6.2.4. Protein adsorption on crosslinked nanocomposites

Figures 6.3.A-C show the adsorption of collagen-I, fibrin, and fibronectin after 1, 5, and 9 days of incubation with BNNT, BNNP and PPF disks quantified by bicinchoninic acid assay (BCA). The adsorption of collagen-I on the nanocomposites was similar or higher compared to PPF baseline control in a time-dependent manner (Figure 6.3.A). After 9 days of incubation, BNNT and BNNP nanocomposites showed ~41±5% and 18±9% collagen-I adsorption, respectively; significantly higher than PPF control which showed 5±3% collagen-I adsorption. In contrary to collagen-I, the adsorption of fibrin and fibronectin on the nanocomposites were similar or lower compared to PPF adsorption at all-time points (Figure 6.3.B and 6.3.C). BNNT, BNNP and PPF disks showed 47±1%, 49±1%, and 52±2% fibrin adsorption, respectively, after incubation for 5 days. After 9 days of incubation, BNNT and BNNP nanocomposites showed 39±1% and 45±1% fibrin adsorption, respectively; that was significantly lower than 50±2% adsorption observed for PPF control. Moreover, BNNT and BNNP and PPF samples showed 6±1%, 5±1%, and 7±2% fibronectin adsorption, respectively, after incubation for 5 days. Similarly, BNNT and BNNP nanocomposites and PPF composites showed 5±1%, 4±2%, and

6±2% fibronectin adsorption after incubation for 9 days, respectively. There were no significant differences in the measured fibronectin adsorption across all time points.

6.2.5. *In vitro* cytocompatibility study of nanocomposites

Figure 6.4 displays the viability (assessed by Presto Blue® assay) of MC3T3 cells and their LDH release after exposure to nanomaterials dispersions, non-crosslinked nanocomposites, crosslinked nanocomposites and degraded nanocomposites.

6.2.5.1. Cytocompatibility of BNNT and BNNP nanomaterials

Figure 6.4.A shows the viability of cells upon exposure to BNNT and BNNP dispersions. After 24 hours incubation with 100 μg/mL nanomaterial concentration, MC3T3 cells showed 99±13% and 83±16% viability for BNNTs and BNNPs, respectively (Figure 6.4.A). Incubation with 10 μg/mL nanomaterial concentration MC3T3 cells showed 77±14% and 90±9% viability for BNNTs and BNNPs, respectively. Finally, MC3T3 cells incubated with 1 μg/mL nanomaterial concentration media showed ~100% cell viability for both the nanomaterials.

Figure 6.4.B shows the cytotoxicity inferred from LDH release (normalized to positive control) after exposure to aqueous dispersions of BNNT and BNNP nanomaterials at 1-100 μg/mL concentrations. After 24 hours incubation with 100 μg/mL concentrations of BNNTs and BNNPs, the cells secreted 21±4% and 27±8% LDH, respectively. LDH release reduced upon incubation a lower nanoparticle concentrations. Cells incubated with 10 μg/mL dispersions of BNNTs and BNNPs showed 27±2% and 16±8% LDH release, respectively. Finally, the cells incubated with 1 μg/mL dispersions of BNNTs and BNNPs showed 19±4 and -28±5% LDH release, respectively.

6.2.5.2. Cytocompatibility of components prior to crosslinking

Figure 6.4.C shows the viability of MC3T3 cells assessed by Presto Blue® assay after exposure to different concentrations of unreacted components extracted from nanocomposite blends. MC3T3 cells showed 4±6%, 6±7% and 3±4% viability after 24 hours of incubation with 1X experimental media of NVP/PPF, NVP/PPF/BNNTs and NVP/PPF/BNNPs blends, respectively. Cell viability increased with further dilutions; 10X experimental media showed 46±5%, 48±6% and 42±3% viability for NVP/PPF, NVP/PPF/BNNTs and NVP/PPF/BNNPs, respectively. Finally, MC3T3 cells incubated with 100X extracted media showed ~100% viability for all three experimental groups.

Figure 6.4.D displays the LDH release (normalized to positive control) upon exposure to unreacted components of BNNT and BNNP nanocomposite blends. After 24 hours incubation, 1X extracts of unreacted NVP/PPF, NVP/PPF/BNNTs and NVP/PPF/BNNPs blends showed 92±6%, 93±2%, and 91±2% LDH release, respectively. Incubation with 10X experimental media showed 51±5%, 52±2% and 50±1% LDH release for NVP/PPF, NVP/PPF/BNNTs and NVP/PPF/BNNPs, respectively. Finally, 100X experimental media showed 24±2%, 25±1% and 23±1% LDH release for NVP/PPF, NVP/PPF/BNNTs and NVP/PPF/BNNPs.

6.2.5.3. Cytocompatibility of crosslinked nanocomposites

Figure 6.4.E displays the results of Presto Blue® assay for viability of MC3T3 cells after 24-h exposure to the extracts of crosslinked nanocomposites. Cells treated with 1X extracts of crosslinked BNNT and BNNP nanocomposites after 24 hours incubation showed 84±6% and 81±11% viability, respectively, whereas the cells exposed to 1X extract of PPF controls showed 93±2% cell viability. Cells treated with 10X dilutions of extracts from crosslinked samples after

24 hours incubation showed 90±4%, 90±2% and 83±1% viability for BNNT, BNNP, and PPF samples, respectively. Cells treated with 100X dilutions of crosslinked nanocomposites or PPF control after 24 hours incubation showed ~92-96% viability for all three experimental groups. Overall, the results indicated that ≥80% MC3T3 cells are viable at each treatment concentration.

Figure 6.4.F shows LDH release by MC3T3 detected using LDH assay after 24-h exposure to extracts of the crosslinked nanocomposites. 1X extracts of the crosslinked BNNT and BNNP nanocomposites showed 10±6% and 21±6% LDH release, respectively. PPF controls showed 15±6% LDH release. For 10X dilutions, 12±8%, 22±10%, and 17±5% LDH release were measured from extracts of crosslinked BNNT, BNNP and PPF samples, respectively. 100X dilutions of BNNT, BNNP, and PPF experimental groups showed 18±5%, 25±4% and 24±6% LDH release, respectively.

6.2.5.4. Cytocompatibility of degradation products

Figure 6.4.G shows the viability of MC3T3 cells assessed by Presto Blue® assay upon exposure to degradation products of BNNT, BNNP, and PPF experimental groups. After 24 hours incubation with 2X extracts of degraded nanocomposites, MC3T3 cells showed 40±16%, 30±3% and 41±2% viability for BNNT, BNNP, and PPF samples, respectively. Incubation with 10X experimental media showed up to 80±5%, 93±8% and 81±11% viability for BNNT, BNNP, and PPF samples, respectively. Finally, incubation with 100X extracts of degradation products showed ~100% cell viability for all experimental groups.

Figure 6.4.H displays the normalized LDH release by MC3T3 cells after exposure to the extracts of nanocomposite degradation products. After 24 hours of exposure to 2X degradation

extracts, MC3T3 cells showed 82±18% and 82±14% LDH release for BNNT and BNNP nanocomposites, respectively. PPF controls showed 78±19% LDH release. For 10X dilutions, 30±3%, 10±10%, and 30±4% LDH release was measured for BNNT, BNNP, and PPF experimental groups, respectively. 100X dilutions showed 13±4%, 27±5% and 7±2% LDH release for BNNT, BNNP, and PPF experimental groups, respectively.

6.2.5.5. Osmolarity of degradation products

Figure 6.5 shows osmolarity of the extracts of degradation products. The osmolarity of 2X experimental media of degraded BNNT and BNNP nanocomposites was 242±4 mOsm and 210±1 mOsm, respectively. The extracts of degraded BNNT, BNNP, and PPF nanocomposites showed osmolarity values between 271-284 mOsm (for 10X extracts) and 298-304 mOsm range for 100X extracts, respectively. The osmolarity values of PPF control and $Ca_3(PO)_4$ control solution (400 μg/ml) were ~230 mOsm and 110 mOsm, respectively; significantly lower than all the experimental groups. The osmolarity of blank MEM-α media was also recorded and was 304±1 mOsm.

6.2.5.6. Cell attachment and spreading on crosslinked nanocomposites

Figure 6.6.A shows the fraction of attached cells (counted using hemocytometer) on BNNT, BNNP, and PPF crosslinked disks, after 24 hours of incubation. BNNT, BNNP and PPF disks showed 65±4%, 60±3%, and 57±6% cell attachment, respectively. TCPS control showed 87±7% cell attachment. Although no significant difference in cell attachment was observed between BNNT, BNNP and PPF disks, all three groups exhibited a significantly lower cell attachment compared to TCPS control.

Figure 6.6.B shows representative confocal scanning laser microscopy images of MC3T3 cells evenly spread out covering the surface of all experimental groups. The cell spreading observed on nanocomposites was comparable to TCPS controls. In addition to confocal imaging, SEM analysis was also performed to characterize cell attachment and spreading on the surfaces of crosslinked nanocomposites.

Figure 6.6.C displays SEM images of the surface of BNNT, BNNP, and PPF disks after cell culture for 5 days. All the experimental groups including PPF controls were completely covered with MC3T3 cells (marked with black arrows). The deposition of extra cellular matrix (ECM; marked with white arrows) can also be observed. MC3T3 cells displayed their characteristic spindle-shaped morphology with the formation of numerous cytoplasmic filopodia extensions (marked with circles).

6.3. Discussions

The objective of this study was to investigate the compressive mechanical properties and the *in vitro* cytocompatibility of BNNT and BNNP reinforced PPF nanocomposites. Prior to nanocomposite fabrication and testing, the structural and chemical properties of nanomaterials were characterized by TEM and Raman spectroscopy as discussed in chapter 3. Raman spectra showed the presence of impurities, functional groups and/ or defects. The presence of functional groups and defects results in better nanomaterials/polymer interaction [50]. BNNTs and BNNPs were dispersed at 0.2 wt.% due to the following reasons: a) nanomaterials form micron sized aggregates in PPF matrix at concentrations higher than 0.2 wt. % and b) PPF with higher nanomaterial loading concentration shows changes in the viscoelastic behavior that may induce formation of air pockets during fabrication of nanocomposites [50].

The results of compressive mechanical testing (Figure 6.2 and Table 6.1) taken together showed that BNNPs are more efficient in reinforcing polymers. It has been shown that a uniform dispersion, high specific surface area, and extraordinary mechanical properties of nanomaterials in conjunction with the presence of functional groups on their surface results in a better load transfer from polymeric network to nanoparticles and an increasd crosslinking density of nanocomposites [48].

For both of BNNTs and BNNPs nanomaterials, high compressive modulus in the range of 250-1200 GPa have been reported [163, 331]. Due to the synthesis process, functional groups such as oxides, epoxides, amines, nitrates, nitriles, nitrites and methyl can attach to the surface of both BNNTs and BNNPs [332-334, 339, 340] and the improved nanomaterial/polymer interface and dispersitivity of nanomaterials [50]. Although Figure 6.1 shows well dispersion for BNNTs and BNNPs, some observations suggest that BNNTs tend to form bundles of nanomaterials [34, 341] acting as a stress-concentration point that might facilitate localized deformation under load and reduce mechanical strength [342]. Our observations are in agreement with Li et al. [343]; they have reported a uniform dispersion of BNNPs in polymeric matrices. BNNPs have been reported to have higher specific surface area compared to BNNTs (1427 m^2g^{-1} for BNNPs [344] compared versus to 254-789 m^2g^{-1} for BNNTs [345]). BNNPs also possess lower aspect ratio compared to BNNTs [346]. The addition of BNNTs and BNNPs did not cause a significant increase in crosslinking density of nanocomposites compared to PPF baseline control (Figure 6.2.D) which was in contrast with our previous observations for metallic-sulfide nanomaterials in chapter 4. These difference might be due to the different molecular forces resulting from different functional groups on the surface of nanomaterials. Thus, these two factors (specific

surface area and nanomaterial dispersion state) may play a dominant role and may be responsible for observed variation in the mechanical properties.

Adsorption of proteins on nanocomposite surfaces can play an important role in regulating cell viability, attachment and proliferation [66, 347]. Adsorption of collagen-I, fibrin and fibronectin proteins on crosslinked nanocomposites was specifically studied because they play an important role in governing cell adhesion and viability thereby supporting tissue regeneration. Collagen-I is a primary ECM protein responsible for providing structural support to new tissue growth [348], fibrin is responsible for formation of blood clots and regulation of inflammatory response [349] (crucial for bone healing process), and fibronectin is responsible for cell adhesion via integrin binding [350]. The increased time dependent collagen-I protein adsorption on the surface of nanocomposites (Figure 6.3.A) may be attributed to the presence of inorganic nanomaterials that leads to an increased surface roughness and incorporation of functional groups on the surface of nanocomposite. Interestingly, increased surface area of BNNPs compared to BNNTs [344, 345] resulted in better nanomaterial/protein interaction in accordance with previous studies that had shown that increase in surface roughness and intramolecular forces (as a result of protein/ functional groups interactions) can improve protein adsorption [351]. This increased protein adsorption may in turn cause an increased cell adhesion to the surface of nanocomposites [347].

MC3T3 pre-osteoblasts cells were used in this study for cytotoxicity studies as they are widely accepted for *in vitro* cytotoxicity testing of polymeric nanocomposites designed for bone tissue engineering applications [352]. The comprehensive evaluation of *in vitro* cytocompatibility of BNNT and BNNP nanocomposites included cytotoxicity assessment of non-crosslinked nanocomposite blends, crosslinked nanocomposite specimens, and their degradation

products. Prior to crosslinking and during nanocomposite degradation *in vivo*, cells will interact with released BNNTs and BNNPs from PPF nanocomposites. Therefore, cytotoxicity of BNNT and BNNP dispersions was analyzed. It has been reported that cytotoxicity assays such as MTT and XTT produce insoluble formazan crystals that interact with layered nanomaterials to produce erroneous results [353]. Previous studies demonstrated that Presto Blue® and LDH assays do not interfere with these type of nanomaterials [354], and thus they were used in this study.

Cytotoxicity analysis using Presto Blue® and LDH assays show that BNNT and BNNP dispersions at 100 μg/mL concentration were non-toxic at incubation times up to 24 hours (Figure 6.4.A and 6.4.B). Our results are in agreement with a previously reported study by Chen et. al. wherein ~100% viability for HEK-2 cells was observed after 4 days of exposure to BNNTs at 100 μg/ml concentration [355]. Figure 6.4.C and 6.4.D displays a dose-dependent cytotoxicity of nanocomposite blends prior to crosslinking (1X>10X and 100X). For use as an injectable system, PPF nanocomposites can crosslink *in situ* within a few minutes. Therefore, *in vivo* exposure of cells to non-crosslinked nanocomposite blends would be minimal. Furthermore, small PPF oligomers, NVP crosslinker, BNNTs and BNNPs (components that will directly interact with cells *in vivo* post-injection) will be cleared from the injection site by blood circulation. PPF is a biocompatible polymer, and BNNT/BNNP dispersions do not show acute cytotoxicity (Figure 6.4.A and 6.4.B). Therefore, the acute cytotoxicity observed for 1X experimental solutions can be attributed to major contributions from unreacted crosslinker. A similar dose-dependent acute cytotoxicity response for non-crosslinked PPF macromers was observed by Timmer et. al. [299], Shi et. al. [80], and Farshid et. al. [354] wherein the observed cytotoxicity was primarily attributed to the leaching of crosslinking agent and radical initiator components.

Crosslinking of PPF nanocomposites prevents the leaching of toxic non-crosslinked components such as NVP crosslinker and residual BP radial initiator [311, 354]. Therefore, dose-dependent cytotoxicity of crosslinked PPF nanocomposites (following this trend: 1X > 10X > 100X) typically show low cytotoxicity than non-crosslinked counterparts (Figure 6.4.C and 6.4.D) These observations are in agreement with previous reports [80, 354]. In this study, BNNT and BNNP nanocomposites showed ~85-90% crosslinking density (Figure 6.2.C), thereby preventing the release of non-crosslinked macromers that leads to less cytotoxicity.

After implantation PPF, nanocomposites undergo gradual hydrolysis *in vivo* to form degradation products such as propylene glycol, fumaric acid and degraded nanomaterials [80, 175, 354]. The *in vitro* and *in vivo* degradation of BNNTs and BNNPs still needs to be investigated. however, the degradation of PPF polymer has been investigated [338]. Crosslinked PPF degrades slowly; therefore, an accelerated degradation mechanism is typically used that hydrolyzes PPF in one week [299]. Previous reports use HCl and NaOH to accelerate the hydrolytic degradation of ester bonds in PPF-DA (polypropylene fumarate-diacrylate) [80]. This process forms NaCl that increases the osmolarity (>1000 mOsm) of degradation products. Cells in hypertonic medium shrink due to exosmosis of water resulting in cell membrane damages. Thus, it would be difficult to assess whether any observed cytotoxicity is due to high osmolarity or by the PPF degradation products. In this study, weaker degrading agents such as phosphoric acid (H_3PO_4) and calcium hydroxide ($Ca(OH)_2$) were used for accelerated degradation of PPF. These agents form insoluble calcium phosphate ($Ca_3(PO_4)_2$) crystals that can be easily removed. Furthermore Figure 6.5 displays that $Ca_3(PO_4)_2$ undergoes partial ionization resulting in lower osmolarity values (210-242 mOsm for 2X degradation extracts) of the degradation products. BNNTs and BNNPs do not induce cytotoxicity response up to 100 µg/ml (Figure 6.4.A and

6.4.B), therefore the acute dose-dependent cytotoxicity of degradation products (2X > 10X > 100X) in Figure 6.4.G and 6.4.H can be attributed primarily due to the interaction of cells with PPF degradation products mainly composed fumaric- and acrylic- acids [194, 336]. These results are consistent with previous reports that show PPF degradation products elicit a dose-dependent response [80, 192, 197]. Taken together, viability and cytotoxicity observed for MC3T3 cells after exposure to degradation products and osmolarity measurements suggest that the dose-dependent cytotoxicity trend is inversely proportional to osmolarity: 2X >10X and 100X.

Attachment and spreading of MC3T3 cells on nanocomposite surfaces, analyzed by cell counting (Figure 6.6.A), confocal fluorescence imaging (Figure 6.6.B) and SEM (Figure 6.6.C) The results indicated good cell viability, attachment, and spreading of MC3T3 cells on all experimental groups. Lower number of MC3T3 cells attached onto BNNT, BNNP and PPF disks compared to TCPS control after 24-hours of incubation might be a result of plasma treatment that adds negative charges on the surface of TCPS [80, 354, 356]. We did not investigate time points after 5 days. We expect an insignificant difference in fraction of attached cells among BNNT, BNNP, and PPF samples compared to TCPS control at later time points.

Significant cell attachment, spreading, and proliferation observed on all nanocomposite surfaces after 5 days of culture (Figure 6.6.B and 6.6.C) confirms excellent cytocompatibility. The cell attachment would result in the deposition of ECM components (Figure 6.6.C) on nanocomposites. The deposition of ECM also reduces the interaction of cells with insoluble components such as poly(vinyl pyrrolidone) [299] and traces of non-crosslinked macromers (acting as cell attachment inhibitors [80]). Therefore, deposition of ECM components further promotes cell attachment and proliferation resulting in high density of MC3T3 cells on nanocomposite surfaces after incubation for 5days. Additionally, the presence of BNNTs and

BNNPs in PPF matrix may increase the nanoscale surface roughness of the nanocomposites. It has been widely reported that nano-topography can improve cell adhesion by adsorption of protein molecules such as collagen-I [66].

To the best of our knowledge, this is the first systematic investigation of mechanical properties and *in vitro* cytocompatibility of (1-D) boron nitride nanotubes (BNNTs) and (2-D) boron nitride nanoplatelets (BNNPs) for reinforcing biodegradable PPF polymers and the development of novel bone grafts. Synthetic polymers lack the required mechanical properties to support native load bearing bone [357]. Therefore, the development nanoparticle-reinforced, mechanically strong, biocompatible polymeric nanocomposites and scaffolds for bone tissue engineering applications is an active area of research [23, 308, 358]. The use of nanostructured bone implants and fixtures may have several advantages over conventional polymeric and metallic implants. The presence of these nanomaterials in the scaffold matrix may lead to accelerated bone healing, better tissue-implant integration, and permit non-invasive monitoring of bone healing processes [359-361]. Our results indicate that although both nanomaterials lead to an increase in compressive mechanical properties, application of 2-D nanoplatelets resulted in a further reinforcement in comparison with 1-D nanotubes. Interestingly, in addition to cytocompatibility of nanomaterials, non-crosslinked nanocomposite components, crosslinked nanocomposites and degradation products of nanocomposites all showed cytocompatibility similar to cytocompatible PPF control. Moreover, the presence of both BNNT and BNNP nanomaterials resulted in a better protein adsorption and cell spreading on the surface of PPF nanocomposite. The positive results of this study expands the application of BNNT and BNNP nanomaterials for fabrication of ultra-strong and cytocompatible synthetic bone grafts may

overcome several challenges associated with metallic implant based bone treatment strategies and open avenues for their *in vivo* safety and efficacy studies.

6.4. Conclusions

Biodegradable polymeric nanocomposites were fabricated at low loading concentrations of 1-D and 2-D boron nitride nanomaterials (0.2 wt% of BNNTs and BNNPs) dispersed in the polymer poly(propylene fumarate) (PPF) and crosslinking agent N-vinyl pyrrolidone (NVP). After crosslinking, both BNNT and BNNP nanocomposites exhibit significant mechanical reinforcement compared to PPF composites; 2-D nanomaterials (BNNPs) were more effective in reinforcing mechanical properties than 1-D nanomaterials (BNNTs). Additionally, both nanocomposites showed a significantly higher adsorption of collagen-I compared to PPF control. Moreover, the cytotoxicity profiles for non-crosslinked components, crosslinked nanocomposites and their degradation products were similar to PPF baseline control. Furthermore, the crosslinked nanocomposites show an excellent cell attachment, spreading and ECM deposition. The results of this study demonstrate that BNNT and BNNP reinforced biodegradable polymeric nanocomposites are cytocompatible. These findings open new avenues towards the development of multi-porpuse, high-strength, nanomaterial-reinforced, lightweight polymeric nanocomposites as bone grafts for bone tissue engineering application.

6.5. Tables

Table 6.1. Mechanical properties of PPF nanocomposites.

	Compressive modulus (MPa)	**Increase in compressive modulus compared to PPF (%)**	**Compressive yield strength (MPa)**	**Increase in compressive strength compared to PPF (%)**
PPF	308±19	-	16±1	-
BNNT	354±38	15 %	17±2	6%
BNNP	426±55	38 %	21±6	31%

6.6. Figures

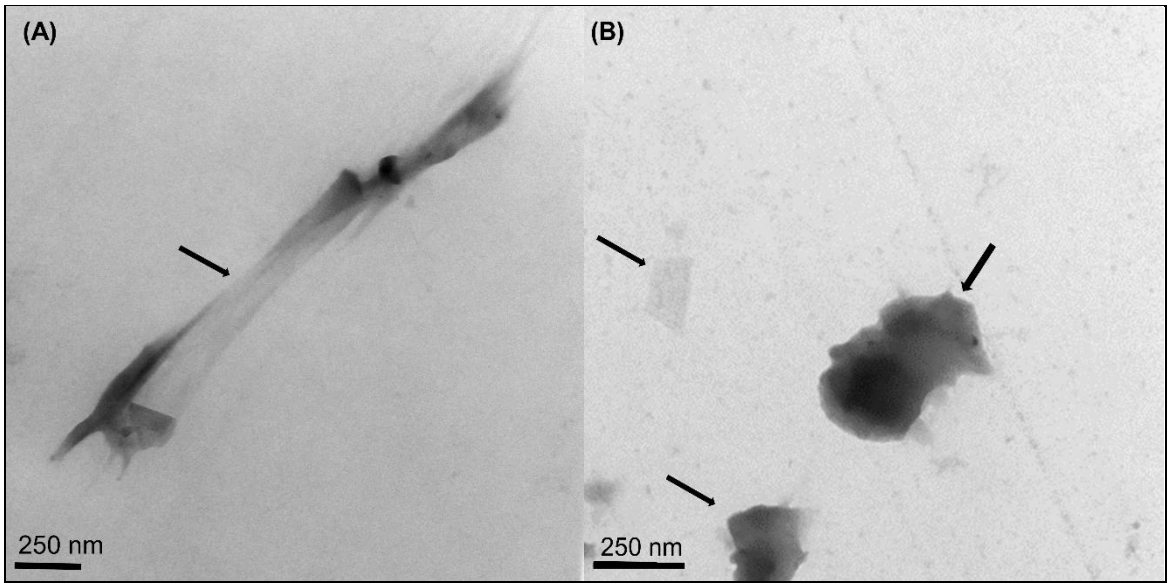

Figure 6.1. TEM images of: A) BNNT and B) BNNP nanocomposites (Black arrows correspond to nanomaterials).

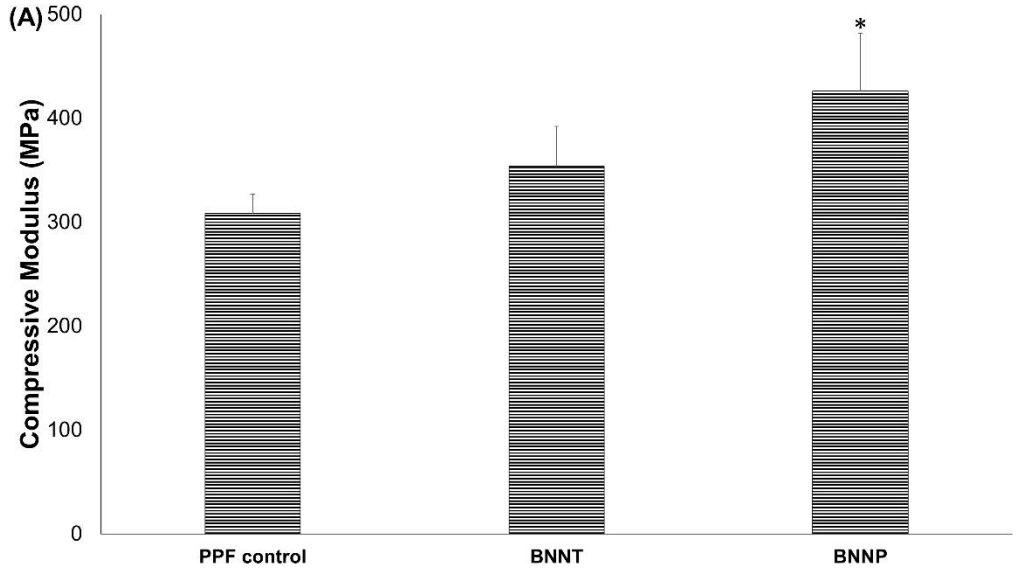

Figure 6.2.A) Compressive modulus, B) compressive yield strength and C) crosslinking density of PPF nanocomposites. Error bars represent standard deviations for n=3 samples. The symbol "*" indicates statistically significant difference with respect to PPF baseline control ($p < 0.05$) (Continued on the next page).

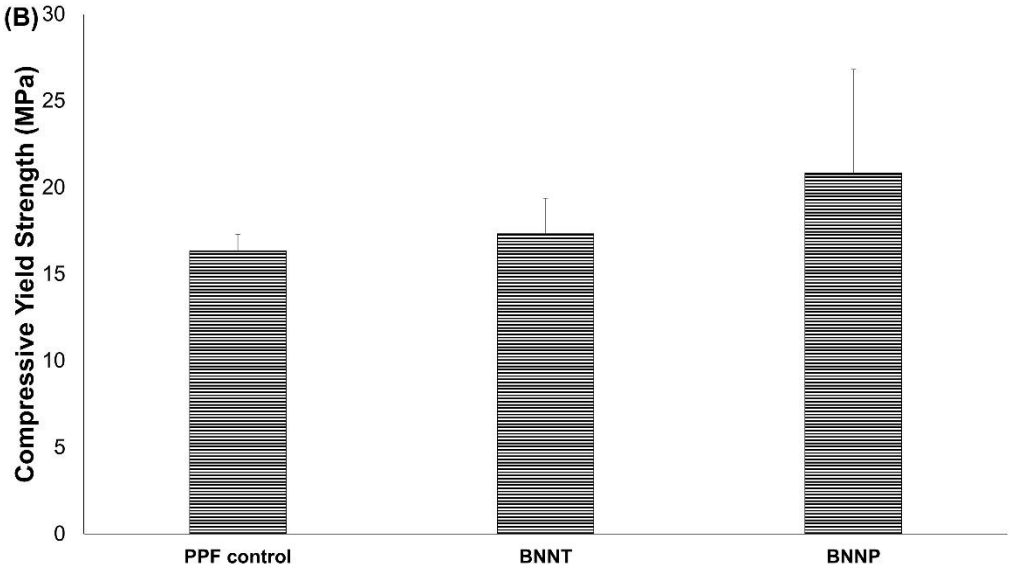

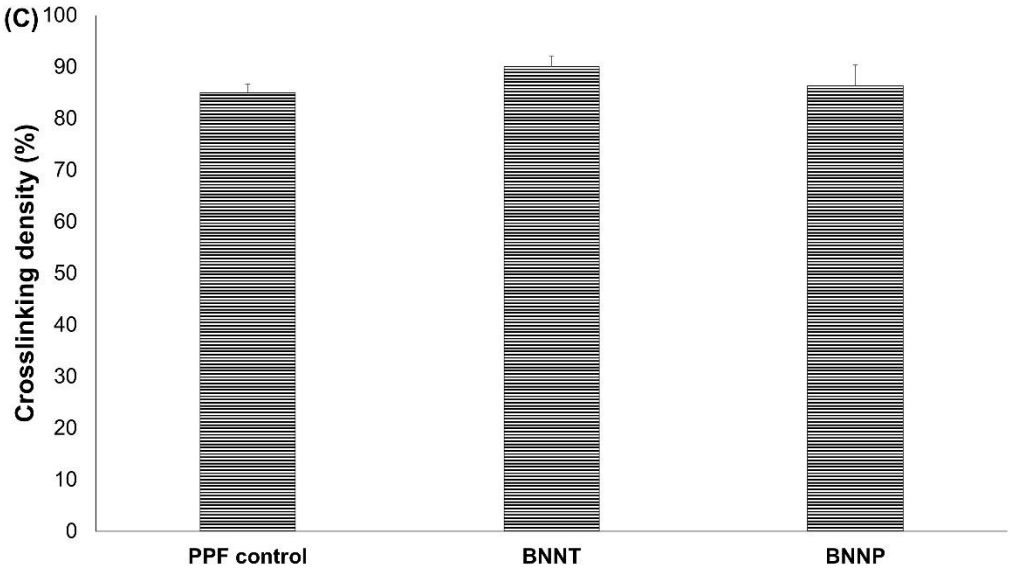

Figure 6.2.C) crosslinking density of PPF nanocomposites (continued from the previous page).

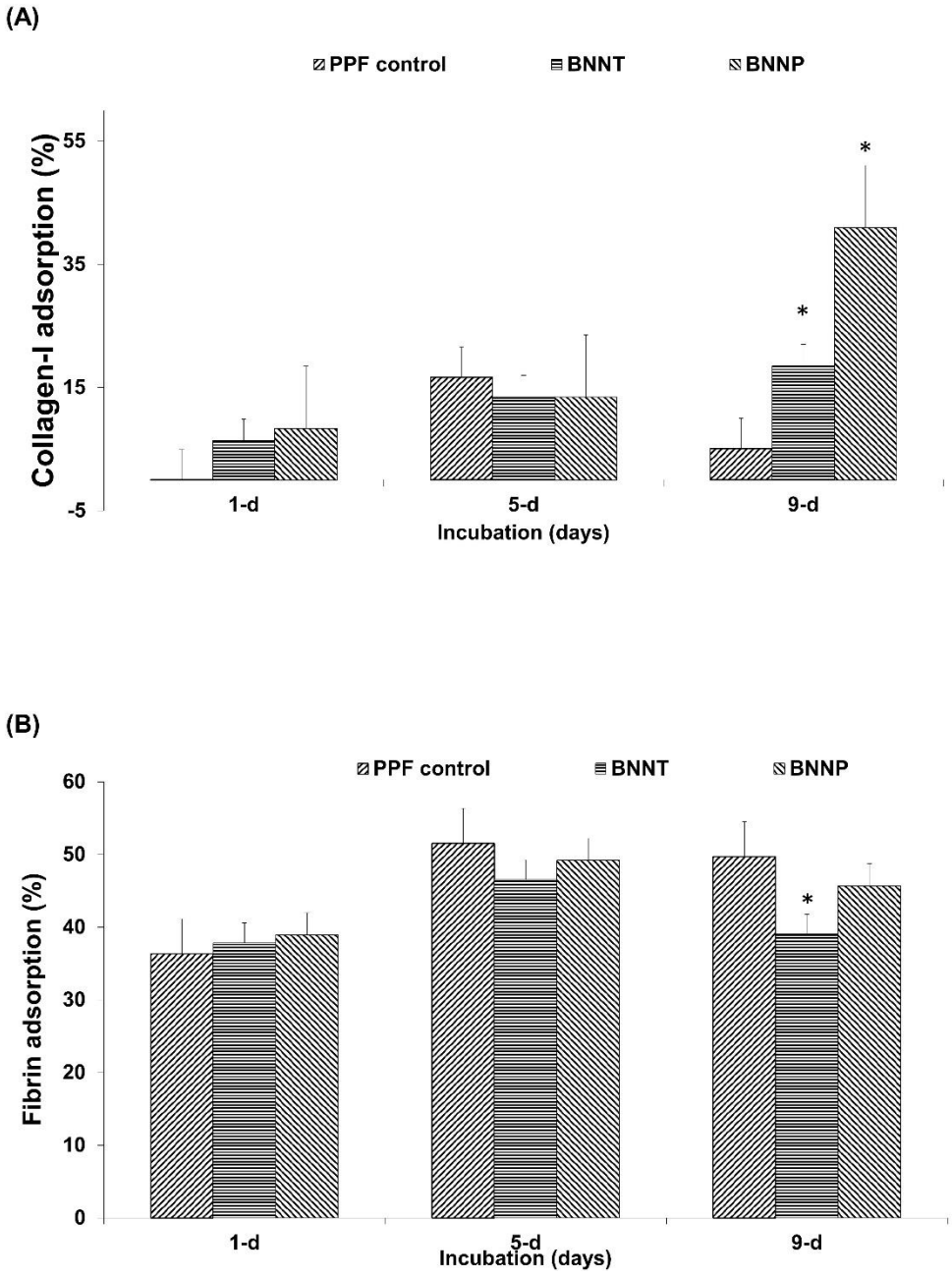

Figure 6.3. Adsorption of: A) collagen-I, B) fibrin and C) fibronectin after 1, 5 and 9 days incubation at 37°C on the crosslinked PPF nanocomposites (Error bars represent standard deviations for n=6 and the symbol "*" indicates statistically significant difference with respect to PPF baseline control ($p < 0.05$) (Continued on the next page).

(C)

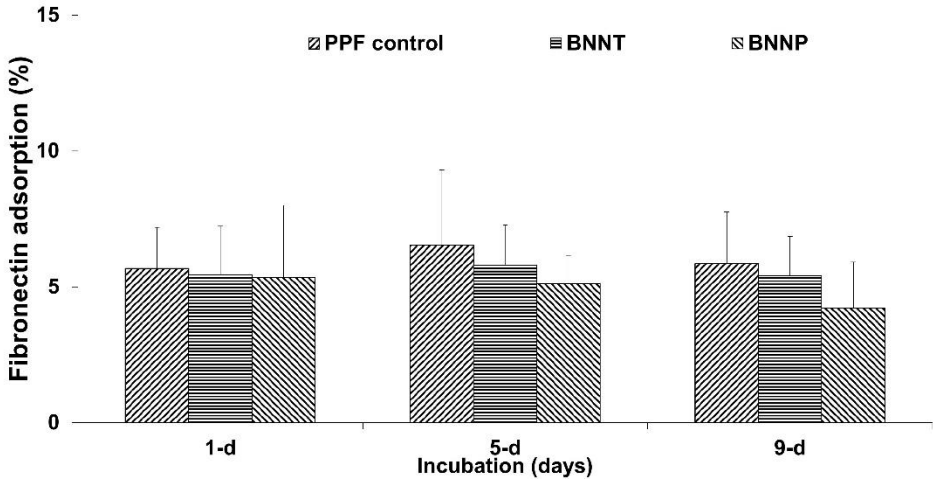

Figure 6.3.C) Adsorption of fibronectin after 1, 5 and 9 days incubation at 37°C on crosslinked PPF nanocomposites (Continued from the previous page).

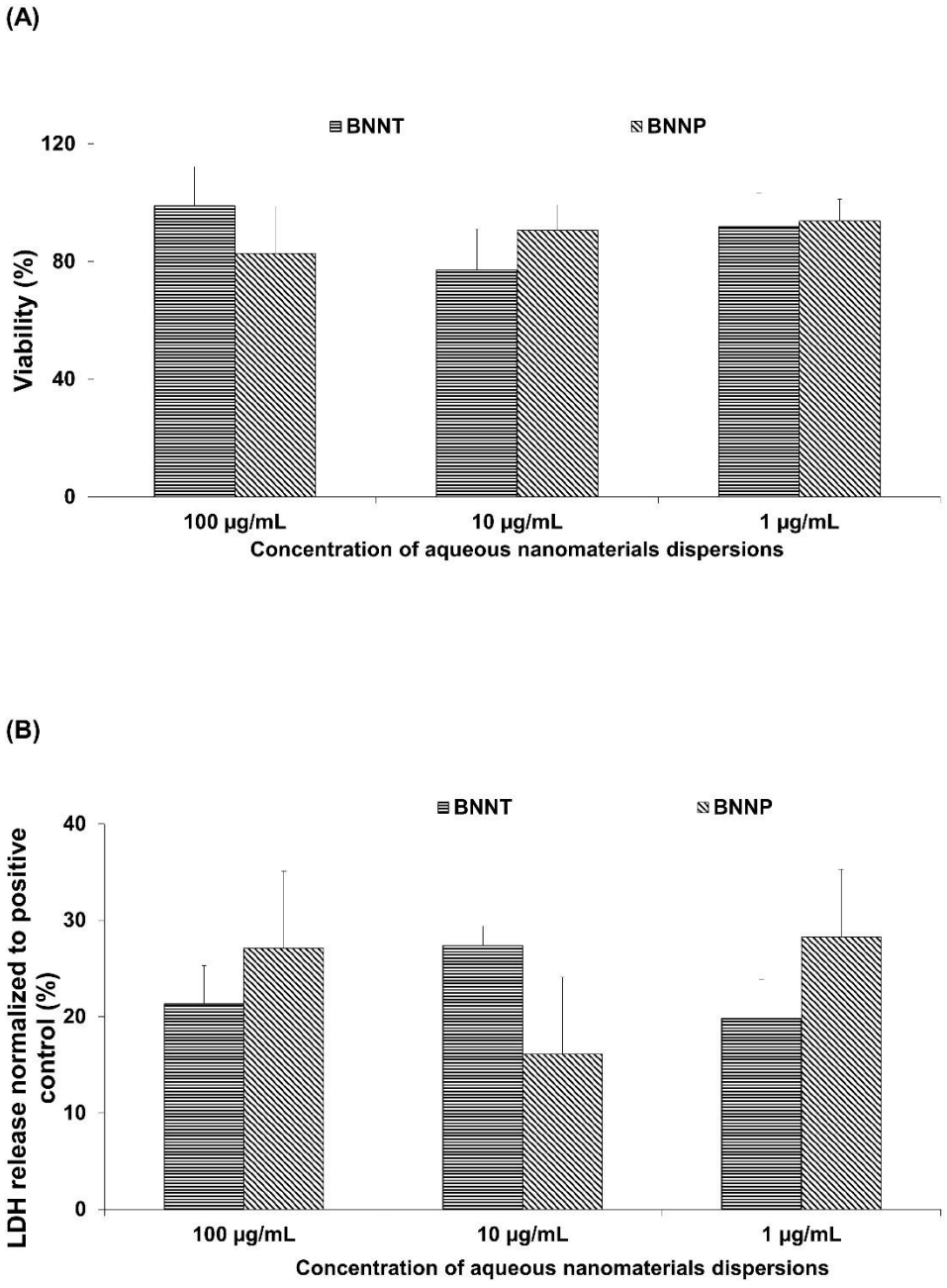

Figure 6.4.A) Viability and B) LDH release for MC3T3 cells after 24-h exposure to: the aqueous dispersions of nanomaterials. Data has been normalized with respect to live and dead controls, and error bars represent standard deviations for n=6 samples. No statistically significant difference was detected (continued on the next page).

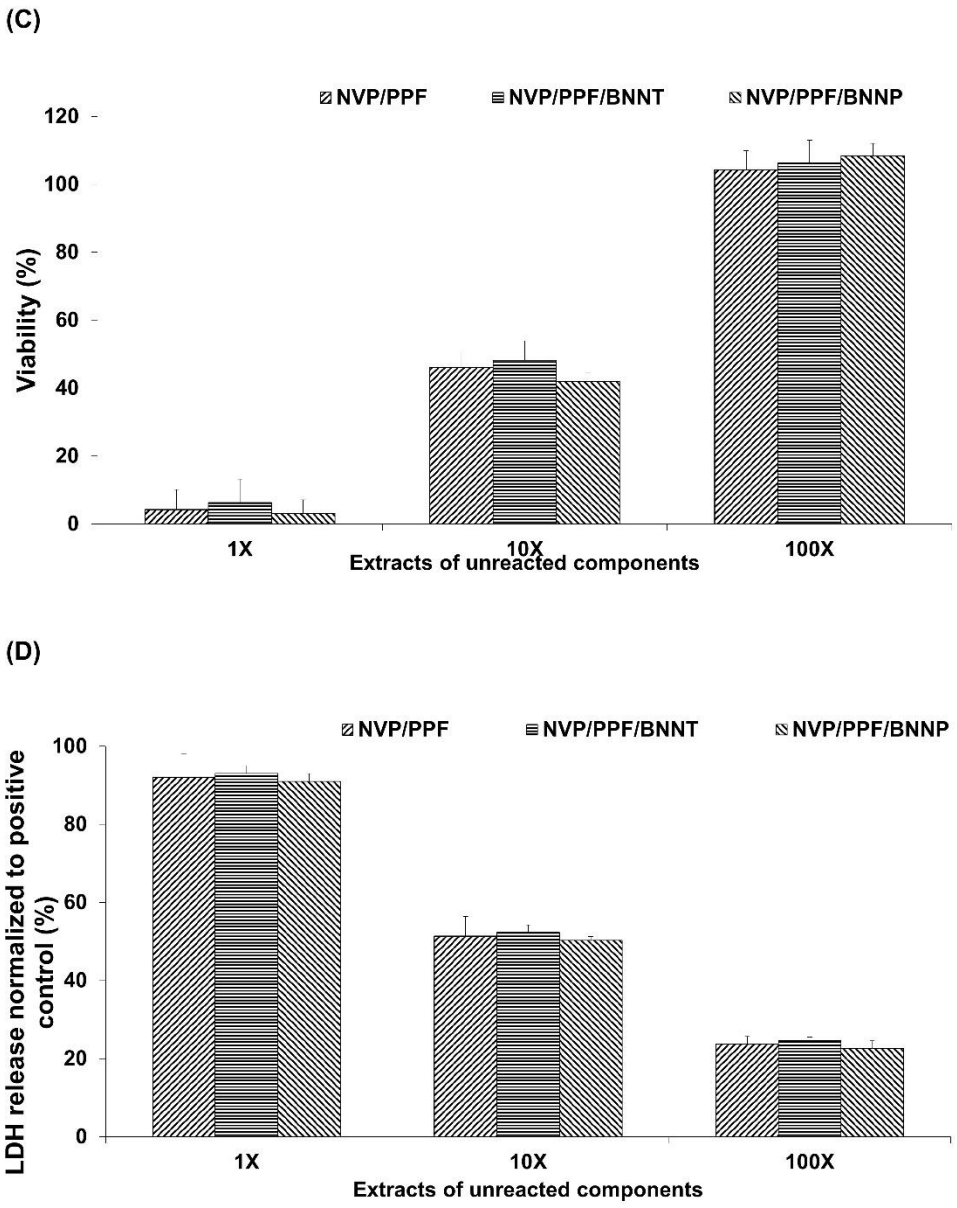

Figure 6.4.C) Viability and, D) LDH release for MC3T3 cells after 24-h exposure to the extracts of unreacted components. Data has been normalized with respect to live and dead controls, and error bars represent standard deviations for n=6 samples. No statistically significant difference was detected (Continued on the next page).

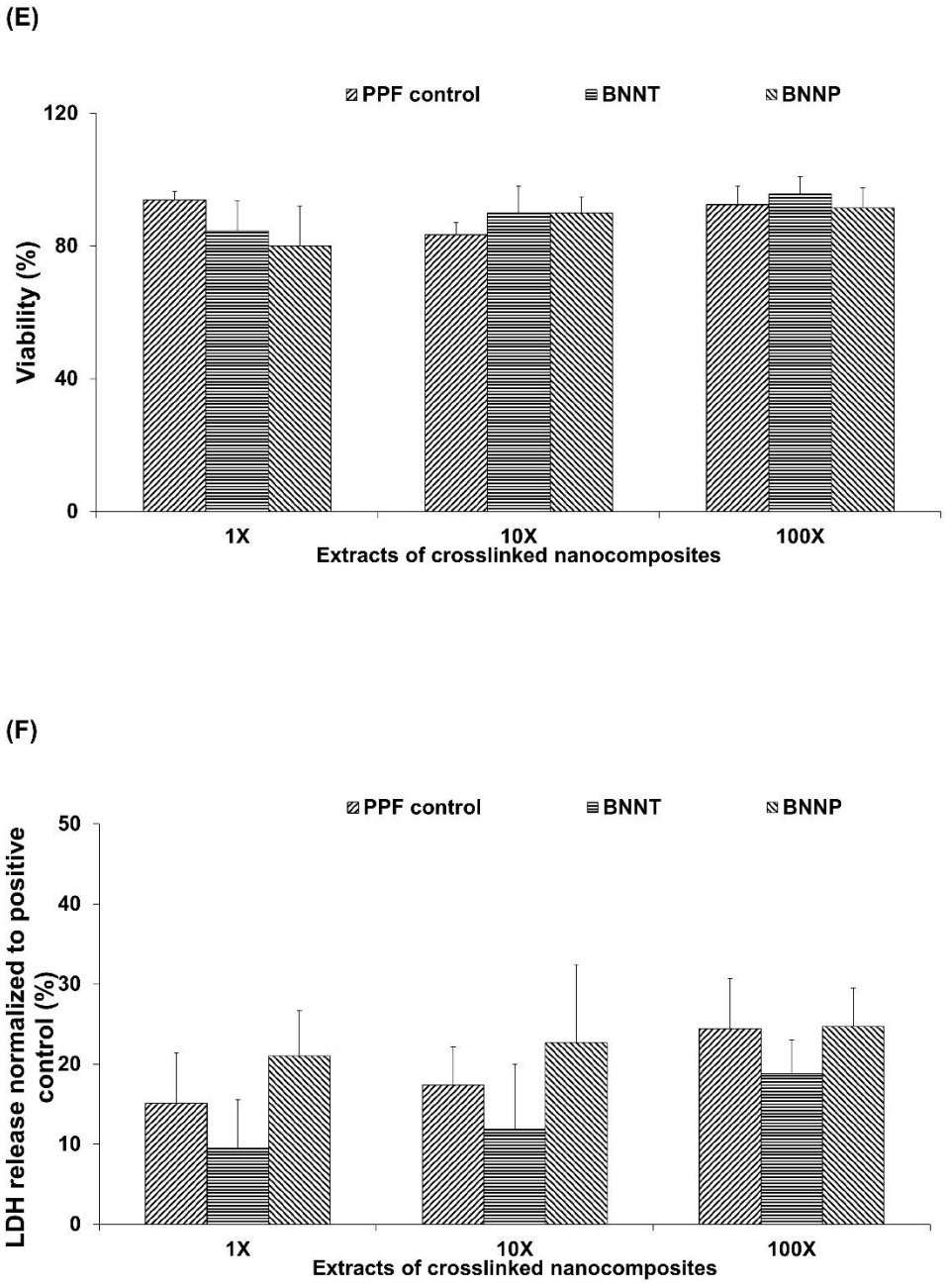

Figure 6.4.E) Viability and, F) LDH release for MC3T3 cells after 24-h exposure to the extracts of crosslinked nanocomposites. Data has been normalized with respect to live and dead controls, and error bars represent standard deviations for n=6 samples. No statistically significant difference was detected (Continued on the next page).

(G)

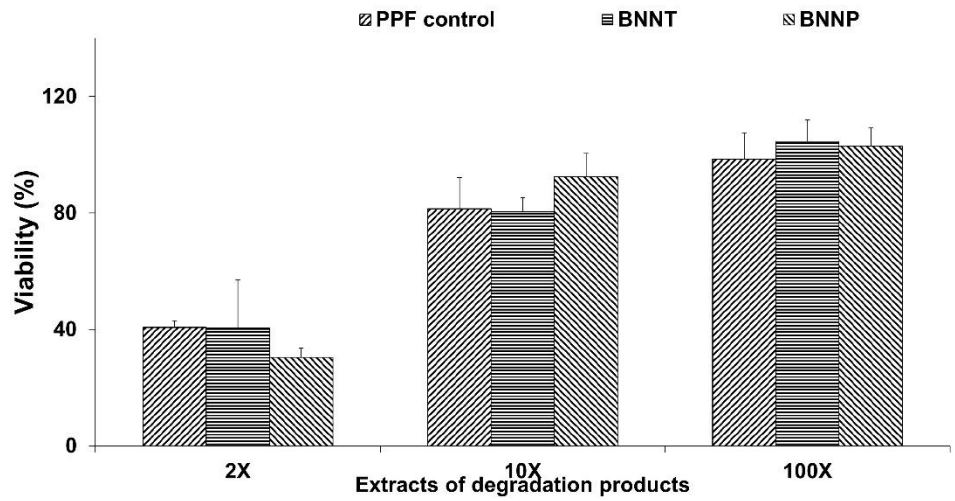

(H)

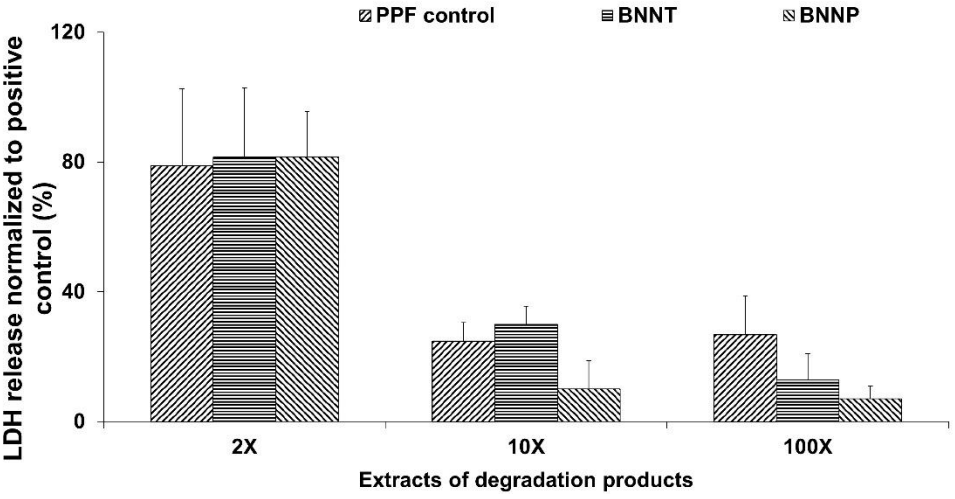

Figure 6.4.G) Viability and, H) LDH release for MC3T3 cells after 24-h exposure to: the extracts of degradation products. Data has been normalized with respect to live and dead controls, and error bars represent standard deviations for n=6 samples. (Continued from the previous page).

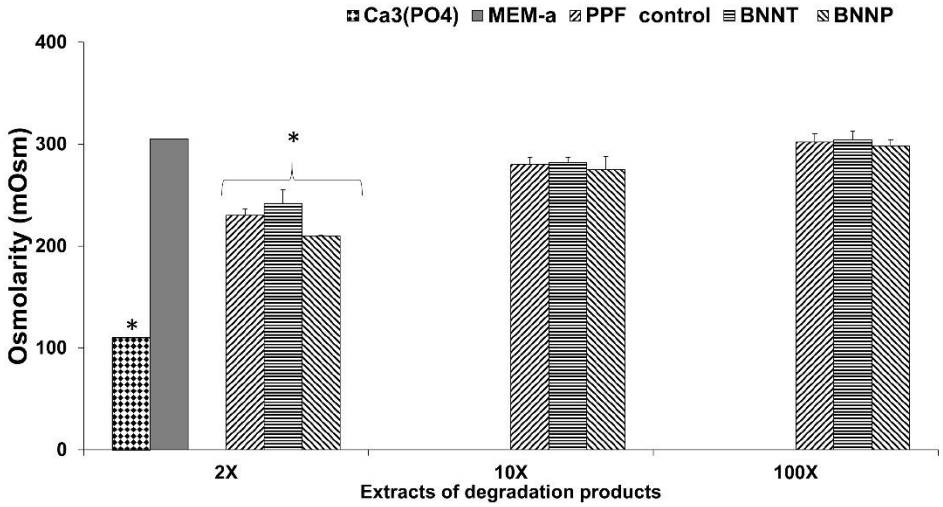

Figure 6.5. Osmolarity of degradation extracts. Error bars represent standard deviations for n=6 samples. The symbol "*" indicates statistically significant difference osmolarity with respect to MEM-α media ($p < 0.05$).

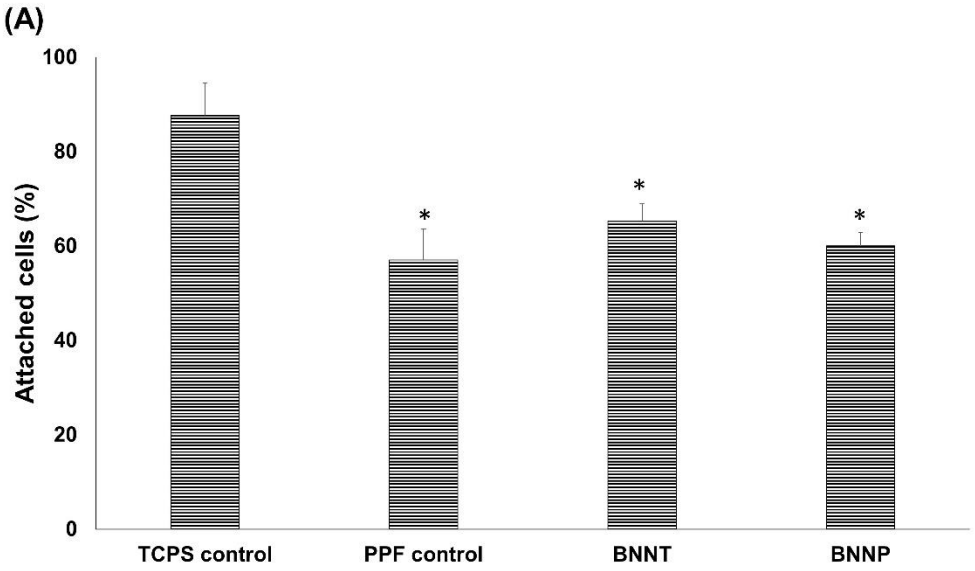

Figure 6.6.A) Fraction of attached MC3T3 cells on the surface of nanocomposites and TCPS control after 24-h incubation (Error bars represent standard deviations for n=3 samples and the symbol "*" indicates significant difference with respect to TCPS control ($p < 0.05$). (Continue on the next page)

(B)

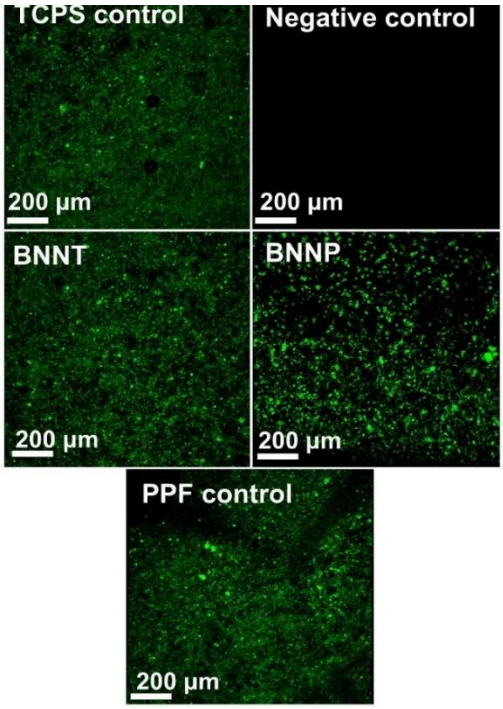

Figure 6.6.B) Confocal fluorescent images of MC3T3 cells spreading on crosslinked nanocomposites after 5 days of cell culture (continued from the previous page).

(C)

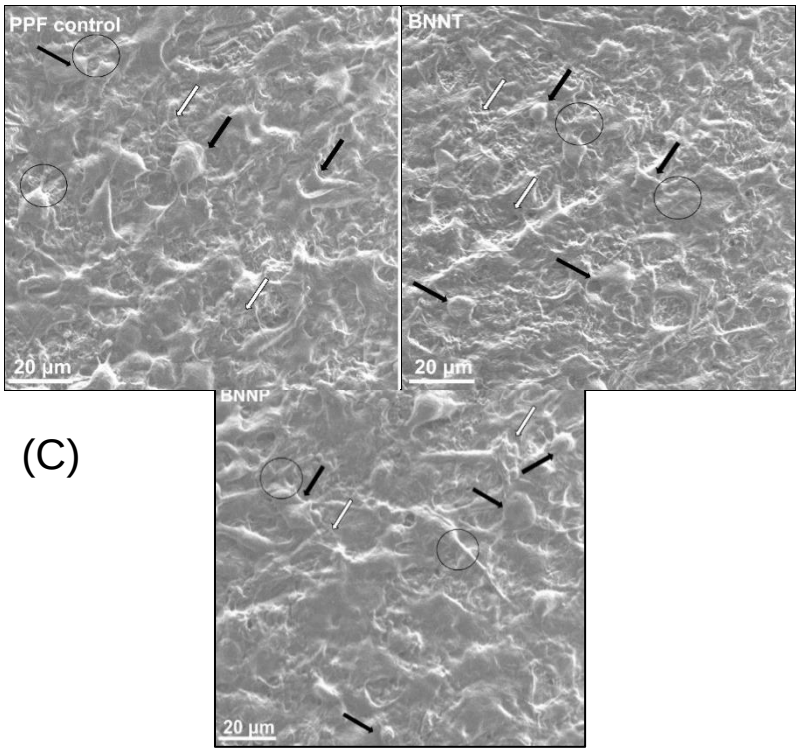

Figure 6.6.C) SEM images of the nanocomposites after 5 days of cell culture (The cells and their filopodia etensions are marked with black arrows and circles, respectively. ECM is marked using white arrows marks).

Chapter 7: Mechanical properties and cytocompatibility of porous biodegradable PPF nanocomposites

7.1. Introduction

In the previous chapters (chapter 4, 5 and 6) the mechanical properties and the *in vitro* cytocompatibility of nonporous PPF nanocomposites reinforced with inorganic and carbon nanomaterials were investigated. In this chapter we will discuss the mechanical properties and *in vitro* cytocompatibility of porous PPF nanocomposite scaffolds.

Porous polymeric scaffolds are key components in bone tissue engineering field that have been additionally used for therapeutic and imaging purposes. These components can permit new bone formation while providing temporary mechanical support [362]. Polymers such as chitosan [363], poly(lactic-co-glycolic acid) (PLGA) [364], polycaprolactone (PCLA) [365], poly(propylene fumarate) (PPF [19]), polyurethane (PU [27]), poly (D,L-lactic acid) (PDLLA [366]) and polyethylene glycol (PEG [367]) have been used towards the fabrication of scaffolds for bone tissue engineering applications. Generally, these polymeric scaffolds lack the required mechanical properties for tissue engineering of load bearing bones. Therefore, nanoparticles such as SWCNTs, MWCNTs, SWGONRs, MWGONRs, GONPs, and MSNPs have been used as reinforcing agents to improve the mechanical properties of polymeric scaffolds [368].

The efficacy of organic and inorganic 1-D and 2-D nanomaterials for preparing biodegradable, biocompatible and injectable PPF nanocomposites have been reported [50, 62,

369, 370]. In previous chapters, we used various 1-D nanomaterials such as boron nitride (BNNTs), carbon nanotubes (CNTs) and tungsten disulfide nanotubes (WSNTs) as well as 2-D nanomaterials such as boron nitride nanoplatelets (BNNPs), graphene oxide nanoplatelets (GONPs), molybdenum disulfide nanoplatelets (MSNPs) and graphene oxide nanoribbons (GONRs) were used as reinforcing agents for PPF nanocomposites. While a limited number of studies have been performed on investigation of mechanical properties [26, 49, 192], *in vitro* cytotoxicity [80, 299] and *in vivo* biocompatibility [81, 257] of carbon nanotubes- and alumoxane- incorporated PPF porous scaffolds, to the best of our knowledge no research has been done on efficacy of aforementioned nanomaterials for fabrication of biodegradable porous nanocomposite implants for bone tissue engineering applications.

In this chapter, we investigated the efficacy of inorganic (WSNTs, BNNTs, MSNPs and BNNPs) and carbon nanomaterials (SWGONRs, MWGONRs and GONPs) for reinforcement of PPF; a biodegradable, biocompatible and injectable unsaturated linear polyester [288] and compare them to non-reinforced PPF and carbon nanotube composites (SWCNTs and MWCNTs). Towards this aim, highly porous PPF nanocomposite scaffolds (with greater than 80% porosity) were fabricated using low loading concentration of nanomaterials and their microstructure was characterized. Then, the compressive mechanical testing and sol-fraction analysis was performed to explain the trends in mechanical properties of nanostructure-reinforced PPF scaffolds. Next, protein adsorption on crosslinked PPF nanocomposites for collagen-I protein (the main component of ECM) was examined in order to explain cell adhesion and extra cellular matrix (ECM) formation on nanocomposite scaffolds. Finally, the *in vitro* cellularity of MC3T3 pre-osteoblasts on the crosslinked PPF nanocomposite scaffolds was

investigated to study their cytocompatibility. The experimental procedures followed for this study are summarized in Figure 7.1.

7.2. Results

7.2.1. Characterization of porous scaffolds with SEM

Figure 7.2 displays the cross-section SEM images of highly porous nanocomposite scaffolds after salt leaching (Representative images of BNNP nanocomposite and PPF baseline control is presented in Figures 7.2.A and 7.2.B). The pores (marked with black arrows) are interconnected and have similar morphologies and size of cubic salt crystals with diameter of ~300 μm. The pores were separated with thin walls of polymer (marked with white arrows). This observation was in agreement with the high volume percentage porosity (calculated based on the measurement of weight and dimensions of scaffolds) shown in Table 7.1. Additionally, SEM imaging showed the formation of additional voids (marked with circle) during the fabrication process.

7.2.2. Compressive mechanical testing of scaffolds

Figure 7.3 and Table 7.2.A display the compressive modulus, offset compressive yield strength and ultimate strength of WSNT, BNNT, MSNP and BNNP nanocomposite scaffolds along with PPF baseline control. The compressive modulus, offset compressive yield strength and ultimate compressive strength for GONP, MWGONR, SWGONR, MWCNT and SWCNT nanocomposite scaffolds are presented in Figure 7.4 and Table 7.2.B.

Table 7.2.A compares the mechanical properties of inorganic nanocomposite scaffolds and PPF baseline control. The addition of nanomaterials increased compressive modulus of PPF

polymer which is 10±3 MPa increased to 11±3 MPa, 12±2 MPa, 14±1 MPa and 18±3 MPa for WSNT, BNNT, MSNP and BNNP nanocomposite scaffolds, respectively. Also, for inorganic nanocomposites offset yield strength of PPF polymer (293±69 KPa) increased to 350±42 KPa, 375±4 KPa, 312±9 KPa and 364±54 KPa for WSNT, BNNT, MSNP and BNNP nanocomposite scaffolds, respectively. Moreover, the ultimate strength of PPF scaffolds (329±37 KPa) increased to 375±46 KPa, 394±7 KPa, 351±17 KPa and 415±58 KPa for WSNT, BNNT, MSNP and BNNP nanocomposite scaffolds, respectively. However, only BNNP nanocomposites showed a significantly higher compressive modulus compared to PPF baseline control (marked with "*" in Figure 7.3).

Table 7.2.B compares the mechanical properties of 2-D carbon nanocomposites with PPF baseline control and SWCNT and MWCNT nanocomposites (positive control). The compressive modulus for GONP, MWGONR, SWGONR, MWCNT and SWCNT scaffolds was 19.3±1.9 MPa, 18.4±0.5 MPa, 13.8±1.7 MPa, 13.6±2.2 MPa, 13.1±0.8 MPa, that was higher than PPF control scaffold (12.2±1.9 MPa). Additionally, all carbon nanocomposites showed higher compressive yield strength compared to PPF control. PPF scaffolds showed a offset yield strength of 152±10.3 KPa whereas GONP, MWGONR, SWGONR, MWCNT and SWCNT nanocomposite scaffolds showed 250.1±40.8 KPa, 275±16.1 KPa, 211±58.5 KPa, 188.7±11.1 KPa, 168.7±27.9 KPa compressive yield strength. Furthermore GONP, MWGONR, SWGONR, MWCNT and SWCNT scaffolds showed 261.7±64.1 KPa, 283.3±21.2 KPa, 251±36.7 KPa, 241.7±36.1 KPa, 197.7±35.6 KPa ultimate strength that was higher than PPF baseline control (201.7±10.3 KPa). Among carbon nanocomposite scaffolds, GONP and MWGONR nanocomposites showed significantly higher compressive modulus compared to PPF base line control (marked with "*" in Figure 7.4), MWGONR nanocomposites also showed a significantly

higher offset yield strength (marked with "*" in Figure 7.4). No other significant difference between carbon nanocomposite scaffolds and PPF baseline control was detected for offset compressive yield strength and compressive ultimate strength. GONP nanocomposites showed a significantly higher compressive modulus compared to SWCNT and MWCNT nanocomposites (marked with "**"). No other significant difference in the compressive mechanical properties of 1-D and 2-D nanocomposites were detected.

7.2.3. Sol-fraction analysis of scaffolds

Figure 7.4.D displays the crosslinking density of inorganic PPF nanocomposite scaffolds in comparison with PPF baseline control. The crosslinking density of nanocomposites was calculated based on the fraction of polymer that is not soluble in methylene chloride [313]. The crosslinking density values for PPF, WSNT, BNNT, MSNP, and BNNP experimental groups were ~92%, ~91%, ~93%, ~92% and ~90%, respectively. No significant difference was detected among different experimental and control groups.

The results of sol-fraction analysis for carbon nanocomposite scaffolds are displayed in Figure 7.4.D GONP, MWGONR, SWGONR, MWCNT and SWCNT nanocomposite scaffolds showed ~90%, ~86%, ~86%, ~84%, ~87% crosslinking density compared to ~83% crosslinking density in PPF baseline control. No statistically significant increase in crosslinking density between nanocomposite and PPF baseline was detected.

7.2.4. Protein adsorption

Figure 7.5 shows collagen-I adsorption on organic and carbon nanocomposite scaffolds quantified using bicinchoninic acid (BCA) assay. BCA assay is a widely used assay for protein detection that works based on the reduction of green Cu^{2+} (cupric sulfate reagent) to purple Cu^{+} ion due to interaction with proteins. The reaction brings about a change in absorbance that can be quantified using a plate reader [207]. After 1 day of incubation, only BNNP nanocomposites showed ~12% (marked with "*" in Figure 7.5) protein adsorption. Protein adsorption for the other experimental groups were similar to the PPF control. As Figure 7.5.A shows, PPF control and WSNT, BNNT, MSNP and BNNP nanocomposites showed ~11%, ~23%, ~22%, ~21 and ~32% protein adsorption after 1 day of incubation. The collagen-I adsorption increased to ~4%, ~37%, ~31%, ~38%, and ~39% after 5 days of incubation for PPF, WSNT, BNNT, MSNP and BNNP nanocomposite scaffolds, respectively. PPF control and WSNT, BNNT, MSNP and BNNP nanocomposite scaffolds showed ~6%, ~29%, ~33%, ~22% and ~32% collagen-I adsorption, respectively. Among experimental groups, BNNP nanocomposites showed a significantly higher collagen-I adsorption compared to PPF baseline control (marked with "*" in Figure 7.5).

Figure 7.5.B shows collagen-I adsorption on carbon nanocomposite scaffolds in comparison with PPF baseline control. PPF control and SWCNT, MWCNT, SWGONR, MWGONR and GONP nanocomposite scaffolds showed ~26%, ~20%, ~28%, ~29%, ~32%, and ~26% protein adsorption for 1 day of incubation. The collagen-I adsorption increased to ~33%, ~33%, ~41%, ~44%, ~34%, and ~41% after 5 days incubation for PPF control and SWCNT, MWCNT, SWGONR, MWGONR and GONP nanocomposite scaffolds, respectively. PPF control and SWCNT, MWCNT, SWGONR, MWGONR and GONP nanocomposite scaffolds

showed ~45%, ~47%, ~51%, ~48%, ~46% and ~45% collagen-I adsorption, respectively. No significant difference compared to PPF baseline control was detected for carbon nanocomposite scaffolds.

7.2.5. Cellularity on nanocomposite scaffolds

Figure 7.6.a (A, B) shows the number of viable MC3T3 cells on inorganic and carbon nanocomposite scaffolds after 1, 5, and 9 days of incubation detected by QuantiFluor® and Presto Blue® assays. Quantiflour® assay detects the level of double-stranded deoxyribonucleic acid (ds-DNA) present in cell lysate, ds-DNA content is correlated to cell numbers with respect to standard curve [371]. As seen in Figure 7.6.a (A, B), PPF control and WSNT, BNNT, MSNP and BNNP nanocomposite scaffolds showed ~$17*10^3$, ~$19*10^3$, ~$19*10^3$, ~$21*10^3$ and ~$18*10^3$ viable cells (from initially seeded $100*10^3$ cells) after 1 day of incubation. ~$71*10^3$, ~$73*10^3$, ~$72*10^3$, ~$75*10^3$ and ~$73*10^3$ viable cells were observed for PPF control and WSNT, BNNT, MSNP and BNNP scaffolds after 5 days incubation, respectively. After 9 days of incubation, the number of viable MC3T3 cells increased to ~$147*10^3$, ~$153*10^3$, ~$149*10^3$, ~$148*10^3$ and ~$147*10^3$ cells for PPF control and WSNT, BNNT, MSNP and BNNP scaffolds, respectively. No significant difference between number of viable cells was detected. Results of Presto Blue® showed a similar trend although a higher number of cells were detected: ~$38*10^3$-$42*10^3$ cells, ~$80*10^3$-$100*10^3$ and ~$120*10^3$-$160*10^3$ cells after 1, 5 and 9 days of incubation, respectively.

Figure 7.6.b (A, B) shows the number of viable MC3T3 cells on the carbon nanocomposite scaffolds assessed using Quantifluor® and Presto Blue® assays. PPF control and SWCNT, MWCNT, SWGONR, MWGNR and GONP nanocomposite scaffolds showed ~$51*10^3$, ~$50*10^3$, ~$48*10^3$, ~$51*10^3$, ~$45*10^3$ and ~$49*10^3$ viable cells (from initially seeded

100*10^3 cells) after 1 day of incubation. ~106*10^3, ~94*10^3, ~91*10^3, ~92*10^3, ~102*10^3 and ~103*10^3 viable cells were observed for PPF control and SWCNT, MWCNT, SWGONR, MWGONR and GONP scaffolds after 5 days incubation, respectively. After 9 days of incubation number of viable MC3T3 cells increased to ~163*10^3, ~148*10^3, ~142*10^3, ~132*10^3 , ~154*10^3 and ~160*10^3 cells for PPF control SWCNT, MWCNT, SWGONR, MWGONR and GONP scaffolds, respectively. No significant differences were detected between the groups. Results of Presto Blue® shows a similar trend although a higher number of cells were detected: ~60*10^3-62*10^3 cells, ~120*10^3-130*10^3 and ~160*10^3-170*10^3 cells after 1, 5 and 9 days of incubation, respectively.

7.2.6. *In vitro* studies to characterize cellular spreading and infiltration into the scaffolds

MC3T3 cell spreading and infiltration inside PPF control and nanocomposite scaffolds were investigated using confocal microscopy (Figure 7.7). For confocal imaging, the cells were stained with calcein-AM dye which is a nonfluorescent dye and that changes to a green-fluorescent dye upon hydrolysis by intercellular esterases [372]. After 5 days of incubation, the confocal microscopy showed uniformly spread MC3T3 cells that successfully had infilterated the experimental scaffolds. No significant differences in cell morphology and spreading were detected between experimental groups. Confocal images suggested that after 5 days of incubation, viable cells (with ~10 μm) infilterate inside the pores due to large pore sizes (~300 μm) of the nanocomposite scaffolds.

SEM image of BNNP nanocomposite scaffold in Figure 7.8 provides more details regarding MC3T3 cell attachment and their spreading inside the pores of nanocomposite scaffolds. MC3T3 cells after 5 days of incubation were well spread and showed good infiltration

inside the pores of BNNP nanocomposite scaffolds with the formation of filopodia. The pores inside the scaffolds were partially covered by cells (marked with black arrows) and their filopodia extensions (white arrows). Furthermore, extracellular matrix (ECM; marked with circles in Figure 7.8.A) can be clearly observed suggesting the formation a ECM network inside the porous scaffolds. SEM imaging of MC3T3 cell spreading on the nanocomposite scaffolds in shown in Figure 7.8. Representative images of BNNP nanocomposite and PPF baseline control are shown. The SEM images show a complete uniform cellular coverage on the surface of nanocomposite scaffolds numerous filopodia and cellular extensions from MC3T3 cells attaching to the underlying nanocomposite surface (marked with black circle in Figure 7.8.B).

7.2.7. Collagen-I expression on nanocomposite scaffolds

The fluorescence confocal microscopy images of collagen-I (major component of ECM) deposition for experimental groups is shown in Figure 7.9. The primary anti collagen-I antibody used in this study binds to helical collagen-I proteins expressed by MC3T3 cells and can be visualized using a secondary mouse antibody tagged by a fluorophore (such as rhodamine) [373]. The results showed that MC3T3 cells are surrounded and embedded in a 3-D network of collagen-I ECM expressed by MC3T3 cells. This 3-D network provides a template for cell attachment, proliferation and new bone formation.

7.3. Discussions

This study systematically investigated the mechanical properties and *in vitro* cytocompatibility of porous PPF nanocomposite scaffolds reinforced with inorganic nanomaterials such as tungsten disulfide nanotubes (WSNTs), boron nitride nanotubes (BNNTs),

molybdenum disulfide nanoplatelets (MSNPs) and boron nitride nanoplatelets (BNNPs) and carbon nanomaterials such as single- and multi-walled graphene oxide nanoribbons (SWGONRs and MWGONRs), single- and multi-walled carbon nanotubes (SWCNTs and MWCNTs) and graphene oxide nanoplatelets (GONPs). The nanomaterial loading concentration of 0.2 wt. % was used for nanocomposite scaffold fabrication due to the following reasons as discussed in chapter 4: 1) viscoelastic behavior of PPF at nanomaterials concentration greater than 0.2 wt. % results in formation of additional pores during scaffold fabrication, 2) it is a challenge to achieve a uniform nanomaterial dispersion in the polymer matrix at concentrations > 0.2 wt% due to aggregation. No surfactants were used in this study.

For the application of polymeric scaffolds as osteoconductive bone grafts they should provide temporary mechanical support at early stages of bone mineralization, they should be biocompatibility and support bone tissue ingrowth [30]. It is desirable for the grafts to be highly porous (greater than 80% volume percentage porosity) to allow cell infiltration, efficient extracellular matrix deposition, ossification (formation of new bone) and waste exclusions [30]. However, the mechanical properties of the porous grafts drastically decreases with increase in porosity. Studies have reported up to 2 order of magnitude decrease in compressive and flexural mechanical properties (modulus and yield strength) of porous scaffolds compared to their nonporous counterparts [26, 50]. Studies have reported the effect of nanomaterials as reinforcing agents to improve the mechanical properties of polymeric scaffolds for bone tissue engineering applications, however the mechanical properties of those implants were insufficient to permit their application as bone grafts [6, 374-376]. Therefore, in this study, we investigated the effects of 1-D and 2-D nanomateirals with high intrinsic mechanical properties as reinforcing agents for PPF polymeric scaffolds. 1-D and 2-D nanomaterials have extraordinary physiochemical

properties such as ultra-high mechanical strength and large specific surface area along with the presence of functional groups to improve nanomaterial-polymer interaction for better reinforcement.

Herein, we studied the mechanical properties of nanocomposite scaffolds (compressive modulus, compressive yield and ultimate strength) reinforced with various 1-D and 2-D carbon and inorganic nanomaterials and compared them to the non-reinforced PPF baseline control. Among the nanomaterials studied in this chapter, only single- and multi-walled carbon nanotubes (SWCNTs and MWCNTs) have been reported previously [90, 97, 184, 377, 378] for development of porous bone grafts scaffolds. The cytocompatibility of porous nanocomposite scaffolds were studied using MC3T3 pre-osteoblasts murine cells that are widely accepted mammalian cell lines for bone tissue engineering research [352]. Similar to Green et al. [379], the cellularity was defined as number of viable cells and was detected based on double stranded di-nucleic acid (ds-DNA) content in cells and corroborated using Presto Blue® assay.

As discussed in chapter 3, TEM imaging of nanomaterials shows that WSNTs and BNNTs have tubular morphology while MSNPs and BNNPs exhibit polygonal sheet-like form in accordance with the literature [158, 174, 380, 381]. The morphology of carbon nanomaterials used in this study (especially graphene oxide nanoribbons and graphene oxide nanoplatelets) were also in accordance with the existing literature [123, 382]. Importantly, unzipping and synthesis of graphene oxide platelets introduces functional groups on the surface of nanomaterials [50] resulting in their better dispersion. The TEM images confirmed the homogenous dispersion of the nanomaterials in the polymeric matrix, a pre-requisite for good nanomaterials/polymer interface resulting in an efficient load transfer and improved mechanical properties [273].

As discussed in chapter 3, the Raman spectra of nanomaterials were in agreement with literature [50, 219, 220, 222, 339, 380, 383]. The presence of functional groups on the surface of nanomaterials leads to a better nanomaterial/polymer interface. Moreover, a uniform dispersion of nanomaterials (compared to bundled nanomaterials) in the polymeric networks is desired; nanomaterial aggregates lead to localized stress concentration during compressional loading. The minor peaks observed in the spectra were results of structural defects and functional groups in carbon nanostructures [50]. Presence of functional groups such as hydroxyls and oxysulfides on the surface of 2-D nanomaterials increase the van-der walls intermolecular forces and leads to better dispersion compared to carbon nanotubes [33]. Additionally, presence of functional groups leads to an increase in surface energy of the nanocomposites [384] and improves the crosslinking density of nanocomposite scaffolds.

The formation of highly porous scaffolds after salt-leaching (Figure 7.2) was observed. A homogenous distribution in pore sizes and regular cubic shape decreases the stress concentration initiated by pores [385] and delays crack propagation when subjected to mechanical loads. As SEM image confirmed, the large size of pores (~300 μm) facilitate ingrowth of the MC3T3 cells (during seeding stage) inside the scaffolds and facilitates the removal of cellular wastes from the vicinity of viable cells. Moreover, the rough inner surface of pores might be favorable for adsorption of collagen-I and attachment of MC3T3 cells [66]

Although the introduction of porosity provides path ways for the cell growth and formation of new bone (ossification), the tradeoff of making porous structures is a substantial decrease in mechanical properties (approximately two order of magnitude compared to nonporous nanocomposites [50, 62]). To improve the mechanical properties of these scaffolds

for bone tissue engineering applications, the chemical composition of nanomaterials and their architecture (pore size, distribution and volume percentage) needs to be finely tuned.

In order to investigate the mechanical properties of nanocomposite scaffolds in this work, a 1 KN load cell was used to increase the sensitivity of the measurements (application of higher load cells would result in rapid failure of porous scaffolds). As shown in Figure 7.3, the presence of organic and inorganic nanomaterials increases the compressive mechanical properties (compressive modulus, compressive yield strength and ultimate strength) due to high mechanical strength of nanomaterials, efficient load transfer in nanomaterial/polymer interface and increase in crosslinking density of the polymer networks [48]. Additionally, other factors such as homogenous pore size and pore distribution also have a favorable effect on the mechanical properties of the scaffolds [52, 53]. WSNTs, BNNTs, BNNPs, and MSNPs have very high compressive modulus (compared to metals such as stainless-steel with ~200 GPa young's modulus [386]) of ~150 GPa [62], ~1220 GPa [52], ~271 GPa [330, 387], and ~210 GPa [62, 106, 388], respectively. The compressive modulus of inorganic 1-D and 2-D nanomaterials are even comparable to ultra-strong carbon nanotubes with a compressive modulus of ~1600 GPa [389] and graphene oxide with a compressive modulus of 250 GPa [390].

The sol-fraction analysis was performed to assess the changes in the crosslinking density of the polymic nanocomposites. The sol-fraction analysis (Figure 7.4) shows no significant difference in crosslinking density of nanocomposite scaffolds compared to the PPF baseline control. However, the functional groups on the surface (residues of synthesis process) of nanomaterials result in the formation of a better nanomaterial/polymer interface that eventually leads to more efficient load transfer (in agreement with Kim et al. [391] on the role of functional groups in increasing mechanical properties of carbon nanotube reinforced polymeric

nanocomposites). As seen in Table 7.2, similar to our findings in chapter 4 that a large surface area leads to a better nanomaterial/polymeric network interface, the inorganic 2-D nanomaterials were more effective in the increasing mechanical properties of the nanocomposite scaffolds. The trend for mechanical properties of inorganic nanocomposite scaffolds was: PPF baseline control < 1-D nanocomposites < 2-D nanocomposites.

As displayed in Figure 7.2.B, for carbon nanocomposite scaffolds, although only a few significant differences were detected among the results for the compressive mechanical tests, the trend for mechanical properties of nanocomposite scaffolds was: PPF < (SWCNT and MWCNT) < (SWGONR and MWGONR) < GONP scaffolds. An increase in the mechanical properties of 2-D carbon nanocomposite scaffolds compared to 1-D nanocomposites (Table 7.2.B), was in agreement with our previous results for nonporous PPF nanocomposites. The increase in crosslinking density of nanocomposite scaffolds followed the following trend: GONP > (SWGONR and MWGONR) > (SWCNT and MWCNT) > PPF.

In addition to mechanical strength, the nanocomposite scaffolds should provide a template for extracellular matrix (ECM) deposition and subsequent ossification, therefore adsorption of collagen-I protein (collagen-I acts as the backbone of ECM [392]) was investigated. The time-dependent increase in collagen-I adsorption for all inorganic and carbon nanocomposite scaffolds compared to PPF scaffold in Figure 7.5 was in agreement with the reports on the effect of nanomaterials on increasing surface energy and surface roughness that eventually leads to a better protein adsorption [66, 347, 393]. The improved adsorption of proteins on the surface of nanocomposites (Table 7.3) leads to better adsorption of growth factors and hormones that are necessary for proliferation and differentiation. Additionally, absorbed proteins will act as an anchor for cell attachment [394]. As observed in Figure 7.5, the

protein adsorption did not significantly after 5 days incubation that might be due to the saturated surface for collagen-I adsorption.

The time-dependent increase of collagen-I shows the capability of nanocomposite scaffolds for adsorption of collagen-I protein inside the pores. Moreover, collagen-I adsorption followed the following trend for inorganic and carbon nanomaterials: 2-D nanocomposites > 1-D nanocomposites > PPF baseline control. The results of protein adsorption study suggested that the presence of nanomaterials in the polymeric network increases the surface roughness and increases protein adsorption [395]. Because nanomaterials loading concentrations are very low (0.2 wt. %) and they may have a small share in governing overall surface roughness and surface energy, the protein adsorption for different nanomaterials were not significantly different.

Displayed in Figure 7.6 is a time-dependent increase in number of viable MC3T3 cells on all experimental groups showing an excellent cytocompatibility of the nanocomposite scaffolds (similar to PPF control). Although Presto Blue® assay showed a higher number of cells compared to Quantifluor® assay (Figure 7.6) as carbon nanomaterials bind to ds-DNA [379], the trend was similar and in accordance with the study carried out by Shi et al. [26]. A possible explanation for the excellent cellularity in all nanocomposite scaffolds compared to PPF baseline control might be the high crosslinking density in polymeric networks that prevents release of the unreacted components into the cell culture media. Moreover, an increased protein adsorption results in an enhanced cellular attachment and reduces cell apoptosis [396]. The excellent cytocompatibility of nanocomposite scaffolds can also be attributed to the excellent cytocompatibility of PPF [299] and low nanomaterial loading concentrations [80, 105, 135, 171, 397-399]. Addition of these nanomaterials not only do not adversely affect cytocompatibility, it improves cell adhesion and adsorption of ECM proteins [65].

The confocal images and SEM images after 5 days incubation (Figures 7.7 and 7.8) showed an excellent cell spreading and infiltration on nanocomposites and confirmed cytocompatibility of the nanocomposite scaffolds (in agreement with Shi et al. [19]). The confocal images showed a similar morphology of MC3T3 cells grown on nanocomposite scaffolds and PPF baseline control. Despite the presence of residual materials from synthesis process (such as benzoyl peroxide, uncreated NVP and trapped solvents [299, 311, 369]) and nanomaterial aggregates [80, 369, 370, 400], the salt leaching process reduces the cytotoxicity by leaching toxic components before cell culture. Moreover, the presence of cellular extensions and cell infiltration on the scaffolds along with extracellular matrix (ECM) deposition observed in Figure 7.8 show desirable effects of these nanocomposites on early stage bone formation. The confocal fluorescence images of the infiltrated MC3T3 cells visually validates the results of cellularity assays. Due to the large available surface for cell spreading inside the pores, number of viable MC3T3 cells continue to rise from day 1 to day 9 of incubation. Two factors that slow down the increase in number of MC3T3 cells during longer incubation times are static cell culture that limits transport of new cells inside scaffolds and lack of blood vessel formation in *in vitro* models [401].

Morphology of well-spread MC3T3 cells with extended filopodia observed in SEM images was similar to the MC3T3 cells cultured on tissue culture poly styrene (TCPS) reported by Lourenco et al. [402]. SEM images further confirmed the excellent cellularity and cell spreading. The large interconnected pores allow migration of MC3T3 cells (with ~10 μm diameter) inside the pores. Similar to our *in vitro* findings, in an *in vivo* model, after the stem cells differentiate toward mature osteoblasts they will deposit ECM and calcium phosphate

inside the pores [352]. These processes will result in the formation of new bone [81] that gradually replaces the degrading polymeric networks [336].

The surface of nanocomposite scaffolds were covered by secreted collagen-I (Figure 7.9) and showed that, not only MC3T3 cells are viable inside the nanocomposite scaffolds, they tend to secrete collagen-I and deposit ECM. Since the cell attachment plays an important role in signaling cells toward differentiation, a better attachment will result in an improvement in new bone formation [403] and suppresses cell apoptosis [396].

To the best of our knowledge, this is the first systematic investigation of carbon and inorganic 1-D and 2-D nanomaterials (SWGONRs, MWGONRs, GONPs, SWCNTs, MWCNTs, WSNTs, BNNTs, MSNPs and BNNPs) as reinforcing agents to prepare porous nancomposite scaffolds. In this study, their effect on the compressive mechanical properties, protein adsorption and cytocompatibility of biodegradable PPF nanocomposite scaffolds was investigated. The compressive mechanical testing showed that 2-D carbon and inorganic nanomaterials increase compressive mechanical properties and protein adsorption (compared to non-reinforced PPF). These nanocomposites are cytocompatible. The results of this research open avensues for *in vivo* biocompability analysis of these scaffolds in animal models.

7.4. Conclusions

In conclusion, highly porous PPF nanocomposite scaffolds using carbon (SWCNT, MWCNT, SWGONRs, MWGONRs and GONPs) and inorganic (WSNTs, BNNTs, MSNPs and BNNPs) nanomaterials were fabricated toward the development of porous bone grafts for bone tissue engineering applications. While compressive modulus of 2-D nanocomposites (for both inorganic and carbon nanocomposites was slightly higher compared to 1-D nanocomposites and

PPF baseline control), they showed higher compressive mechanical strength and compressive ultimate strength as well. The mechanical reinforcement was dependent on morphology of nanomaterials, surface roughness, specific surface area, surface energy, their dispersion and presence of functional groups in the nanomaterial/polymer interface and followed the trend: graphene platelets > graphene oxide nanoribbons > carbon nanotubes (for carbon nanomaterials) and 2-D nanoplatelets > 1-D nanotubes > PPF baseline control (for inorganic nanomaterials). Moreover, all nanocomposite scaffolds showed excellent cytocompatibility for mouse MC3T3 pre-osteoblasts (similar to PPF scaffolds) confirmed by high numbers of viable cells infiltrated inside the porous structure. Additionally, MC3T3 cells were found to secrete collagen-I inside the pores forming ECM (confirmed by IHC). This study showed that by harnessing physiochemical properties of 2-D and 1-D nanomaterials can lead to the development of stronger nanocomposite scaffolds with excellent cytocompatibility which can support new bone formation. This new class of light-weight, biocompatible, biodegradable and strong nanocomposites can be used for bone tissue engineering applications.

7.5. Tables

Table 7.1. Porosity of: A) inorganic and b) carbon nanocomposite scaffolds.

(A)	PPF control	WSNT	BNNT	MSNP	BNNP
Porosity (%)	83.6±0.4	83.6±0.5	83.7±0.5	83.5±0.7	83.3±0.6

(B)	PPF control	SWCNT	MWCNT	SWGONR	MWGONR	GONP
Porosity (%)	84.1±0.4	84.3±0.2	82.7±0.5	84.5±0.3	82.6±0.9	83.6±0.3

Table 7.2.A) Comparison of compressive mechanical properties for inorganic nanocomposite scaffolds: (a) compressive modulus, (b) offset yield strength and (c) ultimate strength.

(a)	Compressive modulus (MPa)	% increase compared to PPF	% increase compared to WSNT	% increase compared to BNNT
MSNP	14±1	0-114	0-87	0-50
BNNP	18±3	15-200	7-162	7-110

(b)	Yield strength (KPa)	% increase compared to PPF	% increase compared to WSNT	% increase compared to BNNT
MSNP	312±9	0-43	0-4	0
BNNP	364±54	0-87	0-35	0-12

(c)	Ultimate strength (KPa)	% increase compared to PPF	% increase compared to WSNT	% increase compared to BNNT
MSNP	351±29	0-25	0-15	0
BNNP	415±87	0-64	0-53	0-29

(A)

Table 7.2.B) Comparison of compressive mechanical properties for carbon nanocomposite scaffolds: a) compressive modulus, b) offset yield strength and c) ultimate strength.

(a)	Compressive modulus (MPa)	% increase compared to PPF	% increase compared to SWCNT	% increase compared to MWCNT
SWGONR	13.8±1.7	0-52	0-27	0-36
MWGONR	18.4±0.5	26-85	29-66	13-66
GONP	19.3±1.8	23-107	26-75	14-86

(b)	Offset yield strength (KPa)	% increase compared to PPF	% increase compared to SWCNT	% increase compared to MWCNT
SWGONR	211±58	0-90	0-91	0-52
MWGONR	275±16	60-106	32-107	30-64
GONP	250±41	29-105	6-107	13-64

(c)	Ultimate strength (KPa)	% increase compared to PPF	% increase compared to SWCNT	%increase compared to MWCNT
SWGONR	251±37	0-50	0-77	0-40
MWGONR	283±21	24-60	13-88	0-49
GONP	262±64	0-70	0-101	0-59

(B)

Table 7.3. Comparison of protein adsorption after 9 days: A) inorganic and B) carbon nanocomposite scaffolds.

(A)	Collagen-I adsorption (%)	% increase compared to PPF	% increase compared to WSNT	% increase compared to BNNT
MSNP	22.4±6.6	96-729	0-20	0-27
BNNP	31.9±7.3	204-1027	0-64	0-73

(B)	% Collagen-I adsorption	% increase compared to PPF	% increase compared to SWCNT	% increase compared to MWCNT
SWGONR	47.6±5.9	0-40	0-60	0-25
MWGONR	46.4±5.5	0-35	0-55	0-21
GONP	44.6±1.7	0-20	0-38	0-9

7.6. Figures

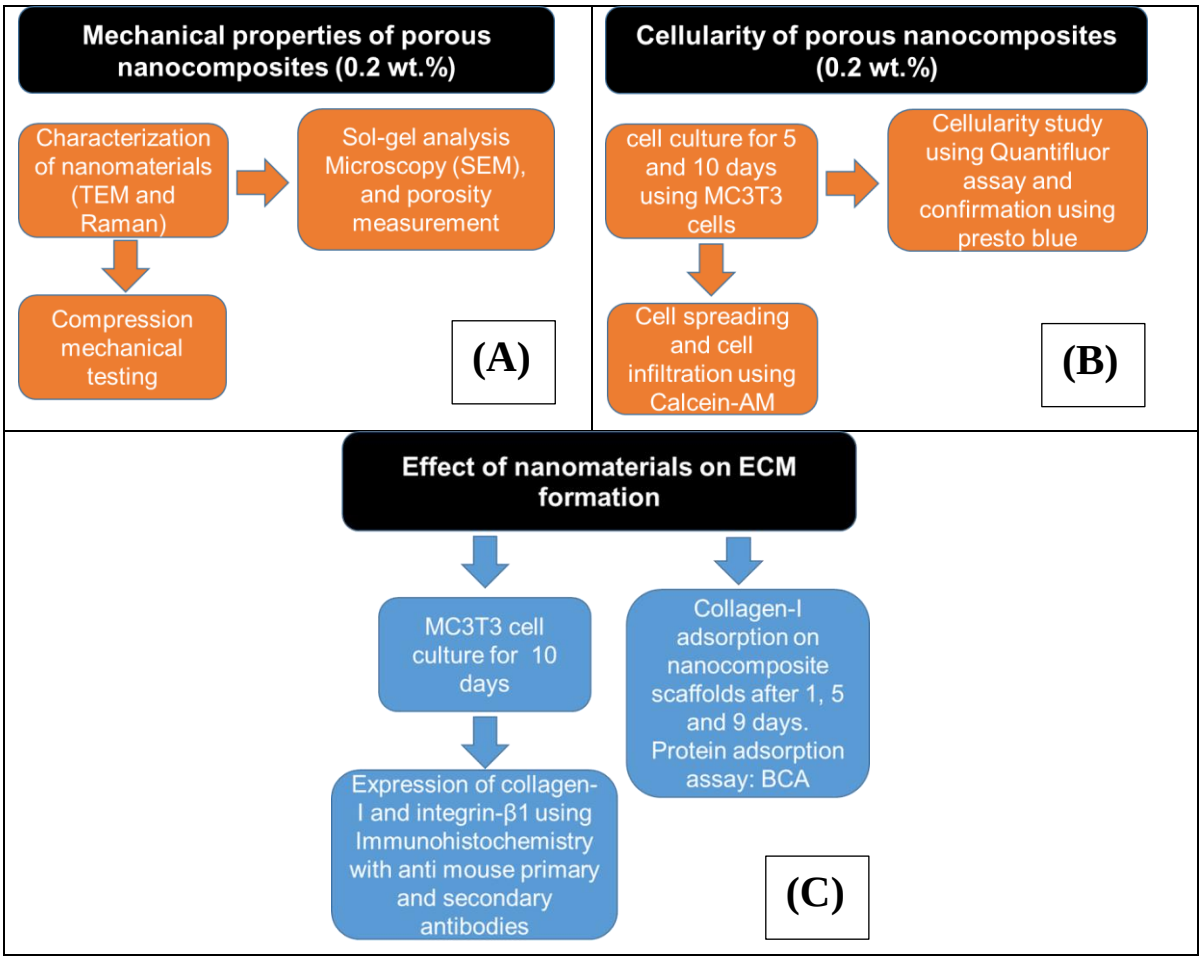

Figure 7.1. Flowchart of studying the A) mechanical properties, B) cytocompatibility and C) ECM formation of nanocomposite scaffolds.

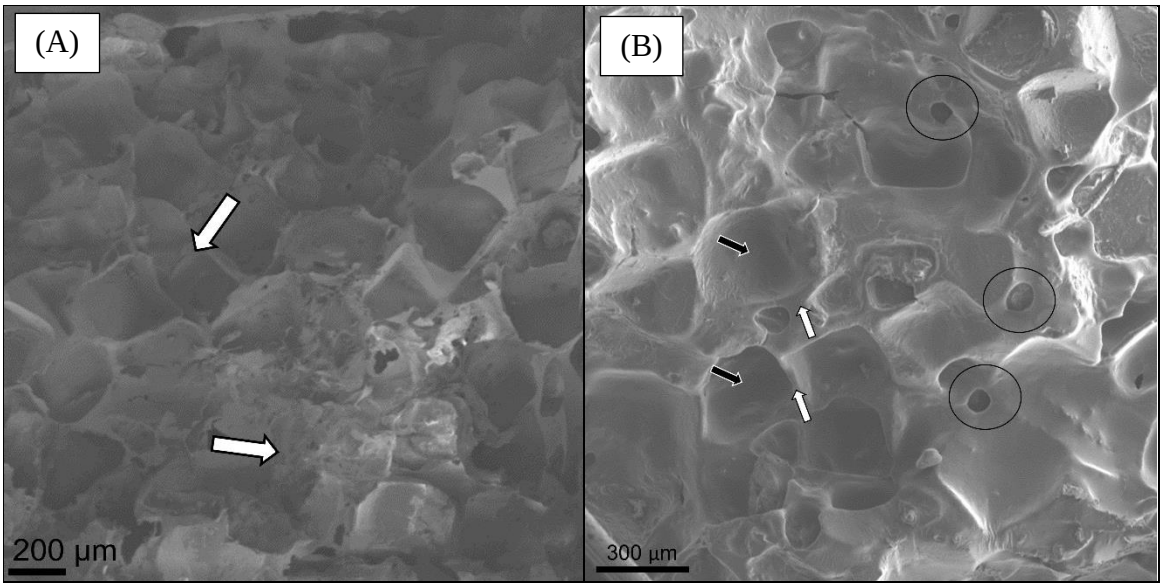

Figure 7.2.A) SEM image of: A) PPF baseline control B) BNNP nanocomposite scaffolds (due to similarity in SEM images between experimental groups only PPF data is shown).

(C)

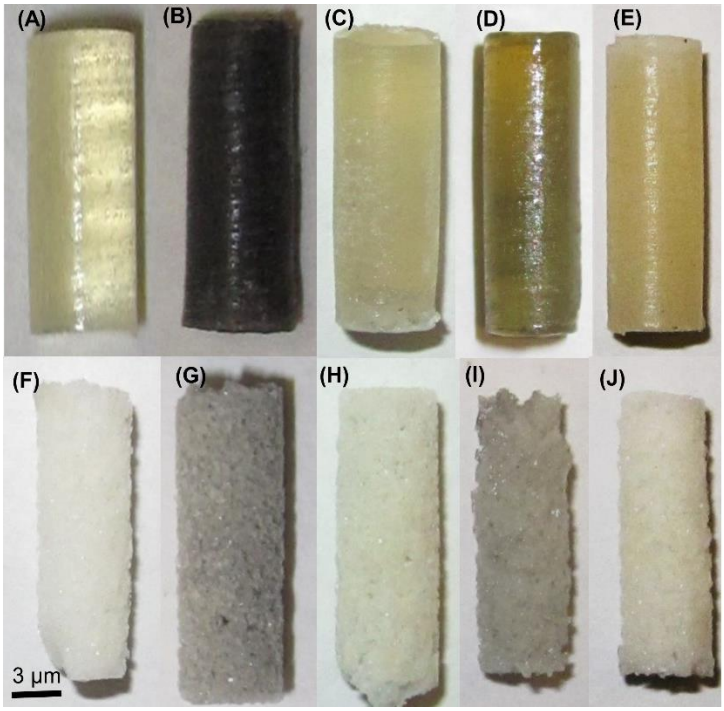

Figure 7.2.C) Digital images of nanocomposite scaffolds and their dense counter-parts: A) PPF baseline control and B) WSNT, C) BNNT, D) MSNP, and E) BNNP.

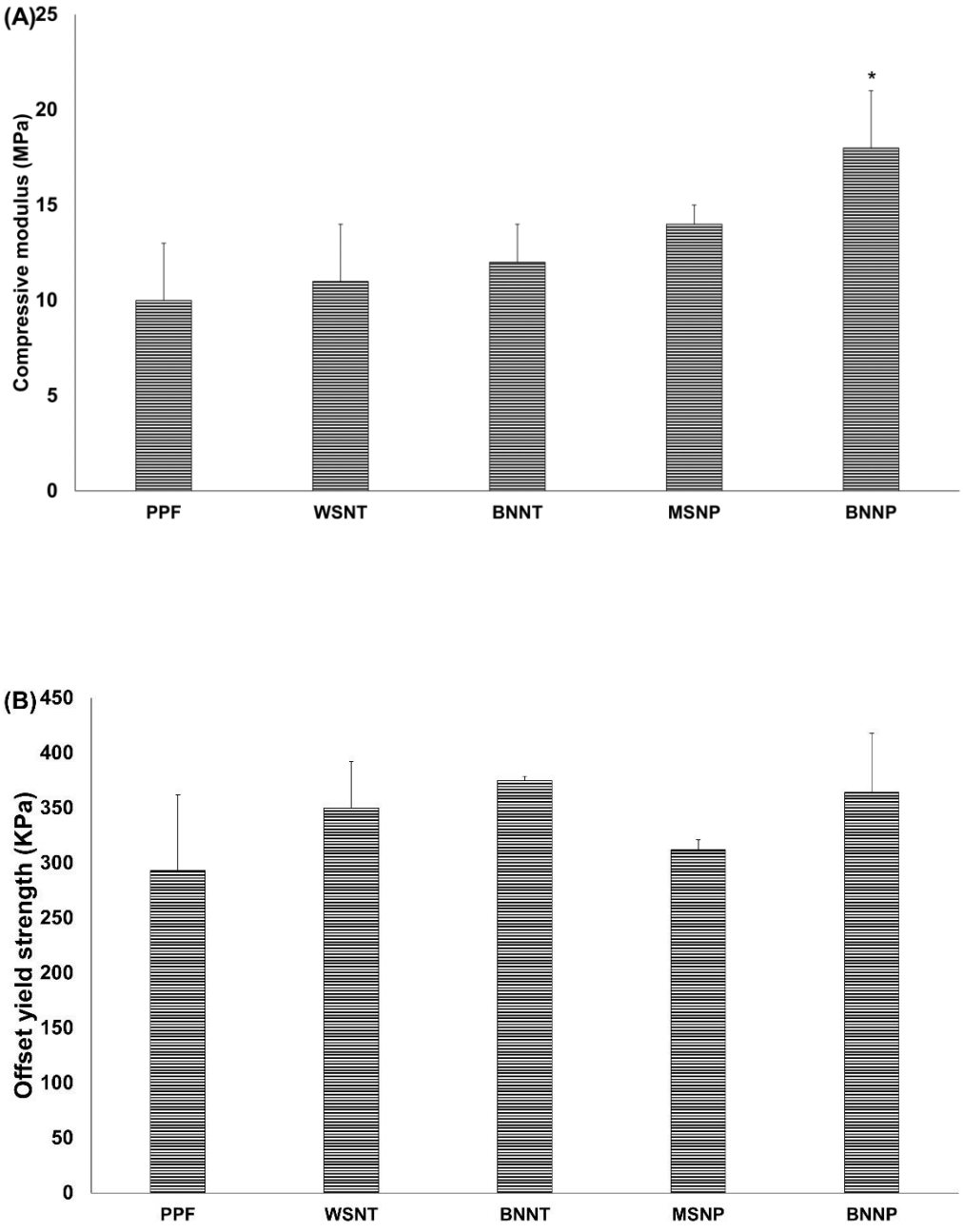

Figure 7.3. The mechanical properties of inorganic nanocomposites scaffolds: A) Compressive modulus, B) compressive yield strength C) offset yield strength and D) sol-fraction analysis. Error bars represent standard deviations for three samples (n=3). Statistically significant differences ($p < 0.05$) with respect to PPF baseline control have been indicated using "*" symbol (continued on the next page).

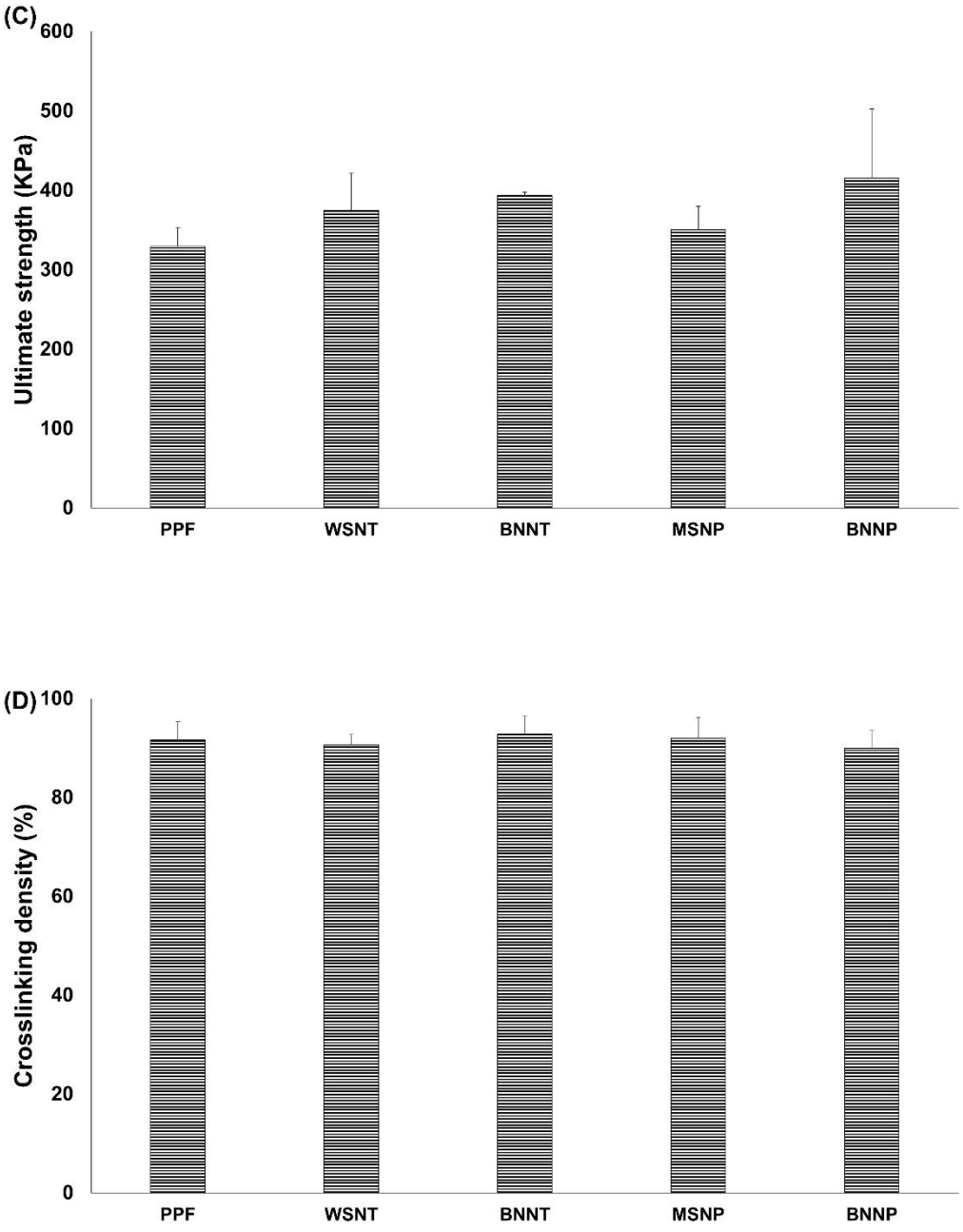

Figure 7.2. The mechanical properties of inorganic nanocomposites scaffolds: C) offset yield strength and D) sol-fraction analysis of PPF nanocomposites and baseline control. Error bars represent standard deviations for three samples (n=3). Statistically significant differences ($p < 0.05$) with respect to PPF baseline control have been indicated using "*" symbol (continued from the previous page).

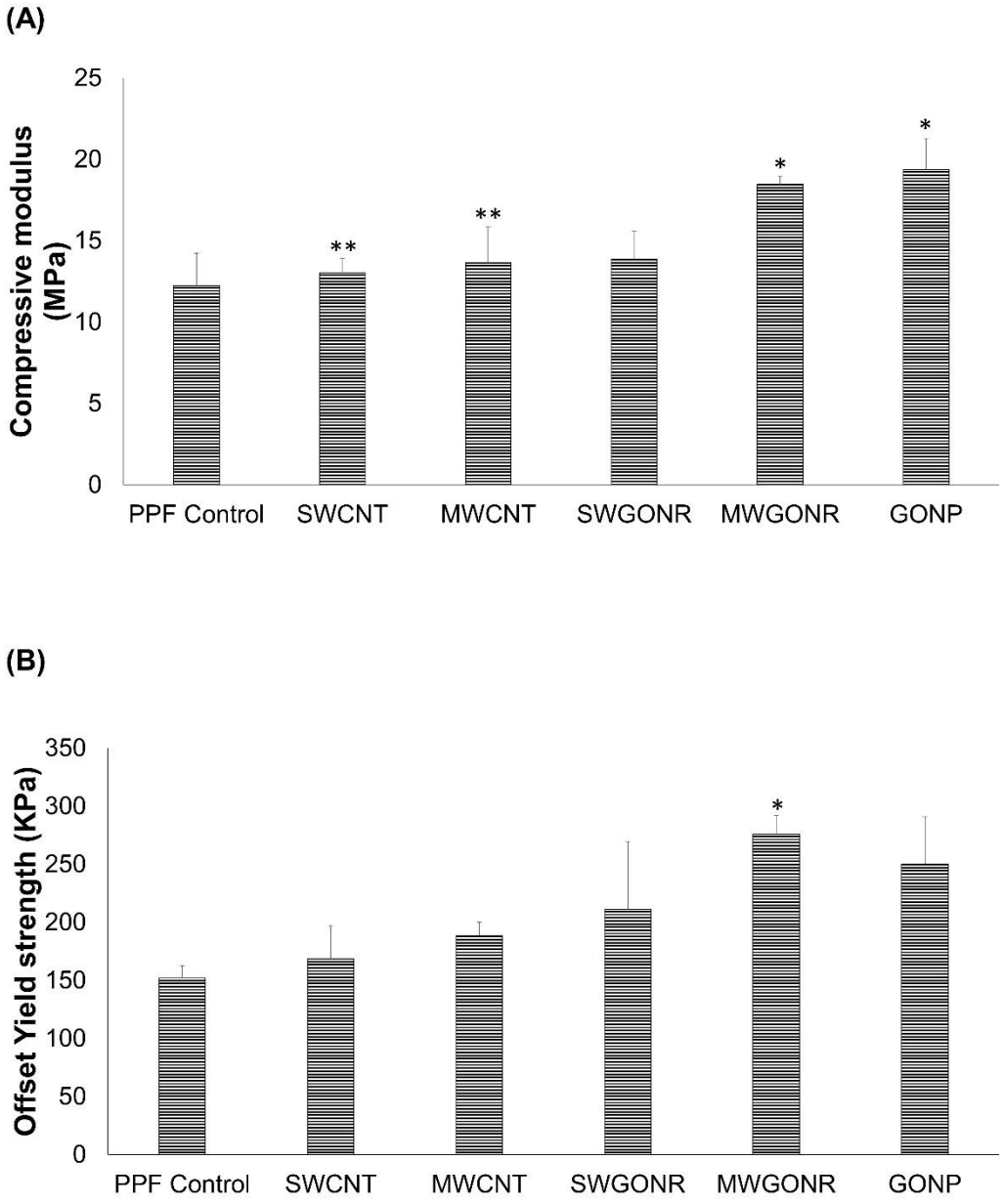

Figure 7.4. The mechanical properties of carbon nanocomposites scaffolds: A) Compressive modulus, B) offset yield strength. Error bars represent standard deviations for three samples (n=3). Statistically significant differences ($p < 0.05$) with respect to PPF baseline control have been indicated using "*" and the significant difference with respect GONP nanocomposite scaffold is marked with"**" (Continued on the next page).

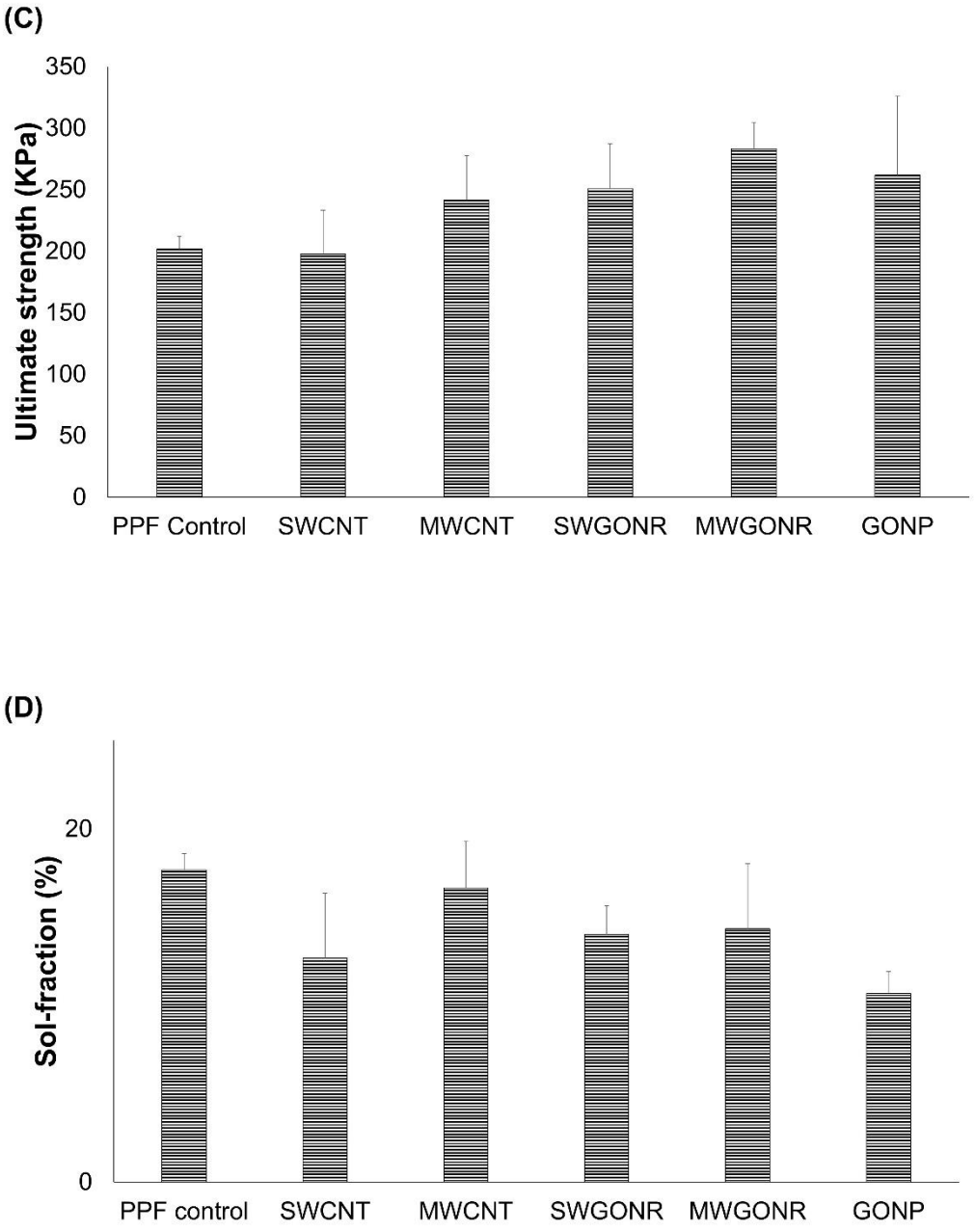

Figure 7.4. The mechanical properties of carbon nanocomposites scaffolds: C) the ultimate strength and D) sol-fraction analysis. Error bars represent standard deviations for three samples (n=3). Statistically significant differences ($p < 0.05$) with respect to PPF baseline control have been indicated using "*" and the significant difference with respect GONP nanocomposite scaffold is mared with"**"

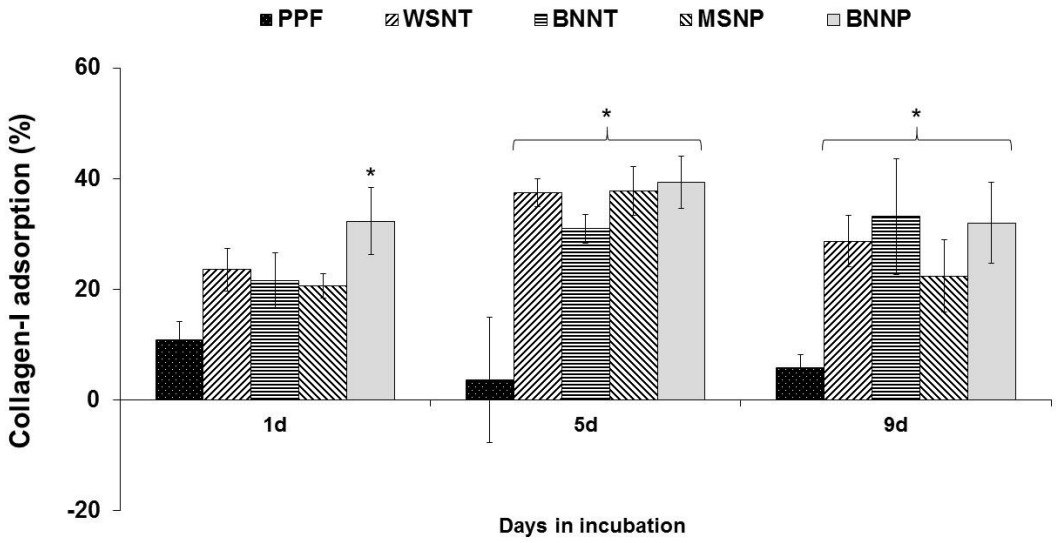

Figure 7.5.A) Collagen-I protein adsorption after 1, 5, and 9 days incubation at 37°C on the inorganic PPF nanocomposites. Data has been normalized with respect to PS control and error bars represent standard deviations for six samples (n=6). The symbol "*" indicates statistically significant difference with respect to PPF baseline control ($p < 0.05$).

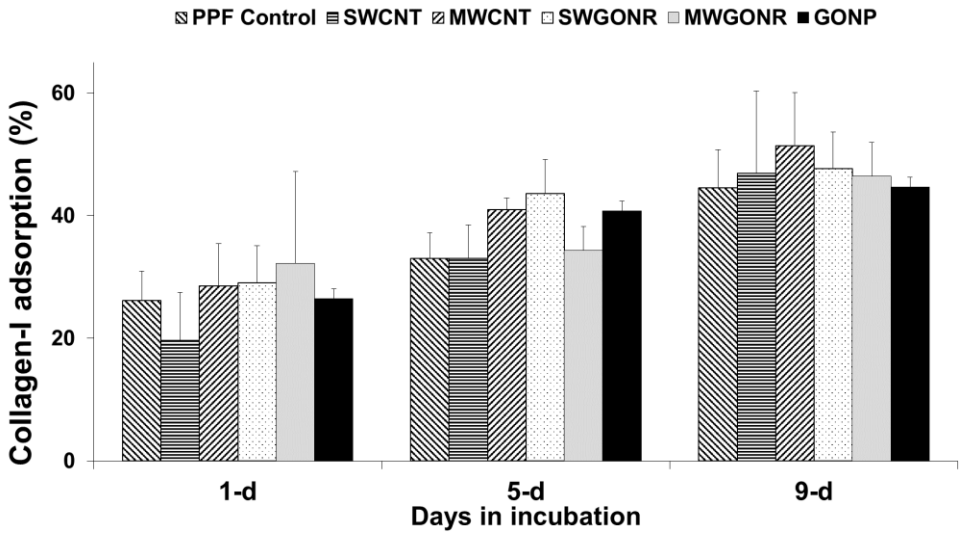

Figure 7.5.B) Collagen-I protein adsorption after 1, 5, and 9 days incubation at 37°C on carbon PPF nanocomposites. Data has been normalized with respect to PS control and error bars represent standard deviations for six samples (n=6).

(a)

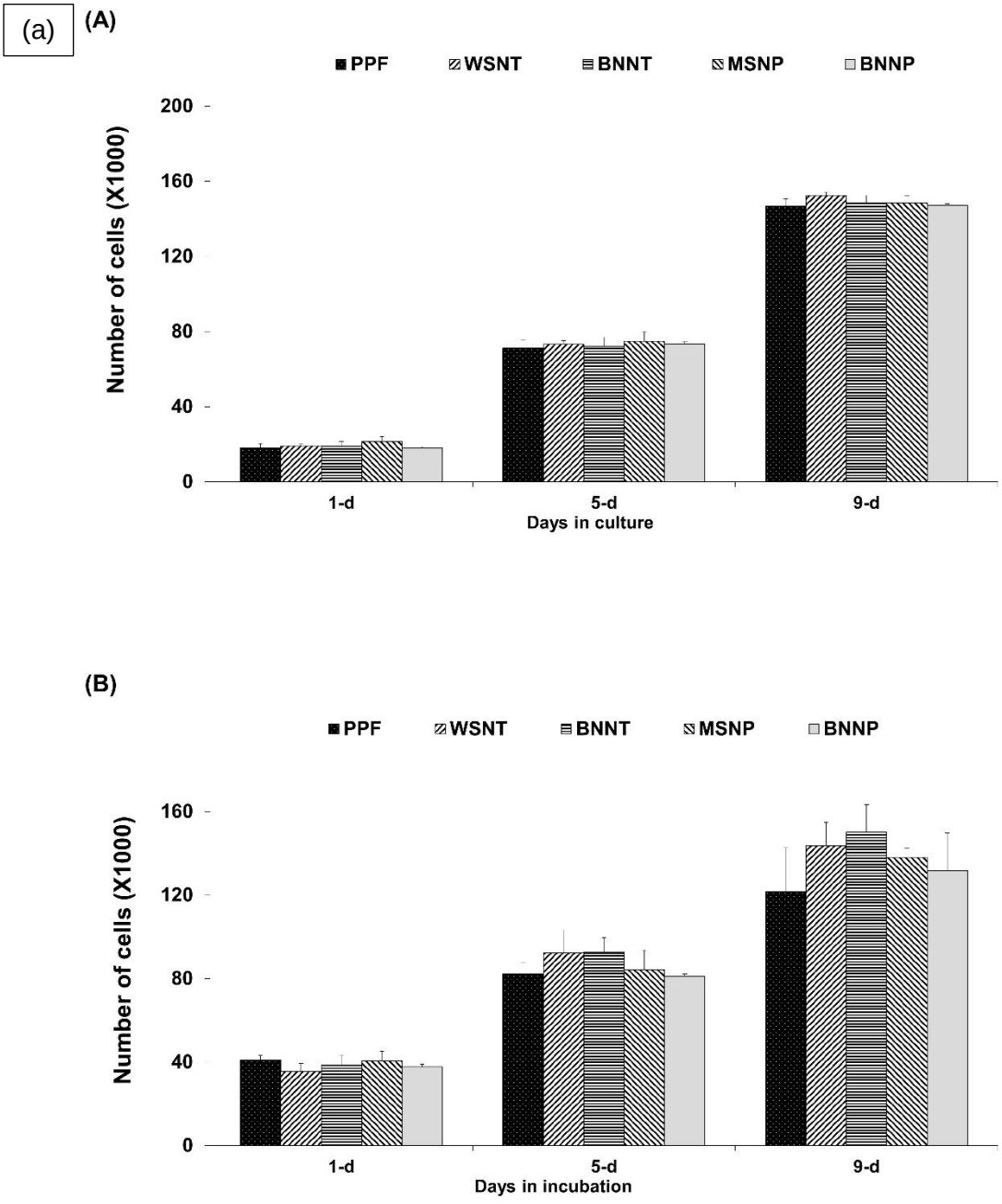

Figure 7.6.a) Number of viable of MC3T3 cells on porous inorganic scaffolds after 1, 5 and 9 days incubation using: (A) Quantiflour® and (B) Presto Blue® assays. Data has been normalized with respect to live and dead controls and error bars represent standard deviations for five samples (n=5).

(b)

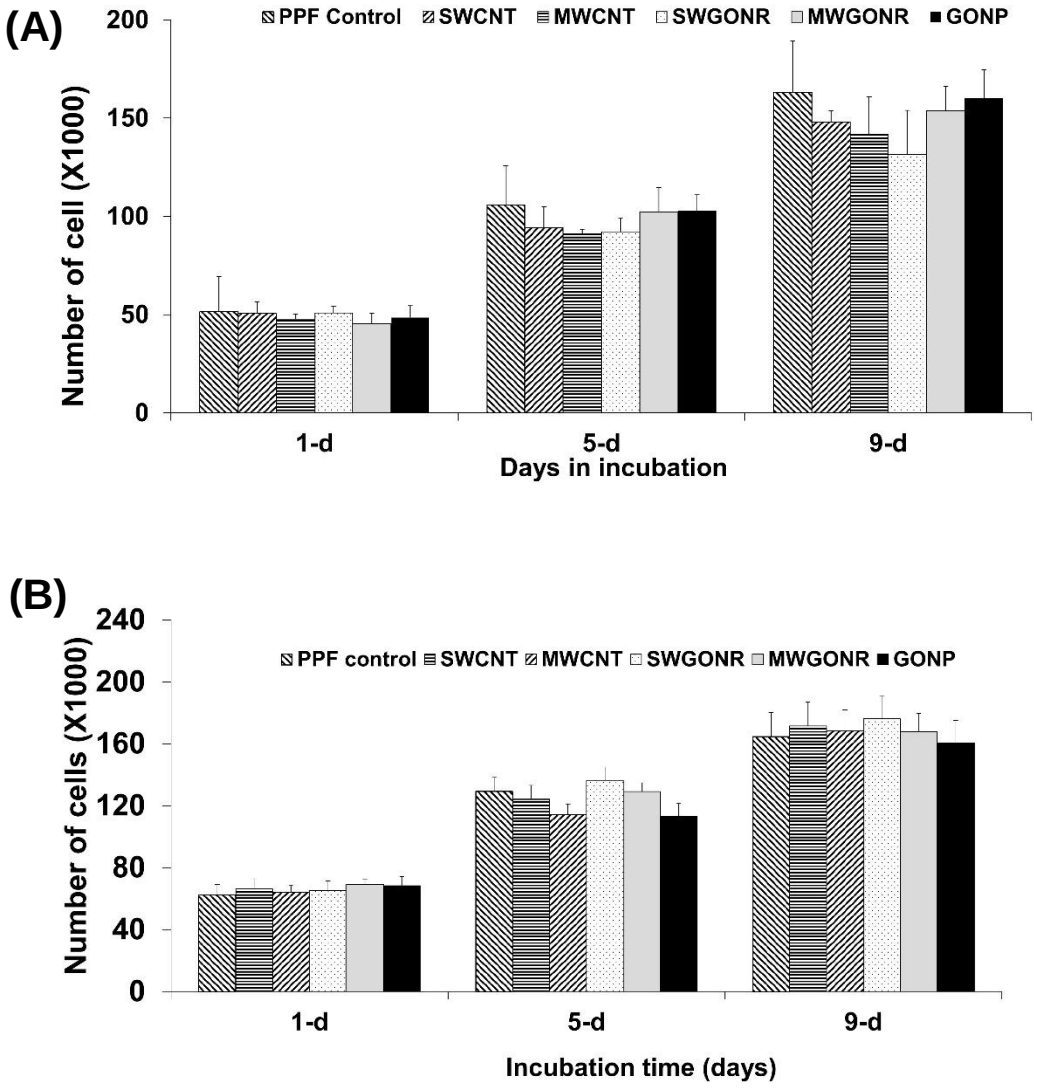

Figure 7.6.b) Cellularity of MC3T3 cells on porous scaffolds after 1, 5 and 9 days incubation using: (A) Quantiflour® and (B) Presto Blue® assay. Data has been normalized with respect to live and dead controls and error bars represent standard deviations for five samples (n=5).

(a)

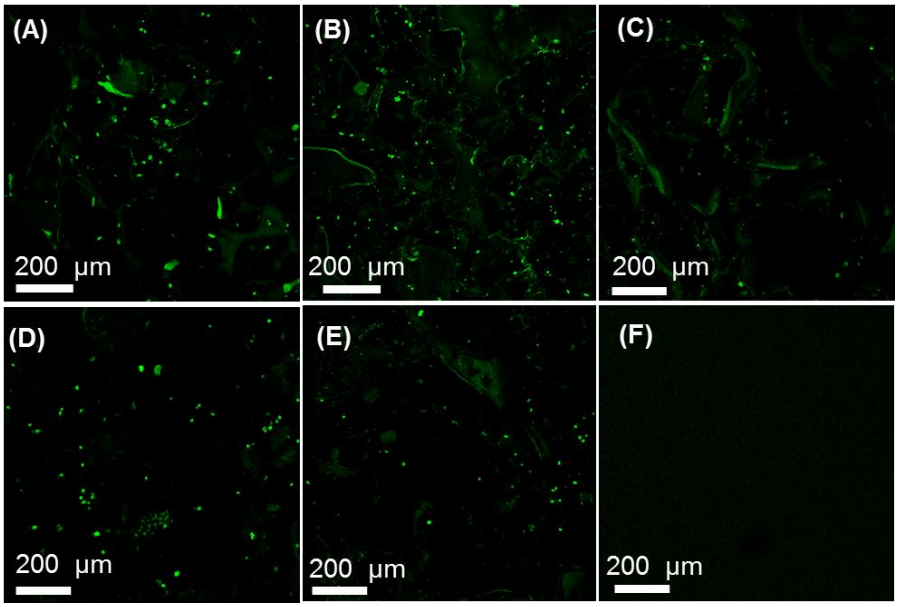

Figure 7.7.a) Representative fluorescent microscopy images of attached MC3T3 cells on nanocomposite scaffolds after 5 days incubation: (A) PPF baseline control, (B) WSNT, (C) BNNT, (D) MSNP and (E) BNNP and (F) negative control.

(b)

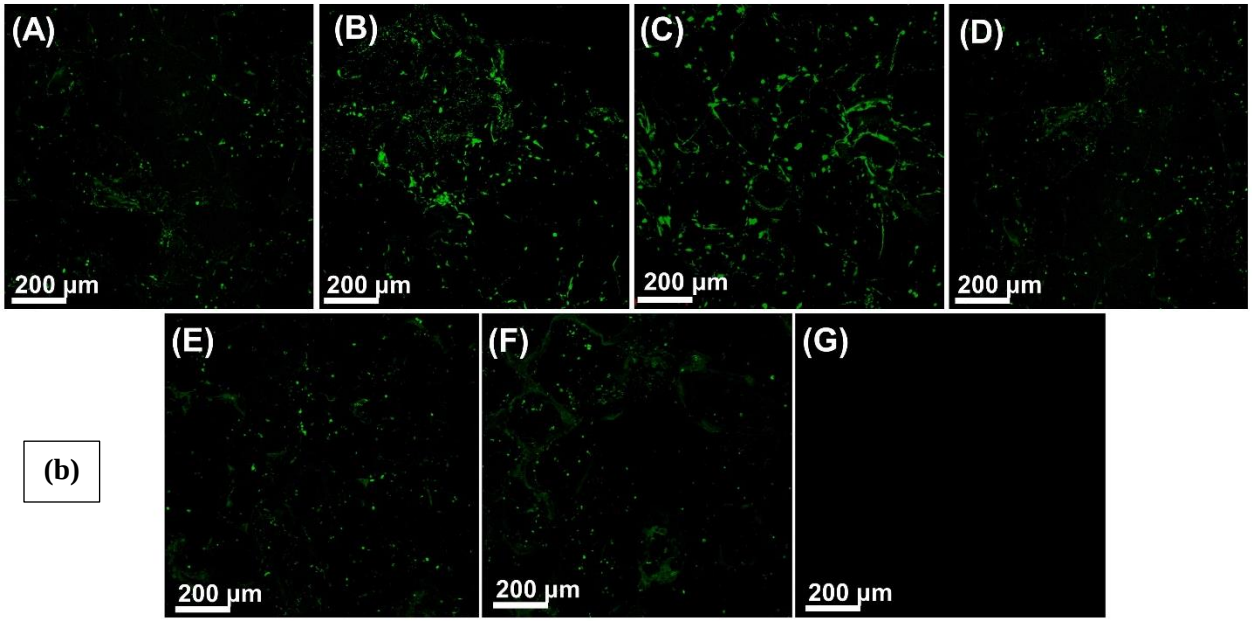

Figure 7.7.b) Representative fluorescent microscopy images of attached MC3T3 cells on nanocomposite scaffolds after 5 days incubation: (A) PPF baseline control (B) SWCNT, (C) MWCNT, (D) SWGONR (E) MWGONR, (F) GONP nanocomposite scaffolds and (G) negative control.

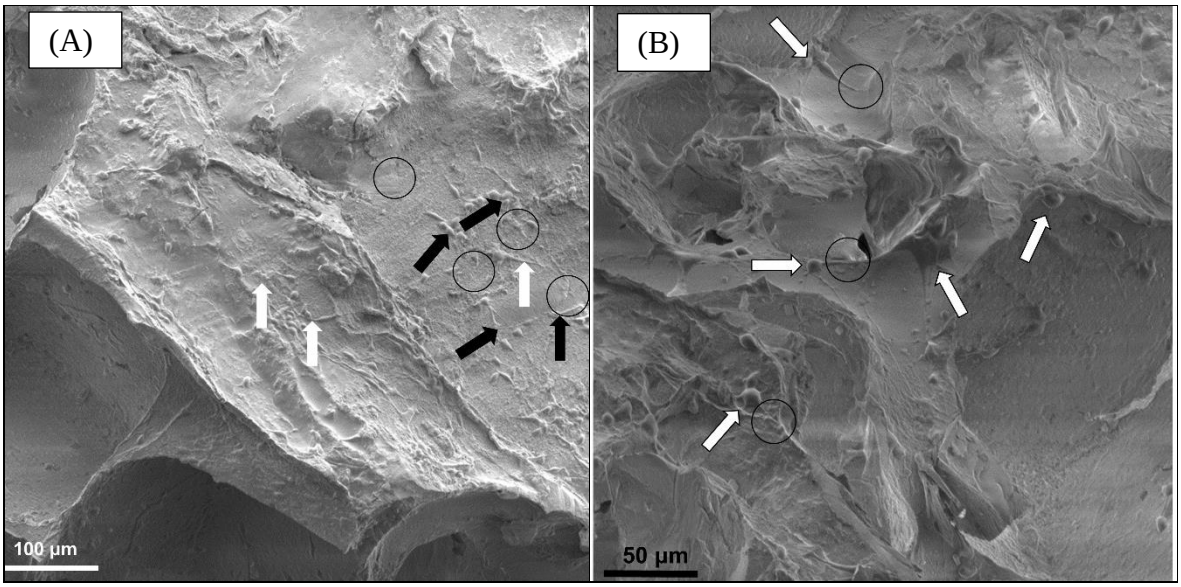

Figure 7.8. Representative SEM images of: A) PPF baseline control and B) BNNP nanocomposite scaffolds after 5 days of cell culture (Due to similarity with other nanocomposite only data of PPF and BNNP nanocomposite scaffolds is shown here).

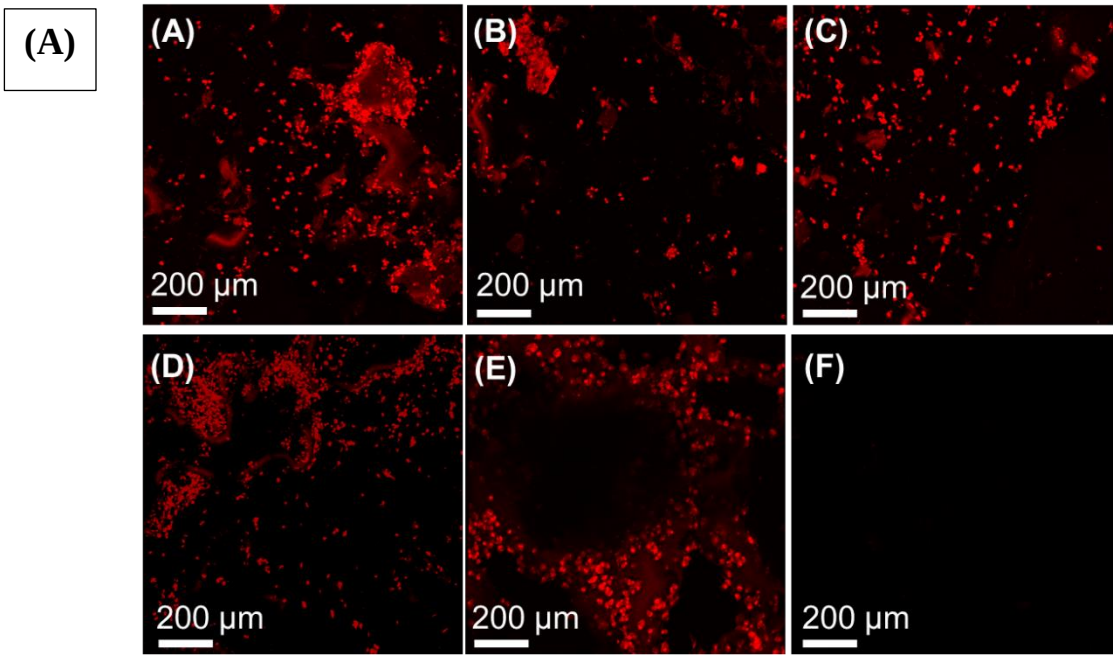

Figure 7.9.A) Immunohistochemistry images of collagen-I expression on (A) PPF baseline control (B) WSNT, (C) BNNT, (D) MSNP (E) BNNP nanocomposite scaffolds and (F) negative control.

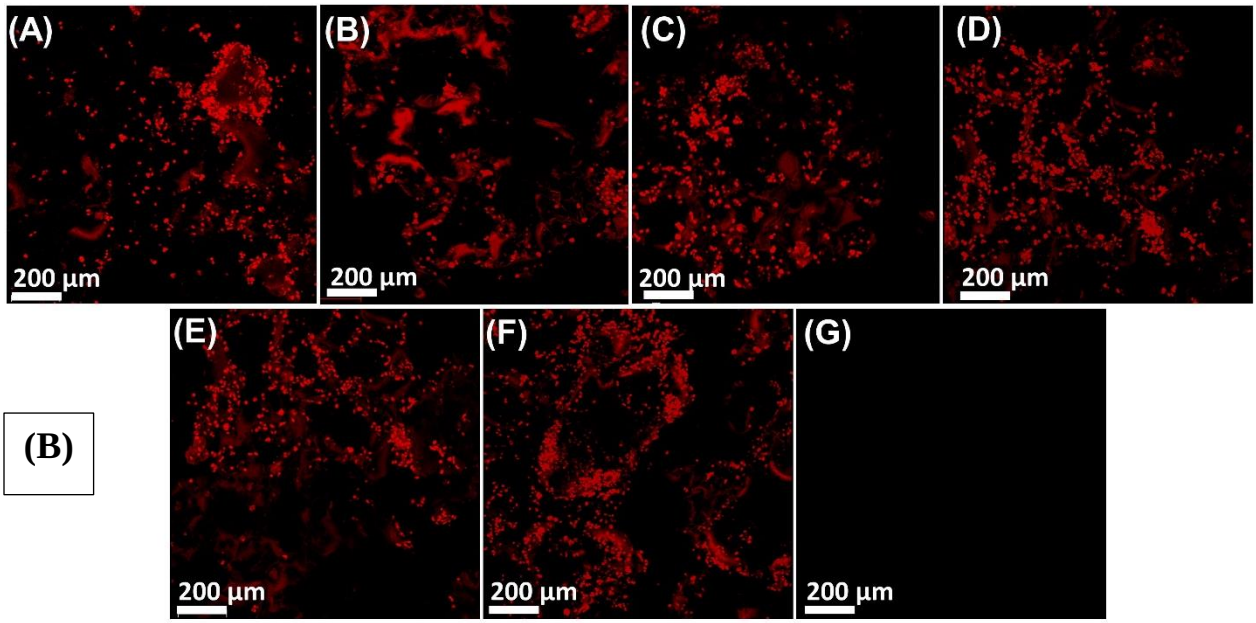

Figure 7.9.B) Immunohistochemistry images of collagen-I expression on (A) PPF baseline control (B) SWCNT, (C) MWCNT, (D) SWGONR (E) MWGONR, (F) GONP nanocomposite scaffolds and (G) negative control.

Chapter 8: Ostogenic Differentiation and Calcium Mineralization in 1-D and 2-D Nanomaterial-Reinforced Polymeric Scaffolds

8.1. Introduction

In the previous chapter, we investigated the mechanical properties, and the *in vitro* cytocompatibility of porous nanocomposite PPF scaffolds reinforced using 1-D and 2-D carbon and inorganic nanomaterials. In this chapter, we will provide insights on bioactivity of nanocomposite scaffolds and the effect of 1-D and 2-D nanomaterials on *in vitro* osteogenic differentiation and calcium mineralization (for MC3T3 pre-osteoblasts) for new bone formation (flowchart shown in Figure 8.1).

There has been a growing interest in the use of various nanomaterials for bone tissue engineering as reinforcing agents, materials assisting healing process and permitting monitoring of tissue regeneration [404]. Bioactive nanomaterials such as hydroxyapatite [405, 406], alumoxane [407], clay [408], alumina [409], zirconia [410] and titania [411] have been investigated as reinforcing agents to improve the mechanical properties of chitosan [410], poly(glycolic acid) (PLGA) [405], poly lactic acid) (PLA) [22], poly(caprolactone) PCL [412] and poly(propylene fumarate) (PPF) [413]. Nanomaterials have high mechanical strength, surface roughness, large surface area, biocompatibility, bioactivity and potential for drug delivery, their application is associated with limitations such as cytotoxicity at high nanomaterial loading concentration, and biodegradation and biodistribution concerns [414]. Moreover, it is desirable to produce smart polymeric biomaterials that are responsive to electrical and magnetic

fields, thermal, acoustic and light sources that can lead to a controlled forming (especially for injectable application when they can eliminate the need for an excessive external heat that is fatal for surrounding cells) and monitoring after implantation (to track bone healing status, control implant's shape and degradation rate [415]). To address these needs, 1-D and 2-D nanomaterials have been used for bone tissue engineering applications. These nanomaterial significantly increase mechanical strength and toughness of polymeric nanocomposites at low nanomaterial loading concentrations and are cytocompatible permitting biomedical applications. Furthermore, physical properties of these nanomaterials such as extra-large surface area and electronic structure provides new opportunities to develop novel bone tissue engineering biomaterials capable of delivering drugs, being imaged and even receive external signals (electrical, magnetic, thermal, acoustic and light) for stimulation.

Bioactivity has been studied for some of the nanomaterials used in this work. CNTs [81, 416] and graphene [374] had exhibited desirable *in vitro* and *in vivo* bioactivity. Ajayan et al. showed that CNTs under the effect of alternating electrical field can cause stimulation in stem cells [98] and Danti et al. showed that BNNTs can promote osteoblastic differentiation when subjected to photo-thermal waves [112]. Surprisingly, their bioactivity has not been studied for bone tissue engineering applications. Towards answering this gap in available inoformation, in this chapter, we will investigate the effect of the 1-D and 2-D carbon and inorganic nanomaterials on the osteogenic differentiation in terms of their effect on alkaline phosphatase activity (ALP, an indicator of early stage osteoblastic differentiation) and calcium mineralization for murine MC3T3 pre-osteoblasts (as an indicator of calcium phosphate deposition). Confocal and electron scanning microscopy were used to image cells and expression of integrin β-1 on nanocomposite scaffolds.

8.2. Results

8.2.1. Structural characterization of nanocomposite scaffolds

Figure 8.2 shows the porous structure of PPF nanocomposite scaffolds (porosity values for experimental and control groups are presented in Table 8.1). As seen in the SEM micrograph, the structure was composed of interconnected pores with 300 μm diameter (similar to sodium chloride particles used to induce porosity). The pores were separated by thin walls of polymer in the form of interconnected channels to permit cell infiltration and transport of nutrients as well as cell wastes. Due to similarity of nanocomposite scaffolds, only the microstructure of BNNP nanocomposite is presented in Figure 8.2.

8.2.2. Cellularity of MC3T3 cells on scaffolds

8.2.2.1. Double stranded DNA (ds-DNA) content on nanocomposite scaffolds

Figure 8.3 displays the number of viable cells detected using Quantifluor® assay on nanocomposite scaffolds. This assay is comprised of fluorescent dyes that interact with the double stranded-DNA chains and can be used to quantify number of live cells in the samples [417]. Out of the $50*10^3$ initial MC3T3 seeded cells, PPF, SWCNT, MWCNT, SWGONR, MWGONR, GONP, BNNT, WSNT, BNNP and MSNP scaffolds showed ~$245*10^3$, ~$173*10^3$, ~$177*10^3$, ~$174*10^3$, ~$170*10^3$, ~$190*10^3$, ~$219*10^3$, ~$254*10^3$, ~$210*10^3$ and ~$200*10^3$ cells after incubation with osteogenesis media at 37ºC for 14 days, respectively. After 21 days, number of the cells detected on each of the scaffolds slightly increased to ~$218*10^3$, ~$209*10^3$, ~$189*10^3$, ~$255*10^3$, ~$257*10^3$, ~$261*10^3$, ~$181*10^3$, ~$239*10^3$, ~$197*10^3$ and ~$161*10^3$ cells for PPF, SWCNT, MWCNT, SWGONR, MWGONR, GONP, BNNT, WSNT, BNNP and MSNP scaffolds, respectively. After 28 days incubation at 37ºC, the number of viable MC3T3 cells did not significantly change: ~$268*10^3$, ~$235*10^3$, ~$240*10^3$, ~$255*10^3$,~$205*10^3$,

~296*10^3, ~264*10^3, ~239*10^3, ~311*10^3 and ~272*10^3 cells for PPF, SWCNT, MWCNT, SWGONR, MWGONR, GONP, BNNT, WSNT, BNNP and MSNP scaffolds, respectively. The difference in number of cells only refers to the number of attached cells on each scaffold and does not imply difference in cytocompatibility of various nanocomposite scaffolds.

8.2.2.2. Microscopy of MC3T3 cells on the scaffolds

Figure 8.4 shows the confocal fluorescence images of MC3T3 cell spreading and infiltration into the nanocomposite scaffolds after 14 days of incubation. Calcein-AM is a nonfluorescent dye which is converted to a green-fluorescent dye after the hydrolysis of acetoxymethyl ester group by intracellular esterase [418]. Similar to PPF baseline control, all of the nanocomposite scayes ffolds showed a good cell infiltration and spreading (compared to the negative control) similar to PPF baseline control. The suitable size of the pores (300 μm diameter) allows cells to migrate inside the nanocomposite scaffolds during the seeding stage.

Figure 8.5 shows the scanning electron microscopy (SEM) image of BNNP nanocomposite scaffold after 14 days of incubation (SEM image of BNNP nanocomposite is shown as a representation for all nanocomposite groups). SEM image shows the surface of a 300 μm pore containing MC3T3 cells (diameter of 10 μm, marked with white arrows in Figure 8.5), with extended filopodia attaching to the underlying extracellular matrix (ECM) (marked with black circles in Figure 8.5).

8.2.2.3. Immunohistochemistry of integrin-β1 expression

Figure 8.6 shows the confocal fluorescence images of integrin-β1 protein expression on the nanocomposite scaffolds after 14 days of incubation. All of samples expressed integrin-β1

protein; no significant difference in the protein distribution among the experimental groups was observed. The integrin-β1 transmembrane proteins connect the cells to the ECM on nanocomposite scaffolds.

8.2.3. Alkaline phosphatase activity (ALP) of MC3T3 cells

The intracellular alkaline phosphatase (ALP) activity for MC3T3 cells after incubation with osteogenic media after 14, 21 and 28 days on nanocomposite scaffolds is shown in Figure 8.7. PPF controls and SWCNT, MWCNT, SWGONR, MWGONR, GONP, BNNT, WSNT, BNNP and MSNP scaffolds showed ~$0.25*10^{-8}$, ~$0.52*10^{-8}$, ~$0.26*10^{-8}$, ~$2.24*10^{-8}$, ~$1.70*10^{-8}$, ~$3.12*10^{-8}$, ~$0.90*10^{-8}$, ~$1.41*10^{-8}$, ~$3.77*10^{-8}$ and ~$3.12*10^{-8}$ (μmol/min.cell) ALP activity after 14 days, respectively. All of the experimental groups showed higher ALP activity after 21 days; PPF control and SWCNT, MWCNT, SWGONR, MWGONR, GONP, BNNT, WSNT, BNNP and MSNP scaffolds showed ~$2.51*10^{-8}$, ~$2.81*10^{-8}$, ~$2.08*10^{-8}$, ~$3.28*10^{-8}$, ~$3.37*10^{-8}$, ~$3.70*10^{-8}$, ~$3.24*10^{-8}$, ~$3.25*10^{-8}$, ~$4.47*10^{-8}$ and ~$4.07*10^{-8}$ (μmol/min.cell), respectively. After 28 days ALP activity of the scaffolds either did not change significantly or slightly increased to ~$2.05*10^{-8}$ ~$2.18*10^{-8}$, ~$2.13*10^{-8}$, ~$4.62*10^{-8}$, ~$4.66*10^{-8}$, ~$5.59*10^{-8}$, ~$3.38*10^{-8}$, ~$3.68*10^{-8}$, ~$4.30*10^{-8}$, and ~$4.90*10^{-8}$ (μmol/min.cell). In general, 1-D inorganic nanocomposite scaffolds and 2-D organic and inorganic nanocomposite scaffolds showed significant increase in ALP activity in comparison with PPF baseline control (marked with "*" in Figure 8.7) with 2-D inorganic nanocomposites being slightly more bioactive.

8.2.4. Calcium deposition on scaffolds

Calcium content (normalized to cell numbers) after 14, 21 and 28 days of incubation is shown in Figure 8.8. PPF control and SWCNT, MWCNT, SWGONR, MWGONR, GONP,

BNNT, WSNT, BNNP and MSNP scaffolds showed ~$0.86*10^{-3}$, ~$1.58*10^{-3}$, ~$2.22*10^{-3}$, ~$5.44*10^{-3}$, ~$4.52*10^{-3}$, ~$5.82*10^{-3}$, ~$3.87*10^{-3}$, ~$3.83*10^{-3}$, ~$6.49*10^{-3}$ and ~$4.06*10^{-3}$ (mg/µ.lit.cell) calcium mineralization after 14 days, respectively. After 21 days groups showed higher calcium content; PPF control and SWCNT, MWCNT, SWGONR, MWGONR, GONP, BNNT, WSNT, BNNP and MSNP scaffolds showed ~$2.15*10^{-3}$, ~$2.97*10^{-3}$, ~$3.61*10^{-3}$, ~$5.81*10^{-3}$, ~$6.82*10^{-3}$, ~$5.09*10^{-3}$, ~$3.74*10^{-3}$, ~$4.69*10^{-3}$, ~$7.16*10^{-3}$ and ~$7.77*10^{-3}$ (mg/µlit.cell) calcium content per cell, respectively. After 28 days of inubation, the calcium content in the scaffolds further increased to ~$4.23*10^{-3}$, ~$4.55*10^{-3}$, ~$4.23*10^{-3}$, ~$6.73*10^{-3}$, ~$7.67*10^{-3}$, ~$7.48*10^{-3}$, ~$5.86*10^{-3}$, ~$6.19*10^{-3}$, ~$8.60*10^{-3}$ and ~$8.45*10^{-3}$ (mg/µlit.cell), respectively. One-dimensional inorganic nanocomposite scaffolds and 2-D carbon and inorganic nanocomposite scaffolds showed a significant increase in calcium content in comparison of PPF baseline control scaffold (marked with "*" in Figure 8.8.A). The microstructure of BNNP nanocomposite scaffold after 28 days cell culture is displayed in Figure 8.8.B. Only microstructure of BNNP nanocomposite scaffolds is presented as a representative image of all nanocomposite groups. The surface of nanocomposite scaffolds was covered with calcium phosphate depositions which was corroborated by arsenazo-3 assay.

8.3. Discussions

In previous chapters we showed that 1-D and 2-D nanomaterials used in this study significantly enhance the mechanical properties of PPF scaffolds without adversely affecting their cytocompatibility. For their application as a porous bone grafts, in addition to osteoconductivity, the nanocomposites should support osteogenic differentiation and calcium mineralization i.e. promote ossification. Previous reports show bioactivity of nanomaterials such

as: calcium phosphate [419], titania [420], zirconia [421] and aluminosilicate glasses [28] towards osteogenic differentiation of MC3T3 pre-osteoblast and their calcium mineralization. In case of 1-D and 2-D nanomaterials only bioactivity of carbon nanotubes [374], graphene oxide [371, 422] and titanium dioxide nanotubes [423] have been investigated. The bioactivity response of other selected nanomaterials for this study is not known.

In this chapter, we systematically investigated the bioactivity of 1-D and 2-D nanomaterials towards osteogenic differentiation and calcium mineralization using MC3T3 murine [424, 425] cell line. MC3T3 cells have been extensively used for bone tissue engineering [420]. Similar to previous chapters, a nanomaterial loading concentration of 0.2 wt. % was used which leads to maximum mechanical reinforcement without the presence of dispersing agents [78], and the well stablished salt-leaching method was utilized to fabricate porous scaffolds [26, 426].

As reviewed in chapter 3, to characterize the structural and chemical composition of nanomaterials, TEM and Raman spectroscopy were performed. TEM imaging of nanomaterials showed a similar nanostructure and chemical compositions as reported previously [202, 334, 427-430]. The synthesis of nanomaterials introduces functional groups on their surface that in conjunction with other physiochemical properties of nanomaterials such as surface roughness and high specific surface area might affect cellular interactions such as osteoegnic differentiation and calcium mineralization [431-433]. Moreover, a homogenous distribution of nanomaterials in the porous nanocomposite scaffold as a result of functional groups on their surface [95] may result in better cell-substrate interactions.

As displayed in Figure 8.2, the high porosity of nanocomposite scaffolds (Table 8.1) supoprted cell in-growth, neutrient exchange, waste removal and calcium mineralization. The microstructures were comparable to the other reports for fabrication of bone tissue engineering scaffolds [26, 434]. Karageorgiou et al. reported that porosity leades to in increase surface roughness and more cell functions such as: osteoblastic differentiation and mineralization [435].

The number of MC3T3 cells on scaffolds (Figure 8.3) shows that a large fraction of seeded cells were viable during ostegenic differentiation and mineralization study. Previously, in chapters 5, 6 and 7 we had shown excellent cytocompatibility of porous and nonporous PPF nanocomposites *in vitro*. The number of the cells seeded on the scaffolds cannot be accurately controlled because a large portion of the cells do not attach to the scaffold during seeding stage, but since the expression of ECM proteins and calcium mineralization is correlated to number of cells, it is necessary to investigate the number of cells to assess their osteoblastic differentiation activity [371, 436]. Therefore, ALP activity and mineralized calcium phosphate were divided by cell numbers.

The confocal microscopy of MC3T3 cells on all experimental samples in Figure 8.4 showed a similar cell infiltration and spreading suggesting that MC3T3 cells could successfully attach to the scaffolds and deposit extracellular matrix (ECM). As osteogenic differentiation progresses, the calcium phosphate mineral will nucleate inside the porous structures forming new bone ECM [437, 438]. Confocal imaging on a cross section of the center of the scaffolds confirm that the static cell culture procedure prevented a large number of MC3T3 cells from migrating inside the pores. Additionally, as the nanocomposite undergoes degradation, a larger portion of bone graft will be substituted with the new bone [358].

The SEM micrographs of MC3T3 cells after 14 days cell culture on the scaffolds (Figure 8.5) was similar to the report by Kizuki et al. [439] showing that on bioactive surfaces, pre-osteoblasts tend to proliferate, spread, extend their filopodia extensions and facilitate formation of bone extracellular matrix [440]. Furthermore, SEM analysis coroboratted confocal images and showed excellent tendency of nanocomposite scaffolds as an osteoconductive substrate.

As Figure 8.6 shows the expression of integrin-β_1 inside the porous structure of scaffolds. The integrins are helical transmembrane protein; $\alpha_1\beta_1$, $\alpha_2\beta_1$, $\alpha_3\beta_1$, $\alpha_4\beta_1$, $\alpha_5\beta_1$, $\alpha_6\beta_1$ and $\alpha_7\beta_1$ that act as anchors and attach to extracellular matrix (ECM) support cell proliferation and/or osteogenic differentiation [441]. Since integrin-β_1 is a typical protein connecting the cells to the ECM matrix, collagen network, laminin and fibronectin, we decided to study the distribution of β_1-integrin expression using immunohistochemistry. The results of immunohistochemistry analysis confirmed the expression of β_1-integrin by MC3T3 cells inside the nanocomposite scaffolds.

Presence of functional groups, large specific surface area and surface roughness increases the energy and reactivity of nanocomposites and increases the protein adsorption on the surface that subsequently improves the attachment of pre-osteoblasts to the substrate [65, 442]. Boyan et al. has reported a systematically improved hormone responsiveness as surface roughness increases affecting osteogenic differentiation through protein kinase A and phospholipase A_2 pathways [443]. The pristine SWCNTs and MWCNTs do not have functional groups on their surface and are often found as aggregates in the polymeric matrix, therefore the only effective parameter in for SWCNT and MWCNT nanocomposite scaffolds is the increased surface roughness. On the other hand, inorganic nanotubes (WSNTs and BNNTs) contain functional groups such as sulfides and amines as a result of synthesis method [252, 444], which improve their dispersion in the polymeric matrix along with protein adsorption. For 2-D carbon

nanocomposites, as a result of unzipping process the surface area will increase along with the incorporation of functional groups such as sulfides and hydroxyls due to the synthesis method. The syntheiss method utilizes acids such as sulfuric acid [123, 215] which results in high reactivity on the surface for 2-D inorganic nanomaterials.

Figure 8.7 depicts that all nanocomposite scaffolds show a time-dependent increase in the levels of intercellular ALP activity in the nanocomposite scaffolds compared to PPF baseline control with a trend: PPF baseline control < 1-D carbon nanocomposites < 1-D inorganic nanocomposites and 2-D carbon nanocomposites < 2-D inorganic nanocomposites (shown in Table 8.2). ALP is a biomarker for the early stage osteogenic differentiation [445] and as osteogenesis is induced, the ALP activity will increase. The increase in surface energy, surface roughness and functional groups on the surface play key roles in increasing ALP activity. Many reports articulate similar effects [65, 446] on osteogenic differentiation. Nayak et al. [447] and Zhang et al. [448] have reported a higher ALP activity in the presence of graphene and carbon nanotubes, respectively. Lee et al. have reported that the formation of chemical bonds on the surface of nanomaterials results in a better adsorption of osteogenesis-inducing factors such as ascorbic acid and β-glycerolphosphate [449].

As seen in Figure 8.8.A, calcium deposition also shows a time-dependent increase with a trend: PPF baseline control < 1-D carbon nanocomposites < 1-D inorganic nanocomposites and 2-D carbon nanocomposites < 2-D inorganic nanocomposites (values are shown in Table 8.3). Increased surface roughness and functional groups on the surface of nanomaterials play an important role in increasing calcium mineralization [450, 451]. Similar to the ALP activity, we think that the combined effect of higher surface area and functional groups dictate ALP activity and calcium deposition trend with 2-D inorganic nanomaterials > 2-D carbon nanomaterials > 1-

D inorganic nanomaterials > 1-D carbon nanomaterials. Furthermore, the SEM image of nanocomposite scaffolds in Figure 8.8.B confirms deposition of calcium ECM on the surface of nanocomposite scaffolds [452].

To the best of our knowledge, this is the first systematic investigation of the effects of 1-D and 2-D inorganic and carbon nanomaterials on the bioactivity of the polymeric nanocomposite bone grafts. For this research 1-D and 2-D nanomaterials such as: graphene oxide nanoribbons (GONRs), graphene oxide nanoplatelets (GONPs), boron nitride nanotubes (BNNTs), tungsten disulfide nanotubes (WSNTs), molybdenum disulfide nanoplatelets (MSNPs) and boron nitride nanoplatelets (MSNPs) were incorporated in biodegradable poly(propylene fumarate) (PPF) scaffolds and their *in vitro* osteogenicc differentiation was assessed by analyzing alkaline phosphatase (ALP) activity and calcium phosphate mineralization. In general, the results of our study showed a higher ALP activity and calcium mineralization on the nanocomposites compared to PPF polymer following this trend: 2-D inorganic nanocomposites > 2-D carbon nanocomposites and 1-D inorganic nanocomposites > 1-D carbon nanocomposites. Results of this study showed that the extraordinary physiochemical properties of 1-D and 2-D nanomaterials not only increase the mechanical properties of nanocomposite scaffolds, but they are bioactive and increase ostegogenic differentiation and calcium mineralization. These properties can be utilized towards the fabrication of multi-functional bioactive mechanically strong nanocomposite scaffolds for bone tissue engineering.

8.4. Conclusions

Nanocomposite scaffolds with 2 wt. % of inorganic and carbon nanomaterials such as single- and multi-walled graphene oxide nanoribbons (SWGONRs and MWGONRs), graphene

oxide nanoplatelets (GONPs), boron nitride nanotubes (BNNTs), tungsten disulfide nanotubes (WSNTs), molybdenum disulfide nanoplatelets (MSNPs) and boron nitride nanoplatelets (MSNPs) were fabricated using poly(propylene fumarate) (PPF) polymer and N-vinyl pyrrolidone (NVP) crosslinker. Highly porous nanocomposite scaffolds (porosity > 80 vol. %) were fabricated using salt-leaching and were structurally characterized and tested for their *in vitro* osteogenic differentiation using MC3T3 cells. The osteogenic differentiation was investigated by alkaline phosphate (ALP) activity, integrin-β1 expression and calcium phosphate mineralization. The results of this study showed that presence of functional groups on the surface of nanomaterials and an increased surface roughness promotes osteogenic differentiation and calcium phosphate mineralization. Our results showed that the bioactivity followed the trend: 2-D inorganic scaffolds > 2-D carbon scaffolds > 1-D scaffolds > 1-D scaffolds > PPF scaffolds. Results of this study open new avenues towards the development of a new class of strong, biodegradable, biocompatible and bioactive nanocomposite scaffolds for bone tissue engineering applications.

8.5. Tables

Table 8.1. Porosity of the experimental groups used for this study.

Sample	**Porosity (%)**
PPF control	83±2
SWCNT	81±4
MWCNT	83±5
SWGONR	81±5
MWGONR	81±5
GONP	83+4
BNNT	82±2
WSNT	82±4
BNNP	80±4
MSNP	84±2

Table 8.2. Comparison of alkaline phosphatase (ALP) activity for the experimental groups after 28 days.

28-days	**ALP activity (μ.mol/min.cell)*10^{-8}**	**% compared to PPF**	**% compared to SWCNT**	**% compared to MWCNT**
SWGONR	4.62±0.12	322-357	274-309	98-141
MWGONR	4.66±0.01	335-351	304-335	104-138
GONP	5.59±0.01	423-439	364-383	145-185
BNNT	3.38±0.03	213-228	178-194	47-74
WSNT	3.68±0.11	235-265	198-227	57-93
BNNP	4.30±0.15	288-329	246-285	82-126
MSNP	4.90±0.11	349-383	299-333	111-155

Table 8.3. Comparison of calcium mineralization on different experimental groups after 28 days.

28-days	**Ca content (mg/μlit.cell)*10^{-3}**	**% compared to PPF**	**% compared to SWCNT**	**% compared to MWCNT**
SWGONR	6.73±0.11	54-63	42-54	54-63
MWGONR	7.67±0.17	75-87	61-76	75-88
GONP	7.48±0.18	70-83	56-72	70-83
BNNT	5.85±0.11	34-42	23-34	34-43
WSNT	6.19±0.05	43-49	32-41	44-50
BNNP	8.60±0.09	98-108	83-96	99-108
MSNP	8.45±0.16	93-106	78-94	94-106

8.6. Figures

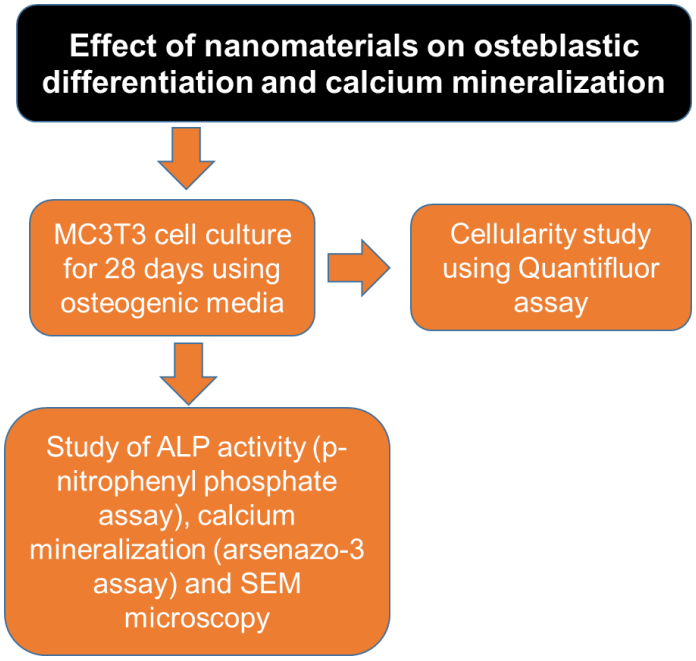

Figure 8.1.Flowchart of the experimental procedure used in this chapter.

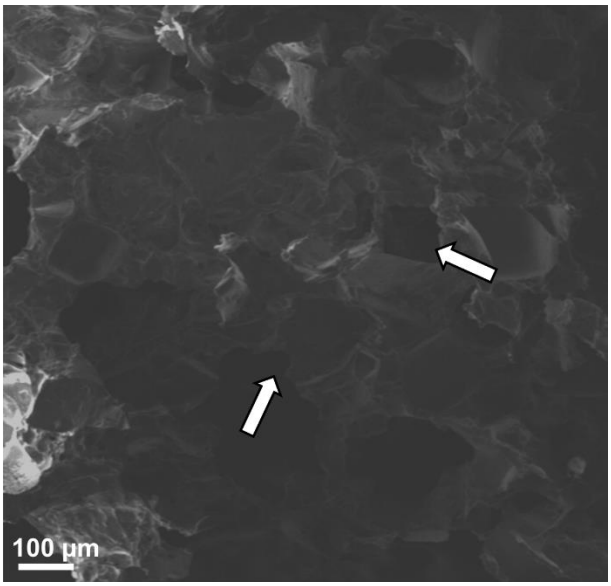

Figure 8.2. SEM image of BNNP nanocomposite scaffold (due to similarity in SEM images between experimental groups only the data related to BNNP nanocomposite is presented).

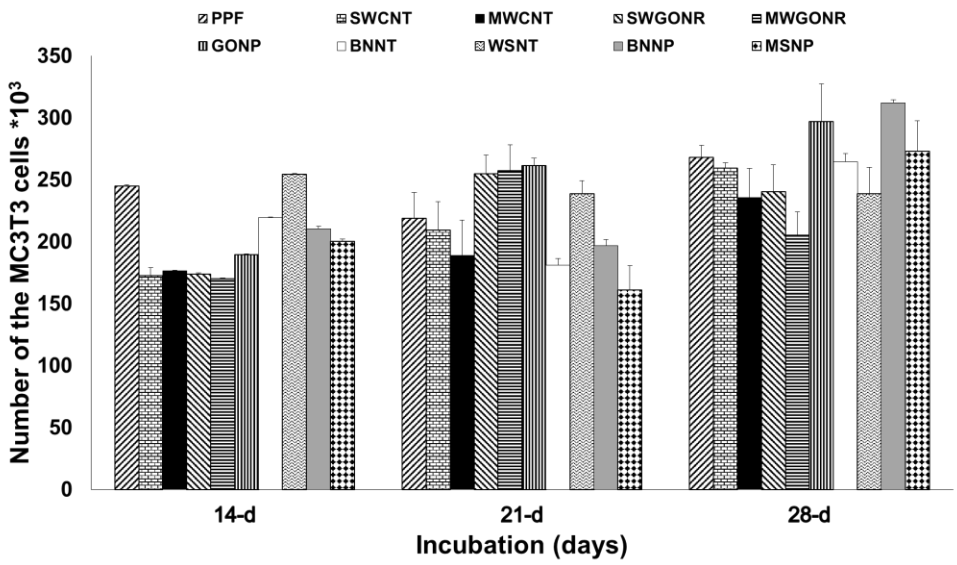

Figure 8.3. Number of viable cells on nanocomposite scaffolds and PPF baseline control detected using Quantifluor® assay. Error bars represent standard deviations for five samples (n=5).

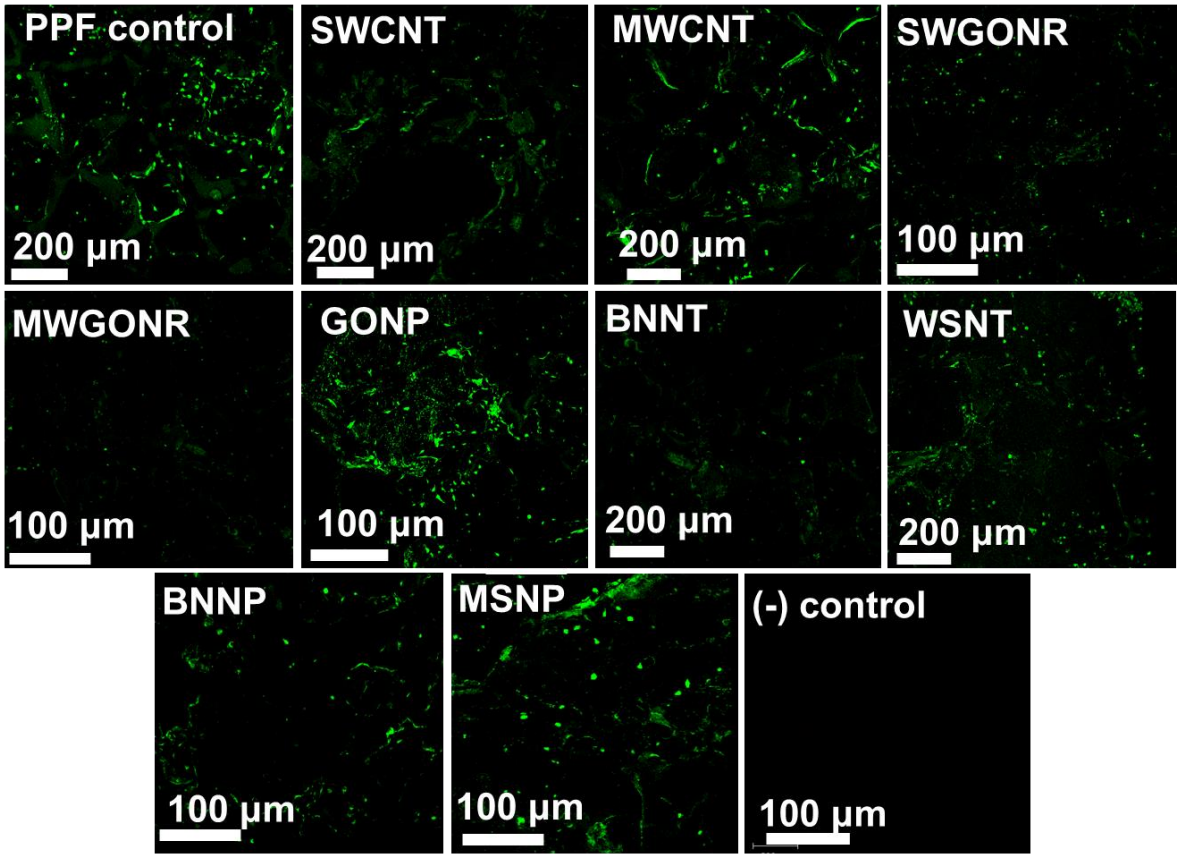

Figure 8.4. Fluorescence confocal scanning laser microscopy of MC3T3 cells on experimental samples after 14 days of incubation.

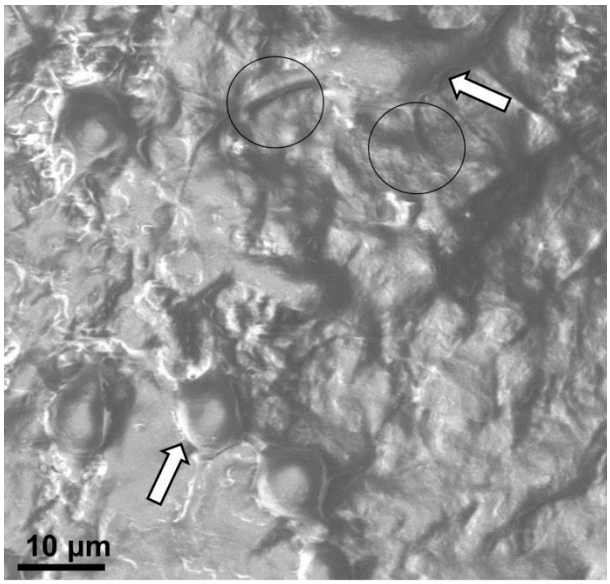

Figure 8.5. SEM image of BNNP nanocomposite scaffold after MC3T3 cell culture for 14 days (due to similarity in SEM images between experimental groups only thedata related to BNNP nanocomposite is presented).

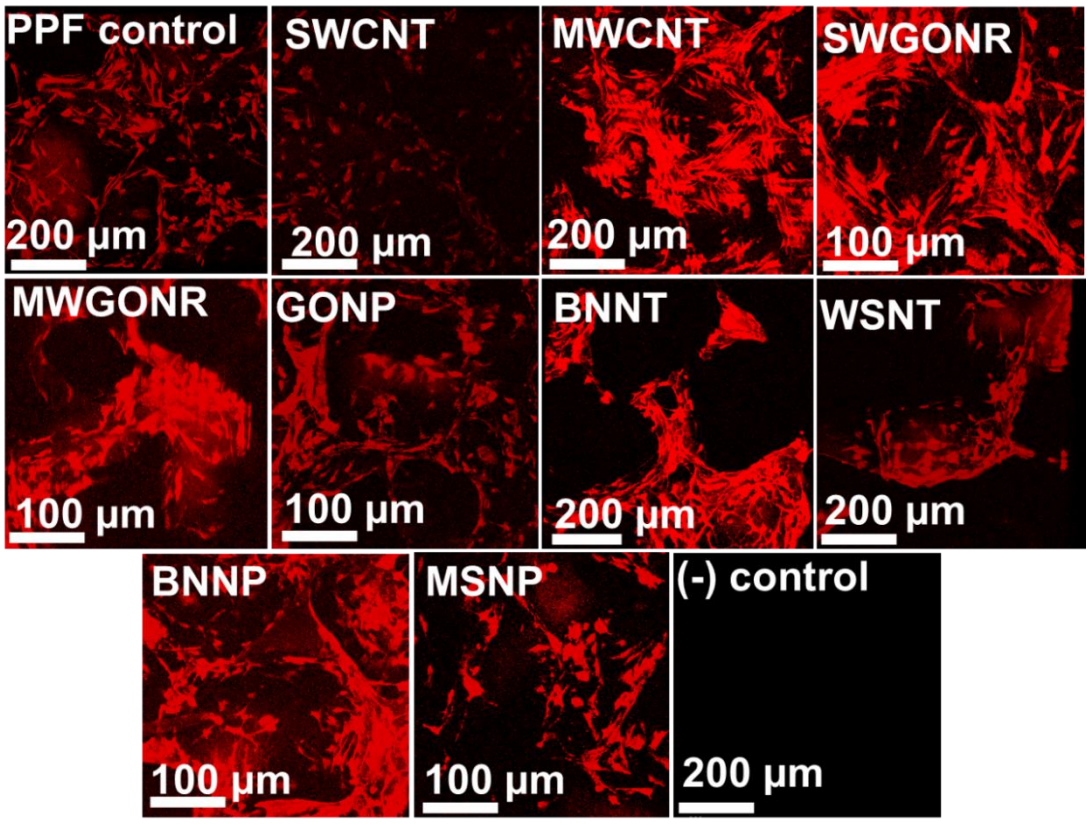

Figure 8.6. Immunohistochemistry of integrin-β1 expression on experimental groups after 14 days.

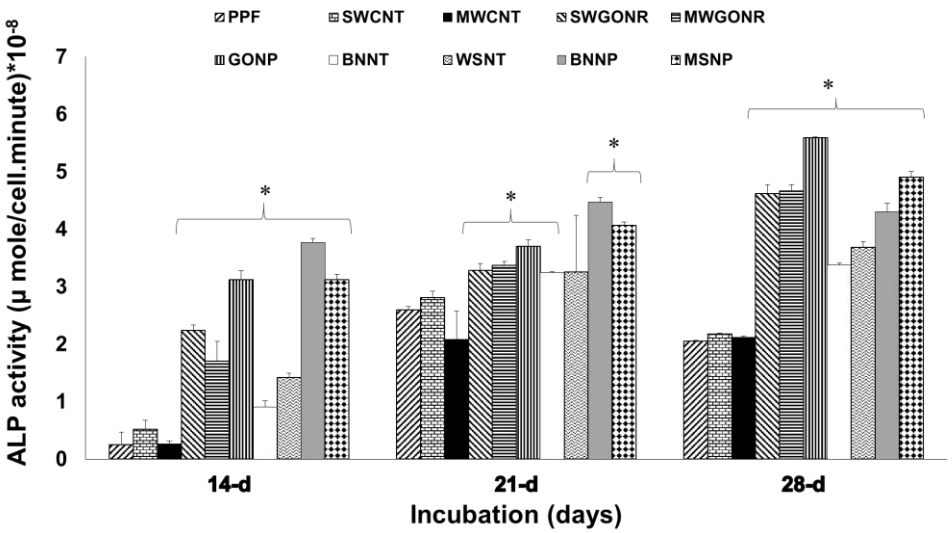

Figure 8.7. Alkaline phosphatase activity of MC3T3 cells after 14, 21 and 28 days of cell culture on experimental groups for five samples (n=5). ("*" marks the significant difference ($p<0.05$) with PPF baseline control).

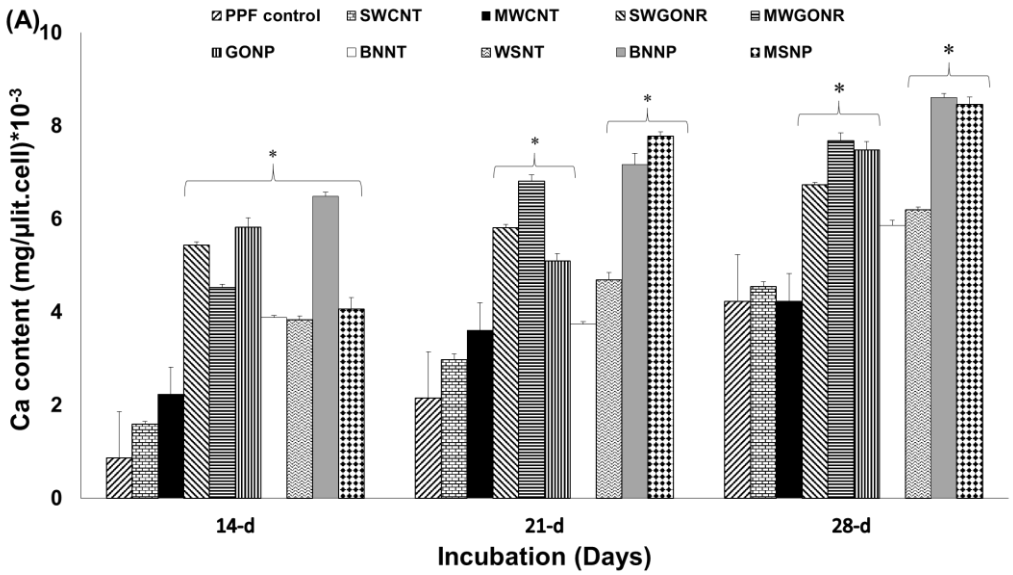

Figure 8.8.A) Calcium mineralization by MC3T3 cells after 14, 21 and 28 days of cell culture on experimental groups for five samples (n=5) ("*" marks the significant difference ($p<0.05$) with PPF baseline control) (continued on the next page).

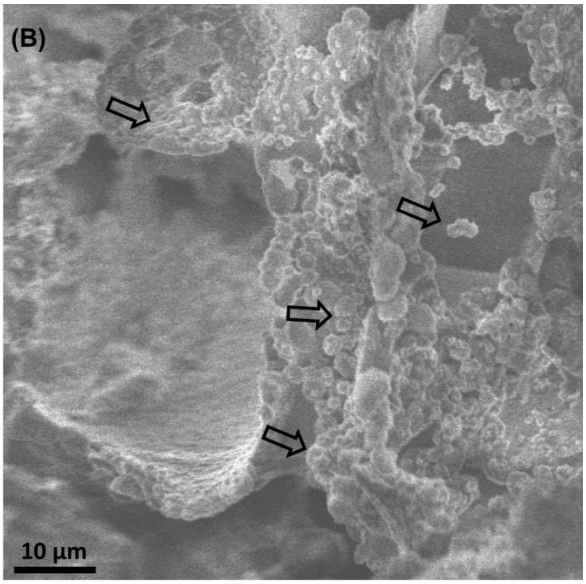

Figure 8.7.B) SEM of calcium mineralization by MC3T3 cells on BNNP nanocomposite after 28 days incubation (due to similarity of microstructures in low magnifications, only BNNP data is presented) (continued from the previous page).

Chapter 9: Summary, conclusions and suggestion for future research

9.1. Summary

In this study, we investigated the use of novel one- and two-dimensional (1-D and 2-D) organic and inorganic nanomaterials as reinforcing agents to improve the mechanical properties of PPF. The current polymeric bone tissue engineering scaffolds possess insufficient mechanical strength and metallic implants induce stress shielding. Therefore, there is a need for mechanically strong polymeric scaffolds for bone tissue engineering. In this study, we have harnessed the extraordinary physiochemical properties of 1-D and 2-D nanomaterials to address these challanges.

Nanomaterials possess high intrinsic mechanical properties and can permit multifunctional attributes such as stimulating, drug delivery and non-invasive monitoring. In this work we incorporated 1-D and 2-D inorganic and carbon nanomaterials into biodegradable and biocompatible polymers and utilize their extraordinary physical and chemical properties (such as electronic structure, extra-large surface area, high mechanical strength, surface roughness, high surface energy, high defect density and etc.) towards the fabrication of strong and biocompatible multifunctional tissue engineering nanocomposites and porous scaffolds. We have characterized the mechanical properties of nanomaterial-reinforced PPF nancomposites and scaffolds. In additional to mechanical properties, equally important is the assessment of their biological impact on the cells, therefore the *in vitro* cell response to the nanocomposites were also investigated in this research. Finally, the effects of various organic and inorganic nanomaterials on the bioactivity of PPF nancomopsites and scaffolds was investigated. The nanomaterials of

this study were graphene oxide nanoribbons (GONRs, 2-D), graphene oxide nanoplatelets (GONPs, 2-D), tungsten disulfide nanotubes (WSNTs, 1-D), boron nitride nanotubes (BNNTs, 1-D), molybdenum disulfide nanoplatelets (MSNPs, 2-D) and boron nitride nanoplatelets (BNNPs, 2-D). Poly(propylene fumarate) (PPF) polymer was used as the baseline control and carbon nanotubes (CNTs, 1-D) nanocomposites were used as positive controls for mechanical testing studies. PPF was used in this study as it is a biodegradable, biocompatible and injectable polymer widely used for bone tissue engineering research [453]

The nanomaterials used in this study have been explored for several commercial industrial and biomedical applications such as thermal barriers [124, 164], lubricants [160, 454], batteries [84, 113, 145, 167], photo catalysts [143, 166], hydrogen storage devices [99], super-capacitors [68, 83, 132, 144], sensors [86, 101, 116, 134, 148], transistors [67, 85, 100, 114], tissue engineering applications [72, 74, 119, 137, 153, 178, 179], bio-imaging [73, 87, 104, 147, 161, 170, 180] and nanomedicine [71, 88, 105, 126, 135, 149, 171, 181]. Furthermore, studies have reported mechanical properties [15, 26, 49, 90, 136, 138, 152], *in vitro* [80, 97, 110, 121, 130, 135, 154, 156, 165, 174] and *in vivo* [81, 82, 96, 109, 131, 140, 155, 195] cyto- and bio-compatibility of these nanocomposites for bone tissue engineering application. However, the results of these studies can not be compared with each other and there exist no direct investigation on the efficacy of these nanomaterials as reinforcing agents or nanocomposites for bone tissue engineering. Therefore, in this work we systematically investigated the mechanical properites and cytocompatibility of PPF nanocomposites to address this gap. We also investigated the bioactivity of these nanocomposites towards osteogenesis.

PPF was synthesized by a two-step reaction of propylene glycol and di-ethyl fumarate and nanomaterials (at a low 0.01 - 0.2 wt. % nanomaterial loading concentration) were added and

dispersed using ultrasonication. After solvent removal and crosslinking, porous and non-porous PPF nanocomposites were prepared and used for the mechanical testing and *in vitro* studies. The microstructural and chemical characterizations such as Raman spectroscopy, atomic force microscopy (AFM) and transmission electron microscopy (TEM) was used to analyze SWCNTs, MWCNTs, SWGONRs, MWGONRs, GONPs, MSNPs, WSNTs, BNNTs and BNNPs. Briefly, the results showed that synthesis of PPF polymer and nanomaterials was in agreement with literature [50, 62, 135, 195, 216-238]. A large surface area of nanomaterials, structural defects and presence of functional groups on their surface are the main factors responsible for increased mechanical properties and *in vitro* response of the nanocomposites (cytocompatibility and bioactivity). Briefly, TEM confirmed the tubular morphology for SWCNTs, MWCNTs, BNNTs and WSNTs; ribbon-like morphology for SWGONRs and MWGONRs; disc-shaped morphology for GONPs and hexagonal morphology for MSNPs and BNNPs. Raman spectroscopy clearly showed the presence of functional groups on the surface of synthesized nanomaterials. The large surface area was confirmed by Brunauer-Emmett-Teller (BET) analysis of nanomaterials (as high as 1500 m^2/g). Raman spectroscopy also showed presence of defects in the structure of nanomaterials which can lead to stronger interface between nanomaterial and polymeric network [455].

It was shown that the presence of 1-D and 2-D nanomaterials even at very low loading concentrations significantly improves the compressive and flexural strength of nonporous nanocomposites and for porous nanocomposite scaffolds. Several dependent and independent factors such as better dispersion of nanomaterials [79], increased surface energy, presence of functional groups on the surface of nanomaterials such as oxysulfide in WSNTs and MSNPs

[48], epoxides in BNNTs [456] and defects in their structure [457] contribute in the improvement of mechanical properties in polymeric nanocomposites.

The results of the mechanical tests showed a clear and consistent trend in the values of compressional and flexural modulus and yield strength for both porous and nonporous nanocomposites: MSNP > GONP > MWGONR > SWGONR > WSNT > MWCNT > SWCNT > pristine PPF. The comparisons showed that 2-D nanomaterials reinforce the mechanical properties better than 1-D nanomaterials probably due to less stress concentration in nanomaterial/polymer interface. Moreover, the nanoplatelets were better reinforcing agents than nanoribbons probably due to better dispersion and an increased interface between nanomaterial and polymeric network. On the other hand, the inorganic nanostructures of this study reinforce the PPF polymer significantly better than their carbon counterparts probably due to presence of more functional groups from synthesis on their surface and less aggregation. The increase molecular interactions at nanomaterial/polymer interface increases the crosslinking density which in turn increases the mechanical properties of polymeric nanocomposites. The results of BET analysis followed this trend: MWGONRs > SWCNTs > MWCNTs > SWGONRs > GONPs > MSNPs > WSNTs. The mechanical properties of nanocomposites also showed an inverse relationship between the aspect ratio of nanostructures and the mechanical properties of the reinforced nanocomposites: larger aspect ratio results in more stress concentration in the structures and increased the probability of crack nucleation when subjected to a mechanical load.

The sol-fraction analysis investigated the effect of nanomaterials on the crosslinking density of PPF polymer [184] with the following trend: 2-D > 1-D > PPF controls. This effects is probably due to the presence of functional groups and an increased surface area that results in a higher crosslinking density in the nanocomposites compared to pristine PPF. The surface area,

aspect ratio, sol-fraction and TEM analysis results taken together indicated nanostructure's morphology, as well as number of functional groups, and structural defects for the nanostructures are key factors affecting their mechanical properties.

The *in vitro* cytocompatibility studies using MC3T3 and NIH3T3 mammalian cell lines was performed using nanocomposites from each experimental group yielding the maximum mechanical properties. The *in vitro* cytotoxicity studies were performed before crosslinking, after crosslinking and after accelerated degradation of the nanocomposites. Our results show that the cytotoxic effects of unreacted components decreases in a dose-dependent manner by dilution, although at higher doses an acute cytotoxicity was observed. The rapid *in situ* crosslinking of PPF after injection minimizes this cytotoxicity (in agreement to the previous studies [299]). The excellent cytocompatibility of crosslinked PPF nanocomposites suggestes that an increased crosslinking density prevents the leaching of potentially toxic components (such as unreacted NVP crosslinker [310] and the remaining of BP radical initiator [311, 312]). The degradation products showed a dose-dependent cytotoxicity that decreased with gradual dilution of the media containing degradation products. Due to low nanomaterials loading concentrations, the dose-dependent cytotoxicity was more as a result of degradation products from PPF and NVP than the nanomaterials.

The excellent cell attachment and cell spreading on surface of the crosslinked nanocomposites can be attributed to an increased protein adsorption on the surface of nanocomposites due to the presence of functional groups, structural defects, increased surface roughness and increased surface energy [319, 320]. Deposition of collagen-I protein was also observed suggesting that cells on nanocomposite surfaces can form extracellular matrix (ECM).

For the porous nanocomposite scaffolds (~85% porosity), presence of the 1-D and 2-D nanomaterials led to an increase in the compressive modulus, compressive yield strength and ultimate strength compared to PPF baseline control. Although the mechanical properties were two orders of magnitude lower than their nonporous counterparts, the observed increase in the mechanical properties can be attributed to the homogenous dispersion, surface energy, surface roughness, presence of functional groups on the surface and large specific surface area for nanomaterials [48]. Similar to the mechanical properties, adsorption of collagen-I protein on porous scaffolds also followed the trend: 2-D nanocomposites > 1-D nanocomposites > PPF baseline control. The *in vitro* cytocompatibility study on the scaffolds showed no signs of cytotoxicity and confirmed presence of healthy and proliferating cells. Confocal and SEM images showed cell infiltration and spreading inside nanocomposite scaffolds. Moreover, immunohistochemistry of collagen-I expression showed that cells secrete collagen-I protein as they are attaching to the nanocomposite scaffolds. The collagen-I deposition is vital for ossification (in stages like: cell proliferation, osteoblastic differentiation and calcium mineralization) [65].

Our study showed that the increased surface roughness, surface energy and the presence of functional groups is beneficial for osteogenic differentiation and calcium mineralization. The high porosity of nanocomposite scaffolds (≥80 vol. %) provided channels for cell in-growth, nutrient exchange and transporting the wastes from MC3T3 cells. The nanocomposite scaffolds also showed the expression of integrin-β1 protein that plays an important role in osteogenic differentiation [441]. After the treatment with osteogenesis media, all of nanocomposite scaffold showed a time-dependent and higher level of ALP activity (as sign early stage osteoblastic differentiation [445]) and calcium mineralization compared to the pristine PPF. We hypothesize

that the presence of functional groups, surface energy, structural defects, high specific surface area and surface roughness increases the reactivity of nanocomposite surfaces and thus protein adsorption [65, 442, 450, 451], thereby supporting osteogenesis and deposition of calcium phosphate in the ECM. The trend for intracellular ALP activity and calcium mineralization in nanocomposite scaffolds compared to PPF baseline control was PPF baseline control < 1-D carbon nanocomposites < 1-D inorganic nanocomposites and 2-D carbon nanocomposites < 2-D inorganic nanocomposites.

To the best of our knowledge, this study is one of the first systematic studies on use of 1-D and 2-D carbon and inorganic nanomaterials towards the development of bone tissue engineering nanocomposites and scaffolds. These 1-D and 2-D nanomaterials based on their extraordinary physiochemical properties have high specific surface area, are highly dispersible in the polymeric networks, have high surface energy, contain defects in their structures and have strong atomic bonds and can be used in reinforcement of biodegradable polymeric bone grafts. Furthermore, the nanocomposites of this study showed excellent cytocompatibility and bioactivity and can be used to fabricate osteoconductive and osteoinductive nanocomposite polymeric scaffolds. Harnessing of these extraordinary properties can be beneficial in development of new class of injectable, ultra-strong, light weight, biocompatible and bioactive bone grafts. These nanostructures have been used in drug delivery, bioimaging applications and therefore can permit the development of multifunctional scaffolds with these attributes.

9.2. Conclusions

The following conclusions can be drawn from this work:

- Mixing nanomaterials in solvent, a uniform dispersion using ultrasonic waves, can be utilized to prepare porous and nonporous nanocomposite scaffolds at low concentration of nanomaterials without using dispersants.
- The nanomaterials used in this study had strong atomic bonds, large surface area, structural defects, high surface energy, and functional groups on their surface and very high mechanical strength.
- The one- and two-dimensional nanomaterials improved the mechanical properties of porous and nonporous nanocomposites even at very low loading concentrations due to their extraordinary physiochemical properties.
- These nanomaterials do not affect cytocompatibility of bone grafts.
- Cytotoxicity of non-reacted and degraded nanocomposites components is due to polymer components rather than low concentrations of nanomaterials.
- The nanomaterials improved protein adsorption on the bone grafts and, therefore, are desirable for new bone formation because they can easily interact with cells.
- The nanomaterials do not adversely affect bioactivity of the nanocomposites, in fact as a result of increased surface energy, structural defects and their surface chemistry they show a better protein adsorption and improve *in vitro* osteogenic differentiation and calcium phosphate deposition.
- The results of this study can be used to develop the next generation of strong, biodegradable biocompatible and bioactive bone grafts for bone tissue engineering applications.

- These nanocomposites can be used for drug delivery, real-time non-invasive monitoring of tissue engineering processes.
- Inorganic nanomaterials subject of this study showed better mechanical properties and *in vitro* cell response that might be related to their surface chemistry.
- Two-dimensional nanomaterials were more efficacious reinforcing agents and showed low cytotoxicity profile probably due to the increased surface area, better dispersion and more defects in their structure.

9.3. Suggestions for future work

Except for carbon nanotubes and graphene, other carbon and inorganic nanomaterials investigated in this study are new in the field of biomedical engineering. For example degradation mechanisms of most of nanomaterials used in this study except carbon nanostructures is not known. The cytotoxicity mechanisms, and effects of these nanomaterials on gene and protein expression using techniques such as western- and northern-blotting should be investigated .

As we know, the functionalization of nanomaterial have some effects on their dispersion and chemistry of their surface. Although many different functional groups such as oxy, carboxyl amine and nitrile [355, 384, 458, 459] functional groups are present on these nanomaterials, a systematic investigation of these functional groups on the mechanical properties and nanomaterial dispersion can lead to new insights. These molecular interactions can be utilized to increase the nanomaterials loading concentration that can lead to even better mechanical properties.

Another area that needs more investigation is biodegradation and biodistribution of these nanomaterials. Although *in vitro* degradation of some of alumoxane and carbon nanocomposites have been investigated [80, 301], more elaborate studies for degradation of other nanomaterials are needed. To date, only biodegradation and biodistribution of carbon nanotubes [460] and graphene [461] have been investigated.

As we know, a biodegradable bone graft is gradually being replaced by new bone. Although *in vitro* and *in vivo* degradation of nanocomposites and a change in mechanical properties during this degradation has been studied [51, 52, 197, 336, 462-464], there are a lot of

unknown factors for instance how we can control and alter the pace of biodegradation and bone tissue regeneration process. The change of mechanical properties during biodegradation requires more in-depth studies. Another interesting avenue that can be explored is controlling the degradation of nanocomposites and scaffolds by stimulating these nanomaterials using external sources.

The *in vivo* biocompatibility of the nanomaterials and nanocomposites should be studied by subcutaneous implantation on animals such as rats. The next step can be the implantation in bone sites. Moreover, bioactivity, mechanical properties during degradation, and side-effects of implanting such nanocomposites in animal models should be investigated. After preliminary *in vivo* studies, the research can be extended to large animal models and eventually can be considered for phase-1 clinical trials.

References

[1] Kasten P, Vogel J, Geiger F, Niemeyer P, Luginbühl R, Szalay K. The effect of platelet-rich plasma on healing in critical-size long-bone defects. Biomaterials. 2008;29:3983-92.

[2] Giannoudis PV, Dinopoulos H, Tsiridis E. Bone substitutes: an update. Injury. 2005;36:S20-S7.

[3] Nair LS, Laurencin CT. Biodegradable polymers as biomaterials. Progress in polymer science. 2007;32:762-98.

[4] Pal S. The Medical Device Market and Ethical Issues of Implants. Design of Artificial Human Joints & Organs: Springer; 2014. p. 377-94.

[5] Tabata Y. Biomaterial technology for tissue engineering applications. Journal of The Royal Society Interface. 2009;6:S311-S24.

[6] Hutmacher DW. Scaffolds in tissue engineering bone and cartilage. Biomaterials. 2000;21:2529-43.

[7] Bauer TW, Muschler GF. Bone graft materials: an overview of the basic science. Clinical orthopaedics and related research. 2000;371:10-27.

[8] Hollinger JO, Brekke J, Gruskin E, Lee D. Role of bone substitutes. Clinical orthopaedics and related research. 1996;324:55-65.

[9] Betz RR. Limitations of autograft and allograft: new synthetic solutions. Orthopedics. 2002;25:s561-70.

[10] Hollinger JO, Einhorn TA, Doll B, Sfeir C. Bone tissue engineering: CRC Press; 2004.

[11] International A, Davis JR. Handbook of materials for medical devices: ASM international; 2003.

[12] Puleo D, Nanci A. Understanding and controlling the bone–implant interface. Biomaterials. 1999;20:2311-21.

[13] Witte F. The history of biodegradable magnesium implants: a review. Acta Biomaterialia. 2010;6:1680-92.

[14] Hulbert S, Young F, Mathews R, Klawitter J, Talbert C, Stelling F. Potential of ceramic materials as permanently implantable skeletal prostheses. Journal of biomedical materials research. 1970;4:433-56.

[15] Seitz H, Rieder W, Irsen S, Leukers B, Tille C. Three-dimensional printing of porous ceramic scaffolds for bone tissue engineering. Journal of Biomedical Materials Research Part B: Applied Biomaterials. 2005;74:782-8.

[16] Tang Y-R, Lin D-W, Gao Y, Xu J, Guo B-H. Prominent Nucleating Effect of Finely Dispersed Hydroxyl-Functional Hexagonal Boron Nitride on Biodegradable Poly (butylene succinate). Industrial & Engineering Chemistry Research. 2014;53:4689-96.

[17] Middleton JC, Tipton AJ. Synthetic biodegradable polymers as orthopedic devices. Biomaterials. 2000;21:2335-46.

[18] Gogolewski S, Gorna K. Biodegradable polyurethane cancellous bone graft substitutes in the treatment of iliac crest defects. Journal of Biomedical Materials Research Part A. 2007;80:94-101.

[19] Shi X, Mikos AG. Poly (propylene fumarate): CRC Press: Boca Raton, FL; 2006.

[20] Shin H, Quinten Ruhe P, Mikos AG, Jansen JA. In vivo bone and soft tissue response to injectable, biodegradable oligo (poly (ethylene glycol) fumarate) hydrogels. Biomaterials. 2003;24:3201-11.

[21] Jose MV, Thomas V, Johnson KT, Dean DR, Nyairo E. Aligned PLGA/HA nanofibrous nanocomposite scaffolds for bone tissue engineering. Acta biomaterialia. 2009;5:305-15.

[22] Saito N, Okada T, Horiuchi H, Murakami N, Takahashi J, Nawata M, et al. Biodegradable poly-D, L-lactic acid-polyethylene glycol block copolymers as a BMP delivery system for inducing bone. The Journal of Bone & Joint Surgery. 2001;83:S92-S8.

[23] Koo JH. Polymer nanocomposites: McGraw-Hill Professional Pub.; 2006.

[24] Bohner M. Resorbable biomaterials as bone graft substitutes. Materials Today. 2010;13:24-30.

[25] Rezwan K, Chen Q, Blaker J, Boccaccini AR. Biodegradable and bioactive porous polymer/inorganic composite scaffolds for bone tissue engineering. Biomaterials. 2006;27:3413-31.
[26] Shi X, Sitharaman B, Pham QP, Liang F, Wu K, Edward Billups W, et al. Fabrication of porous ultra-short single-walled carbon nanotube nanocomposite scaffolds for bone tissue engineering. Biomaterials. 2007;28:4078-90.
[27] Hutmacher DW, Sittinger M, Risbud MV. Scaffold-based tissue engineering: rationale for computer-aided design and solid free-form fabrication systems. TRENDS in Biotechnology. 2004;22:354-62.
[28] Norman JJ, Desai TA. Methods for fabrication of nanoscale topography for tissue engineering scaffolds. Annals of biomedical engineering. 2006;34:89-101.
[29] Huang Z-M, Zhang Y-Z, Kotaki M, Ramakrishna S. A review on polymer nanofibers by electrospinning and their applications in nanocomposites. Composites science and technology. 2003;63:2223-53.
[30] Liu X, Ma PX. Polymeric scaffolds for bone tissue engineering. Annals of biomedical engineering. 2004;32:477-86.
[31] Taboas J, Maddox R, Krebsbach P, Hollister S. Indirect solid free form fabrication of local and global porous, biomimetic and composite 3D polymer-ceramic scaffolds. Biomaterials. 2003;24:181-94.
[32] Hutmacher DW. Scaffold design and fabrication technologies for engineering tissues—state of the art and future perspectives. Journal of Biomaterials Science, Polymer Edition. 2001;12:107-24.
[33] Ramanathan T, Abdala A, Stankovich S, Dikin D, Herrera-Alonso M, Piner R, et al. Functionalized graphene sheets for polymer nanocomposites. Nature nanotechnology. 2008;3:327-31.
[34] Zhi C, Bando Y, Shen G, Tang C, Golberg D. Boron nitride nanotubes: nanoparticles functionalization and junction fabrication. Journal of nanoscience and nanotechnology. 2007;7:530-4.
[35] Sahoo NG, Rana S, Cho JW, Li L, Chan SH. Polymer nanocomposites based on functionalized carbon nanotubes. Progress in Polymer Science. 2010;35:837-67.
[36] Mistry AS. Degradation and biocompatibility of a fumarate-based/alumoxane nanocomposite for bone tissue engineering. 2007.
[37] Wei G, Ma PX. Structure and properties of nano-hydroxyapatite/polymer composite scaffolds for bone tissue engineering. Biomaterials. 2004;25:4749-57.
[38] Schuler M, Trentin D, Textor M, Tosatti SG. Biomedical interfaces: titanium surface technology for implants and cell carriers. 2006.
[39] Hunter G, Jani SC. Prosthetic devices employing oxidized zirconium and other abrasion resistant surfaces contacting surfaces of cross-linked polyethylene. Google Patents; 2003.
[40] Guo Z, Pereira T, Choi O, Wang Y, Hahn HT. Surface functionalized alumina nanoparticle filled polymeric nanocomposites with enhanced mechanical properties. Journal of Materials Chemistry. 2006;16:2800-8.
[41] Chen Q, Miyata N, Kokubo T, Nakamura T. Bioactivity and Mechanical Properties of Poly (dimethylsiloxane)-Modified Calcia–Silica Hybrids with Added Titania. Journal of the American Ceramic Society. 2003;86:806-10.
[42] Vaia RA, Giannelis EP. Polymer nanocomposites: status and opportunities. MRS bulletin. 2001;26:394-401.
[43] Misra SK, Ohashi F, Valappil SP, Knowles JC, Roy I, Silva SRP, et al. Characterization of carbon nanotube (MWCNT) containing P (3HB)/bioactive glass composites for tissue engineering applications. Acta biomaterialia. 2010;6:735-42.
[44] Yang J, Tian M, Jia Q-X, Shi J-H, Zhang L-Q, Lim S-H, et al. Improved mechanical and functional properties of elastomer/graphite nanocomposites prepared by latex compounding. Acta Materialia. 2007;55:6372-82.
[45] Kim HW, Lee HH, Knowles J. Electrospinning biomedical nanocomposite fibers of hydroxyapatite/poly (lactic acid) for bone regeneration. Journal of Biomedical Materials Research Part A. 2006;79:643-9.

[46] MacDonald RA, Laurenzi BF, Viswanathan G, Ajayan PM, Stegemann JP. Collagen–carbon nanotube composite materials as scaffolds in tissue engineering. Journal of Biomedical Materials Research Part A. 2005;74:489-96.
[47] Lahiri D, Dua R, Zhang C, de Socarraz-Novoa I, Bhat A, Ramaswamy S, et al. Graphene nanoplatelet-induced strengthening of ultrahigh molecular weight polyethylene and biocompatibility in vitro. ACS applied materials & interfaces. 2012;4:2234-41.
[48] Ajayan PM, Tour JM. Materials science: nanotube composites. Nature. 2007;447:1066-8.
[49] Sitharaman B, Shi X, Tran LA, Spicer PP, Rusakova I, Wilson LJ, et al. Injectable in situ cross-linkable nanocomposites of biodegradable polymers and carbon nanostructures for bone tissue engineering. Journal of Biomaterials Science, Polymer Edition. 2007;18:655-71.
[50] Lalwani G, Henslee AM, Farshid B, Lin L, Kasper FK, Qin Y-X, et al. Two-Dimensional Nanostructure-Reinforced Biodegradable Polymeric Nanocomposites for Bone Tissue Engineering. Biomacromolecules. 2013;14:900-9.
[51] Jayabalan M, Shalumon K, Mitha M, Ganesan K, Epple M. Effect of hydroxyapatite on the biodegradation and biomechanical stability of polyester nanocomposites for orthopaedic applications. Acta Biomaterialia. 2010;6:763-75.
[52] Peter SJ, Miller ST, Zhu G, Yasko AW, Mikos AG. In vivo degradation of a poly (propylene fumarate)/β-tricalcium phosphate injectable composite scaffold. Journal of biomedical materials research. 1998;41:1-7.
[53] Gardiner A, Weitzel PP. Bone graft substitutes in sports medicine. Sports medicine and arthroscopy review. 2007;15:158-66.
[54] Gojny FH, Wichmann M, Köpke U, Fiedler B, Schulte K. Carbon nanotube-reinforced epoxy-composites: enhanced stiffness and fracture toughness at low nanotube content. Composites Science and Technology. 2004;64:2363-71.
[55] Zhang Y, Iijima S. Elastic response of carbon nanotube bundles to visible light. Physical review letters. 1999;82:3472.
[56] Slepyan GY, Maksimenko S, Lakhtakia A, Yevtushenko O. Electromagnetic response of carbon nanotubes and nanotube ropes. Synthetic metals. 2001;124:121-3.
[57] Lu H, Yao Y, Huang WM, Leng J, Hui D. Significantly improving infrared light-induced shape recovery behavior of shape memory polymeric nanocomposite via a synergistic effect of carbon nanotube and boron nitride. Composites Part B: Engineering. 2014;62:256-61.
[58] Meng Q, Hu J. A review of shape memory polymer composites and blends. Composites Part A: Applied Science and Manufacturing. 2009;40:1661-72.
[59] Leng J, Lan X, Liu Y, Du S. Shape-memory polymers and their composites: stimulus methods and applications. Progress in Materials Science. 2011;56:1077-135.
[60] Mather PT, Luo X, Rousseau IA. Shape memory polymer research. Annual Review of Materials Research. 2009;39:445-71.
[61] Tenne R, Redlich M. Recent progress in the research of inorganic fullerene-like nanoparticles and inorganic nanotubes. Chemical Society Reviews. 2010;39:1423-34.
[62] Lalwani G, Henslee AM, Farshid B, Parmar P, Lin L, Qin Y-X, et al. Tungsten disulfide nanotubes reinforced biodegradable polymers for bone tissue engineering. Acta Biomaterialia. 2013;9:8365-73.
[63] Wan AC, Ying JY. Nanomaterials for in situ cell delivery and tissue regeneration. Advanced drug delivery reviews. 2010;62:731-40.
[64] Kim K, Dean D, Lu A, Mikos AG, Fisher JP. Early osteogenic signal expression of rat bone marrow stromal cells is influenced by both hydroxyapatite nanoparticle content and initial cell seeding density in biodegradable nanocomposite scaffolds. Acta Biomaterialia. 2011;7:1249-64.

[65] Deligianni DD, Katsala N, Ladas S, Sotiropoulou D, Amedee J, Missirlis Y. Effect of surface roughness of the titanium alloy Ti–6Al–4V on human bone marrow cell response and on protein adsorption. Biomaterials. 2001;22:1241-51.
[66] Recum AFV, Shannon CE, Cannon CE, Long KJ, Kooten TGV, Meyle J. Surface roughness, porosity, and texture as modifiers of cellular adhesion. Tissue engineering. 1996;2:241-53.
[67] Seidel R, Graham AP, Unger E, Duesberg GS, Liebau M, Steinhoegl W, et al. High-current nanotube transistors. Nano Letters. 2004;4:831-4.
[68] Kaempgen M, Chan CK, Ma J, Cui Y, Gruner G. Printable thin film supercapacitors using single-walled carbon nanotubes. Nano letters. 2009;9:1872-6.
[69] Landi BJ, Ganter MJ, Cress CD, DiLeo RA, Raffaelle RP. Carbon nanotubes for lithium ion batteries. Energy & Environmental Science. 2009;2:638-54.
[70] Liu C, Fan Y, Liu M, Cong H, Cheng H, Dresselhaus MS. Hydrogen storage in single-walled carbon nanotubes at room temperature. Science. 1999;286:1127-9.
[71] Liu Z, Chen K, Davis C, Sherlock S, Cao Q, Chen X, et al. Drug delivery with carbon nanotubes for in vivo cancer treatment. Cancer research. 2008;68:6652-60.
[72] Lalwani G, Cai X, Nie L, Wang LV, Sitharaman B. Graphene-based contrast agents for photoacoustic and thermoacoustic tomography. Photoacoustics. 2013;1:62-7.
[73] Ananta JS, Matson ML, Tang AM, Mandal T, Lin S, Wong K, et al. Single-walled carbon nanotube materials as T 2-weighted MRI contrast agents. The Journal of Physical Chemistry C. 2009;113:19369-72.
[74] Gao G, Cagin T, Goddard III WA. Energetics, structure, mechanical and vibrational properties of single-walled carbon nanotubes. Nanotechnology. 1998;9:184.
[75] Cai X, Paratala BS, Hu S, Sitharaman B, Wang LV. Multiscale photoacoustic microscopy of single-walled carbon nanotube-incorporated tissue engineering scaffolds. Tissue Engineering Part C: Methods. 2011;18:310-7.
[76] Mitchell CA, Krishnamoorti R. Non-isothermal crystallization of in situ polymerized poly (ε-caprolactone) functionalized-SWNT nanocomposites. Polymer. 2005;46:8796-804.
[77] Tsuji H, Kawashima Y, Takikawa H, Tanaka S. Poly (L-lactide)/nano-structured carbon composites: Conductivity, thermal properties, crystallization, and biodegradation. Polymer. 2007;48:4213-25.
[78] Shi X, Hudson JL, Spicer PP, Tour JM, Krishnamoorti R, Mikos AG. Rheological behaviour and mechanical characterization of injectable poly (propylene fumarate)/single-walled carbon nanotube composites for bone tissue engineering. Nanotechnology. 2005;16:S531.
[79] Ma P-C, Siddiqui NA, Marom G, Kim J-K. Dispersion and functionalization of carbon nanotubes for polymer-based nanocomposites: a review. Composites Part A: Applied Science and Manufacturing. 2010;41:1345-67.
[80] Shi X, Sitharaman B, Pham QP, Spicer PP, Hudson JL, Wilson LJ, et al. In vitro cytotoxicity of single-walled carbon nanotube/biodegradable polymer nanocomposites. Journal of Biomedical Materials Research Part A. 2008;86:813-23.
[81] Sitharaman B, Shi X, Walboomers XF, Liao H, Cuijpers V, Wilson LJ, et al. < i> In vivo</i> biocompatibility of ultra-short single-walled carbon nanotube/biodegradable polymer nanocomposites for bone tissue engineering. Bone. 2008;43:362-70.
[82] Li X, Gao H, Uo M, Sato Y, Akasaka T, Feng Q, et al. Effect of carbon nanotubes on cellular functions in vitro. Journal of Biomedical Materials Research Part A. 2009;91:132-9.
[83] Frackowiak E, Metenier K, Bertagna V, Beguin F. Supercapacitor electrodes from multiwalled carbon nanotubes. Applied Physics Letters. 2000;77:2421-3.
[84] Yuan L, Yuan H, Qiu X, Chen L, Zhu W. Improvement of cycle property of sulfur-coated multi-walled carbon nanotubes composite cathode for lithium/sulfur batteries. Journal of Power Sources. 2009;189:1141-6.

[85] Ravindran S, Chaudhary S, Colburn B, Ozkan M, Ozkan CS. Covalent coupling of quantum dots to multiwalled carbon nanotubes for electronic device applications. Nano Letters. 2003;3:447-53.
[86] Lu G, Ocola LE, Chen J. Room-Temperature Gas Sensing Based on Electron Transfer between Discrete Tin Oxide Nanocrystals and Multiwalled Carbon Nanotubes. Advanced Materials. 2009;21:2487-91.
[87] Richard C, Doan B-T, Beloeil J-C, Bessodes M, Tóth É, Scherman D. Noncovalent functionalization of carbon nanotubes with amphiphilic Gd3+ chelates: toward powerful T1 and T2 MRI contrast agents. Nano letters. 2008;8:232-6.
[88] Yang D, Yang F, Hu J, Long J, Wang C, Fu D, et al. Hydrophilic multi-walled carbon nanotubes decorated with magnetite nanoparticles as lymphatic targeted drug delivery vehicles. Chemical Communications. 2009:4447-9.
[89] George R, Kashyap K, Rahul R, Yamdagni S. Strengthening in carbon nanotube/aluminium (CNT/Al) composites. Scripta Materialia. 2005;53:1159-63.
[90] Lin C, Wang Y, Lai Y, Yang W, Jiao F, Zhang H, et al. Incorporation of carboxylation multiwalled carbon nanotubes into biodegradable poly (lactic-co-glycolic acid) for bone tissue engineering. Colloids and Surfaces B: Biointerfaces. 2011;83:367-75.
[91] Amirian M, Chakoli AN, Sui J, Cai W. Enhanced shape memory effect of poly (L-lactide-co-ε-caprolactone) biodegradable copolymer reinforced with functionalized MWCNTs. Journal of Polymer Research. 2012;19:1-10.
[92] Feng J, Sui J, Chakoli AN, Cai W. EFFECT OF MULTI-WALLED CARBON NANOTUBES ON THE BIODEGRADABLE BEHAVIOR OF POLY (L-LACTIDE) IN VITRO. International Journal of Modern Physics B. 2009;23:1503-9.
[93] Lee S-D, Kwon O-J, Chun BC, Cho JW, Park J-S. Effects of mechanical strain on the electric conductivity of multiwalled carbon nanotube (MWCNT)/polyurethane (PU) composites. Fibers and Polymers. 2009;10:71-6.
[94] Ma PC, Kim J-K, Tang BZ. Effects of silane functionalization on the properties of carbon nanotube/epoxy nanocomposites. Composites Science and Technology. 2007;67:2965-72.
[95] Song YS, Youn JR. Influence of dispersion states of carbon nanotubes on physical properties of epoxy nanocomposites. Carbon. 2005;43:1378-85.
[96] Abarrategi A, Gutierrez MC, Moreno-Vicente C, Hortigüela MJ, Ramos V, Lopez-Lacomba JL, et al. Multiwall carbon nanotube scaffolds for tissue engineering purposes. Biomaterials. 2008;29:94-102.
[97] Sahithi K, Swetha M, Ramasamy K, Srinivasan N, Selvamurugan N. Polymeric composites containing carbon nanotubes for bone tissue engineering. International journal of biological macromolecules. 2010;46:281-3.
[98] Supronowicz P, Ajayan P, Ullmann K, Arulanandam B, Metzger D, Bizios R. Novel current-conducting composite substrates for exposing osteoblasts to alternating current stimulation. Journal of Biomedical Materials Research. 2002;59:499-506.
[99] Baierle RJ, Piquini P, Schmidt TM, Fazzio A. Hydrogen adsorption on carbon-doped boron nitride nanotube. The Journal of Physical Chemistry B. 2006;110:21184-8.
[100] Hao S, Zhou G, Duan W, Wu J, Gu B-L. Tremendous spin-splitting effects in open boron nitride nanotubes: application to nanoscale spintronic devices. Journal of the American Chemical Society. 2006;128:8453-8.
[101] Yum K, Yu M-F. Measurement of wetting properties of individual boron nitride nanotubes with the Wilhelmy method using a nanotube-based force sensor. Nano letters. 2006;6:329-33.
[102] Huang Q, Bando Y, Zhao L, Zhi C, Golberg D. pH sensor based on boron nitride nanotubes. Nanotechnology. 2009;20:415501.
[103] Chowdhury R, Adhikari S. Boron-nitride nanotubes as zeptogram-scale bionanosensors: Theoretical investigations. Nanotechnology, IEEE Transactions on. 2011;10:659-67.

[104] Menichetti L, De Marchi D, Calucci L, Ciofani G, Menciassi A, Forte C. Boron nitride nanotubes for boron neutron capture therapy as contrast agents in magnetic resonance imaging at 3T. Applied Radiation and Isotopes. 2011;69:1725-7.
[105] Ciofani G, Raffa V, Yu J, Chen Y, Obata Y, Takeoka S, et al. Boron nitride nanotubes: a novel vector for targeted magnetic drug delivery. Current nanoscience. 2009;5:33-8.
[106] Vaccarini L, Goze C, Henrard L, Hernandez E, Bernier P, Rubio A. Mechanical and electronic properties of carbon and boron–nitride nanotubes. Carbon. 2000;38:1681-90.
[107] Ricotti L, das Neves RP, Ciofani G, Canale C, Nitti S, Mattoli V, et al. Boron nitride nanotube-mediated stimulation modulates F/G-actin ratio and mechanical properties of human dermal fibroblasts. Journal of nanoparticle research. 2014;16:1-14.
[108] Bansal NP, Hurst JB, Choi SR. Boron Nitride Nanotubes-Reinforced Glass Composites. Journal of the American Ceramic Society. 2006;89:388-90.
[109] Ciofani G, Danti S, Nitti S, Mazzolai B, Mattoli V, Giorgi M. Biocompatibility of boron nitride nanotubes: An up-date of< i> in vivo</i> toxicological investigation. International journal of pharmaceutics. 2013;444:85-8.
[110] Li X, Cui R, Liu W, Sun L, Yu B, Fan Y, et al. The use of nanoscaled fibers or tubes to improve biocompatibility and bioactivity of biomedical materials. Journal of Nanomaterials. 2013;2013:14.
[111] Huang X, Zhi C, Jiang P, Golberg D, Bando Y, Tanaka T. Polyhedral Oligosilsesquioxane-Modified Boron Nitride Nanotube Based Epoxy Nanocomposites: An Ideal Dielectric Material with High Thermal Conductivity. Advanced Functional Materials. 2013;23:1824-31.
[112] Danti S, Ciofani G, Moscato S, D'Alessandro D, Ciabatti E, Nesti C, et al. Boron nitride nanotubes and primary human osteoblasts: in vitro compatibility and biological interactions under low frequency ultrasound stimulation. Nanotechnology. 2013;24:465102.
[113] Wang G, Bewlay S, Yao J, Liu H, Dou S. Tungsten disulfide nanotubes for lithium storage. Electrochemical and solid-state letters. 2004;7:A321-A3.
[114] Nagapriya K, Goldbart O, Kaplan-Ashiri I, Seifert G, Tenne R, Joselevich E. Torsional stick-slip behavior in WS 2 nanotubes. Physical review letters. 2008;101:195501.
[115] Prasad S, Zabinski J. Lubricants: super slippery solids. Nature. 1997;387:761-3.
[116] Huang K-J, Liu Y-J, Cao J-T, Wang H-B. An aptamer electrochemical assay for sensitive detection of immunoglobulin E based on tungsten disulfide–graphene composites and gold nanoparticles. RSC Advances. 2014;4:36742-8.
[117] Rapoport L, Fleischer N, Tenne R. Fullerene-like WS2 Nanoparticles: Superior Lubricants for Harsh Conditions. Advanced Materials. 2003;15:651-5.
[118] Zhu YQ, Sekine T, Li YH, Fay MW, Zhao YM, Patrick Poa C, et al. Shock-absorbing and failure mechanisms of WS2 and MoS2 nanoparticles with fullerene-like structures under shock wave pressure. Journal of the American Chemical Society. 2005;127:16263-72.
[119] Wang W, Liao S, Liu M, Zhao Q, Zhu Y. Polymer Composites Reinforced by Nanotubes as Scaffolds for Tissue Engineering. International Journal of Polymer Science. 2014;2014.
[120] Díez-Pascual AM, Naffakh M, Marco C, Ellis G. Rheological and tribological properties of carbon nanotube/thermoplastic nanocomposites incorporating inorganic fullerene-like WS2 nanoparticles. The Journal of Physical Chemistry B. 2012;116:7959-69.
[121] Goldman EB, Zak A, Tenne R, Kartvelishvily E, Levin-Zaidman S, Neumann Y, et al. Biocompatibility of Tungsten Disulfide Inorganic Nanotubes and Fullerene-Like Nanoparticles with Salivary Gland Cells. Tissue Engineering Part A. 2014.
[122] Lu G, Scudder H, Kioussis N. Hydrogen-induced unzipping of single-walled carbon nanotubes. Physical Review B. 2003;68:205416.
[123] Kosynkin DV, Higginbotham AL, Sinitskii A, Lomeda JR, Dimiev A, Price BK, et al. Longitudinal unzipping of carbon nanotubes to form graphene nanoribbons. Nature. 2009;458:872-6.

[124] Kosynkin DV, Lu W, Sinitskii A, Pera G, Sun Z, Tour JM. Highly conductive graphene nanoribbons by longitudinal splitting of carbon nanotubes using potassium vapor. ACS nano. 2011;5:968-74.
[125] Eda G, Fanchini G, Chhowalla M. Large-area ultrathin films of reduced graphene oxide as a transparent and flexible electronic material. Nature nanotechnology. 2008;3:270-4.
[126] Liu Z, Robinson JT, Sun X, Dai H. PEGylated nanographene oxide for delivery of water-insoluble cancer drugs. Journal of the American Chemical Society. 2008;130:10876-7.
[127] Zhao H, Min K, Aluru N. Size and chirality dependent elastic properties of graphene nanoribbons under uniaxial tension. Nano letters. 2009;9:3012-5.
[128] Bortz DR, Heras EG, Martin-Gullon I. Impressive fatigue life and fracture toughness improvements in graphene oxide/epoxy composites. Macromolecules. 2011;45:238-45.
[129] Terrones M, Botello-Méndez AR, Campos-Delgado J, López-Urías F, Vega-Cantú YI, Rodríguez-Macías FJ, et al. Graphene and graphite nanoribbons: Morphology, properties, synthesis, defects and applications. Nano Today. 2010;5:351-72.
[130] Tian B, Wang C, Zhang S, Feng L, Liu Z. Photothermally enhanced photodynamic therapy delivered by nano-graphene oxide. Acs Nano. 2011;5:7000-9.
[131] Akhavan O, Ghaderi E, Emamy H. Nontoxic concentrations of PEGylated graphene nanoribbons for selective cancer cell imaging and photothermal therapy. Journal of Materials Chemistry. 2012;22:20626-33.
[132] Wang H, Wang Y, Hu Z, Wang X. Cutting and unzipping multiwalled carbon nanotubes into curved graphene nanosheets and their enhanced supercapacitor performance. ACS applied materials & interfaces. 2012;4:6827-34.
[133] Zhang Z, Sun Z, Yao J, Kosynkin DV, Tour JM. Transforming carbon nanotube devices into nanoribbon devices. Journal of the American Chemical Society. 2009;131:13460-3.
[134] Dong X, Long Q, Wang J, Chan-Park MB, Huang Y, Huang W, et al. A graphene nanoribbon network and its biosensing application. Nanoscale. 2011;3:5156-60.
[135] Mullick Chowdhury S, Lalwani G, Zhang K, Yang JY, Neville K, Sitharaman B. Cell specific cytotoxicity and uptake of graphene nanoribbons. Biomaterials. 2013;34:283-93.
[136] Wang Y, Shi Z, Yin J. Unzipped multiwalled carbon nanotubes for mechanical reinforcement of polymer composites. The Journal of Physical Chemistry C. 2010;114:19621-8.
[137] Yoon OJ, Jung CY, Sohn IY, Kim HJ, Hong B, Jhon MS, et al. Nanocomposite nanofibers of poly (d, l-lactic-co-glycolic acid) and graphene oxide nanosheets. Composites Part A: Applied Science and Manufacturing. 2011;42:1978-84.
[138] Chen X, Chen X, Lin M, Zhong W, Chen X, Chen Z. Functionalized Multi-Walled Carbon Nanotubes Prepared by In Situ Polycondensation of Polyurethane. Macromolecular Chemistry and Physics. 2007;208:964-72.
[139] Neffe AT, Hanh BD, Steuer S, Lendlein A. Polymer networks combining controlled drug release, biodegradation, and shape memory capability. Advanced Materials. 2009;21:3394-8.
[140] Zhang X, Yin J, Peng C, Hu W, Zhu Z, Li W, et al. Distribution and biocompatibility studies of graphene oxide in mice after intravenous administration. Carbon. 2011;49:986-95.
[141] Tung VC, Allen MJ, Yang Y, Kaner RB. High-throughput solution processing of large-scale graphene. Nature nanotechnology. 2008;4:25-9.
[142] Hummers Jr WS, Offeman RE. Preparation of graphitic oxide. Journal of the American Chemical Society. 1958;80:1339-.
[143] Akhavan O, Ghaderi E. Photocatalytic reduction of graphene oxide nanosheets on TiO2 thin film for photoinactivation of bacteria in solar light irradiation. The Journal of Physical Chemistry C. 2009;113:20214-20.
[144] Stoller MD, Park S, Zhu Y, An J, Ruoff RS. Graphene-based ultracapacitors. Nano letters. 2008;8:3498-502.

[145] Han P, Wang H, Liu Z, Chen X, Ma W, Yao J, et al. Graphene oxide nanoplatelets as excellent electrochemical active materials for VO 2+/and V 2+/V 3+ redox couples for a vanadium redox flow battery. Carbon. 2011;49:693-700.
[146] Becerril HA, Mao J, Liu Z, Stoltenberg RM, Bao Z, Chen Y. Evaluation of solution-processed reduced graphene oxide films as transparent conductors. ACS nano. 2008;2:463-70.
[147] Kanakia S, Toussaint JD, Chowdhury SM, Lalwani G, Tembulkar T, Button T, et al. Physicochemical characterization of a novel graphene-based magnetic resonance imaging contrast agent. International journal of nanomedicine. 2013;8:2821.
[148] Dong H, Gao W, Yan F, Ji H, Ju H. Fluorescence resonance energy transfer between quantum dots and graphene oxide for sensing biomolecules. Analytical chemistry. 2010;82:5511-7.
[149] Chowdhury SM, Kanakia S, Toussaint JD, Frame MD, Dewar AM, Shroyer KR, et al. In Vitro Hematological and In Vivo Vasoactivity Assessment of Dextran Functionalized Graphene. Scientific reports. 2013;3.
[150] Gómez-Navarro C, Weitz RT, Bittner AM, Scolari M, Mews A, Burghard M, et al. Electronic transport properties of individual chemically reduced graphene oxide sheets. Nano letters. 2007;7:3499-503.
[151] Kim H, Abdala AA, Macosko CW. Graphene/polymer nanocomposites. Macromolecules. 2010;43:6515-30.
[152] Fan H, Wang L, Zhao K, Li N, Shi Z, Ge Z, et al. Fabrication, mechanical properties, and biocompatibility of graphene-reinforced chitosan composites. Biomacromolecules. 2010;11:2345-51.
[153] Pinto AM, Moreira S, Gonçalves IC, Gama FM, Mendes AM, Magalhães FD. Biocompatibility of poly (lactic acid) with incorporated graphene-based materials. Colloids and Surfaces B: Biointerfaces. 2013;104:229-38.
[154] Wu S, Zhao X, Cui Z, Zhao C, Wang Y, Du L, et al. Cytotoxicity of graphene oxide and graphene oxide loaded with doxorubicin on human multiple myeloma cells. International journal of nanomedicine. 2014;9:1413.
[155] Zhan L, Yanxia G, Xiaoyong Z, Wei Q, Qiaohui F, Yan L, et al. Biodistribution of co-exposure to multi-walled carbon nanotubes and graphene oxide nanoplatelets radiotracers. Journal of Nanoparticle Research. 2011;13:2939-47.
[156] Bressan E, Ferroni L, Gardin C, Sbricoli L, Gobbato L, Ludovichetti FS, et al. Graphene based scaffolds effects on stem cells commitment. Journal of translational medicine. 2014;12:296.
[157] Warner JH, Rummeli MH, Bachmatiuk A, Büchner B. Atomic resolution imaging and topography of boron nitride sheets produced by chemical exfoliation. ACS nano. 2010;4:1299-304.
[158] Zhi C, Bando Y, Tang C, Kuwahara H, Golberg D. Large-scale fabrication of boron nitride nanosheets and their utilization in polymeric composites with improved thermal and mechanical properties. Advanced Materials. 2009;21:2889-93.
[159] Dean C, Young A, Meric I, Lee C, Wang L, Sorgenfrei S, et al. Boron nitride substrates for high-quality graphene electronics. Nature nanotechnology. 2010;5:722-6.
[160] Cho D-H, Kim J-S, Kwon S-H, Lee C, Lee Y-Z. Evaluation of hexagonal boron nitride nano-sheets as a lubricant additive in water. Wear. 2013;302:981-6.
[161] Lin L, Xu Y, Zhang S, Ross IM, Ong A, Allwood DA. Fabrication and Luminescence of Monolayered Boron Nitride Quantum Dots. Small. 2014;10:60-5.
[162] Wang Q, Wang W, Lei J, Xu N, Gao F, Ju H. Fluorescence Quenching of Carbon Nitride Nanosheet through Its Interaction with DNA for Versatile Fluorescence Sensing. Analytical chemistry. 2013;85:12182-8.
[163] Boldrin L, Scarpa F, Chowdhury R, Adhikari S. Effective mechanical properties of hexagonal boron nitride nanosheets. Nanotechnology. 2011;22:505702.

[164] Yu J, Huang X, Wu C, Wu X, Wang G, Jiang P. Interfacial modification of boron nitride nanoplatelets for epoxy composites with improved thermal properties. Polymer. 2012;53:471-80.
[165] Weng Q, Wang B, Wang X, Hanagata N, Li X, Liu D, et al. Highly Water-Soluble, Porous and Biocompatible Boron Nitrides for Anticancer Drug Delivery. ACS nano. 2014.
[166] Lukowski MA, Daniel AS, Meng F, Forticaux A, Li L, Jin S. Enhanced Hydrogen Evolution Catalysis from Chemically Exfoliated Metallic MoS2 Nanosheets. Journal of the American Chemical Society. 2013;135:10274-7.
[167] Xiao J, Choi D, Cosimbescu L, Koech P, Liu J, Lemmon JP. Exfoliated MoS2 nanocomposite as an anode material for lithium ion batteries. Chemistry of Materials. 2010;22:4522-4.
[168] Lee K, Gatensby R, McEvoy N, Hallam T, Duesberg GS. High-Performance Sensors Based on Molybdenum Disulfide Thin Films. Advanced Materials. 2013;25:6699-702.
[169] Lee K, Kim HY, Lotya M, Coleman JN, Kim GT, Duesberg GS. Electrical characteristics of molybdenum disulfide flakes produced by liquid exfoliation. Advanced Materials. 2011;23:4178-82.
[170] Chou SS, De M, Kim J, Byun S, Dykstra C, Yu J, et al. Ligand conjugation of chemically exfoliated MoS2. Journal of the American Chemical Society. 2013;135:4584-7.
[171] Wang N, Wei F, Qi Y, Li H, Lu X, Zhao G, et al. Synthesis of Strongly Fluorescent Molybdenum Disulfide Nanosheets for Cell-targeted Labelling. ACS applied materials & interfaces. 2014.
[172] Hu KH, Hu XG, Sun XJ. Morphological effect of MoS 2 nanoparticles on catalytic oxidation and vacuum lubrication. Applied Surface Science. 2010;256:2517-23.
[173] Feng X, Wang X, Xing W, Zhou K, Song L, Hu Y. Liquid-exfoliated MoS 2 by chitosan and enhanced mechanical and thermal properties of chitosan/MoS 2 composites. Composites Science and Technology. 2014;93:76-82.
[174] Wu H, Yang R, Song B, Han Q, Li J, Zhang Y, et al. Biocompatible inorganic fullerene-like molybdenum disulfide nanoparticles produced by pulsed laser ablation in water. ACS nano. 2011;5:1276-81.
[175] Kasper FK, Tanahashi K, Fisher JP, Mikos AG. Synthesis of poly (propylene fumarate). Nature protocols. 2009;4:518-25.
[176] Haesslein A, Ueda H, Hacker MC, Jo S, Ammon DM, Borazjani RN, et al. Long-term release of fluocinolone acetonide using biodegradable fumarate-based polymers. Journal of Controlled Release. 2006;114:251-60.
[177] Fisher JP, Vehof JW, Dean D, van der Waerden JP, Holland TA, Mikos AG, et al. Soft and hard tissue response to photocrosslinked poly (propylene fumarate) scaffolds in a rabbit model. Journal of biomedical materials research. 2002;59:547-56.
[178] Temenoff JS, Mikos AG. Injectable biodegradable materials for orthopedic tissue engineering. Biomaterials. 2000;21:2405-12.
[179] Drury JL, Mooney DJ. Hydrogels for tissue engineering: scaffold design variables and applications. Biomaterials. 2003;24:4337-51.
[180] Avti PK, Hu S, Favazza C, Mikos AG, Jansen JA, Shroyer KR, et al. Detection, mapping, and quantification of single walled carbon nanotubes in histological specimens with photoacoustic microscopy. PloS one. 2012;7:e35064.
[181] Kretlow JD, Klouda L, Mikos AG. Injectable matrices and scaffolds for drug delivery in tissue engineering. Advanced drug delivery reviews. 2007;59:263-73.
[182] Yang SH, Hong D, Lee J, Ko EH, Choi IS. Artificial spores: cytocompatible encapsulation of individual living cells within thin, tough artificial shells. Small. 2013;9:178-86.
[183] Weber S, Halm S, Du Vall M, Whitney K, Blaich G, Bury D. N-vinylpyrrolidone dimer (VPD), a novel excipient for oral drugs: Repeat-dose oral toxicity in Sprague–Dawley rats. Toxicology Letters. 2012;210:324-31.

[184] Shi X, Hudson JL, Spicer PP, Tour JM, Krishnamoorti R, Mikos AG. Injectable nanocomposites of single-walled carbon nanotubes and biodegradable polymers for bone tissue engineering. Biomacromolecules. 2006;7:2237-42.
[185] Hilborn J. In vivo injectable gels for tissue repair. Wiley Interdisciplinary Reviews: Nanomedicine and Nanobiotechnology. 2011;3:589-606.
[186] Hakimi Mehr D. Biomimetic synthesis of poly (propylene-fumarate)-calcium phosphate composites for tissue engineering2006.
[187] Hakimimehr D, Liu D-M, Troczynski T. In-situ preparation of poly (propylene fumarate)—hydroxyapatite composite. Biomaterials. 2005;26:7297-303.
[188] Puppi D, Chiellini F, Piras A, Chiellini E. Polymeric materials for bone and cartilage repair. Progress in Polymer Science. 2010;35:403-40.
[189] Hesaraki S, Alizadeh M, Borhan S, Pourbaghi-Masouleh M. Polymerizable nanoparticulate silica-reinforced calcium phosphate bone cement. Journal of Biomedical Materials Research Part B: Applied Biomaterials. 2012;100:1627-35.
[190] Salarian M, Xu WZ, Biesinger MC, Charpentier PA. Synthesis and characterization of novel TiO 2-poly (propylene fumarate) nanocomposites for bone cementation. Journal of Materials Chemistry B. 2014;2:5145-56.
[191] Kim H-W, Shin S-Y, Kim H-E, Lee Y-M, Chung C-P, Lee H-H, et al. Bone formation on the apatite-coated zirconia porous scaffolds within a rabbit calvarial defect. Journal of biomaterials applications. 2007.
[192] Mistry AS, Cheng SH, Yeh T, Christenson E, Jansen JA, Mikos AG. Fabrication and in vitro degradation of porous fumarate-based polymer/alumoxane nanocomposite scaffolds for bone tissue engineering. Journal of Biomedical Materials Research Part A. 2009;89:68-79.
[193] Derakhshan AA, Rajabi L. Review on applications of carboxylate–alumoxane nanostructures. Powder Technology. 2012;226:117-29.
[194] Mistry AS, Pham QP, Schouten C, Yeh T, Christenson EM, Mikos AG, et al. In vivo bone biocompatibility and degradation of porous fumarate-based polymer/alumoxane nanocomposites for bone tissue engineering. Journal of Biomedical Materials Research Part A. 2010;92A:451-62.
[195] Sitharaman B, Shi X, Walboomers XF, Liao H, Cuijpers V, Wilson LJ, et al. In vivo biocompatibility of ultra-short single-walled carbon nanotube/biodegradable polymer nanocomposites for bone tissue engineering. Bone. 2008;43:362-70.
[196] Horch RA, Shahid N, Mistry AS, Timmer MD, Mikos AG, Barron AR. Nanoreinforcement of Poly(propylene fumarate)-Based Networks with Surface Modified Alumoxane Nanoparticles for Bone Tissue Engineering. Biomacromolecules. 2004;5:1990-8.
[197] Mistry A, Mikos A, Jansen J. Degradation and biocompatibility of a poly (propylene fumarate)-based/alumoxane nanocomposite for bone tissue engineering. Journal of Biomedical Materials Research Part A. 2007;83:940-53.
[198] Kokubo T, Kim H-M, Kawashita M. Novel bioactive materials with different mechanical properties. Biomaterials. 2003;24:2161-75.
[199] Hyers R, SanSoucie M. Porous calcium phosphate networks for synthetic bone material. Google Patents; 2010.
[200] Pelker RR, Friedlaender GE, Markham TC. Biomechanical properties of bone allografts. Clinical orthopaedics and related research. 1983;174:54-7.
[201] Chen T, Zeng B, Liu J, Dong J, Liu X, Wu Z, et al. High throughput exfoliation of graphene oxide from expanded graphite with assistance of strong oxidant in modified Hummers method. Journal of Physics: Conference Series: IOP Publishing; 2009. p. 012051.

[202] Castro-Guerrero CF, Deepak FL, Ponce A, Cruz-Reyes J, Del Valle-Granados M, Fuentes-Moyado S, et al. Structure and catalytic properties of hexagonal molybdenum disulfide nanoplates. Catalysis Science & Technology. 2011;1:1024-31.
[203] Standard A. D695-08. Standard Test Method for Compressive Properties of Rigid Plastics, USA. 2008.
[204] Standard A. D790-07: Standard Test Method for Flexural Properties of Unreinforced and Reinforced Plastics and Electrical Insulation Materials. American Society for Testing and Materials1997.
[205] Standard A. D695–02a. Standard Test Method for Compressive Properties of Rigid Plastics, American Society for Testing and Materials.
[206] Cornelius RM, Wojciechowski PW, Brash JL. Measurement of protein adsorption kinetics by an< i> in situ</i>,“real-time,” solution depletion technique. Journal of colloid and interface science. 1992;150:121-33.
[207] Walker JM. The bicinchoninic acid (BCA) assay for protein quantitation. The Protein Protocols Handbook: Springer; 2009. p. 11-5.
[208] Boncler M, Różalski M, Krajewska U, Podsędek A, Watala C. Comparison of PrestoBlue and MTT assays of cellular viability in the assessment of anti-proliferative effects of plant extracts on human endothelial cells. Journal of Pharmacological and Toxicological Methods. 2014;69:9-16.
[209] Decker T, Lohmann-Matthes M-L. A quick and simple method for the quantitation of lactate dehydrogenase release in measurements of cellular cytotoxicity and tumor necrosis factor (TNF) activity. Journal of Immunological Methods. 1988;115:61-9.
[210] Wallin R, Arscott E. A practical guide to ISO 10993-5: Cytotoxicity. MEDICAL DEVICE AND DIAGNOSTIC INDUSTRY. 1998;20:96-8.
[211] Bünger C, Jahnke A, Stange J, De Vos P, Hopt U. MTS Colorimetric Assay in Combination with a Live-Dead Assay for Testing Encapsulated L929 Fibroblasts in Alginate Poly-l-Lysine Microcapsules In Vitro. Artificial organs. 2002;26:111-6.
[212] Thorwarth M, Rupprecht S, Falk S, Felszeghy E, Wiltfang J, Schlegel K. Expression of bone matrix proteins during de novo bone formation using a bovine collagen and platelet-rich plasma (prp)—an immunohistochemical analysis. Biomaterials. 2005;26:2575-84.
[213] Salasznyk RM, Williams WA, Boskey A, Batorsky A, Plopper GE. Adhesion to vitronectin and collagen I promotes osteogenic differentiation of human mesenchymal stem cells. BioMed Research International. 2004;2004:24-34.
[214] Marascuilo LA, McSweeney M. Nonparametric post hoc comparisons for trend. Psychological Bulletin. 1967;67:401.
[215] Stankovich S, Dikin DA, Piner RD, Kohlhaas KA, Kleinhammes A, Jia Y, et al. Synthesis of graphene-based nanosheets via chemical reduction of exfoliated graphite oxide. Carbon. 2007;45:1558-65.
[216] Stankovich S, Piner RD, Nguyen ST, Ruoff RS. Synthesis and exfoliation of isocyanate-treated graphene oxide nanoplatelets. Carbon. 2006;44:3342-7.
[217] Malard L, Pimenta M, Dresselhaus G, Dresselhaus M. Raman spectroscopy in graphene. Physics Reports. 2009;473:51-87.
[218] Cançado L, Pimenta M, Neves B, Medeiros-Ribeiro G, Enoki T, Kobayashi Y, et al. Anisotropy of the Raman spectra of nanographite ribbons. Physical review letters. 2004;93:047403.
[219] Dresselhaus M, Dresselhaus G, Jorio A, Souza Filho A, Saito R. Raman spectroscopy on isolated single wall carbon nanotubes. Carbon. 2002;40:2043-61.
[220] Hasi F, Simon F, Kuzmany H, Concha R, Loiseau A. Raman Spectroscopy Of Boron Nitride Nanotubes And Boron Nitride- Carbon Composites. Electronic Properties of Novel Nanostructures. 2005;786:340-4.
[221] Song L, Ci L, Lu H, Sorokin PB, Jin C, Ni J, et al. Large scale growth and characterization of atomic hexagonal boron nitride layers. Nano letters. 2010;10:3209-15.

[222] Bar-Sadan M, Enyashin A, Gemming S, Popovitz-Biro R, Hong S, Prior Y, et al. Structure and stability of molybdenum sulfide fullerenes. The Journal of Physical Chemistry B. 2006;110:25399-410.
[223] Rothschild A, Frey G, Homyonfer M, Tenne R, Rappaport M. Synthesis of bulk WS2 nanotube phases. Material Research Innovations. 1999;3:145-9.
[224] Lalwani G, Kwaczala AT, Kanakia S, Patel SC, Judex S, Sitharaman B. Fabrication and characterization of three-dimensional macroscopic all-carbon scaffolds. Carbon. 2013;53:90-100.
[225] Kong J, Soh HT, Cassell AM, Quate CF, Dai H. Synthesis of individual single-walled carbon nanotubes on patterned silicon wafers. Nature. 1998;395:878-81.
[226] Saito T, Matsushige K, Tanaka K. Chemical treatment and modification of multi-walled carbon nanotubes. Physica B: Condensed Matter. 2002;323:280-3.
[227] Sun X, Liu Z, Welsher K, Robinson JT, Goodwin A, Zaric S, et al. Nano-graphene oxide for cellular imaging and drug delivery. Nano research. 2008;1:203-12.
[228] Higginbotham AL, Kosynkin DV, Sinitskii A, Sun Z, Tour JM. Lower-defect graphene oxide nanoribbons from multiwalled carbon nanotubes. ACS nano. 2010;4:2059-69.
[229] Zhang Q, Xu Z, Li H, Wu L, Cao G, Li K. Synthesis of MoS2 Nanosheets by Solid-State Reaction in CVD Furnace. Integrated Ferroelectrics. 2011;128:125-9.
[230] Mackie EB, Galvan DH, Adem E, Talapatra S, Yang G, Migone AD. Production of WS2 nanotubes by an activation method. Advanced Materials. 2000;12:495-8.
[231] Agnihotri S, Mota JP, Rostam-Abadi M, Rood MJ. Structural characterization of single-walled carbon nanotube bundles by experiment and molecular simulation. Langmuir. 2005;21:896-904.
[232] Lehman JH, Terrones M, Mansfield E, Hurst KE, Meunier V. Evaluating the characteristics of multiwall carbon nanotubes. Carbon. 2011;49:2581-602.
[233] Rafiee MA, Lu W, Thomas AV, Zandiatashbar A, Rafiee J, Tour JM, et al. Graphene nanoribbon composites. ACS nano. 2010;4:7415-20.
[234] Mullick Chowdhury S, Lalwani G, Zhang K, Yang JY, Neville K, Sitharaman B. Cell specific cytotoxicity and uptake of graphene nanoribbons. Biomaterials. 2012.
[235] Chen J, Li S-L, Gao F, Tao Z-L. Synthesis and Characterization of WS2 Nanotubes. Chemistry of Materials. 2003;15:1012-9.
[236] Elizondo-Villarreal N, Velázquez-Castillo R, Galván DH, Camacho A, José Yacamán M. Structure and catalytic properties of molybdenum sulfide nanoplatelets. Applied Catalysis A: General. 2007;328:88-97.
[237] Leela Mohana Reddy A, Tanur AE, Walker GC. Synthesis and hydrogen storage properties of different types of boron nitride nanostructures. International Journal of Hydrogen Energy. 2010;35:4138-43.
[238] Wang L, Sun C, Xu L, Qian Y. Convenient synthesis and applications of gram scale boron nitride nanosheets. Catalysis Science & Technology. 2011;1:1119-23.
[239] Dinopoulos H, Dimitriou R, Giannoudis PV. RETRACTED: Bone graft substitutes: What are the options? The Surgeon. 2012;10:230-9.
[240] Yaszemski MJ, Payne RG, Hayes WC, Langer RS, Aufdemorte TB, Mikos AG. The ingrowth of new bone tissue and initial mechanical properties of a degrading polymeric composite scaffold. Tissue engineering. 1995;1:41-52.
[241] Sharifi S, Kamali M, Mohtaram NK, Shokrgozar MA, Rabiee SM, Atai M, et al. Preparation, mechanical properties, and in vitro biocompatibility of novel nanocomposites based on polyhexamethylene carbonate fumarate and nanohydroxyapatite. Polymers for Advanced Technologies. 2011;22:605-11.
[242] Fang L, Leng Y, Gao P. Processing and mechanical properties of HA/UHMWPE nanocomposites. Biomaterials. 2006;27:3701-7.
[243] Liu H, Webster TJ. Mechanical properties of dispersed ceramic nanoparticles in polymer composites for orthopedic applications. International journal of nanomedicine. 2010;5:299.

[244] Treacy M, Ebbesen T, Gibson J. Exceptionally high Young's modulus observed for individual carbon nanotubes. 1996.
[245] Deng L, Eichhorn SJ, Kao C-C, Young RJ. The effective young's modulus of carbon nanotubes in composites. ACS applied materials & interfaces. 2011;3:433-40.
[246] Mitchell CA, Bahr JL, Arepalli S, Tour JM, Krishnamoorti R. Dispersion of functionalized carbon nanotubes in polystyrene. Macromolecules. 2002;35:8825-30.
[247] Dyke CA, Tour JM. Overcoming the insolubility of carbon nanotubes through high degrees of sidewall functionalization. Chemistry-A European Journal. 2004;10:812-7.
[248] Thess A, Lee R, Nikolaev P, Dai H, Petit P, Robert J, et al. Crystalline ropes of metallic carbon nanotubes. Science-AAAS-Weekly Paper Edition. 1996;273:483-7.
[249] Lee C, Wei X, Kysar JW, Hone J. Measurement of the elastic properties and intrinsic strength of monolayer graphene. science. 2008;321:385-8.
[250] Castellanos-Gomez A, Poot M, Steele GA, van der Zant HS, Agraït N, Rubio-Bollinger G. Elastic properties of freely suspended MoS2 nanosheets. Advanced Materials. 2012;24:772-5.
[251] Bertolazzi S, Brivio J, Kis A. Stretching and breaking of ultrathin MoS2. Acs Nano. 2011;5:9703-9.
[252] Zohar E, Baruch S, Shneider M, Dodiuk H, Kenig S, Tenne R, et al. The effect of WS2 nanotubes on the properties of epoxy-based nanocomposites. Journal of Adhesion Science and Technology. 2011;25:1603-17.
[253] Reddy CS, Zak A, Zussman E. WS 2 nanotubes embedded in PMMA nanofibers as energy absorptive material. Journal of Materials Chemistry. 2011;21:16086-93.
[254] Zhi CY, Bando Y, Terao T, Tang C, Golberg D. Dielectric and thermal properties of epoxy/boron nitride nanotube composites. Pure & Applied Chemistry. 2010;82.
[255] Stankovich S, Dikin DA, Dommett GH, Kohlhaas KM, Zimney EJ, Stach EA, et al. Graphene-based composite materials. Nature. 2006;442:282-6.
[256] Yu M-F, Lourie O, Dyer MJ, Moloni K, Kelly TF, Ruoff RS. Strength and breaking mechanism of multiwalled carbon nanotubes under tensile load. Science. 2000;287:637-40.
[257] Mistry AS, Pham QP, Schouten C, Yeh T, Christenson EM, Mikos AG, et al. In vivo bone biocompatibility and degradation of porous fumarate-based polymer/alumoxane nanocomposites for bone tissue engineering. Journal of Biomedical Materials Research Part A. 2010;92:451-62.
[258] Pinto AM, Cabral J, Tanaka DAP, Mendes AM, Magalhães FD. Effect of incorporation of graphene oxide and graphene nanoplatelets on mechanical and gas permeability properties of poly (lactic acid) films. Polymer International. 2013;62:33-40.
[259] Song P, Cao Z, Cai Y, Zhao L, Fang Z, Fu S. Fabrication of exfoliated graphene-based polypropylene nanocomposites with enhanced mechanical and thermal properties. Polymer. 2011;52:4001-10.
[260] Rafiee MA, Rafiee J, Wang Z, Song H, Yu Z-Z, Koratkar N. Enhanced mechanical properties of nanocomposites at low graphene content. ACS nano. 2009;3:3884-90.
[261] Chatterjee S, Nüesch F, Chu BT. Comparing carbon nanotubes and graphene nanoplatelets as reinforcements in polyamide 12 composites. Nanotechnology. 2011;22:275714.
[262] Coleman JN, Khan U, Blau WJ, Gun'ko YK. Small but strong: a review of the mechanical properties of carbon nanotube–polymer composites. Carbon. 2006;44:1624-52.
[263] Zhou K, Jiang S, Bao C, Song L, Wang B, Tang G, et al. Preparation of poly (vinyl alcohol) nanocomposites with molybdenum disulfide (MoS 2): structural characteristics and markedly enhanced properties. RSC Advances. 2012;2:11695-703.
[264] Paratala BS, Jacobson BD, Kanakia S, Francis LD, Sitharaman B. Physicochemical characterization, and relaxometry studies of micro-graphite oxide, graphene nanoplatelets, and nanoribbons. PloS one. 2012;7:e38185.
[265] Guo X. Mechanical properties of cortical bone and cancellous bone tissue. Bone mechanics handbook. 2001;2:10.

[266] Girishkumar G, Hall TD, Vinodgopal K, Kamat PV. Single wall carbon nanotube supports for portable direct methanol fuel cells. The Journal of Physical Chemistry B. 2006;110:107-14.
[267] Ajayan P. Nanotubes from carbon. Chemical reviews. 1999;99:1787-800.
[268] Srinivas G, Zhu Y, Piner R, Skipper N, Ellerby M, Ruoff R. Synthesis of graphene-like nanosheets and their hydrogen adsorption capacity. Carbon. 2010;48:630-5.
[269] SikáKim W, IláKim Y, JináKim H, YoungáHwanag J, YoungáMoon S, BoáShim K, et al. Fabrication of a large scale transparent conducting film using transformed few-layered graphene nanoribbons obtained from unzipping of single wall carbon nanotubes. Journal of Materials Chemistry. 2011;21:15655-9.
[270] Kardos J. Critical issues in achieving desirable mechanical properties for short fiber composites. Pure and applied chemistry. 1985;57:1651-7.
[271] May P, Khan U, O'Neill A, Coleman JN. Approaching the theoretical limit for reinforcing polymers with graphene. Journal of Materials Chemistry. 2012;22:1278-82.
[272] Fisher JP, Dean D, Mikos AG. Photocrosslinking characteristics and mechanical properties of diethyl fumarate/poly (propylene fumarate) biomaterials. Biomaterials. 2002;23:4333-43.
[273] Bai J, Allaoui A. Effect of the length and the aggregate size of MWNTs on the improvement efficiency of the mechanical and electrical properties of nanocomposites—experimental investigation. Composites Part A: applied science and manufacturing. 2003;34:689-94.
[274] Ajayan PM, Banhart F. Nanotubes: strong bundles. Nature Materials. 2004;3:135-6.
[275] Schoenfeld C, Lautenschlager E, Meyer Jr P. Mechanical properties of human cancellous bone in the femoral head. Medical and Biological engineering. 1974;12:313-7.
[276] O'kelly K, Tancred D, McCormack B, Carr A. A quantitative technique for comparing synthetic porous hydroxyapatite structures and cancellous bone. Journal of Materials Science: Materials in Medicine. 1996;7:207-13.
[277] Du C, Ma H, Ruo M, Zhang Z, Yu X, Zeng Y. An experimental study on the biomechanical properties of the cancellous bones of distal femur. Bio-medical materials and engineering. 2006;16:215-22.
[278] REILLY DT, BURSTEIN AH. The mechanical properties of cortical bone. The Journal of Bone & Joint Surgery. 1974;56:1001-22.
[279] SUCHÝ T, Balik K, ČERNÝ M, Sochor M, Hulejova H, PEŠÁKOVÁ V, et al. A composite based on glass fibers and siloxane matrix as a bone replacement. Ceramics-Silikáty. 2008;52:29-36.
[280] Rho JY, Ashman RB, Turner CH. Young's modulus of trabecular and cortical bone material: ultrasonic and microtensile measurements. Journal of biomechanics. 1993;26:111-9.
[281] Choi K, Kuhn JL, Ciarelli MJ, Goldstein SA. The elastic moduli of human subchondral, trabecular, and cortical bone tissue and the size-dependency of cortical bone modulus. Journal of biomechanics. 1990;23:1103-13.
[282] Sabir MI, Xu X, Li L. A review on biodegradable polymeric materials for bone tissue engineering applications. Journal of Materials Science. 2009;44:5713-24.
[283] PETER SJ, MILLER MJ, YASZEMSKI MJ, MIKOS AG. 5. POLYPROPYLENE FUMARATE). Handbook of biodegradable polymers. 1998;7:87.
[284] Santerre J, Woodhouse K, Laroche G, Labow R. Understanding the biodegradation of polyurethanes: from classical implants to tissue engineering materials. Biomaterials. 2005;26:7457-70.
[285] Hyon SH, Jin F, Jamshidi K, Tsutsumi S, Kanamoto T. Biodegradable ultra high strength poly (L-lactide) rods for bone fixation. Macromolecular Symposia: Wiley Online Library; 2003. p. 355-68.
[286] He S, Timmer M, Yaszemski M, Yasko A, Engel P, Mikos A. Synthesis of biodegradable poly (propylene fumarate) networks with poly (propylene fumarate)–diacrylate macromers as crosslinking agents and characterization of their degradation products. Polymer. 2001;42:1251-60.
[287] Suggs LJ, Shive MS, Garcia CA, Anderson JM, Mikos AG. In vitro cytotoxicity and in vivo biocompatibility of poly (propylene fumarate-co-ethylene glycol) hydrogels. Journal of biomedical materials research. 1999;46:22-32.

[288] He S, J Yaszemski M, Yasko AW, Engel PS, Mikos AG. Injectable biodegradable polymer composites based on poly (propylene fumarate) crosslinked with poly (ethylene glycol)-dimethacrylate. Biomaterials. 2000;21:2389-94.
[289] Suggs LJ, West JL, Mikos AG. Platelet adhesion on a bioresorbable poly (propylene fumarate-co-ethylene glycol) copolymer. Biomaterials. 1999;20:683-90.
[290] Engh C, Bobyn J, Glassman A. Porous-coated hip replacement. The factors governing bone ingrowth, stress shielding, and clinical results. Journal of Bone & Joint Surgery, British Volume. 1987;69:45-55.
[291] LALWANI G, Sitharaman B. MULTIFUNCTIONAL FULLERENE-AND METALLOFULLERENE-BASED NANOBIOMATERIALS. Nano LIFE. 2013;3.
[292] Coleman JN, Khan U, Gun'ko YK. Mechanical reinforcement of polymers using carbon nanotubes. Advanced Materials. 2006;18:689-706.
[293] Balasundaram G, Webster TJ. An Overview of Nano-Polymers for Orthopedic Applications. Macromolecular bioscience. 2007;7:635-42.
[294] Shi X, Sitharaman B, Pham QP, Spicer PP, Hudson JL, Wilson LJ, et al. In vitro cytotoxicity of single-walled carbon nanotube/biodegradable polymer nanocomposites. Journal of Biomedical Materials Research Part A. 2008;86A:813-23.
[295] Wang X, Jia G, Wang H, Nie H, Yan L, Deng X, et al. Diameter effects on cytotoxicity of multi-walled carbon nanotubes. Journal of nanoscience and nanotechnology. 2009;9:3025-33.
[296] Akhavan O, Ghaderi E, Akhavan A. Size-dependent genotoxicity of graphene nanoplatelets in human stem cells. Biomaterials. 2012;33:8017-25.
[297] Chang Y, Yang S-T, Liu J-H, Dong E, Wang Y, Cao A, et al. In vitro toxicity evaluation of graphene oxide on A549 cells. Toxicology Letters. 2011;200:201-10.
[298] Pardo M, Shuster-Meiseles T, Levin-Zaidman S, Rudich A, Rudich Y. Low Cytotoxicity of Inorganic Nanotubes and Fullerene-Like Nanostructures in Human Bronchial Epithelial Cells: Relation to Inflammatory Gene Induction and Antioxidant Response. Environmental science & technology. 2014;48:3457-66.
[299] Timmer MD, Shin H, Horch RA, Ambrose CG, Mikos AG. In vitro cytotoxicity of injectable and biodegradable poly (propylene fumarate)-based networks: unreacted macromers, cross-linked networks, and degradation products. Biomacromolecules. 2003;4:1026-33.
[300] Mistry AS, Mikos AG, Jansen JA. Degradation and biocompatibility of a poly (propylene fumarate)-based/alumoxane nanocomposite for bone tissue engineering. Journal of Biomedical Materials Research Part A. 2007;83:940-53.
[301] Armentano I, Dottori M, Puglia D, Kenny JM. Effects of carbon nanotubes (CNTs) on the processing and in-vitro degradation of poly (DL-lactide-co-glycolide)/CNT films. Journal of Materials Science: Materials in Medicine. 2008;19:2377-87.
[302] Jing X, Mi HY, Salick MR, Peng XF, Turng LS. Preparation of thermoplastic polyurethane/graphene oxide composite scaffolds by thermally induced phase separation. Polymer Composites. 2013.
[303] Butterick TA, Nixon JP, Pérez-Leighton CE, Billington CJ, Kotz CM. Orexin A influences lipid peroxidation and neuronal metabolic status in a novel immortalized hypothalamic cell line. Society for Neuroscience Abstracts 2011, Online: Washington, DC p. 2011;88.
[304] Bueno C, Villegas ML, Bertolotti SG, Previtali CM, Neumann MG, Encinas MV. The Excited-State Interaction of Resazurin and Resorufin with Aminesin Aqueous Solutions. Photophysics and Photochemical Reaction¶. Photochemistry and Photobiology. 2002;76:385-90.
[305] Lee Y, Geckeler KE. Cytotoxicity and cellular uptake of lysozyme-stabilized gold nanoparticles. Journal of Biomedical Materials Research Part A. 2012;100:848-55.

[306] Zhao H, Zhu B, Sekine J, Luo S-C, Yu H-h. Oligoethylene-Glycol-Functionalized Polyoxythiophenes for Cell Engineering: Syntheses, Characterizations, and Cell Compatibilities. ACS applied materials & interfaces. 2012;4:680-6.
[307] Wang K, Cai L, Jesse S, Wang S. Poly (ε-caprolactone)-Banded Spherulites and Interaction with MC3T3-E1 Cells. Langmuir. 2012;28:4382-95.
[308] Sahoo NG, Pan YZ, Li L, He CB. Nanocomposites for bone tissue regeneration. Nanomedicine. 2013;8:639-53.
[309] Liu H, Webster TJ. Nanomedicine for implants: A review of studies and necessary experimental tools. Biomaterials. 2007;28:354-69.
[310] Timmer MD, Ambrose CG, Mikos AG. In vitro degradation of polymeric networks of poly (propylene fumarate) and the crosslinking macromer poly (propylene fumarate)-diacrylate. Biomaterials. 2003;24:571-7.
[311] Swauger JE, Dolan PM, Zweier JL, Kuppusamy P, Kensler TW. Role of the benzoyloxyl radical in DNA damage mediated by benzoyl peroxide. Chemical research in toxicology. 1991;4:223-8.
[312] Cameron G, Bryce W, McWalter I. Thermal degradation of polystyrene—5. Effects of initiator residues. European polymer journal. 1984;20:563-9.
[313] Timmer MD, Ambrose CG, Mikos AG. Evaluation of thermal-and photo-crosslinked biodegradable poly (propylene fumarate)-based networks. Journal of Biomedical Materials Research Part A. 2003;66:811-8.
[314] Kotchey GP, Hasan SA, Kapralov AA, Ha SH, Kim K, Shvedova AA, et al. A Natural Vanishing Act: The Enzyme-Catalyzed Degradation of Carbon Nanomaterials. Accounts of Chemical Research. 2012;45:1770-81.
[315] Xing W, Lalwani G, Rusakova I, Sitharaman B. Degradation of Graphene by Hydrogen Peroxide. Particle & Particle Systems Characterization. 2014.
[316] Waymouth C. Osmolality of mammalian blood and of media for culture of mammalian cells. In vitro. 1970;6:109-27.
[317] Higgins CB, Sovak M, Schmidt WS, Kelley MJ, Newell JD. Direct myocardial effects of intracoronary administration of new contrast materials with low osmolality. Investigative radiology. 1980;15:39-46.
[318] Ge C, Du J, Zhao L, Wang L, Liu Y, Li D, et al. Binding of blood proteins to carbon nanotubes reduces cytotoxicity. Proceedings of the National Academy of Sciences. 2011;108:16968-73.
[319] Khang D, Kim SY, Liu-Snyder P, Palmore GTR, Durbin SM, Webster TJ. Enhanced fibronectin adsorption on carbon nanotube/poly (carbonate) urethane: independent role of surface nano-roughness and associated surface energy. Biomaterials. 2007;28:4756-68.
[320] Kane RS, Stroock AD. Nanobiotechnology: Protein-Nanomaterial Interactions. Biotechnology progress. 2007;23:316-9.
[321] Cui D, Tian F, Ozkan CS, Wang M, Gao H. Effect of single wall carbon nanotubes on human HEK293 cells. Toxicology letters. 2005;155:73-85.
[322] Bryant SJ, Anseth KS. Controlling the spatial distribution of ECM components in degradable PEG hydrogels for tissue engineering cartilage. Journal of Biomedical Materials Research Part A. 2003;64:70-9.
[323] Shi X, Gong H, Li Y, Wang C, Cheng L, Liu Z. Graphene-based magnetic plasmonic nanocomposite for dual bioimaging and photothermal therapy. Biomaterials. 2013;34:4786-93.
[324] Adini A, Redlich M, Tenne R. Medical applications of inorganic fullerene-like nanoparticles. Journal of Materials Chemistry. 2011;21:15121-31.
[325] Chen Y, Tan C, Zhang H, Wang L. Two-dimensional graphene analogues for biomedical applications. Chemical Society Reviews. 2015.
[326] Wang Y, Li Z, Wang J, Li J, Lin Y. Graphene and graphene oxide: biofunctionalization and applications in biotechnology. Trends in Biotechnology. 2011;29:205-12.

[327] Akdim B, Pachter R, Duan X, Adams WW. Comparative theoretical study of single-wall carbon and boron-nitride nanotubes. Physical Review B. 2003;67:245404.
[328] Golberg D, Bando Y, Huang Y, Terao T, Mitome M, Tang C, et al. Boron nitride nanotubes and nanosheets. Acs Nano. 2010;4:2979-93.
[329] Ishigami M, Aloni S, Zettl A. Properties of boron nitride nanotubes. AIP Conference Proceedings2003. p. 94-9.
[330] Arenal R, Wang M-S, Xu Z, Loiseau A, Golberg D. Young modulus, mechanical and electrical properties of isolated individual and bundled single-walled boron nitride nanotubes. Nanotechnology. 2011;22:265704.
[331] Vaccarini L, Goze C, Henrard L, Hernández E, Bernier P, Rubio A. Mechanical and electronic properties of carbon and boron–nitride nanotubes. Carbon. 2000;38:1681-90.
[332] Meng W, Huang Y, Fu Y, Wang Z, Zhi C. Polymer composites of boron nitride nanotubes and nanosheets. Journal of Materials Chemistry C. 2014;2:10049-61.
[333] Lin Y, Williams TV, Connell JW. Soluble, exfoliated hexagonal boron nitride nanosheets. The Journal of Physical Chemistry Letters. 2009;1:277-83.
[334] Dai XJ, Chen Y, Chen Z, Lamb PR, Li LH, du Plessis J, et al. Controlled surface modification of boron nitride nanotubes. Nanotechnology. 2011;22:245301.
[335] Lahiri D, Rouzaud F, Richard T, Keshri AK, Bakshi SR, Kos L, et al. Boron nitride nanotube reinforced polylactide–polycaprolactone copolymer composite: Mechanical properties and cytocompatibility with osteoblasts and macrophages in vitro. Acta biomaterialia. 2010;6:3524-33.
[336] Peter SJ, Nolley JA, Widmer MS, Merwin JE, Yaszemski MJ, Yasko AW, et al. In vitro degradation of a poly (propylene fumarate)/β-tricalcium phosphate composite orthopaedic scaffold. Tissue Engineering. 1997;3:207-15.
[337] He S, Timmer MD, Yaszemski MJ, Yasko AW, Engel PS, Mikos AG. Synthesis of biodegradable poly(propylene fumarate) networks with poly(propylene fumarate)–diacrylate macromers as crosslinking agents and characterization of their degradation products. Polymer. 2001;42:1251-60.
[338] Yaszemski MJ, Payne RG, Hayes WC, Langer R, Mikos AG. < i> In vitro</i> degradation of a poly (propylene fumarate)-based composite material. Biomaterials. 1996;17:2127-30.
[339] Zhi C, Bando Y, Tang C, Kuwahara H, Golberg D. Large-Scale Fabrication of Boron Nitride Nanosheets and Their Utilization in Polymeric Composites with Improved Thermal and Mechanical Properties. Advanced Materials. 2009;21:2889-93.
[340] Tang C, Bando Y, Sato T, Kurashima K. A novel precursor for synthesis of pure boron nitride nanotubes. Chem Commun. 2002:1290-1.
[341] Lee R, Gavillet J, de La Chapelle ML, Loiseau A, Cochon J-L, Pigache D, et al. Catalyst-free synthesis of boron nitride single-wall nanotubes with a preferred zig-zag configuration. Physical Review B. 2001;64:121405.
[342] Ahmed S, Jones F. A review of particulate reinforcement theories for polymer composites. Journal of Materials Science. 1990;25:4933-42.
[343] Lin Y, Williams TV, Xu T-B, Cao W, Elsayed-Ali HE, Connell JW. Aqueous dispersions of few-layered and monolayered hexagonal boron nitride nanosheets from sonication-assisted hydrolysis: critical role of water. The Journal of Physical Chemistry C. 2011;115:2679-85.
[344] Lei W, Portehault D, Liu D, Qin S, Chen Y. Porous boron nitride nanosheets for effective water cleaning. Nat Commun. 2013;4:1777.
[345] Tang C, Bando Y, Ding X, Qi S, Golberg D. Catalyzed Collapse and Enhanced Hydrogen Storage of BN Nanotubes. Journal of the American Chemical Society. 2002;124:14550-1.
[346] Chow T. The effect of particle shape on the mechanical properties of filled polymers. Journal of Materials Science. 1980;15:1873-88.

[347] Rechendorff K, Hovgaard MB, Foss M, Zhdanov V, Besenbacher F. Enhancement of protein adsorption induced by surface roughness. Langmuir. 2006;22:10885-8.
[348] Cox MM, Phillips GN. Handbook of proteins: structure, function and methods: Wiley; 2007.
[349] Tang L, Eaton JW. Fibrin (ogen) mediates acute inflammatory responses to biomaterials. The Journal of experimental medicine. 1993;178:2147-56.
[350] Johansson S, Svineng G, Wennerberg K, Armulik A, Lohikangas L. Fibronectin-integrin interactions. Front Biosci. 1997;2:d126-d46.
[351] Yoon J-Y, Park H-Y, Kim J-H, Kim W-S. Adsorption of BSA on highly carboxylated microspheres—quantitative effects of surface functional groups and interaction forces. Journal of colloid and interface science. 1996;177:613-20.
[352] Wang D, Christensen K, Chawla K, Xiao G, Krebsbach PH, Franceschi RT. Isolation and characterization of MC3T3-E1 preosteoblast subclones with distinct in vitro and in vivo differentiation/mineralization potential. Journal of Bone and Mineral Research. 1999;14:893-903.
[353] Belyanskaya L, Manser P, Spohn P, Bruinink A, Wick P. The reliability and limits of the MTT reduction assay for carbon nanotubes–cell interaction. Carbon. 2007;45:2643-8.
[354] Farshid B, Lalwani G, Sitharaman B. In vitro cytocompatibility of one- and two-dimensional nanostructure-reinforced biodegradable polymeric nanocomposites. Journal of Biomedical Materials Research Part A. 2014:n/a-n/a.
[355] Chen X, Wu P, Rousseas M, Okawa D, Gartner Z, Zettl A, et al. Boron Nitride Nanotubes Are Noncytotoxic and Can Be Functionalized for Interaction with Proteins and Cells. Journal of the American Chemical Society. 2009;131:890-1.
[356] van Kooten TG, Spijker HT, Busscher HJ. Plasma-treated polystyrene surfaces: model surfaces for studying cell–biomaterial interactions. Biomaterials. 2004;25:1735-47.
[357] Burg KJ, Porter S, Kellam JF. Biomaterial developments for bone tissue engineering. Biomaterials. 2000;21:2347-59.
[358] Armentano I, Dottori M, Fortunati E, Mattioli S, Kenny J. Biodegradable polymer matrix nanocomposites for tissue engineering: a review. Polymer degradation and stability. 2010;95:2126-46.
[359] De Santis R, Gloria A, Russo T, D'Amora U, Zeppetelli S, Dionigi C, et al. A basic approach toward the development of nanocomposite magnetic scaffolds for advanced bone tissue engineering. Journal of Applied Polymer Science. 2011;122:3599-605.
[360] Yang L, Webster TJ. Nanotechnology controlled drug delivery for treating bone diseases. 2009.
[361] Lalwani G, Sitharaman B. Carbon Nanotechnology in Regenerative Medicine.
[362] Stevens MM. Biomaterials for bone tissue engineering. Materials today. 2008;11:18-25.
[363] Li Z, Ramay HR, Hauch KD, Xiao D, Zhang M. Chitosan–alginate hybrid scaffolds for bone tissue engineering. Biomaterials. 2005;26:3919-28.
[364] Ishaug-Riley S, Crane G, Gurlek A, Miller M, Yasko A, Yaszemski M, et al. Ectopic bone formation by marrow stromal osteoblast transplantation using poly (DL-lactic-co-glycolic acid) foams implanted into the rat mesentery. Journal of Biomedical Materials Research. 1997;36:1-8.
[365] Williams JM, Adewunmi A, Schek RM, Flanagan CL, Krebsbach PH, Feinberg SE, et al. Bone tissue engineering using polycaprolactone scaffolds fabricated via selective laser sintering. Biomaterials. 2005;26:4817-27.
[366] Shikinami Y, Okuno M. Bioresorbable devices made of forged composites of hydroxyapatite (HA) particles and poly-L-lactide (PLLA): Part I. Basic characteristics. Biomaterials. 1999;20:859-77.
[367] Burdick JA, Anseth KS. Photoencapsulation of osteoblasts in injectable RGD-modified PEG hydrogels for bone tissue engineering. Biomaterials. 2002;23:4315-23.
[368] Tjong SC. Mechanical Properties of Polymer Nanocomposites. Polymer Composites with Carbonaceous Nanofillers, Properties and Applications.143-92.

[369] Behzad Farshid GL, Balaji Sitharaman. In Vitro Cytocompatibility of One- and Two-Dimensional Nanostructure-Reinforced Biodegradable Polymeric Nanocomposites Journal of Biomedical Materials Research Part A. 2014 (Accepter, September 2014).
[370] Behzad Farshid GL, Meisam Shirmohammadi, John Simonsen, Balaji Sitharaman. Boron Nitride Nanotubes and Nanoplatelets-Reinforced Biodegradable Polymeric Nanocomposites for Bone Tissue Engineering. Journal of biomedical materials research part A. 2014 (Accepted, September 2014).
[371] Talukdar Y, Rashkow JT, Lalwani G, Kanakia S, Sitharaman B. The effects of graphene nanostructures on mesenchymal stem cells. Biomaterials. 2014;35:4863-77.
[372] Decherchi P, Cochard P, Gauthier P. Dual staining assessment of Schwann cell viability within whole peripheral nerves using calcein-AM and ethidium homodimer. Journal of neuroscience methods. 1997;71:205-13.
[373] Rodríguez JP, Montecinos L, Ríos S, Reyes P, Martínez J. Mesenchymal stem cells from osteoporotic patients produce a type I collagen-deficient extracellular matrix favoring adipogenic differentiation. 2000.
[374] Cheng Q, Rutledge K, Jabbarzadeh E. Carbon nanotube–poly (lactide-co-glycolide) composite scaffolds for bone tissue engineering applications. Annals of biomedical engineering. 2013;41:904-16.
[375] Cheung H-Y, Lau K-T, Lu T-P, Hui D. A critical review on polymer-based bio-engineered materials for scaffold development. Composites Part B: Engineering. 2007;38:291-300.
[376] Gloria A, De Santis R, Ambrosio L. Polymer-based composite scaffolds for tissue engineering. Journal of Applied Biomaterials & Biomechanics. 2010;8.
[377] Liao H, Paratala B, Sitharaman B, Wang Y. Applications of carbon nanotubes in biomedical studies. Biomedical Nanotechnology: Springer; 2011. p. 223-41.
[378] Smart S, Cassady A, Lu G, Martin D. The biocompatibility of carbon nanotubes. Carbon. 2006;44:1034-47.
[379] Pramanik M, Swierczewska M, Wang LV, Green D, Sitharaman B. Single-walled carbon nanotubes as a multimodal-thermoacoustic and photoacoustic-contrast agent. Journal of biomedical optics. 2009;14:034018--8.
[380] Gartsman K, Kaplan-Ashiri I, Tenne R, Rafailov P, Thomsen C. Micro Raman Investigation of WS2 Nanotubes. AIP Conference Proceedings. 2005;786:349-52.
[381] Tang C, Fan S, Li P, Liu Y, Dang H. Synthesis of boron nitride in tubular form. Materials Letters. 2001;51:315-9.
[382] Chen T, Zeng B, Liu J, Dong J, Liu X, Wu Z, et al. High throughput exfoliation of graphene oxide from expanded graphite with assistance of strong oxidant in modified Hummers method. Journal of Physics: Conference Series: IOP Publishing; 2009. p. 012051.
[383] Ferrari A, Meyer J, Scardaci V, Casiraghi C, Lazzeri M, Mauri F, et al. Raman spectrum of graphene and graphene layers. Physical review letters. 2006;97:187401.
[384] Ago H, Kugler T, Cacialli F, Salaneck WR, Shaffer MS, Windle AH, et al. Work functions and surface functional groups of multiwall carbon nanotubes. The Journal of Physical Chemistry B. 1999;103:8116-21.
[385] Ma PX, Choi J-W. Biodegradable polymer scaffolds with well-defined interconnected spherical pore network. Tissue engineering. 2001;7:23-33.
[386] Peckner D, Bernstein IM. Handbook of stainless steels: McGraw-Hill New York, NY; 1977.
[387] Kudin KN, Scuseria GE, Yakobson BI. C 2 F, BN, and C nanoshell elasticity from ab initio computations. Physical Review B. 2001;64:235406.
[388] Zhu YQ, Sekine T, Li YH, Fay MW, Zhao YM, Patrick Poa CH, et al. Shock-Absorbing and Failure Mechanisms of WS2 and MoS2 Nanoparticles with Fullerene-like Structures under Shock Wave Pressure. Journal of the American Chemical Society. 2005;127:16263-72.

[389] Salvetat J-P, Bonard J-M, Thomson N, Kulik A, Forro L, Benoit W, et al. Mechanical properties of carbon nanotubes. Applied Physics A. 1999;69:255-60.
[390] Zhu Y, Murali S, Cai W, Li X, Suk JW, Potts JR, et al. Graphene and graphene oxide: synthesis, properties, and applications. Advanced materials. 2010;22:3906-24.
[391] Kim JA, Seong DG, Kang TJ, Youn JR. Effects of surface modification on rheological and mechanical properties of CNT/epoxy composites. Carbon. 2006;44:1898-905.
[392] Aumailley M, Gayraud B. Structure and biological activity of the extracellular matrix. Journal of Molecular Medicine. 1998;76:253-65.
[393] Sigal GB, Mrksich M, Whitesides GM. Effect of surface wettability on the adsorption of proteins and detergents. Journal of the American Chemical Society. 1998;120:3464-73.
[394] Tamada Y, Ikada Y. Effect of preadsorbed proteins on cell adhesion to polymer surfaces. Journal of colloid and interface science. 1993;155:334-9.
[395] Woo KM, Chen VJ, Ma PX. Nano-fibrous scaffolding architecture selectively enhances protein adsorption contributing to cell attachment. Journal of Biomedical Materials Research Part A. 2003;67:531-7.
[396] Woo KM, Seo J, Zhang R, Ma PX. Suppression of apoptosis by enhanced protein adsorption on polymer/hydroxyapatite composite scaffolds. Biomaterials. 2007;28:2622-30.
[397] Giannona S, Firkowska I, Rojas-Chapana J, Giersig M. Vertically aligned carbon nanotubes as cytocompatible material for enhanced adhesion and proliferation of osteoblast-like cells. Journal of nanoscience and nanotechnology. 2007;7:1679-83.
[398] Sahni D, Jea A, Mata JA, Marcano DC, Sivaganesan A, Berlin JM, et al. Biocompatibility of pristine graphene for neuronal interface: Laboratory investigation. Journal of Neurosurgery: Pediatrics. 2013;11:575-83.
[399] Yan X, Chen J, Yang J, Xue Q, Miele P. Fabrication of free-standing, electrochemically active, and biocompatible graphene oxide− polyaniline and graphene− polyaniline hybrid papers. ACS applied materials & interfaces. 2010;2:2521-9.
[400] Sharifi S, Behzadi S, Laurent S, Forrest ML, Stroeve P, Mahmoudi M. Toxicity of nanomaterials. Chemical Society Reviews. 2012;41:2323-43.
[401] Ishaug SL, Crane GM, Miller MJ, Yasko AW, Yaszemski MJ, Mikos AG. Bone formation by three-dimensional stromal osteoblast culture in biodegradable polymer scaffolds. Journal of biomedical materials research. 1997;36:17-28.
[402] Lourenço BN, Marchioli G, Song W, Reis RL, van Blitterswijk CA, Karperien M, et al. Wettability Influences Cell Behavior on Superhydrophobic Surfaces with Different Topographies. Biointerphases. 2012;7:-.
[403] Thannickal VJ, Lee DY, White ES, Cui Z, Larios JM, Chacon R, et al. Myofibroblast differentiation by transforming growth factor-β1 is dependent on cell adhesion and integrin signaling via focal adhesion kinase. Journal of Biological Chemistry. 2003;278:12384-9.
[404] Zhang L, Webster TJ. Nanotechnology and nanomaterials: promises for improved tissue regeneration. Nano Today. 2009;4:66-80.
[405] Zhang P, Hong Z, Yu T, Chen X, Jing X. In vivo mineralization and osteogenesis of nanocomposite scaffold of poly (lactide-co-glycolide) and hydroxyapatite surface-grafted with poly (L-lactide). Biomaterials. 2009;30:58-70.
[406] Popp JR. Bioactive Poly (Lactic-co-Glycolic Acid)-Calcium Phosphate Scaffolds for Bone Tissue Regeneration 2009.
[407] Horch RA, Shahid N, Mistry AS, Timmer MD, Mikos AG, Barron AR. Nanoreinforcement of poly (propylene fumarate)-based networks with surface modified alumoxane nanoparticles for bone tissue engineering. Biomacromolecules. 2004;5:1990-8.

[408] Chrzanowski W, Kim SY, Neel EAA. Biomedical Applications of Clay. Australian Journal of Chemistry. 2013;66:1315-22.
[409] Bertazzo S, Zambuzzi W, Da Silva H, Ferreira C, Bertran C. Bioactivation of alumina by surface modification: a possibility for improving the applicability of alumina in bone and oral repair. Clinical oral implants research. 2009;20:288-93.
[410] Pattnaik S, Nethala S, Tripathi A, Saravanan S, Moorthi A, Selvamurugan N. Chitosan scaffolds containing silicon dioxide and zirconia nano particles for bone tissue engineering. International journal of biological macromolecules. 2011;49:1167-72.
[411] Brammer KS, Frandsen CJ, Jin S. TiO 2 nanotubes for bone regeneration. Trends in biotechnology. 2012;30:315-22.
[412] Wan C, Chen B. Poly (ε-caprolactone)/graphene oxide biocomposites: mechanical properties and bioactivity. Biomedical Materials. 2011;6:055010.
[413] Shin JH, Lee JW, Jung JH, Cho D-W, Lim G. Evaluation of cell proliferation and differentiation on a poly (propylene fumarate) 3D scaffold treated with functional peptides. Journal of Materials Science. 2011;46:5282-7.
[414] Kunzmann A, Andersson B, Thurnherr T, Krug H, Scheynius A, Fadeel B. Toxicology of engineered nanomaterials: focus on biocompatibility, biodistribution and biodegradation. Biochimica et Biophysica Acta (BBA)-General Subjects. 2011;1810:361-73.
[415] Almeida JPM, Chen AL, Foster A, Drezek R. In vivo biodistribution of nanoparticles. Nanomedicine. 2011;6:815-35.
[416] Park SY, Namgung S, Kim B, Im J, Kim J, Sun K, et al. Carbon nanotube monolayer patterns for directed growth of mesenchymal stem cells. Advanced Materials. 2007;19:2530-4.
[417] Haines AM, Tobe SS, Kobus HJ, Linacre A. Properties of nucleic acid staining dyes used in gel electrophoresis. Electrophoresis. 2014.
[418] Bratosin D, Mitrofan L, Palii C, Estaquier J, Montreuil J. Novel fluorescence assay using calcein-AM for the determination of human erythrocyte viability and aging. Cytometry Part A. 2005;66:78-84.
[419] Auclair-Daigle C, Bureau M, Legoux JG, Yahia LH. Bioactive hydroxyapatite coatings on polymer composites for orthopedic implants. Journal of Biomedical Materials Research Part A. 2005;73:398-408.
[420] St-Pierre J-P, Gauthier M, Lefebvre L-P, Tabrizian M. Three-dimensional growth of differentiating MC3T3-E1 pre-osteoblasts on porous titanium scaffolds. Biomaterials. 2005;26:7319-28.
[421] Lee D-H, Han J-S, Yang J-H, Lee J-B, Kim D-J. MC3T3-E1 cell response to pure titanium, zirconia and nano-hydroxyapatite. International Journal of Modern Physics B. 2009;23:1535-40.
[422] Wan C, Frydrych M, Chen B. Strong and bioactive gelatin–graphene oxide nanocomposites. Soft Matter. 2011;7:6159-66.
[423] Oh S, Daraio C, Chen LH, Pisanic TR, Finones RR, Jin S. Significantly accelerated osteoblast cell growth on aligned TiO2 nanotubes. Journal of Biomedical Materials Research Part A. 2006;78:97-103.
[424] El-Ghannam A, Ducheyne P, Shapiro I. Effect of serum proteins on osteoblast adhesion to surface-modified bioactive glass and hydroxyapatite. Journal of Orthopaedic Research. 1999;17:340-5.
[425] Varanasi V, Saiz E, Loomer P, Ancheta B, Uritani N, Ho S, et al. Enhanced osteocalcin expression by osteoblast-like cells (MC3T3-E1) exposed to bioactive coating glass (SiO 2–CaO–P 2 O 5–MgO–K 2 O–Na 2 O system) ions. Acta biomaterialia. 2009;5:3536-47.
[426] Liao CJ, Chen CF, Chen JH, Chiang SF, Lin YJ, Chang KY. Fabrication of porous biodegradable polymer scaffolds using a solvent merging/particulate leaching method. Journal of biomedical materials research. 2002;59:676-81.
[427] Connell JW, Lin Y. Method for exfoliation of hexagonal boron nitride. Google Patents; 2012.
[428] Costa S, Borowiak-Palen E, Kruszynska M, Bachmatiuk A, Kalenczuk R. Characterization of carbon nanotubes by Raman spectroscopy. Mater Sci-Poland. 2008;26:433-41.

[429] Kudin KN, Ozbas B, Schniepp HC, Prud'Homme RK, Aksay IA, Car R. Raman spectra of graphite oxide and functionalized graphene sheets. Nano letters. 2008;8:36-41.
[430] Viršek M, Jesih A, Milošević I, Damnjanović M, Remškar M. Raman scattering of the MoS 2 and WS 2 single nanotubes. Surface science. 2007;601:2868-72.
[431] Liao H, Andersson A-S, Sutherland D, Petronis S, Kasemo B, Thomsen P. Response of rat osteoblast-like cells to microstructured model surfaces in vitro. Biomaterials. 2003;24:649-54.
[432] Yang X, Roach H, Clarke N, Howdle S, Quirk R, Shakesheff K, et al. Human osteoprogenitor growth and differentiation on synthetic biodegradable structures after surface modification. Bone. 2001;29:523-31.
[433] Benoit DS, Schwartz MP, Durney AR, Anseth KS. Small functional groups for controlled differentiation of hydrogel-encapsulated human mesenchymal stem cells. Nature materials. 2008;7:816-23.
[434] Goldstein AS, Juarez TM, Helmke CD, Gustin MC, Mikos AG. Effect of convection on osteoblastic cell growth and function in biodegradable polymer foam scaffolds. Biomaterials. 2001;22:1279-88.
[435] Karageorgiou V, Kaplan D. Porosity of 3D biomaterial scaffolds and osteogenesis. Biomaterials. 2005;26:5474-91.
[436] Beck GR, Sullivan EC, Moran E, Zerler B. Relationship between alkaline phosphatase levels, osteopontin expression, and mineralization in differentiating MC3T3-E1 osteoblasts. Journal of cellular biochemistry. 1998;68:269-80.
[437] Cowles E, DeRome M, Pastizzo G, Brailey L, Gronowicz G. Mineralization and the expression of matrix proteins during in vivo bone development. Calcified tissue international. 1998;62:74-82.
[438] Stevens MM, George JH. Exploring and engineering the cell surface interface. Science. 2005;310:1135-8.
[439] Kizuki T, Ohgaki M, Katsura M, Nakamura S, Hashimoto K, Toda Y, et al. Effect of bone-like layer growth from culture medium on adherence of osteoblast-like cells. Biomaterials. 2003;24:941-7.
[440] García A, Reyes C. Bio-adhesive surfaces to promote osteoblast differentiation and bone formation. Journal of Dental Research. 2005;84:407-13.
[441] Siebers M, Ter Brugge P, Walboomers X, Jansen J. Integrins as linker proteins between osteoblasts and bone replacing materials. A critical review. Biomaterials. 2005;26:137-46.
[442] Ducheyne P, Qiu Q. Bioactive ceramics: the effect of surface reactivity on bone formation and bone cell function. Biomaterials. 1999;20:2287-303.
[443] Boyan BD, Sylvia VL, Liu Y, Sagun R, Cochran DL, Lohmann CH, et al. Surface roughness mediates its effects on osteoblasts via protein kinase A and phospholipase A 2. Biomaterials. 1999;20:2305-10.
[444] Wu X, An W, Zeng XC. Chemical functionalization of boron-nitride nanotubes with NH3 and amino functional groups. Journal of the American Chemical Society. 2006;128:12001-6.
[445] Sudo H, Kodama H-A, Amagai Y, Yamamoto S, Kasai S. In vitro differentiation and calcification in a new clonal osteogenic cell line derived from newborn mouse calvaria. The Journal of cell biology. 1983;96:191-8.
[446] Seyednejad H, Vermonden T, Fedorovich NE, van Eijk R, van Steenbergen MJ, Dhert WJ, et al. Synthesis and characterization of hydroxyl-functionalized caprolactone copolymers and their effect on adhesion, proliferation, and differentiation of human mesenchymal stem cells. Biomacromolecules. 2009;10:3048-54.
[447] Nayak TR, Andersen H, Makam VS, Khaw C, Bae S, Xu X, et al. Graphene for controlled and accelerated osteogenic differentiation of human mesenchymal stem cells. ACS nano. 2011;5:4670-8.
[448] Zhang D, Yi C, Zhang J, Chen Y, Yao X, Yang M. The effects of carbon nanotubes on the proliferation and differentiation of primary osteoblasts. Nanotechnology. 2007;18:475102.
[449] Lee WC, Lim CHY, Shi H, Tang LA, Wang Y, Lim CT, et al. Origin of enhanced stem cell growth and differentiation on graphene and graphene oxide. ACS nano. 2011;5:7334-41.

[450] Boyan B, Bonewald L, Paschalis E, Lohmann C, Rosser J, Cochran D, et al. Osteoblast-mediated mineral deposition in culture is dependent on surface microtopography. Calcified tissue international. 2002;71:519-29.
[451] Toworfe G, Composto R, Shapiro I, Ducheyne P. Nucleation and growth of calcium phosphate on amine-, carboxyl-and hydroxyl-silane self-assembled monolayers. Biomaterials. 2006;27:631-42.
[452] He G, Dahl T, Veis A, George A. Nucleation of apatite crystals in vitro by self-assembled dentin matrix protein 1. Nature materials. 2003;2:552-8.
[453] PETER SJ, MILLER MJ, YASZEMSKI MJ, MIKOS AG. 5. Poly (propylene fumarate). Handbook of biodegradable polymers: Harwood Academic Publishers Amsterdam; 1997. p. 87-97.
[454] Hilton MR, Bauer R, Didziulis SV, Dugger MT, Keem JM, Scholhamer J. Structural and tribological studies of MoS 2 solid lubricant films having tailored metal-multilayer nanostructures. Surface and Coatings Technology. 1992;53:13-23.
[455] Gouadec G, Colomban P. Raman Spectroscopy of nanomaterials: How spectra relate to disorder, particle size and mechanical properties. Progress in Crystal Growth and Characterization of Materials. 2007;53:1-56.
[456] Lee D, Song SH, Hwang J, Jin SH, Park KH, Kim BH, et al. Enhanced mechanical properties of epoxy nanocomposites by mixing noncovalently functionalized boron nitride nanoflakes. Small. 2013;9:2602-10.
[457] Lin Y, Williams TV, Cao W, Elsayed-Ali HE, Connell JW. Defect functionalization of hexagonal boron nitride nanosheets. The Journal of Physical Chemistry C. 2010;114:17434-9.
[458] Zhi C, Bando Y, Tang C, Huang Q, Golberg D. Boron nitride nanotubes: functionalization and composites. Journal of Materials Chemistry. 2008;18:3900-8.
[459] Chakoli AN, Wan J, Feng JT, Amirian M, Sui JH, Cai W. Functionalization of multiwalled carbon nanotubes for reinforcing of poly (l-lactide-co-ε-caprolactone) biodegradable copolymers. Applied surface science. 2009;256:170-7.
[460] Kagan VE, Konduru NV, Feng W, Allen BL, Conroy J, Volkov Y, et al. Carbon nanotubes degraded by neutrophil myeloperoxidase induce less pulmonary inflammation. Nature nanotechnology. 2010;5:354-9.
[461] Akhavan O, Ghaderi E. Graphene nanomesh promises extremely efficient in vivo photothermal therapy. Small. 2013;9:3593-601.
[462] Suggs LJ, Krishnan RS, Garcia CA, Peter SJ, Anderson JM, Mikos AG. In vitro and in vivo degradation of poly (propylene fumarate-co-ethylene glycol) hydrogels. Journal of biomedical materials research. 1998;42:312-20.
[463] Hedberg EL, Kroese-Deutman HC, Shih CK, Crowther RS, Carney DH, Mikos AG, et al. In vivo degradation of porous poly (propylene fumarate)/poly (DL-lactic-co-glycolic acid) composite scaffolds. Biomaterials. 2005;26:4616-23.
[464] Yaszemski MJ, Payne RG, Hayes WC, Langer R, Mikos AG. In vitro degradation of a poly (propylene fumarate)-based composite material. Biomaterials. 1996;17:2127-30.